IONOSPHERIC IRREGULARITIES IN THE F - REGION AT LOW LATITUDES

SHIKHA RAIZADA

Ph.D. Thesis
JULY 1998

PHYSICAL RESEARCH LABORATORY
NAVRANGPURA, AHMEDABAD 380 009
INDIA

IONOSPHERIC IRREGULARITIES IN THE F - REGION AT LOW LATITUDES

A Thesis Submitted to the
Gujarat University

for

THE DEGREE OF DOCTOR OF PHILOSOPHY
in
PHYSICS

BY

SHIKHA RAIZADA

PHYSICAL RESEARCH LABORATORY
NAVRANGPURA, AHMEDABAD 380 009
INDIA

Dedicated

to

My Parents

CONTENTS

ACKNOWLEDGEMENTS

I have great pleasure in thanking my thesis supervisor Prof. H. S. S. Sinha for his invaluable guidance throughout my Ph.D. work. I am very grateful to him for useful discussions we had, which helped me in understanding the various phenomenon in the earth's atmosphere. His knowledge about the instrumentation and his organising capabilities have benefited me a lot.

I would also like to thank Prof. H. Chandra for going through my thesis inspite of his busy schedule and for giving useful suggestions. The discussions which I had with him during my Ph. D. tenure were very useful and are highly appreciated.

I am extremely grateful to all my group members for their help and co-operation throughout my thesis work. I thank Mr. R. N. Misra for helping me during various stages of my work and for his constant encouragement shown by him. He has always being a source of inspiration to me. Discussions with him were very useful and are duly acknowledged. I thank Mr. N. Dutt for his support and for helping me in data analysis. I am thankful to Mrs Manisha Pandya for her concern and affection shown towards me. I also acknowledge her help in the data analysis. Thanks are due to Messrs. H. D. Parikh, M. B. Dadhania, R. I Patel, S. K. Sharma, , and V. K. Parmar for their help in my work.

I thank Profs. B. H. Subbaraya, S. Prakash, and R. G. Rastogi for their encouragement during my thesis time. I express my deep sense of gratitude for the interest shown by them in my work. I am also grateful to Profs. R. Sridharan and H. Chandra for their comments during my reviews. I thank Profs. Vijay Kumar, D. K. Chakrabarty., S. P. Gupta, and Drs. K P. Subramanian, A. Jayaraman, Shyam Lal, R. Sekar, and S. A. Haider for the encouragement shown by them.

I am also grateful to Dr. Sai Iyer for sorting out some of my computational problems during my thesis work.

Thanks are due to Prof. A. Bhatnagar and Dr. A. Ambastha for their co-operation and help rendered by them in digitising some of the images in Udaipur Solar Observatory (USO). I am thankful to all the staff members of USO for their co-operation.

The help provided by the staff members of the Photographic section, SHAR, during the experimental campaigns conducted from that place is duly acknowledged.

I thank Prof. V. V. Somyajulu of SPL, Trivandrum, for agreeing to our requirements of operating SHAR ionosonde at a very short notice and also for providing the ionosonde data.

I thank Mrs R. B. Barucha and her staff members for the library services. I am thankful to all the computer section staff members for their co-operation. Thanks are due to Mr. S. C. Bhavsar for his prompt services in drafting the diagrams.

My colleagues and friends, Drs Sushma, H. Misra, A. Misra, D. Hooper, K. Pandarinath, Mitaxi, Messrs. Tarun K. Dalai, Mayank Jain, deserve my special thanks for their help and support.

Thanks are due to my family and all my friends for their encouragement throughout my thesis work.

CERTIFICATE

I hereby declare that the work contained in this thesis was carried out at the Physical Research Laboratory, Ahmedabad, India. The results reported herein are original and have not formed the basis for the award of any degree or diploma by any University or Institution.

Author

Shikha Raizada 10/7/98

(Shikha Raizada)

Thesis Supervisor

H.S.S.Si 10/7/98

(Prof. H. S. S. Sinha)

STATEMENT

The work presented in this thesis was carried out by the author at the Physical Research Laboratory, Ahmedabad, India, under the guidance of Prof. H. S. S. Sinha of the Planetary Atmospheres and Aeronomy Division.

The present study is concerned with the different manifestations of irregularities in the F-region during the night, generally known as equatorial spread-F (ESF). These have been studied using various techniques which include (i) optical imaging of very large scale irregularities viz. plasma depletions, (ii) Langmuir probe for electron density fluctuations and (iii) double probe for electric field fluctuations. The author participated in the experimental campaigns conducted from SHAR for taking airglow images of plasma depletions. To investigate the importance of various agencies in ESF, the data obtained from the earlier rocket flights conducted from SHAR was analysed. The author was fully involved in the image processing, rocket data analysis as well as data interpretation.

Chapter 1 briefly reviews the current understanding of ESF phenomena. It discusses the F-region dynamics, various manifestations of nightglow emissions, ionisation irregularities in the ionosphere and their seasonal and longitudinal variations. The contribution and influence of various factors on ESF irregularities is also presented.

Chapter 2 discusses various optical, in-situ and radio techniques used fot the study of irregularities with the emphasis on optical imaging, Langmuir probe and double probe techniques which have been used in the present study. This chapter describes the instrumentation of a ground based Multi-Wavelength All-Sky Optical Imaging System developed at Physical Research Laboratory.

Chapter 3 outlines various instabilities which play a dominant role in the generation of ESF irregularities. The generation mechanism of various nightglow emissions, which have been used in the present work for mapping

of airglow depletions, has been discussed. This chapter includes the experimental campaigns, observations, and procedure of data analysis of optical images. The airglow images have been used for studying the dynamics of F-region irregularities, their zonal scalesizes, degree of depletions etc. A comparison of the present data with that obtained from American sector has also been included.

In Chapter 4 the results obtained from rocket flights conducted from SHAR at the onset time of ESF and during fully developed spread F conditions are presented. The spectral analysis of the irregularities occurring in various altitude regions has been performed and the importance of different agencies in the generation of irregularities has been discussed.

Chapter 5 discusses the electric field measurements which were obtained simultaneously with electron density discussed in the previous chapter. The procedure of electric field determination has been described in this chapter. Correlation studies of electron density fluctuations and electric field perturbations obtained in the vertical and horizontal direction, which have revealed revealed striking results, are also described.

A brief summary of the results obtained in the present work is presented in Chapter 6.

CHAPTER 1

INTRODUCTION

1.1 The Ionosphere

The ionosphere is that region of the earth's atmosphere which is characterised by the presence of a significant number of atoms and molecules and various ionised species so as to affect radio wave propagation. Its lower boundary lies around 55 km. It is considered to extend up to the altitudes of several earth radii. Radar studies of the day time ionosphere revealed a layered structure of electron concentration, which subsequently resulted in the broad classification of the earth's ionosphere into D, E and F regions as shown in Fig. 1.1. The E region of ionisation was the first to be detected and was named after the electric field of the reflected radio wave.

D-region extends from about 60 km to 85 km where electron density is much less than the molecular density. Daytime ionisation in the D-region is believed to result from three main sources: solar radiation in the band 1027-1118 Å acting on O_2 ($1\Delta_g$), solar H Lyman-alpha line at 1216 Å acting on NO, hard X-rays (2-8 Å) which ionise all constituents, including major species such as O_2 and N_2. Part of the atmosphere lying between altitudes of about 90 and 140 km is defined as the E-region. Ionisation

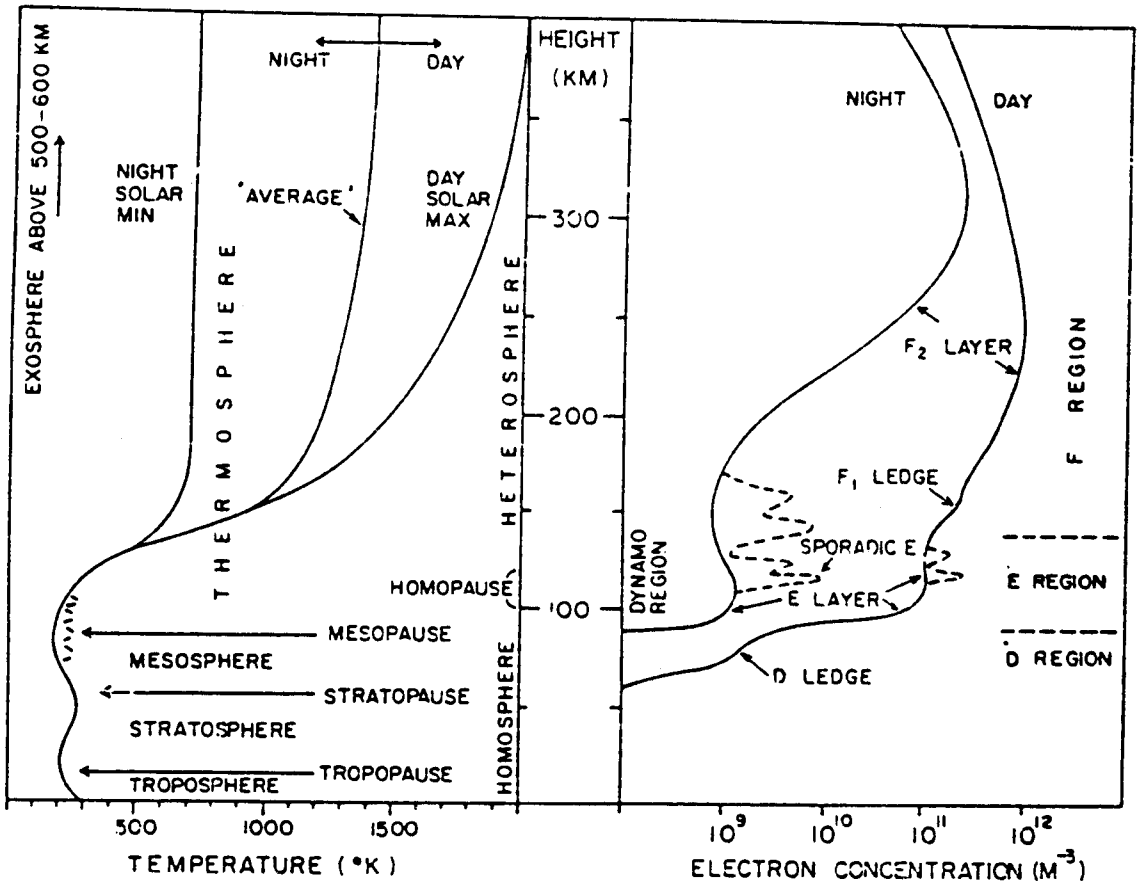

Fig. 1.1 Upper atmospheric nomenclature, classifying various thermal and compositional regions of the neutral gas (left) and electron concentration contours and associated regions (right).

results from EUV radiation with wavelength between 800-1026 Å, absorbed by molecular oxygen, and soft X-rays (10 - 100 Å). The most abundant ions in this region are NO^+ and O_2^+. Region above the 150 km altitude is classified as F region.

1.2 Formation of the Quiescent Ionosphere

Ionosphere results from the processes of ion production, balanced by those of ion loss. The major contribution to production processes comes from the photoionization by solar radiation. The most important atmospheric species at these altitudes are molecular oxygen (O_2), molecular nitrogen (N_2), and atomic oxygen (O). These species when initially in the ground states, can be ionised by photons at wavelengths shorter than 1027 Å, 796 Å, and 912 Å respectively. Longer wavelengths can be effective if the neutral species are in excited state initially. The most important example is the oxygen in metastable state O_2 ($1\Delta_g$), whose ionisation limit lies at 1118 Å. Nitric oxide (NO) is an important contributor to ionisation, despite being a minor constituent. Its ionising limit lies at 1345 Å, therefore, it is susceptible to ionisation by an intense solar emission at 1216 Å, the H Lyman alpha line.

Various factors that contribute to ionisation process during night-time are listed below:

- Cosmic rays from the space penetrate well into the atmosphere and produce ionisation by bombardment, particularly below 70 km.
- Bremsstrahlung radiation, produced by the bombarding electrons when they are stopped by the atmosphere, adds a further source of ionisation. The ionisation rate due to bremsstrahlung is about ten factor smaller than that due to the primary electrons. Below 50 km, it is the major source at times of auroral electron precipitation.
- Hydrogen and Helium atoms, within and beyond the atmosphere, can scatter appreciable solar UV radiation into the earth's shadow cone, providing a source of ionisation.

- Certain stars, emitting in the X-ray band with high intensity, provide a further source both during day and night.
- Molecules ablate from meteoroids which pass through the D and E regions; a fair proportion ionised in this process contribute to metallic ions.

All the above mentioned sources of ionisation must be balanced by the loss processes. The dominant O^+ ion is neutralised either by means of radiative recombination with the ambient electrons, a process complementary to simple photoionization, or by means of charge transfer reactions. The former is an extremely slow process compared to the latter with reaction rate of 10^{-12} cm^2 s^{-1} (Banks and Kockarts, 1973). Atomic ions are converted by charge transfer processes such as

$$O^+ + O_2 \xrightarrow{\gamma} O_2^+ + O \qquad (1.1)$$

$$O^+ + N_2 \xrightarrow{\gamma} NO^+ + N \qquad (1.2)$$

where γ is the rate coefficient. Molecular ions are inherently more susceptible to dissociative recombination, represented by

$$O_2^+ + e \xrightarrow{\alpha} O + O \qquad (1.3)$$

$$NO^+ + e \xrightarrow{\alpha} N + O \qquad (1.4)$$

Here α is rate coefficient. Nitrogen ions are removed via the process given below :

$$N_2^+ + O \xrightarrow{\gamma} NO^+ + N \qquad (1.5)$$

It is clear that the electron loss does not occur directly but by a two stage process.

$$X^+ + A_2 \xrightarrow{\gamma} AX^+ + X \qquad (1.6)$$

$$AX^+ + e \xrightarrow{\alpha} A + X \qquad (1.7)$$

Here A_2 is a common molecular species such as O_2 or N_2. The reaction rates γ and α are typically of the order of 10^{-10} cm^3 s^{-1} and 10^{-7} cm^3 s^{-1} (Banks and Kockarts, 1973).

The loss rate of electrons at most of the heights may be expressed in one of the two simple forms that help to account for ionospheric properties. The first arises when O_2^+ and NO^+ are the dominant ions. The rate of the dissociative recombination reaction is proportional to both the positive-ion concentration (n_+) and the electron concentration (n_e); these two concentrations must be equal to maintain charge neutrality. The loss rate of electrons must then be proportional to n_+n_e, which can be approximated to n_e^2. The second form of loss occurs when the concentration n_+ is dominated by atomic ions, notably O^+. Their frequency of occurrence is proportional to the concentration of the neutral species(n_n) and to n_e. So, the loss rate in this case can be represented by $\gamma\, n_n\, n_e$. Under equilibrium conditions, the production rate, q is given by

$$\frac{1}{q} = \frac{1}{\alpha N^2} + \frac{1}{\beta N} \qquad (1.8)$$

where $\beta = \gamma\, n_n$, and N is the electron concentration.

At low altitudes β is large and so all X^+ are rapidly converted to AX^+. The overall rate is then determined by (1.2) and thus α type processes dominate at lower altitudes. At higher altitudes β is small and then (1.1) is relatively slow and limits the overall rate. The predominant behaviour therefore shifts from α type to β type as the height increases. In the limiting cases,

$$q = \alpha N^2 \qquad \text{when } \beta >> \alpha N$$

$$q = \beta N \qquad \text{when } \beta << \alpha N$$

The transition from α- to β- behaviour is considered to occur at a height where $\beta = \alpha N$.

1.3 F-region

1.3.1 Electron Density

Our interest lies in the F region, which on occasions appears to be split into two, termed as F1 and F2. F1 layer appears as a ledge at the base of the F_2 layer and arises from solar radiation in the range 500-600 Å. In F_2 layer the loss rate is expressed by βN, where β depends on the concentration of neutrals as seen before.

$$O^+ + N_2 \xrightarrow{\gamma} NO^+ + N \qquad (1.9)$$

As atomic ions dominate at F-region altitudes, most of the F region ionisation is contributed from atomic oxygen, and thus production rate $q \propto [O]$. Therefore the equilibrium electron density is

$$N_e = \frac{q}{\beta} \qquad (1.10)$$

$$N_e \propto \exp\left[-\frac{h}{H(O)} + \frac{h}{H(N_2)}\right] \qquad (1.11)$$

where H(O) and $H(N_2)$ are the scale heights for O and N_2. As the masses of N_2 and O are in the ratio of 1.75:1, the electron density varies with altitude as,

$$Ne \propto \left[+0.75\frac{h}{H(O)}\right] \qquad (1.12)$$

The above equation represents a layer whose electron density increases with altitude since the loss rate falls off more rapidly than the production rate. However, above the F_2 peak, transport becomes more important than recombination as the atmospheric density is less at those altitudes. The

maximum in n_e occurs when the two loss processes - β type and transport are equally important.

In the F_2 region electron density is determined mainly by three types of plasma motion :

- Diffusion
- Neutral winds
- Electromagnetic drifts.

Effect of Diffusion

The continuity equation is given as

$$\partial N_e/\partial t = q - L - \text{div}\,(N_e\,\mathbf{v})$$

where q is the rate of production of ions, L is the rate of loss of ions and electrons, N_e is the electron density and $\mathbf{v}$ is the plasma velocity. Plasma diffusion maximises along the geomagnetic field lines. Since the diffusion coefficient is inversely proportional to the neutral density, diffusion increases rapidly with height. Diffusive separation in a plasma differs from that in a neutral gas because as the light electrons separate from the heavier positive ions, an electric field is established so that the electrons and ions move together (ambipolar diffusion).

For an electron-proton gas in the F_2 region, ambipolar electric field, E $\approx$ 0.05 μV/m, and for an electron-oxygen ion gas E $\approx$ 0.77 μV/m. Thus, this coupling causes the mean mass of the electron-ion pair to become half the ion (gas) mass and the plasma scale height is twice that of the neutral mass.

Effect of Neutral winds

Neutral winds result from differential heating of the neutral air by solar radiations, energy input into the auroral zones by electron bombardment and Joule power dissipation. Normally, the air is hottest at sub-solar point, the resulting pressure gradients drive horizontal winds from the dayside to

the nightside. In the F_2 layer, the low collision frequency compared to that of the lower altitudes, restricts the motion of the ions by the horizontal neutral wind, across the Earth's magnetic field. The ions can move along the field but not across it. However, at mid-latitudes, an equatorward wind lifts plasma whereas the poleward wind lowers the plasma in altitude. Because the loss rate decreases with height, the equatorward wind results in an increase of the electron density and the poleward wind decreases it. In low magnetic latitudes, transequatorial winds transport plasma from one hemisphere to the other producing hemispherical asymmetry in the F_2 region.

Effect of Electromagnetic drift

Electromagnetic (**E X B**) drifts are important in the F_2 layer, since it is the main mechanism that can cause plasma to move across magnetic field lines.

At low latitudes vertical **(E X B)** drifts play an important role in establishing the distribution of electron (ion) density in the F_2 region. The height of maximum electron density, h_mF_2, acquires very high altitude (F_2 peak can be above 500 km) by ~ 1900 hrs LT and then falls such that at midnight it is about 100 km lower than at noon. This evening uplift results from the **E X B** drift caused by prereversal enhancement of the eastward electric field which will be discussed later on.

1.3.2 Electric Fields

The ionospheric electric fields play a dominant role in low-latitude electrodynamics. In the equatorial E-region the east-west electric field drives the equatorial electrojet (Untiedt, 1967; Sugiura and Poros, 1969; Richmond, 1973; Forbes and Lindzen, 1977) and the associated plasma instabilities (Fejer and Kelley, 1980). In the F region the plasma transport across the magnetic field lines is controlled by the E X B drift. The daytime upward drift at the equator, and subsequent diffusion along field lines, result in ionisation transport towards higher latitudes, causing the Appleton or equatorial anomaly (Hanson and Moffet, 1966; Anderson, 1973, 1981). The generation of electric fields is discussed below.

1.3.2a Generation of Electric Fields

Electric fields in the ionosphere arise when the ions and electrons respond differently to the forces acting on them. These forces may be related to the plasma pressure gradients, to the magnetic and gravitational fields, and to the atmospheric winds. The electric current associated with the difference between the ion and electron velocities has a finite divergence which is expressed quantitatively by the current divergence equation:

$$\nabla.\mathbf{J} = - \partial\rho_c/\partial t \qquad (1.14)$$

Any charge density, ρ_c, must create electric fields through Poisson's equation

$$\nabla.\mathbf{E} = \rho_c/\varepsilon_o \qquad (1.15)$$

where ε_o is the permittivity of the medium. Thus if the complex forces acting on the ions and electrons create a divergence in the current, an electric field builds up quickly to modify the velocities so that $\nabla.\mathbf{J} = 0$. The time scale, τ, for build up of such a charge density can be estimated from the above equations.

$$\tau \sim \rho_c/\nabla.\mathbf{J} = \varepsilon_o\nabla.\mathbf{E}/\nabla.\mathbf{J} \qquad (1.16)$$

Using $\mathbf{J} = \sigma E$ and assuming σ to be constant,

$$\tau = \varepsilon_o/\sigma \qquad (1.17)$$

Using the lowest value of any component of σ in the ionosphere, the largest value for $\tau = 10^{-6}$ s. Electric fields thus build up very quickly in response to any divergence of **J**. The latter arise whenever there are spatially varying forces on the plasma or when conductivity changes in space. Thus the electric field acts as a free parameter that adjusts in magnitude and direction to fit the requirement that $\nabla.\mathbf{J} = 0$.

At high latitudes when electric fields are applied from an external source due to the solar wind - magnetosphere interaction, the quantity **J.E** is

positive in the ionosphere. The electrical energy is converted into mechanical energy in the ionosphere and is released in the form of heat. Joule heating is a important process at high latitudes and it greatly affects the thermospheric winds. In this case the ionosphere acts like an electrical load on some external generator. Similarly the momentum may be transferred to the thermospheric wind through the ion drag if the ions are driven strongly by an electric field. In such a case the ionosphere-magnetosphere system acts like a motor wherein the electrical energy gets converted into the mechanical energy.

Earle and Kelley (1987) performed spectral analysis of a number of incoherent scatter radar data sets obtained from various locations, for understanding the sources of electric fields with periods in the range of 1 - 10 hours. It was shown that for this range of periods the zonal electric field at Jicamarca has a transition from atmospheric to magnetospheric sources at a K_p level of roughly 3. Below this level of activity, fluctuating atmospheric winds dominate the signal while at higher K_p levels, fluctuations in the magnetospheric electric filed determines the zonal component of the electric field over Jicamarca. Balan et al. (1993) presented the power spectra of the fluctuating component of the east-west electric fields at the magnetic equator. The electric fields were inferred from vertical plasma drift observations from Trivandrum (dip 0.9° S) using HF Doppler radar. They found that the spectra displayed very little day to day variability and have no appreciable changes with geomagnetic activity. From the spectral characteristics of electric field they suggested that the medium scale gravity waves could be a source for the observed fluctuations in the east-west electric fields in the post-sunset F-region. Viswanathan et al. (1993) found good correlation between E and F-region electric field perturbations and suggested that the electric fields in the E-region at low and equatorial latitudes are coherent for the temporal scales of the order of few tens of minutes. They attributed the observed fluctuations in E and F-region electric fields to the medium scale gravity waves.

1.3.2b F region Dynamo

When an electric field is created by a wind, the process is often called a dynamo because of its similarity to a motor driven electric generator in which a conductor is moved across a magnetic field. The basic theory of ionospheric conductivity has been discussed earlier (Cowling, 1945; Baker and Martyn, 1952). The conductivity is strongly anisotropic because of the geomagnetic field. Considering z in upward direction, **B** pointing in y direction which is horizontal and northward, x towards the east , the conductivity tensor is given below

$$\sigma = \begin{pmatrix} \sigma_p & 0 & \sigma_H \\ 0 & \sigma_o & 0 \\ -\sigma_H & 0 & \sigma_P \end{pmatrix} \tag{1.18}$$

where σ_P is the Pederson conductivity, σ_H is the Hall conductivity and σ_o is the longitudinal conductivity and these are expressed as given below.

$$\sigma_P = \frac{ne}{B}\left[\frac{\omega_i \nu_i}{\left(\omega_i^2 + \nu_i^2\right)} - \frac{\omega_e \nu_e}{\left(\omega_e^2 + \nu_e^2\right)}\right] \tag{1.19}$$

$$\sigma_H = \frac{ne}{B}\left[\frac{\omega_e^2}{\left(\omega_e^2 + \nu_e^2\right)} - \frac{\omega_i^2}{\left(\omega_i^2 + \nu_i^2\right)}\right] \tag{1.20}$$

$$\sigma_o = n_e^2\left(\frac{1}{M_i \nu_i} - \frac{1}{m_e \nu_e}\right) \tag{1.21}$$

where ω_i and ω_e are the gyrofrequencies of the ions and electrons respectively, ν_i and ν_e represent the collision frequencies of ions and electrons with the neutrals, M_i is the mass of ions and m_e is the mass of the electrons.

The Pederson and Hall conductivities depend on the ratio of gyrofrequency (ω) to collision frequencies with neutral particles (ν) for both ions and electrons (Rishbeth and Gariott, 1969; Rishbeth, 1981). At any ionospheric height $(\omega/\nu)_e = 10^3(\omega/\nu)_i$. The disparity between their ratios (ω/ν)

causes ions and electrons to move differently in response to an applied electric field E or a neutral wind U. In the F region $\sigma_P >> \sigma_H$ and $\sigma_P << \sigma_o$ The F region electrodynamics can be understood by considering a simple model in which the horizontal magnetic field lines terminate at both ends in an insulating layer. This insulating layer is the E region where the conductivity decreases during the night-time. As the vertical component of the large scale neutral wind field is small most of the times, the eastward component of thermospheric wind with magnitude u, that is uniform with height is assumed. Since $J = \sigma . [E + U \times B]$, an electric current will flow with magnitude and direction given by

$$\mathbf{J} \approx \sigma (\mathbf{u}_x \times \mathbf{B}) \qquad (1.22)$$

The wind driven current is therefore vertically upward with magnitude $J_z = \sigma_P uB$. The current density, J_z is very small with a peak value of the order of 0.01 $\mu A/m^2$. However, σ_P varies with altitude due to its dependence on the product $n\nu_{in}$. The altitude variation of the zonal wind component is small. This implies that $d(\sigma_P uB)/dz \neq 0$. As a consequence an electric field is set up in the vertical direction to produce a divergence free current. However, the E region at the ends of the magnetic field lines, which acts like the insulating plates, due to low conductivity in the night-time, does not allow a magnetic field aligned current to flow at all ($J_y = 0$). During night time the molecular ions are destroyed by recombination in the bottomside of the F layer, thus forming a steep upward density gradient. This situation can be approximated by a slab geometry model with σ_P constant inside the slab and zero elsewhere and with zonal wind u constant else where. Since the current is upward inside the layer and zero outside, charges accumulate at the two boundaries as shown in the Fig. 1.2. The magnitude of the electric field which builds up as a result of these charges is such that

$$J_z = \sigma_P E_Z + \sigma_P uB = 0 \qquad (1.23)$$

which yields $E_Z = -uB$ (6 mV/m for U = 200 m/s, B = 30 μT). The plasma inside the slab will drift with an $(\mathbf{E} \times \mathbf{B})/B^2$ velocity equal in magnitude and

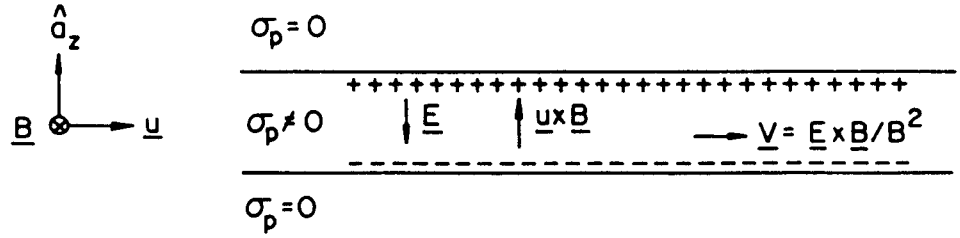

Fig. 1.2 Picture showing electrodynamics of the equatorial F-region assuming a slab geometry model and a constant zonal eastward neutral wind (After *Kelley,* 1989).

direction to the zonal wind speed. Heelis et al. (1974) confirmed that the vertical polarisation field can produce a strong eastward drift of the F region plasma at night which through the operation of ion drag imparts an eastward motion to the neutral air. King-Hele and Walker (1977), explained this on the basis of the net eastward thermospheric wind at night; the super-rotation, revealed by study of the orbital perturbations of artificial satellites.

1.3.2c Morphology of Electric Fields

Most of the recent equatorial electric field data were obtained from F region drift observations with 50 MHz Jicamarca incoherent scatter radar. The drifts $\mathbf{V_i}$ are related to the ambient perpendicular electric field, $E_\perp$, through the relation:

$$\mathbf{E_\perp} = - \mathbf{V_i} \times \mathbf{B} \qquad (1.24)$$

The initial observations of F region vertical drifts were presented by Woodman (1970). The daytime drifts are upwards with an average velocity ~ 20 m/s, corresponding to an eastward electric field of 0.5 mVm^{-1}. The night time drifts are usually slightly larger, but in opposite direction. The day to day and seasonal variations of the vertical drifts during solar maximum and minimum conditions have been reported earlier (Woodman et al., 1977; Fejer et al., 1979; Fejer et al., 1981). The seasonal dependence of the average vertical drifts obtained during magnetically quiet conditions is shown in the Fig. 1.3., where the summer data is representative of moderate

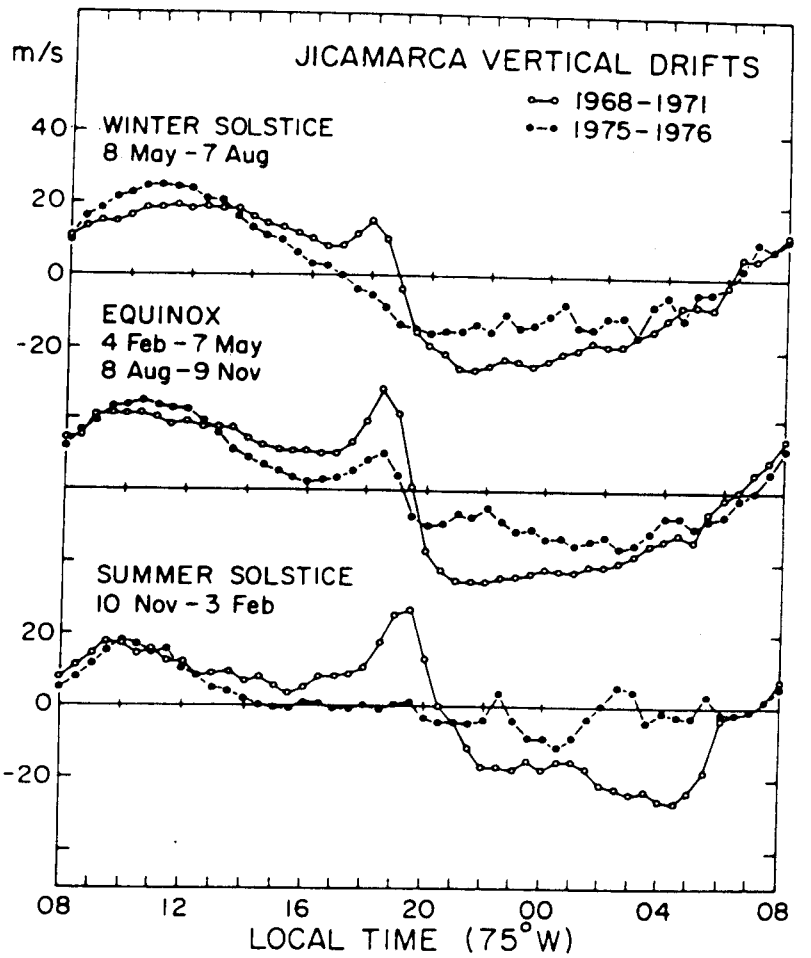

Fig. 1.3 Measured vertical drift component in equatorial F-region (positive values correspond to upward motion). Positive values indicate eastward direction. Open and filled symbols represent solar maximum and minimum activity periods respectively (After *Fejer et al.*, 1979).

magnetic activity. The main features of the solar maximum and minimum data can be summarised as follows:

a) The vertical drift is often strongly enhanced just after sunset but shows no comparable feature near sunrise.

b) During solar maximum, the evening pre-reversal enhancement is observed throughout the year. However, this feature is not seen during solar minimum except during equinoctial months.

c) The evening reversal time from upward day time to downward night time drifts exhibits seasonal and solar cycle variations. During solar minimum, it occurs few hours earlier than at maximum. The reversal time is latest during the summer months at sunspot maximum and earliest during the solar minimum winter months.

d) The solar maximum daytime drifts are slightly smaller except during summer, than the corresponding solar minimum values but the evening and night time drifts are substantially larger at solar maximum than at the minimum.

The F region east-west drifts are driven by the F-region vertical electric field, which is coupled along the magnetic field, lines to the E region at slightly higher latitudes. Their general characteristics, seasonal as well as solar cycle dependence have been reported previously (Woodman, 1972; Fejer at al., 1981). The average F region east-west drifts during solar maximum and solar minimum period can be seen in the Fig. 1.4. The morning and early afternoon drifts are westward with a maximum value ~ 45 ms^{-1} around noon. The night time eastward drifts are maximum at about 2100 hrs LT. Fejer et al. (1981), showed that the east-west drifts display day to day variability with frequent wave like fluctuations. The night time F region eastward drifts measured with the spaced receiver technique in India (Chandra et al., 1970; Rastogi et al., 1972) are of the same order as the Jicamarca drifts. It is to be noted that a zonal eastward drift is due to a

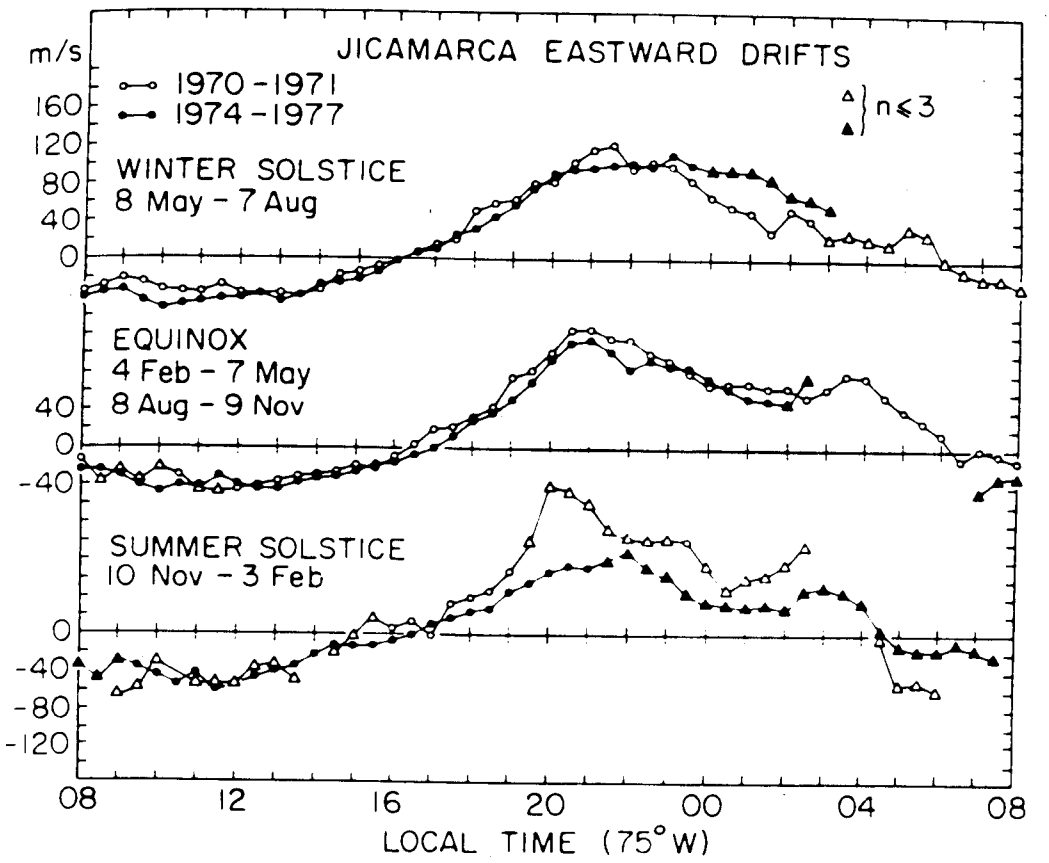

Fig. 1.4 Zonal plasma drifts in the equatorial F-region measured for different seasons and solar conditions. Notations have same meaning as in Fig. 1.3 (After Fejer et al., 1981).

vertically downward electric field, with a 100 m/s drift corresponding to a 2.5 mV/m electric field for $B = 2.5 \times 10^{-5}$ T.

The diurnal variation in the vertical electric field (zonal winds) can be understood using F-region dynamo discussed earlier. At night, the vertical electric field and hence the horizontal plasma flow, is determined by the zonal winds in the F region owing to the poor conductivity of E region This happens as the integrated Pederson conductivity in E region Σ^E_P becomes small and hence E_z is nearly equal to -UB in regions where the integrated Pederson conductivity in F region, Σ^F_P, is large, i.e. near the peak in the F region plasma density. During the day time, however, the E region conductivity is large and the vertical F-region polarisation fields generated through F-region dynamo are short circuited. Therefore for large Σ^E_P the E-region controls the electrodynamics of the ionosphere with the E-region dynamo being driven by tidal winds. Thus the resulting electric fields in the F region during daytime are governed by the winds in E region which tends to be weaker and so the plasma drift is smaller during the day. This explains the diurnal variation in the F region zonal plasma drifts.

The Prereversal Enhancement

The upward drift at the sunset which is the result of the post sunset prereversal enhancement of the zonal field occurs during all epochs and seasons except for solar minimum solstices. This causes the uplift of the F layer to very high altitudes where recombination effects and collisions are less.

The enhancement was reproduced by Heelis et al. (1974) in their numerical simulation work. They found that by considering only a diurnal E region tidal mode in their model, postsunset increase in the F region electric field could not be reproduced. However, when the horizontal conductivity gradients near sunset in the F region dynamo mechanism were incorporated

in the simulation, the calculated vertical velocity showed the pre-reversal enhancement in agreement with the observations as shown in the Fig. 1.5.

Later on, Farley et al. (1986) completely suppressed the E region dynamo and included the E region conductivity along with its loading effect on the F-region electrodynamics and a uniform 200 ms^{-1} eastward wind in their simulation work. Their results showed that (a) the plasma drift rises to a value less than, but comparable to, the wind speed at night and is negligible during daytime due to E region shorting effects and (b) the enhancement at both the terminators, indicating that it is clearly an F region dynamo effect. But the simulation is not applicable at the dawn, where the wind direction is reversed.

The mechanism of the F-region pre-reversal enhancement can be understood by considering a model shown in the Fig. 1.6. Here the vertical plane represents the equatorial plane whose projection onto the southern hemisphere along B is shown in the form of horizontal plane. As discussed in F- region dynamo, the zonal wind , U, blowing across the terminator gives rise to downward vertical electric field E_z on both the sides. As the conductivity along B is large, E_z map along B to an equatorward electric field component at off equatorial latitudes. Since the Hall conductivity during dayside exceeds the night time value by about 10 times, E_z generates a westward Hall current $J_{\theta\varphi}$. Since the current cannot flow in the night side E region, a negative polarisation charge must develop at the terminator which generates E_φ. This field maps back to the F region and causes first an upward (day) and then downward (night) $\mathbf{E} \times \mathbf{B}$ plasma drift.

1.3.3 Airglow

As a result of the photochemical reactions taking place in the upper atmosphere, quanta of radiation are emitted in the ultra violet, the visible or the infra red parts of the electromagnetic spectrum. These emissions comprise the airglow. The airglow emissions depend on the creation of an excited species and its subsequent return to the ground state. The

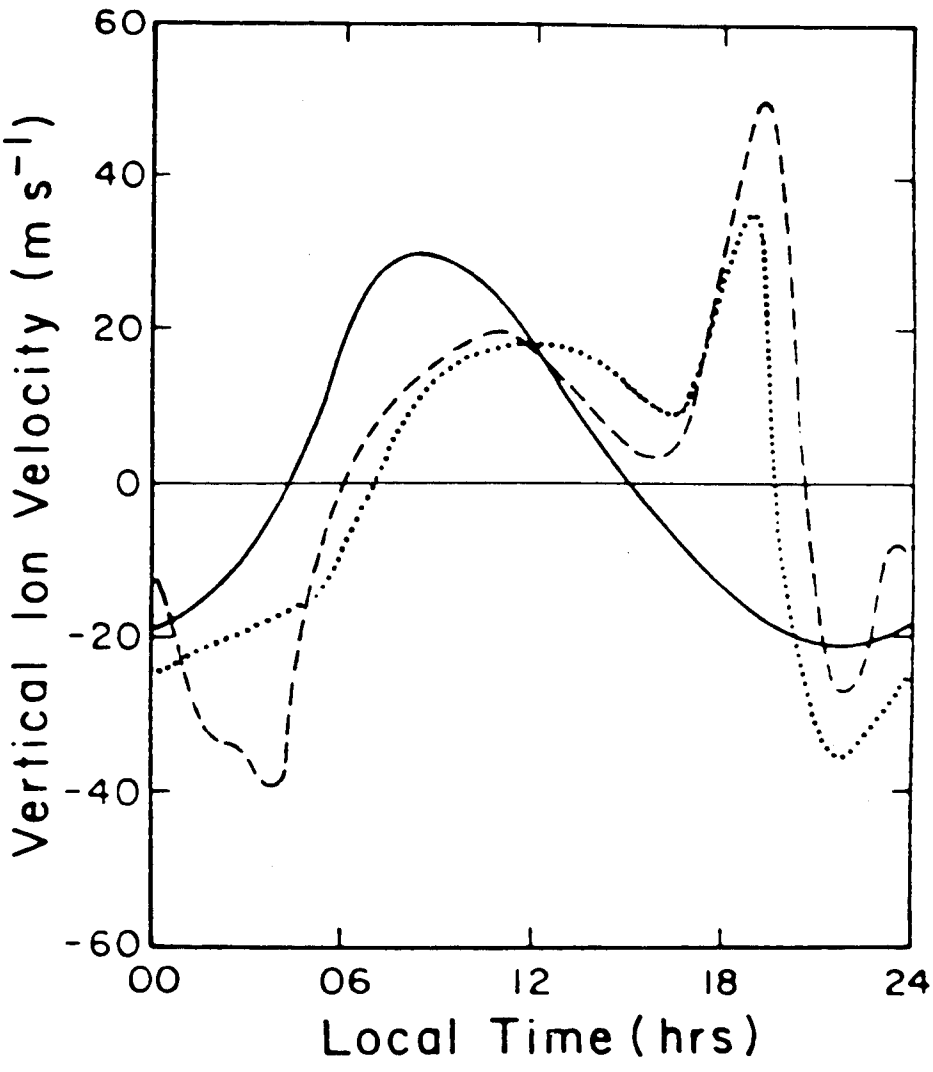

Fig. 1.5 Local time variation of vertical ion drift velocities calculated using different driving wind components. The solid line represent velocities obtained using only the tidal-driven E-region dynamo, while the dashed line includes the F-region dynamo also. Dotted line shows the typical measured vertical plasma drifts (After *Heelis et al.*, 1974).

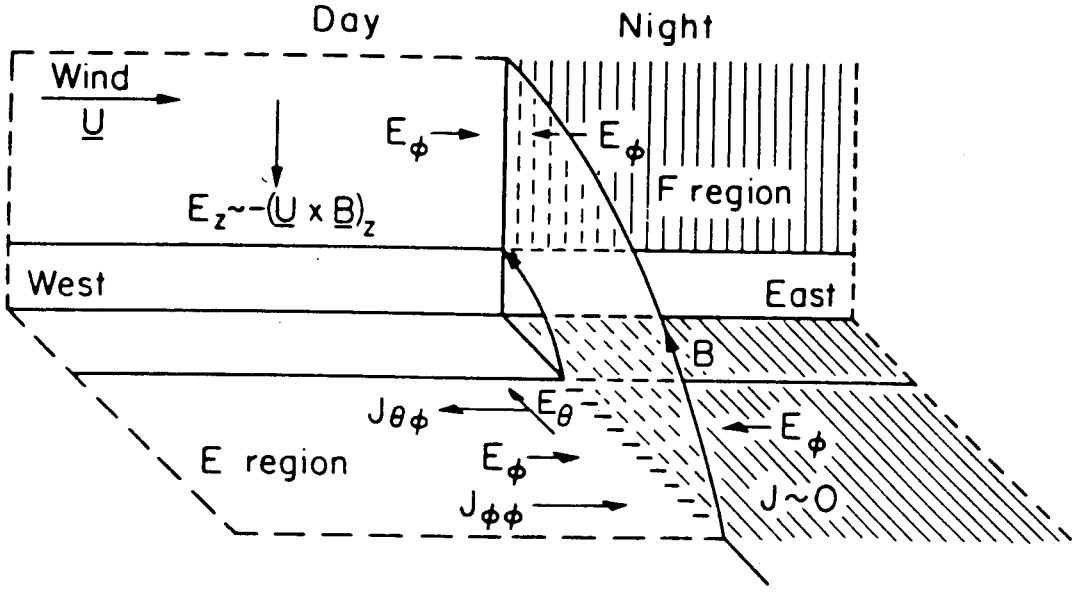

Fig. 1.6 Diagram explaining the mechanism of the F-region pre-reversal enhancement driven by a uniform F-region wind U (After *Farley et al.*, 1986).

immediate causes are of several kinds: (a) radiative recombination reactions; (b) de-excitation of reactions products in excited state; (c) formation of excited species by hot electrons (from ionisation processes) and by electric fields; (d) the excitation by solar radiation, giving rise to resonance emissions.

Many series of airglow emissions are observed arising from atomic oxygen, molecular oxygen, molecular and atomic nitrogen, hydrogen, hydroxyl radicals, nitric oxide and alkali metals. The hydroxyl emissions in the infra red originate at altitudes near 90 km and are important as a mechanism of heat loss. The emissions from alkali metals provide examples of resonant scattering, which are most strongly visible during twilight. The emissions reveal the presence of Na, K, Li, and Ca at the 90 km level. Airglow emissions provide a unique opportunity for studying various interesting phenomenon occurring in the earth's atmosphere. The interaction between neutrals and plasma can modulate the airglow intensity, thus enabling one to study dynamics of the neutrals and ionised species in the regions where the airglow originates. Some of the manifestations of the airglow emissions are discussed below.

Meridional Intensity Gradients (MIG)

This refers to a sharp gradient in the meridional intensity distribution of the nightglow emissions generally observed on magnetically disturbed nights. This feature has been seen in the airglow emissions at 630 nm at mid-latitudes, Arecibo (dip angle ~ 50°) and is observed to move from east to west (Sobral et al., 1978; Herrero and Meriwether, 1980). Herrero and Meriwether (1980) interpreted MIG phenomena in terms of a velocity gradient that is generated by the confluence of opposing meridional neutral winds. The circulation models of Dickinson et al. (1975, 1977) and Roble et al. (1982) predict that under disturbed conditions a reasonable energy source at high latitude (magnetic storm) generates a wind system strong enough to reach the equator as seen in Fig. 1.7. They showed that the

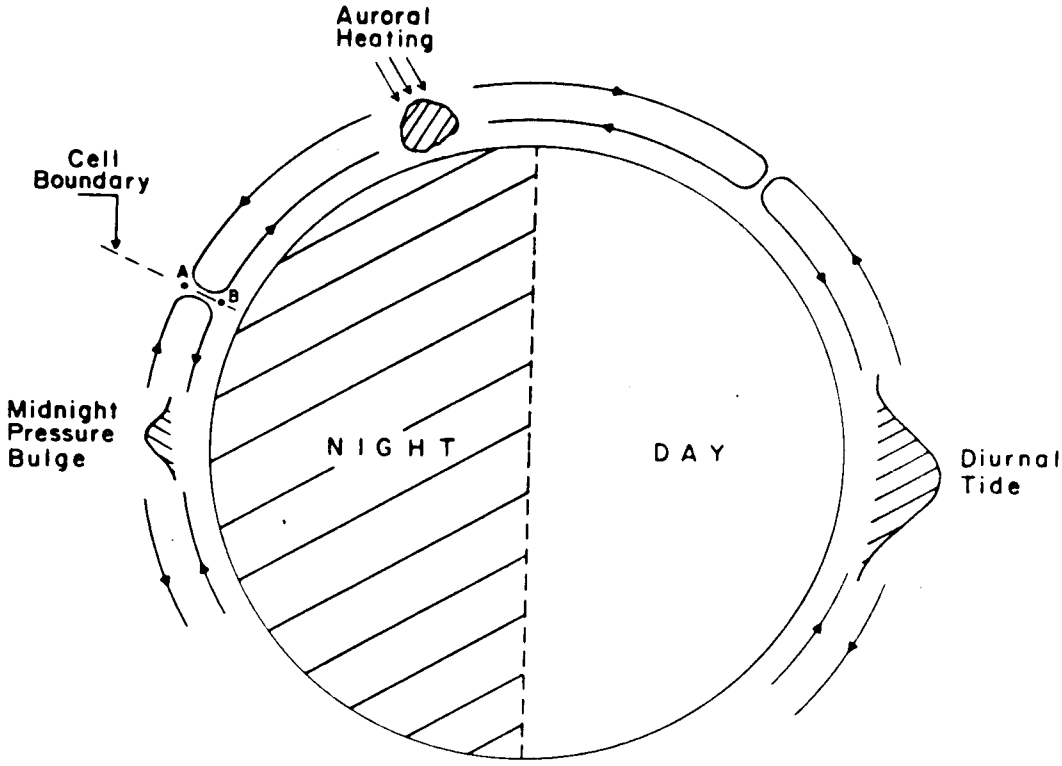

Fig. 1.7 Schematic illustration of global circulation cells in the presence of midnight pressure bulge. Line AB shows the boundary between the pressure bulge cell and the high latitude cell excited by auroral heating (After *Herrero and Meriwether,* 1980).

circulation develops an equatorward mass flow at high altitudes (above 200 km) with a return path towards the pole at an altitude near 100 km. This originates as a result of a circulation system in which midnight sector of the equatorial thermosphere below 200 km is heated by a compressive flow driven by the solar heating on the dayside. At the point of convergence (near midnight), upward and downward motions are generated by virtue of continuity. The auroral heating at high latitudes also produces northward meridional winds penetrating to low latitudes in the summer hemisphere. The southern wind system results from the equatorial midnight pressure bulge that is formed by the thermal tides of the lower atmosphere combined with the in-situ forcing by EUV radiation absorption in the day time. In the presence of magnetic storm the combining effects of the two opposite systems results in a sharp front over a latitudinal width of several hundred kilometres. The ionosphere on the northern side of the front is at a higher altitude resulting in weak airglow whereas on the southern side, the low altitude of the ionosphere causes increased airglow brightness because of enhanced coupling between neutrals and plasma. Herrero and Meriwether (1980) estimated the meridional intensity gradient (0.1 R/km) as well as the magnitude of the winds in the midnight pressure bulge to roughly around 40 m/s which matches closely with the value obtained by Spencer et al. (1979) using the satellite data.

Airglow Enhancements

Greenspan (1966) discovered an enhancement of the atomic oxygen 630 nm airglow in observations which were carried out on board the ship U.S.N.S. Croatan as it travelled from North to South America. They found an intensity pattern as shown in the Fig. 1.8, having an east-west extent of about 50° (3 to 4 hrs duration) and spanning about 20° in the north-south direction. The centre of the pattern displays a region characterised by an airglow intensity 2 to 3 times larger than the background intensity, located at the anti-solar point. Nelson and Cogger (1971) observed 630 nm airglow

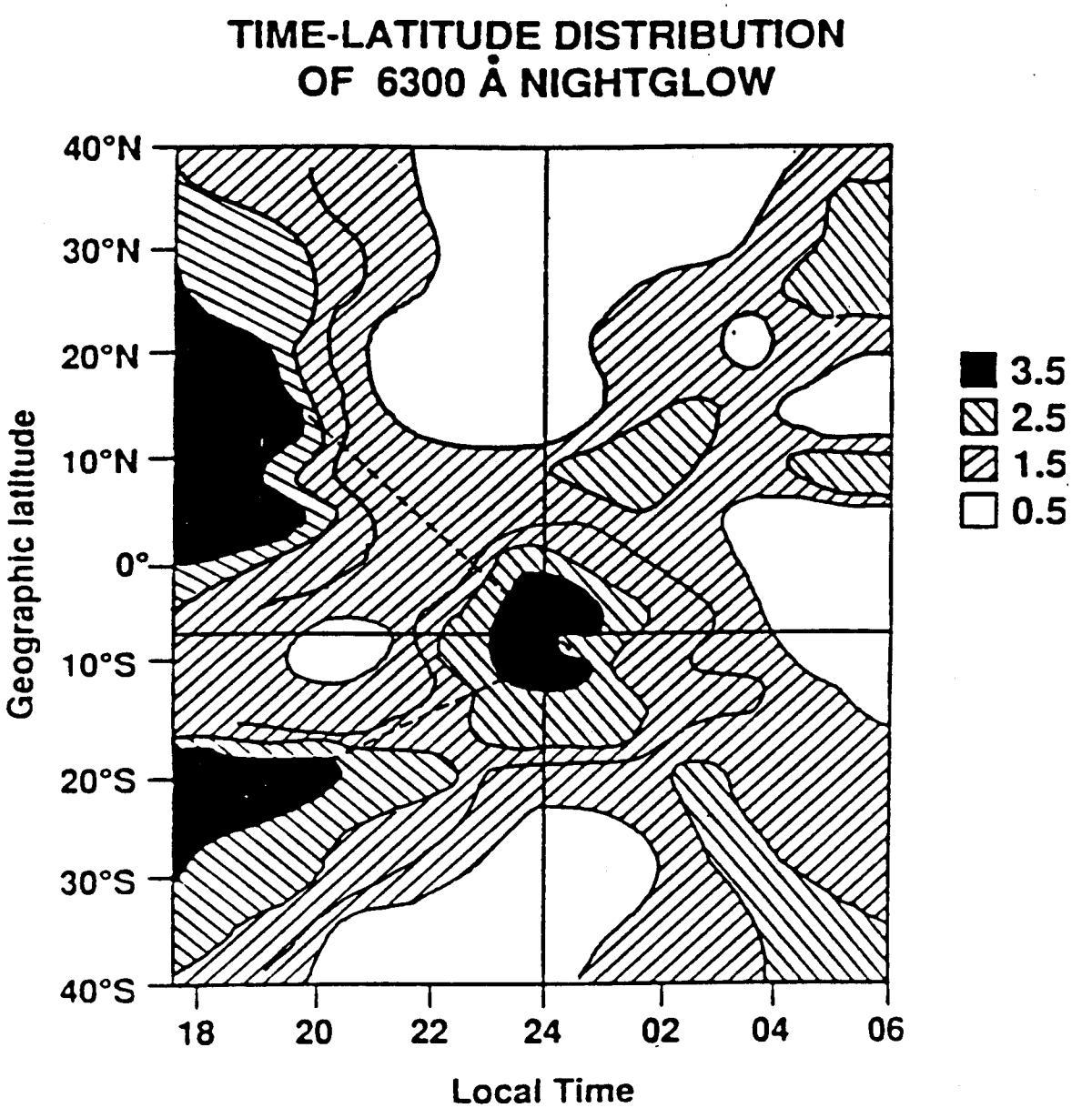

Fig. 1.8 Isophote of OI 630 nm airglow intensity in four shades using relative units of intensity (After *Greenspan,* 1966).

enhancements at Arecibo (18°N) which they associated with the descent of the F region around midnight and also found that the descent occurred at later local times with increasing geomagnetic latitude. Wright (1971), using the spaced receiver technique in Concepcion, Chile (35°S) found a descent of the F region around midnight and concluded that it was due to the variation in neutral wind. He also noted that the descent was strongest near a magnetic dip angle of 45° at both hemispheres. The descent was interpreted in terms of the meridional wind variation by Behnke and Harper (1973) who found that the equatorward wind abates before midnight and frequently reverses to poleward after midnight. In the F region the equatorial midnight pressure bulge controls the night time neutral wind, giving rise to abatements and sometimes reversals of the meridional wind often observed after midnight at Arecibo with incoherent scatter radar (Behnke and Harper, 1973), with the Fabry - Perot interferometer (Burnside et al., 1981; Friedman and Herrero, 1982), and with ionosonde data (Batista et al., 1997). It has been observed that the abatement and reversal of the meridional wind exhibits seasonal variation (Rao and Sastri, 1994; Hari and Krishnamurthy, 1995).

Using the OI 91.9, 130.4 and 135.6 nm UV night glow emissions, observed from STP--78-1 satellite, Abreu et al. (1986) reported enhancements in OI 130.4 and 135.6 nm emission near the magnetic equator believed to be caused by neutral particle precipitation during magnetically disturbed periods. Yee and Abreu (1987) observed an enhancement of the night-time ratio of the OI 630 nm and 557.7 nm emission intensities from AE satellite measurements made near the equator during magnetically disturbed periods. The N_2^+ 391.4 nm emission is normally absent in the tropical nightglow during magnetically quiet conditions. However observation of this emission have been reported during magnetically disturbed conditions from low latitude regions (Tinsley et al., 1982; Rohrbaugh et al., 1983; Sahai et al., 1988). This emission is thought

to arise from the collisional ionisation and excitation of N_2, due to energetic neutral particle (H_2, O, and He atoms) precipitation (Tinsley et al., 1982).

Sometimes the airglow images obtained by all sky imagers, display bright regions of intensity which have been referred as Brightness waves observed during MISETA campaign (Mendillo et al., 1997a). They observed the regions of 557.7 nm and 630 nm brightness which appeared first slightly to the north east of zenith and exits towards the south west. They suggested this to be the consequence of an anomaly associated with the thermal behaviour of the upper atmosphere. They found that the average poleward speed of this feature was around 300 $\pm$ 31 m/s. They conjectured that the brightness wave results from airglow produced by poleward winds generated by the midnight temperature maximum (MTM) which was first reported by in-situ observations of AE-E satellite (Spencer et al., 1979). They indicated that the amplitude of the night-time temperature maximum can sometimes be as large as the principal daytime maximum (Fig. 1.9). Mayr et al. (1979) proposed that MTM is a consequence of the ion-neutral momentum coupling associated with the diurnal variation in the zonal winds and ion density. The block diagram of the generation mechanism as shown in Fig. 1.10. The diurnal tide is generated mainly due to the absorption of solar EUV radiation. The semi-diurnal tide has three major components, one contributed by EUV is small. The other two components are contributed from the combined effects of the tidal waves originating in the lower atmosphere and the momentum coupling associated with the diurnal variations of the wind fields and ion density, which are of comparable magnitude but opposite in phase. Momentum coupling associated with the diurnal variations in the ion drag is the dominant excitation process. These account for the large variabilities in the observed temperatures during the midnight reported earlier (Spencer et al., 1979; Bamgboye and McClure, 1982; Herrero and Spencer, 1982; Ranganath Rao and Sastri, 1994).

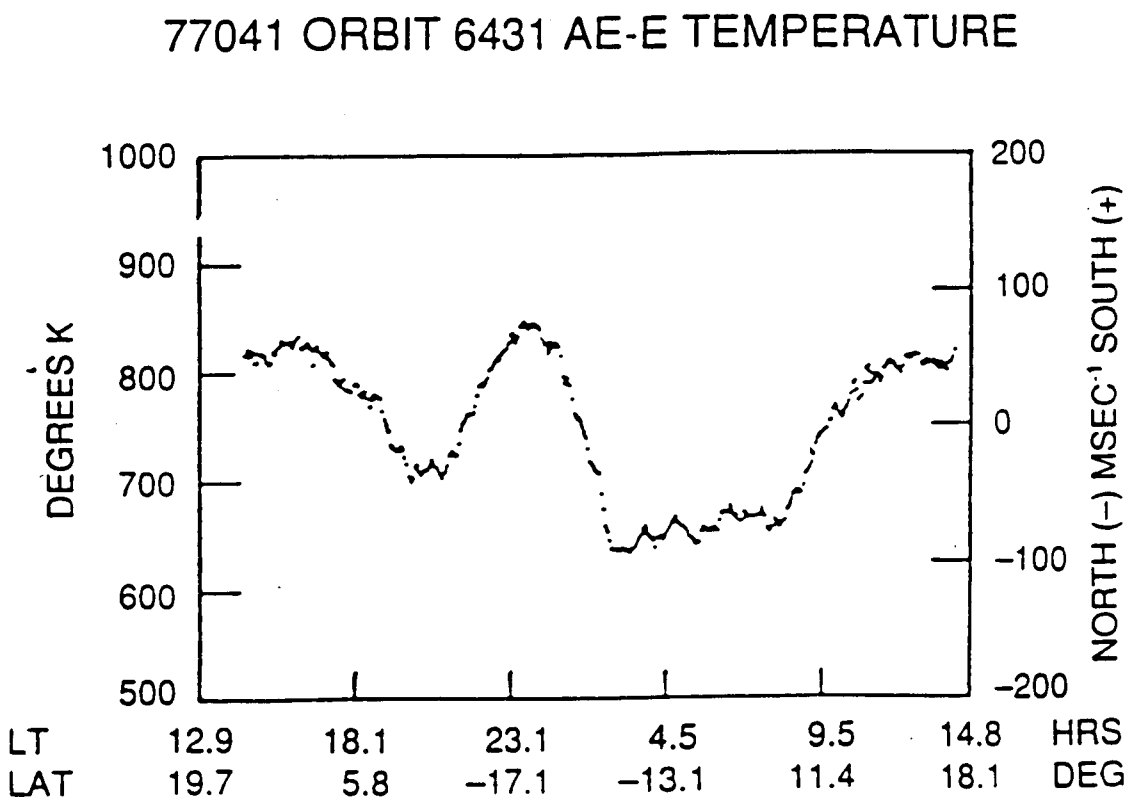

Fig. 1.9 Example showing the largest midnight temperature maximum observed with NATE instrument on the AE-E satellite (After *Spencer et al.*, 1979).

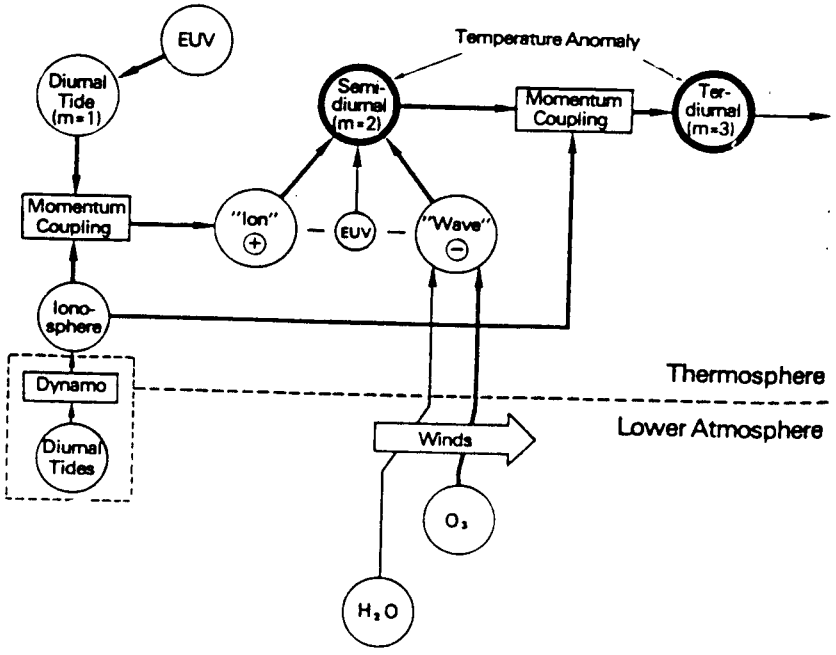

Fig. 1.10 Block diagram illustrating the processes that contribute to the midnight temperature anomaly (After *Mayr et al.*, 1979).

Airglow Depletions

Airglow studies of the equatorial ionosphere revealed departures from uniform airglow contained within the broad intertropical arcs. This new approach was the consequence of a technique developed by Mende and Eather (1976) and Mende et al. (1977), which made use of wide angle optics. Later on Weber et al. (1978, 1980) using this technique, obtained an interesting series of 'equatorial airglow depletions' from all sky imaging observations of 630 nm. They observed that the regions of reduced 630 nm intensity were north-south aligned, had east-west dimensions of 500-700 km, often extended to more than 1200 km in north-south direction. Moore and Weber (1981) modified the system to include 777.4 nm images and associated the equatorial airglow depletions to the ionsopheric irregularities. Mendillo and Baumbgarderner (1982) developed a ground based system for studying the characteristics of airglow depletions and later on followed by others (Rohrbaugh et al., 1989; Mukherjee et al., 1993; Sinha et al., 1996; Sahai et al., 1994a; Bittencourt et al., 1997; Mendillo et al., 1997a, b; Tinsley et al., 1997).

Interferometric observations of 630 nm nightglow from Arequipa, Peru, (16.2°S, 71.4°W, 3.2° dip latitude) revealed airglow depletions different from airglow reductions (Meriwether et al., 1985). They observed a drop in intensity by a factor of 3 to 4 in the depletions and were correlated closely with large increases of equatorward (northward) wind and the 630 nm kinetic temperatures. They suggested that the reduction in airglow intensity results from an upward movement of the ionosphere along the inclined magnetic field lines, driven by the equatorward neutral wind.

1.4 Ionisation Irregularities in the Ionosphere

Various plasma instability phenomena manifest in the form of ionospheric irregularities which can be classified as electrojet irregularities, mesospheric irregularities and F-region irregularities.

The occurrence of an anomalous scattering region in the ionospheric E region close to the dip equator was observed initially from ionosonde records, identified as 'equatorial sporadic E' (E_{sq}) echoes. Matsushita (1951) showed that the intensity of the E_{sq} was well correlated with the electrojet strength. E_{sq} irregularities are confined between 90 - 105 km during the day, and upto $\approx$ 135 km during the night. They are ever present, except for counter electrojet conditions during the day and zero E-W electric fields in the night.

Radar spectral studies have shown the existence of two classes of irregularities, known as type 1 (Bowles at al., 1960, 1963; Bowles and Cohen, 1962) and type 2 (Cohen and Bowles, 1967; Balsley, 1969), associated with electrojet. Type 1 is characterised by a narrow Doppler spectrum with a Doppler shift centred at the corresponding ion-acoustic velocity of the medium. This Doppler shift is independent of the strength of the driving electric field, provided that the corresponding E x B drift is higher than the ion-acoustic velocity. It is also independent of the angle between the drift and direction of the wave vector, **k**, responsible for scattering. This is in contrast with the spectra of type 2 which has a Doppler shift comparable to the projection of E x B drift velocity in the direction of **k**. Type 1 are believed to be produced by two-stream instability (Farley, 1963; Buneman, 1963) and type 2 results from gradient-drift instability (Maeda et al., 1963; Knox, 1964; Tsuda et al., 1966; Whitehead, 1967, 1971; Reid, 1968; Rogister and D'Angelo, 1970; Fejer et al., 1975).

Mesospheric irregularities were also studied using the electron density obtained from large number of rocket flights from Thumba (Sinha, 1992) and from ion density data by (Blix et al., 1990; and Chakrabarty et al., 1989). Number of parameters associated with neutral air turbulence were determined from these studies.

Electron density irregularities, capable of scattering VHF waves, also exist at mesospheric heights which are produced by neutral gas instabilities

(Ecklund et al., 1981). The neutral atmosphere becomes turbulent either because of dynamically unstable shears or because of the overturning of convectively unstable gravity waves. The neutral atmosphere drags the ionisation with it, resulting in the mixing of regions of different electron density in the presence of a primary electron density gradient. MST radars serves as an important tool for studying the neutral dynamics. The irregularities are used as tracers of the velocity field of the neutral gas and of the state of turbulence at these altitudes. Kudeki and Stitt (1990) used high resolution frequency domain Interferometric technique at Jicamarca for studying equatorial mesospheric scattering layer widths and motions. The layers are manifested in RTI plots as preferred altitude regions with strong backscatter signal intensity, lasting over periods of tens of minutes to several hours. Two or three distinct layers are commonly observed at any time during daylight hours, separated from each other by several kilometres in altitude. Lower mesospheric (< 70 km) layers tend to last for longer periods of time than higher mesospheric layers (> 70 km). They found that the layers performed oscillatory vertical motions with the vertical velocities of short - period gravity waves, with amplitudes less than 1 km. Gross characteristics of equatorial mesospheric layering has been discussed in literature (Harper and Woodman, 1977; Fukao et al., 1980; Royrvik, 1983; Kudeki, 1988).

Ionisation irregularities occurring in the equatorial F region are collectively known as equatorial spread-F (ESF). The name originated from the spreading of the ionograms trace from its usual form due to diffuse echoes, which was first observed by Booker and Wells (1938). Spreading of F region traces on ionograms has been divided into two main types. One is range spreading in which two or more traces with different virtual heights are seen at frequencies well below f_0F_2, and seems to be prevalent at lower latitudes. The other is frequency spreading in which the high frequency ends of the traces are branched or blurred, which is more common at higher latitudes.

These irregularities manifest in the form of (a) plasma bubbles which have been observed by in-situ measurements made with satellite and rockets, (b) plasma depletions in airglow images (c) plumes observed by the radar. These are also responsible for scintillations of satellite signal. These irregularities, have been classified in the literature, depending on their occurrence altitudes as observed in the radar RTI maps, into Bottom side, Bottom type, Valley type and Top side spread F.

Topside spread F

Radar observations from Jicamarca showed that the irregularities were generated nearly simultaneously below, above and at the F peak and the ionosphere could be moving upward, downward, or not all when the echoes were received (Farley et al., 1970). Woodman and LaHoz (1976) presented RTI maps which showed the high altitude plumes reaching hundreds of kilometres above the F peak. An example of RTI map is shown in Fig. 1.11. The plumes usually displayed westward tilts. They suggested the plume was due to a bubble rising and moving west in the plasma frame of reference, leaving behind a wake of short wavelength irregularities. Kelley et al. (1976) made a similar suggestion on the basis of simultaneous rocket and radar data.

Bottom-Side and Bottom-Type Spread F

Sometimes the bottomside of the F-region and on occasions, only the very bottom of the F region become unstable. Woodman and Lahoz (1976) referred to this type of irregularities as Bottom-side and Bottom-Type Spread-F shown in the Fig. 1.11. Woodman and LaHoz (1976) suggested that an original perturbation on the bottom of the F-region, which is gravitationally unstable, would grow into a non-linear regime to form a low density bubble which would then rise, due to its buoyancy, to the stable side of the ionosphere. It continues to rise until its field integrated density equals the field integrated density of background. The reasons for the bottomside irregularities to appear only below certain altitudes and why the plumes are

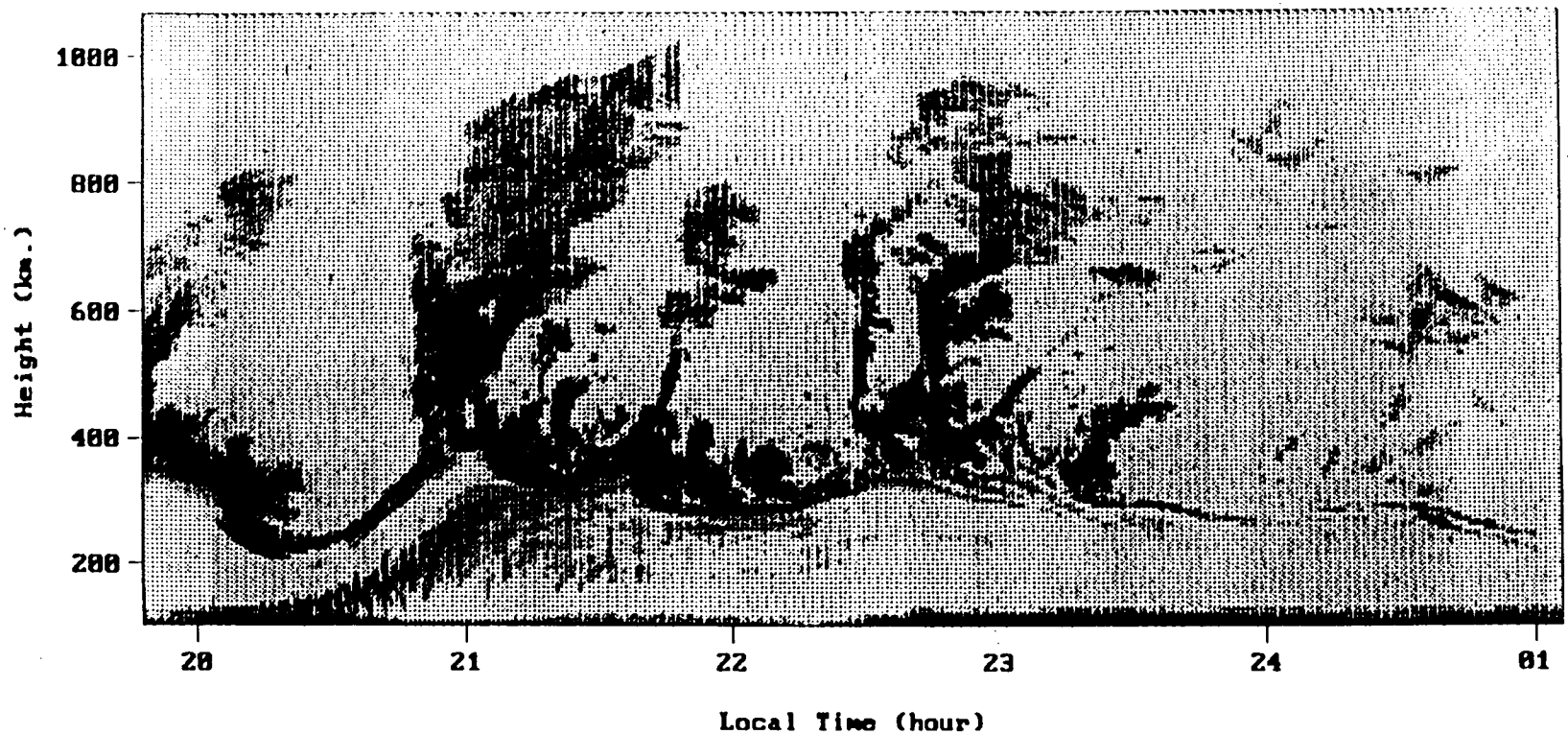

Fig.1.11 Range-Time-Intensity (RTI) plot of echo power received during a strong spread F event showing Plumes, Bottom-side, Bottom-type, Vallry-type spread F and quasi-sinusoidal modulation of the bottom of the structures (After *Woodman and LaHoz,* 1976).

not developed in this case are not yet understood fully. The mechanisms which are quite promising for the generation of irregularities at the bottomside are the Rayleigh-Taylor (R-T) instability (Dungey, 1956; Haerendal, 1974; Hudson and Kennel, 1975) and the E x B instability (Martyn, 1959; Simon, 1963; Linson and Workman, 1970). The linear instability condition for R-T is ∇n should be antiparallel to g and both perpendicular to B, while for the latter ∇n must be antiparallel to E x B drift. These instabilities will be discussed later on. The gravity is always antiparallel to ∇n_e on the bottomside, while the E x B process is only destabilising when the plasma is moving upward. The normal daytime upward plasma motion (Woodman, 1970) is accelerated at sunset before reversing to the normal night time downward motion. Thus this uplift may initiate the E x B process and create finite amplitude irregularities in short time period. Occasionally, magnetospheric electric fields penetrate to the equator (Fejer et al., 1976; Gonzales et al., 1979) and cause an anomalous plasma flow during the night at Jicamarca. This is usually accompanied by a resurgence of spread F activity. Rastogi and Woodman (1978) and Kelley et al. (1979) suggested that this regeneration of spread F is due to E x B instability. The observations indicate that bottom-type irregularities develop when the plasma is marginally unstable and only the region of steepest gradient become unstable (Woodman, 1993).

Sinusoidal irregularities in equatorial F-region in ion number density, characterised by scale sizes of 2 to 20 km, were first discovered by using OGO 6 satellite data (McClure and Hanson, 1973; Dyson et al., 1974). Valladares et al. (1983) observed a new category of ESF irregularities using retarding potential analyser (RPA) and the ion drift meter (IDM) data obtained from the Atmosphere Explorer satellites AE-C and AE-E. They found that these occurred in the bottomside at night in a narrow belt extending approximately $\pm 12°$ from the dip equator and upto 7500 km or more in the east-west direction. They appeared as sinusoidal waves in the ion number density, with crest to trough amplitude that span more than three

orders of magnitude, from 10^3 to 10^6, at altitudes from 190 to 500 km. These were referred to as 'bottomside sinusoidal' (BSS) irregularities, typically having a central wavelength lying in the range from 300 m to 3 km, and having relatively narrow power spectra. The power spectral index is steep (5 or 6) at the shorter wavelength, with a peak in spectrum at $\lambda \sim 1$ km. They invoked theoretical considerations for explaining the peak in the spectrum and suggested that the inclusion of long-wavelength stabilisation due to altitude localisation, and short-wavelength stabilisation due to cross-field diffusion, could modify the collisional R-T instability in such a way to maximise growth rate at this wavelength. Cragin et al., (1985) found that the occurrence frequency of BSS irregularities maximises at the solstices, and has a seasonally dependent longitude distribution and are detected most frequently in the local summer hemisphere.

Valley Type Irregularities

These are the irregularities that develop in the low density region below the F region and above the E region peak (Woodman and LaHoz, 1976). Their presence implies the existence of density gradients at these altitudes, possibly associated with irregular layers of higher electron density, which may be due to meteoric ionisation. These have been observed under the plumes of RTI plots (Woodman and LaHoz, 1976; Kelley et al., (1981); Hysell et al., 1990). The appearance of Valley type irregularities between 20:30 and 21:30 hrs, can be seen in the Fig. 1.11, between 120 km and 300 km that are consistent in many observations in association with well developed plumes. The features suggest that these echoes are associated with irregularities in meteoric ion densities at E region heights which are sucked by the E-W polarisation field responsible for the uplift of the plume. These irregularities would provide the primary gradients for smaller scale instabilities to develop (Woodman, 1993). This interpretation supports the mechanism proposed by the presence of metallic ions observed by satellites which passed through the bubbles (Hanson and Sanatini, 1973).

1.4.1 Seasonal and Longitudinal Dependence of ESF Irregularities

Satellite and multistation observations have revealed distinct longitudinal variations in equatorial irregularity occurrence during a given season (Sharma and Muldrew, 1975; Basu et al., 1976; Aarons et al., 1980; Muldrew, 1980b; Abdu et al., 1983; Abdu, 1993; Kil and Heelis, 1998). The occurrence of equatorial scintillations exhibits variations with both season and longitude (Aarons, 1977; Basu and Basu, 1981). Muldrew (1980b) and Maruyama and Matuura (1980) investigated the global morphology of ESF by using topside sounder data and showed seasonal variation in the longitude of high occurrence probability of ESF and bubbles. Basu and Basu (1985) summarised the longitudinal and seasonal effects of ESF. Rastogi (1980) attributed this morphology to the longitudinal changes in the reversal time of the zonal electric field from eastward to westward in the evening hours. Muldrew (1980a) related it to the E region dynamo field which generates field aligned currents due to a hemispheric asymmetry of the field. Maruyama and Matuura (1984) explained it on the basis of transequatorial component of the thermospheric wind which modifies the Pederson conductivity integrated along the magnetic field line.

Tsunoda (1985) studied the relationship between the occurrence maxima for scintillations and E region sunset times, in the Indian-Pacific as well as in the American-African sector (Fig. 1.12). He explained the observed longitudinal occurrence patterns of scintillations and range type spread-F by showing that the maxima in scintillation activity occur when the solar terminator is most nearly aligned with the geomagnetic flux tubes. They found that when this occurs, the longitudinal gradient in the integrated Pederson conductivity is steep, the primary variation in the gradient being produced by sunset at one of the E layers. However, they suggested that other influencing factors might be playing a role in the seasonal dependence besides coincidence in sunset times of the conjugate E layers because (a) the primary scintillation maxima were occasionally found to be slightly

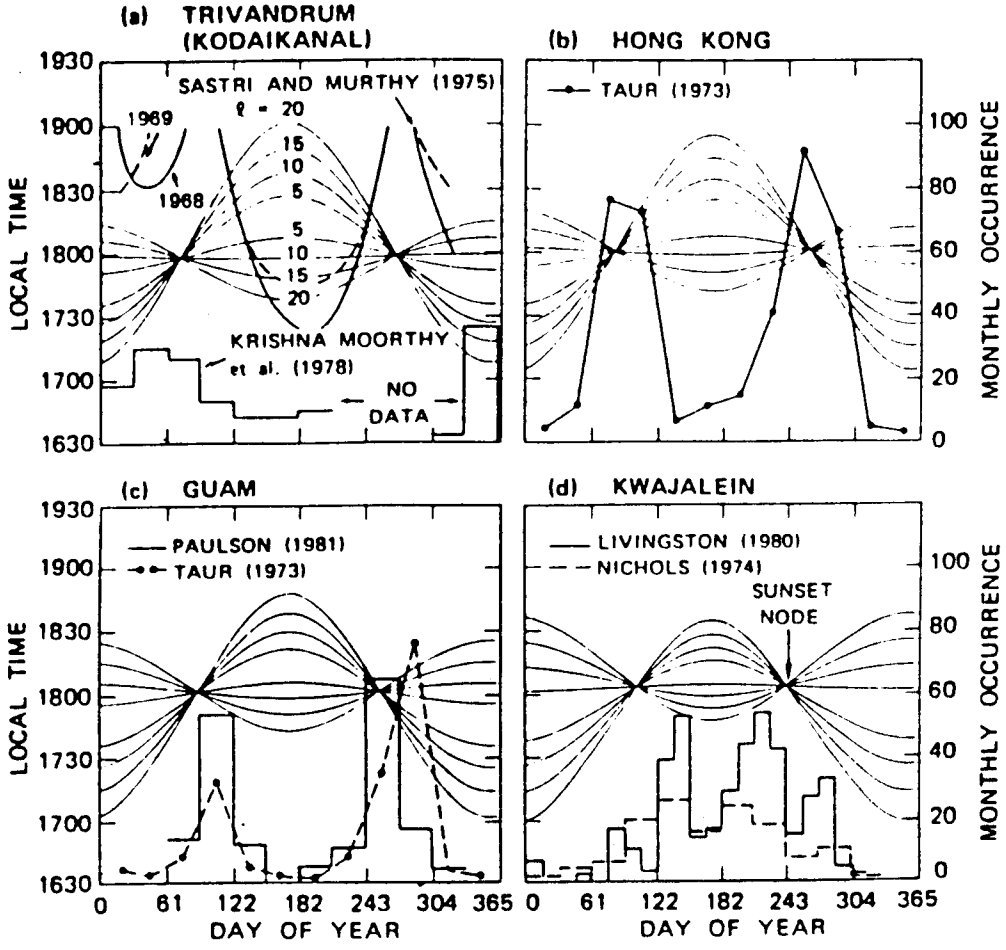

Fig. 1.12 Comparison of the times of equatorial scintillation maximum to those of the sunset nodes in the Indian-Pacific sector (After *Tsunoda*, 1985)

displaced from either one or both of the sunset nodes (b) an asymmetry in the occurrence frequency of scintillations was often observed, e.g. a larger peak was seen to be associated with the fall node than with the spring node at four stations, Hong Kong, Guam, Tangua, and Huancayo, and (c) there appeared an isolated occurrence of scintillation and range type spread-F maximum near the December solstice at Ancon and Kodaikanal.

Maruyama and Matuura (1988) explained the seasonal differences in the occurrence pattern of ESF observed over Fortaleza (declination angle ~ 20° W) and Jicamarca (declination angle ~ 2° E) on the basis of transequatorial thermospheric winds. They showed that the winter-summer asymmetry of the occurrence probability at Jicamarca and other stations close to it can be explained in terms of seasonal changes in E x B drift irrespective of wind. However, the winter summer asymmetry of ESF occurrence at Fortaleza could be explained by considering both the transequatorial wind and E x B drift in their model.

1.4.2 Factors Affecting the Growth of Ionisation Irregularities

The very first observation of equatorial spread-F at Huancayo by Booker and Wells (1938) indicated that the occurrence of spread F was preceded by the rapid increase of height of the F layer after sunset. Similar associations between h'F and spread F were found at other places Ibadan (Lyon et al., 1961) and Thumba (Chandra and Rastogi, 1972). Various factors influencing the growth of irregularities in the F-region are discussed below.

1.4.2a Effect of Neutral Winds

Zonal winds - Eastward neutral winds (U), which are primarily horizontal contribute to the growth of the irregularities through GRT mechanism, only when the ionosphere is tilted (Kelley, 1985). This happens because the cross field instability occurs when E' x B has a component parallel to the density gradient, where,

$$E' = E + U \times B$$

The zonal component of U is eastward at sunset (Sipler and Biondi, 1978). Thus an eastward neutral wind can be destabilising in regions where the isodensity contours are tilted, with ∇n partially westward. The growth is given by

$$\gamma_w = (U \sin\alpha)/L$$

where α is the tilt angle.

Modelling studies by Zalesak et al. (1982) showed that the 'C' shaped structures and the westward tilts of the plumes are the consequences of vertically rising spread F bubbles being caught up in the ambient plasma shear. This shear results from neutral wind at the equator and background layers of finite conductivity connected to the equatorial F-region along magnetic field lines. They also found that it may be the eastward as well as westward wall of the bubble which is subject to secondary instabilities in the presence of eastward neutral wind.

Modelling studies by Chou and Kuo (1993) revealed the formation of patchy structures with quasi periodic characteristics in the presence of strong zonal neutral winds. This was explained on the basis of different ion-neutral and electron-neutral collision frequencies which result in charge separation and produce electric field. The perturbation would be either amplified or damped depending on whether the neutral wind is blowing into or out from the area of positive horizontal density gradient. Consequently, successive instability and stability regions make the quasi periodic patch structures.

Meridional Winds - Effects of the transequatorial thermospheric wind on the ionospheric plasma distribution at low latitudes have been reported in literature (Bittencourt et al., 1976; Bittencourt and Sahai, 1978). According to these, a poleward wind transports ionisation to the lower altitudes along the magnetic field lines through the momentum transfer from the neutral particles to ions and an equatorward wind transports ionisation to the higher

altitudes in the other hemisphere. Thus the transequatorial wind yields hemispheric asymmetry in plasma distribution off the equatorial plane. Maruyama and Matuura (1984) pointed out from the satellite observations that the asymmetric distribution of the ionisation may result in an increase in the magnetic field line integrated Pederson conductivity, which suppresses the growth of the R-T instability.

Mendillo et al. (1992) used the all-sky airglow imaging system at Kwajalein simultaneous with the Altair incoherent observations for the case studies of ESF onset and growth patterns. They showed that subtle changes in north-south thermosphere/ionosphere structure were the only observational patterns which could differentiate the nights of ESF activity from those on which ESF did not occur. It was shown that ESF onset occurred when the airglow patterns associated with the equatorial anomaly were essentially symmetrical about the geomagnetic equator, a condition that occurs when meridional winds are low. The effect of transequatorial winds in inhibiting the growth of irregularities was also discussed by Maruyama (1988).

Recently, Bittencourt et al. (1997) observed the depletions in all-sky imager which were seen on the nights which showed the presence of a large scale structure or fluctuations in the meridional wind velocities. They suggested that these large scale fluctuations in meridional wind are indicative of the presence of a seed perturbation to initiate the R-T mechanism of ionospheric irregularities.

Vertical winds - Vertical winds of significant magnitudes have been observed using different techniques. Anandarao et al. (1978) using barium blob releases by a rocket during evening twilight, measured vertical wind velocities of 10 -20 m/s in the 100 - 200 km height region over Thumba (1.7° dip) which were ascribed to the passage of gravity waves. Biondi and Sipler (1985) measured the Doppler shift of 630.0 nm of OI line emission from the altitude region of 265 km over Natal, Brazil. They inferred a downward wind

speed of 20 m/s followed by an upward wind of equal magnitude for several hours in the night time during quiet time conditions. Significant vertical winds, using barium release vapour experiments over SHAR (5.5°N dip latitude), India, have been reported (Raghavarao et al., 1987, Sridharan et al., 1997), with speeds ranging from 10 to 40 m/s at altitudes from 180 - 290 km. Recently, Laakso et al. (1995) calculated vertical neutral wind from the electric field measurements obtained by San Macro D satellite data and found that it varied from 15 ms^{-1} to 30 ms^{-1} with an average value of 25 ms^{-1}.

Sekar and Raghavarao (1987) argued that the effect of the downward wind is similar to that of the E x B effect and can enhance the growth rate of irregularities even in the presence of downward drift. Hanson et al. (1986) pointed out that the F-region vertical E x B drift increases the effective growth rate just after sunset by an order of magnitude in about an hour when the drift direction is upward. Sekar and Raghavarao (1987) investigated the role of vertical winds in producing irregularities through R-T instabilities. They found that the growth rate (γ) of the perturbations in night time F-region in the presence of vertical wind is given by

$$\gamma = \frac{1}{L}\left[\frac{g}{\nu_{in}} + Wx\left(\frac{\nu_{in}}{\Omega_i}\right) + W_z\right]$$

where the first term in the square brackets represents the R-T instability due to gravitational drift (Haerendal, 1974), the second term represents the effect due to the zonal wind (W_x), the third term shows the contribution of vertical winds (W_z). They showed that a vertical wind of 1 m/s would cause the same effect on the growth rate as a horizontal wind of 200 m/s. It was also pointed out by them that when the plasma density gradient increases with altitude, it is the downward wind velocity that causes the instability while the upward wind prevents the growth of plasma irregularities. Downward vertical wind ($-W_z$) can cause a $(\nu/\Omega)_i W_z$ velocity of ions in the eastward ($-W_z$ x B) direction, while the electron move in westward direction with velocity $(\nu/\Omega)_e W_z$. Rishbeth (1981) showed that $(\nu/\Omega)_i$ is larger by 3 orders

of magnitude as compared to $(\nu/\Omega)_e$ at all ionospheric altitudes. They discussed that the ion velocity due to vertical wind of about 16 m/s at an altitude of 300 km would be around 4.8 cm/s, which is nearly the same as that due to gravitational drift (g/Ω_i = 4.8 cm/s). The ion velocity imparted by the downward wind in the Hall direction adds to the eastward ion motion due to gravitational drift, thus enhancing the growth rate of R-T instability.

1.4.2b Effect of Seeding Agency

Observations have shown that large scale ionospheric irregularities, such as travelling ionospheric disturbances (TIDs) and wavelike fluctuations in the F region electron density, are associated with gravity waves. Hines (1960) recognised similarities between certain TID properties and features of internal gravity waves in the neutral atmosphere. The mechanism by which these waves produce modification in the ambient ionisation has been discussed earlier (Testud and Francois, 1971; Clark et al., 1971; Davis, 1973; Francis, 1974; Yeh and Liu, 1974). It was shown that gravity waves can produce strong ionisation perturbations when the phase speed of a gravity wave is equal to the drift speed of ionisation, which is known as spatial resonance effect (Whitehead, 1971; Beer, 1973). Röttger (1973, 1976, 1978) presented observations of large scale wavelike structures of F-region irregularities and suggested that the wavelike structures were produced by gravity waves at spatial resonance. Ossakow et al. (1979) assumed small perturbation with scalesize of 3 km in the zonal direction in the simulation studies. They showed that the high altitude of the F peak and small bottomside plasma density gradient scale length yield large vertical bubble rise velocities. However, observations indicate bubble structures of much larger horizontal extent than those by the simulations. Zalesak and Ossakow (1980) studied plasma bubbles resulting from large horizontal scale initial perturbations and showed the production of large scale ESF irregularities.

Prakash and Pandey (1980) pointed out that the perturbation electric fields which develop in response to wave driven electric current will be shorted out if the magnetic field can link the regions of positive and negative charge. However, this will not occur for pure zonal propagation, but if a finite meridional component of the gravity wave vector exists, the seeding process may be limited to locations very near to the dip equator. The gravity waves generated as a result of auroral activity propagate from poles to equator, while medium scale TIDs may propagate in any direction. Thus, gravity waves generated in the auroral zone may be less effective for seeding ESF than waves generated by tropospheric sources such as thunderstorms and frontal systems.

Kelley et al. (1981) presented observations which display strong evidence of gravity wave initiation of ESF. They argued that gravity waves are capable of seeding ESF via the spatial resonance mechanism and play an important role in production of plasma bubbles. Hysell et al. (1990) reported the observations of seeding and layering of ESF by gravity waves. Huang and Kelley (1996a) showed that a zonally propagating gravity wave can initiate the R-T instability in the bottomside of the F-region even in the absence of the spatial resonance mechanism. However, their numerical simulation work showed that R-T instability initiated by gravity wave at spatial resonance evolves into plasma bubble faster than in the absence of it. In another computer simulation, Huang and Kelley (1996b) found that the necessary condition for the production of multiple plumes is the presence of seed gravity wave and a small scale initial density perturbation. They suggested that (a) gravity waves are the most suitable candidates for seeding large scale ESF and for determining the outer scale of ESF irregularities and (b) smaller scale perturbations might be due to R-T instability in the presence of velocity shear due to large scale perturbation (Satyanaryana et al., 1984; Kelley et al., 1986), which is possibly due to large scale instability process. Singh et al. (1997b) presented evidence of plasma bubble development from wavy ion density structure, which were

closely associated with simultaneous horizontal neutral wind measurements in the bottomside F layer using the Atmospheric Explorer AE data. They suggested that the wave structures served as initial seed perturbations and were caused by gravity waves.

In most of the work related to the non-linear development of the CRT model (Ossakow, 1981; Kashchekom et al., 1989), a 5% initial perturbation was found to be essential for the formation of plasma bubble within reasonable time limit (< 30 min). However, Mendillo et al. (1992) reported that there exist large number observed ESF onset conditions that are not associated with the level of seed perturbation required by the simulation studies. Sekar et al. (1995) showed that 0.5% perturbation can evolve into a bubble under the influence of vertical wind and electric field.

1.4.2c Storm Effects

It has been observed that the magnetospheric disturbances affect the ESF phenomenon (Chandra and Rastogi, 1972; Rastogi and Woodman, 1978; Das Gupta et al., 1985; Dabas et al., 1988; Tanaka, 1986; Takahashi et al., 1987; Aarons, 1991; Sahai et al., 1994a, 1994b; Abdu, 1997; Bittencourt et al., 1997). Chandra and Rastogi (1972) observed the tendency of spread F to be reduced on disturbed days during any of the seasons. During winter and equinoxes when the spread F is maximum in the premidnight hours, they observed that the post-sunset height rise of h'F to be reduced on disturbed days as compared to that on quiet days. During summer there was no significant post-sunset rise of h'F either on quiet or on disturbed days and the spread was maximum during the predawn hours. Rastogi and Woodman (1978) observed the generation of irregularities during midnight to post midnight period in the radar studies of Jicamarca. They attributed this to the increase in height of the F layer during magnetic disturbances and found that the irregularities were generated when the layer height falls.

Das Gupta et al. (1985) observed the tendency of postmidnight VHF scintillations recorded from Calcutta, India, to be associated with the maximum negative excursion of the horizontal intensity of magnetic field occurring in postmidnight periods. However, no such relation was seen with premidnight excursions. This pointed out that the effects of maximum ring current excursion, Dst, are (i) the postmidnight creation of conditions necessary for the generation of irregularities and (ii) an absence of an effect if the maximum negative excursion occurred after sunset and before midnight. These observations were later on confirmed by Dabas et al. (1988) who studied the effects of geomagnetic disturbances on VHF scintillations in the Indian equatorial region. They also observed that the irregularities were suppressed either completely or partially, if the recovery phase started during local day time hours.

In-situ night time electron density measurements on board the satellite Hinottori by Takahashi et al. (1987) showed ionisation enhancements at low latitudes during disturbed conditions. They pointed out that the ionisation enhancements displayed an equatorial anomaly like structure having a minimum at the dip equator and suggested that the enhancement is induced by low latitude penetration of the magnetospheric electric field during the development phase of the ring current (Tanaka, 1986). The effects of magnetic storms on equatorial Appleton anomaly have been discussed by Rishbeth (1975) and it was shown that the equatorial anomaly is less developed during storm periods. However Fesen et al. (1989) reported enhancements of the anomaly in which the F region critical frequency in the equatorial trough is smaller than during non-disturbed days and the ionisation crests are more pronounced. The above observations suggest that the ionospheric perturbations at low latitudes, during magnetic disturbances, depend in a complex manner on several factors, including storm induced changes in dynamics, heating and composition. Rishbeth et al. (1985) discussed that the ionospheric fluctuations are also dependent on

the latitude, longitude, local time and on the elapsed time from the commencement of the magnetic storm.

Aarons (1991) discussed that the suppression or development of irregularities depends on two factors (a) the history of the individual storm and (b) the state of the local ionospheric parameters before the storm. A brief general explanation for the pattern of inhibition and generation of irregularities is discussed below.

The predominant flow in the ever present ring current is westward which is responsible for the depression in Dst. Equatorial eastward electric fields produce an upward vertical drift during the day. It is known that during the pre-sunset period the F layer height rises. Ring current negative excursions in this time period directly or indirectly have the effect of decreasing the local eastward electric field thus reducing the layer height and possibly the downward velocity of the F layer in the post sunset generation period. At night, zonal westward electric field produces a downward vertical drift. The effect of the ring current in the midnight and post midnight period when the layer height is normally falling in the presence of westward electric field is to create momentarily an eastward electric field and raise the layer height, the change is relatively short lived and layer height than falls creating the irregularities.

Simulation studies on the ionospheric effects, including the OI 630 nm emission, of the neutral atmosphere perturbations due to magnetic storm, at equinox during solar cycle maximum, have been discussed by Fesen et al. (1989). Tinsley et al. (1986) presented an extensive study of low latitude aurora and storm time current systems. Sahai et al. (1988) made simultaneous observations of several night glow emissions from a low latitude station during magnetic disturbances for studying ionospheric F - region storm effects. These optical studies have provided evidence for energetic neutral particle precipitation and disturbed electric fields in the

equatorial and low latitude ionospheric F region under magnetically disturbed conditions.

Sahai et al. (1994a, b) showed a rare case of spread F formation during the month when it is normally absent in the presence of magnetic disturbances. Sahai et al. (1994a) found that the depletions occurred during long lasting periods of moderate and relatively high Dst levels, rather than periods of strong and rapidly increasing negative values of Dst. Recently, Bittencourt et al. (1997) observed the presence of plasma depletions on a night which was preceded by a sudden commencement magnetic storm ($K_p \approx 6$, hourly Dst $\approx$ -8.5 γ) in the evening hours. They also observed that the development of large scale plasma depletions was preceded by an unusually fast post sunset uplifting of the F layer, which they believed to be associated with the SSC magnetic storm effects on the ionospheric electric fields. Abdu (1997) reviewed the results related to the response of the major phenomenon of the equatorial ionosphere-thermosphere system (EITS) to magnetospheric disturbances.

Vats et al. (1978) reported an event of daytime scintillations in the anomaly crest in India following a sudden commencement of magnetic storm. Chandra et al. (1995) observed magnetic storm induced F-region scintillations extending into daytime over Bombay, situated near the anomaly crest region in India on November 12, 1991 and also at Trivandrum, situated close to magnetic equator.

1.5 Theme of the Present Investigation

It is very well known by various ground based experiments in the Indian, American and Pacific regions that the nature of ESF activity is quite different in these sectors. Chandra and Rastogi (1970) showed that the nocturnal average spread F at Huancayo decreased with solar activity in contrast to the behaviour at all other equatorial stations, Ibadan, Djibouti or Kodaikanal where the occurrence was directly related to solar activity. As mentioned before, various observations have indicated that ESF activity

exhibits seasonal variations (Rastogi, 1980; Tsunoda, 1985). Because of the longitudinal variabilities shown by ESF phenomenon a strong need was felt to make *in-situ* and ground based observations of a few key parameters of ESF from the Indian region as the bulk of the *in-situ* and radar work has been conducted in the other zones.

As far as the *in-situ* measurements are concerned, there were five major rocket campaigns in the past, for studying ESF in the American region (Kelley et al., 1976; Morse et al., 1977; Rino et al., 1981; Szuszczewicz et al., 1981; Kelley et al., 1982; Hysell et al., 1994) and a few campaigns in the Indian zone (Prakash et al., 1991; Raghavarao et al., 1987). Simultaneous measurements of electric field and electron density fluctuations were made during PLUMEX-I and CONDOR experiments and by Hysell et al. (1994) in the American zone, which showed that irregularities in the intermediate scales (100 m $< \lambda <$ 2 km) display a power law behaviour with spectral index, n, $\approx$ -2. The steepening of the power spectrum ($n \approx -4.5$) is observed around $\lambda \approx$ 100 m for the irregularities in the transitional range (10 m $< \lambda <$ 100 m) when F layer is high. In the Indian region there is no simultaneous measurement of electron density and electric field in the F-region during ESF. In fact the electric field measurements in the F- region over the Indian zone during ESF are just not there.

A powerful ground based technique to study the large scale features of ESF viz., the plasma depletions, is the optical imaging of 630 nm and 777.4 nm nightglow emissions. In the American region, observations using the optical technique were made by Weber et al. (1978), Mendillo and Baumgarderner (1982), Sahai et al. (1981), Bittencourt et al. (1997) but there were no such observations in the Indian zone.

In view of the above, it was strongly felt to make use of the simultaneous *in-situ* measurements of electron density and electric field fluctuations in the Indian region which were obtained earlier during the ESF. The relationship between electron density fluctuations (δn_e) and electric field fluctuations (δE) serves as an important clue to the plasma instabilities and

processes acting during spread F. This is so because the relation between these quantities is different for different plasma instabilities and may be used as a test for determining which processes dominate as a function of altitude and wavenumber. Thus for RT instability, the relationship between the two quantities is as follows :

$$\delta E_x = -\frac{gB}{\nu_{in}}\left(\frac{\delta n}{n}\right)$$

where δE_x represents the electric field amplitude, ν_{in} is the ion-neural collision frequency, g is gravity and B is the earth's magnetic field.

In drift waves, or in any low frequency electrostatic wave in which electrons can stream along B, the density and potential variations are related by :-

$$\delta E = -ik\left(\frac{kT_e}{e}\right)\frac{\delta n}{n}$$

where k is Boltzmann constant and T_e is electron temperature. Thus the electric field spectrum should be two powers of k less steeply sloped than the density fluctuation spectrum in the above mentioned case.

It is now generally accepted that the primary energy source for the irregularities is gravity, but the microphysics of ESF on various scales and under various conditions is not well established, either experimentally or theoretically. It is here that we felt the necessity of simultaneous measurement of electron density and electric field fluctuations using rocket experiments by providing vertical cuts through the anisotropic irregularities in large and small scales. In view of total absence of data in the Indian sector on various parameters of plasma depletions such as, scalesizes, degree of depletions, tilts, there is a need to study plasma depletions using an all-sky optical imaging system. Thus the present study concerns with the different manifestations of irregularities associated with ESF so as to provide better insight into the ESF properties for facilitating theoretical developments.

CHAPTER 2

TECHNIQUES AND INSTRUMENTATION

2.1 Introduction

Ionospheric irregularities in equatorial and low latitude regions have been a subject of intensive experimental and theoretical investigation in recent past. Experimental techniques based on radio, in-situ and optical probing have been employed to study the wide spectrum of irregularities associated with equatorial spread F (ESF). ESF irregularities occur in a wide range of spatial and temporal scales covering a few orders of magnitude. This chapter discusses the principle of a few techniques, to study the spatial scales, with an emphasis on those techniques which have been used for the present study viz. optical imaging, rocket-borne Langmuir probe and Double probe techniques.

2.2 Optical Techniques

Earth's ionosphere is an exotic chemistry laboratory where a large number of very complex chemical reactions are taking place all the time. The constituents of these chemical reactions include atoms and molecules, in neutral, excited as well as ionised state. Depending upon the type of constituents involved in a particular reaction, processes such as

photoionization, recombination, ion-atom interchange, attachment, detachment etc., take place. The density of constituents, their temperatures and the strength of the electromagnetic radiation exhibit a very large variation with time as well as with altitude. As a result of these chemical reactions, there is a variety of optical emissions from different altitude regions of the ionosphere. These optical emissions are also termed as airglow. As these optical emissions are produced in atomic and molecular reactions, their intensity is generally very small. It is relatively difficult to measure these weak emissions during day time due to the presence of strong solar radiation. The present work concerns the measurement of the weak optical emissions during the night i.e. the night airglow.

Optical techniques, which are used for studying the F-region irregularities, by measuring the nightglow emissions, are basically of three types, viz. photometers, imagers and interferometers.

Photometers

At the input of a photometer there is a small optics which decides the field of view of the system, which is typically a few degrees. The next element is a filter to isolate the specific emission of interest. Generally, interference filters with bandwidths in the range of 0.3 to 5 nm are employed. If the intensity of the emission to be measured is weak, one has to employ an additional filter to correct for the background continuum. The next element is the detector. Photo-multiplier Tube (PMT) is the most commonly used detector. Cooling of photomultipliers and using them in counting mode enable the detection of weak emissions.

There are two types of photometers viz. single field photometers and scanning photometers. In case of single field photometers the look angle of the filter or the tilt is fixed. It is possible to use the single field photometers, to get a spectral scan by making the tilt of filters variable (Eather and Reasoner, 1969). Tilt of the interference filter can also be used to correct for the background continuum without using an additional filter. If the filter is

tilted by small angular increments, it is possible to build a low resolution spectrum (Misawa and Tabeuchi, 1977). Although, it is a function of various parameters, a spectral scan of about 15 nm can be typically obtained by a filter tilt of about 20 degrees. A circular variable interference filter rotated in front of a PMT can also be used to get a very low resolution spectra (Rodrigo et al., 1985). The other type of photometer is the scanning photometer which is used for measuring airglow emission from different regions of sky. This is a slight variant of the single field photometer because here the light from different regions of the entire FOV is sequentially brought in front of the photometer by using an electronically or mechanically controlled mirror motion (Titelbaum and Petitdedier, 1978; Tapely et al., 1981; Meek and Manson, 1983; Takahashi et al., 1985; Sobral et al., 1985). Spatial resolution which can be obtained by scanning photometers lies in the range of 0.5 km to 25 km at 100 km altitude. It is possible to get a better resolution but that is at the cost of either a smaller sky coverage or large time interval between consecutive scans which prevents study of short time variations.

Imagers

The principle of optical imagers is to take a snapshot of the sky in the desired wavelength. Generally the imagers have a very large FOV and because of this the optics at the input of an optical imager is quite complex. The design of an imager is discussed in detail in section 2.2. The isolation of wavelength is achieved by employing interference filters. The detector used in imagers is either a 35 mm camera or a CCD camera. In order to record very faint images, use of image intensifier before the detector is also made. Use of a fish eye lens (180° FOV) to get an all-sky image, a filter wheel to measure a number of emissions and high gain image intensifier has resulted in studying fine details over the entire FOV with exposures as small as a few seconds enabling one to study the dynamics of the species which is responsible for the production of the particular nightglow emission (Peterson

and Kieffaber, 1973; Moreels and Herse, 1977; Weber et al., 1978; Mendillo and Baumgardener, 1982; Mendillo and Tyler, 1983; Molcom et al., 1984; Sahai et al., 1994, Sinha et al., 1996; Bittencourt et al., 1997; Taylor et al., 1997).

Interferometers

The interferometer is based on the interference of two or more beams of light that have originated from a common source which results in interference fringes. There are two basic classes of interferometers, depending on the division of wavefront and division of amplitude. The Young's double pinhole interferometer and Lloyd's mirror employ division of wavefront. For division of amplitude interferometer, a beam splitter is used to pick up a portion of the amplitude of the radiation which is then combined with a second portion of the amplitude. The visibility of the resulting interference fringes is maximum when the amplitude of the two interfering beams are equal. Fabry-Perot interferometer is a multiple beam interferometer since the incoming wave is multiply reflected between the two glass plates, partially silvered on the inner surfaces. As the reflectivity of the two surfaces increases and the number of interfering beam increases, the fringes become sharper. These have been used to study the line profile of a particular emission. The profile of an emission line is usually governed only by the motions of the atoms, and by the associated Doppler effect. The line broadening serves well to define a Doppler temperature representing the region of emission. The whole profile is Doppler shifted in the presence of the neutral winds. The magnitude of the shift in wavelength yields the value of line of sight wind. Such line profile measurements of natural airglow emissions made by using Fabry Perot spectrometer have been reported by several authors (Sipler and Biondi, 1978; Meriwether et al., 1983; Cogger et al., 1985; Sridharan et al., 1991; Gurubaran, 1993).

Both the photometers and imagers can be very effectively used to study the electron density variations in the E- and F- regions of the

ionosphere. For doing this, one has to select those nightglow lines which originate in the altitude region one is interested in and also whose integrated emission at the ground can be approximated to some known function of electron density at the desired altitude range. In the present investigation, 630 nm and 777.4 nm nightglow emission have been used to study electron density distribution around 275 km and F2- peak heights.

2.2.1 Multiwavelength All sky Imaging System (MAIS)

A schematic diagram of the multiwavelength all sky optical imaging instrument developed at PRL is shown in the Fig. 2.1. The system comprises of a fish eye lens, a field lens, a collimating lens, interference filters, imaging lens, an image intensifier and a 35 mm camera. A brief description of the system is given below.

As the dimensions of ionospheric plasma depletions are very large, of the order of a few hundreds to thousand km in N-S and up to about few hundreds of kilometres along E-W direction, a fish eye lens is used at the input so as to capture these structures. This Nikon 8 mm f/2.8 lens has a field of view (FOV) of 180°. The Fish eye forms a circular image of 23 mm diameter. The circular photographic image produced by the fish eye lens is an exact reproduction on a flat plane of all objects encompassed within the 180° field of view. The centre of the image corresponds to the zenith and the distance of any point in the image from the centre, y, is directly proportional to its angle, α, from the zenith. This can be expressed by the equation:

$$y = C\alpha \qquad (2.1)$$

where C is the constant. The relation between the zenith angle and the distance of a point from the image centre is shown in the Fig. 2.2.

A 50 mm/f1.2 lens is employed as a field lens. The purpose of this lens is to slightly converge the light rays which are highly diverging in nature after emerging from the fish eye lens. This lens is placed at such a distance from the fish eye lens so that the aperture of the fish eye lens is imaged on

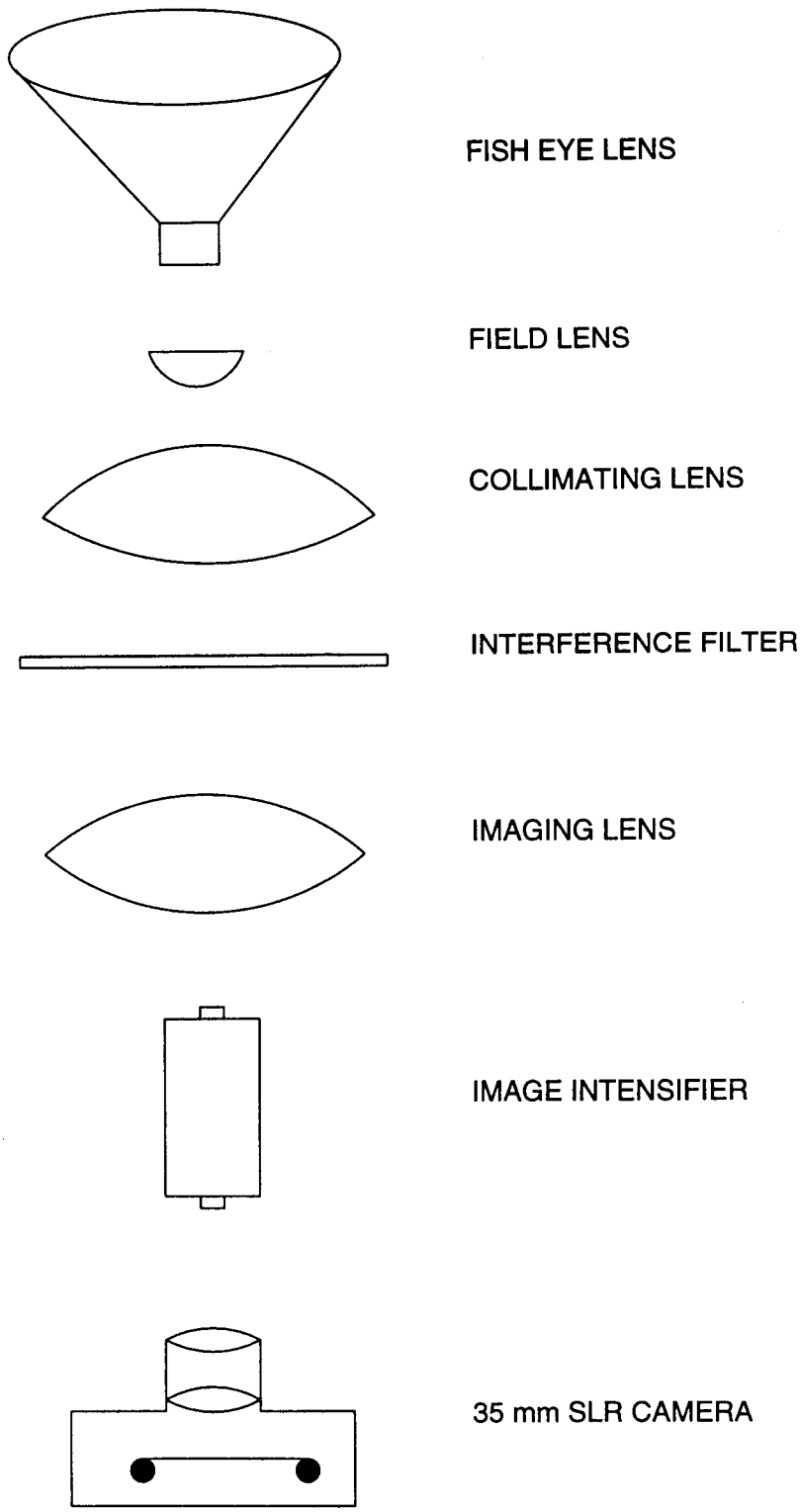

Fig. 2.1 Schematic of Optical Imaging System.

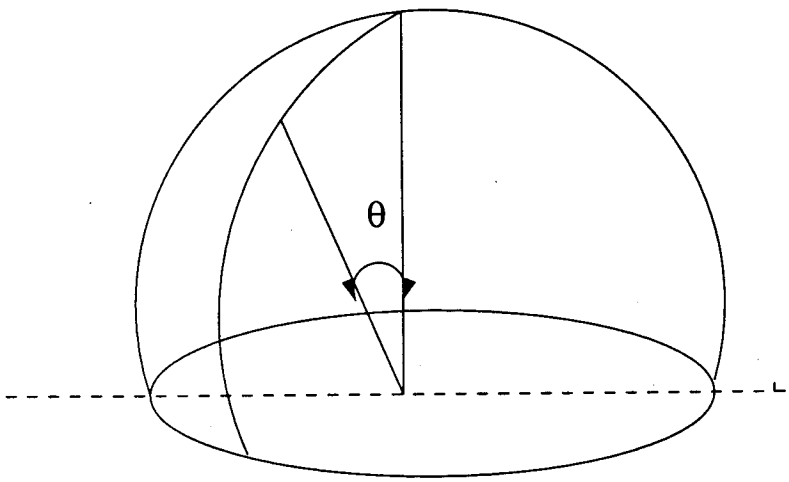

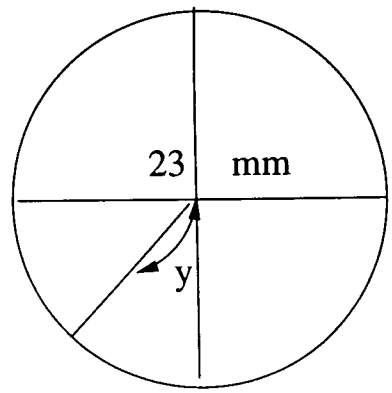

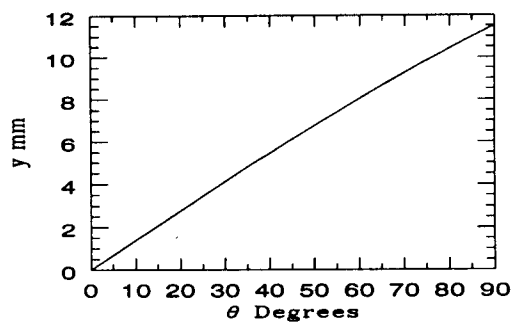

Fig 2.2 Relation between zenith angle and distance of a point from the image center.

to the filter so that although the image position and size is not altered, light throughput is increased.

An 280mm/f2.8 lens is used to collimate the light beam so that all the light falling at the interference filter is parallel the optic axis. The rays emanating from the centre of the lens are parallel to the optic axis but the rays emerging from the edges of lens make a small angle at the interference filter. This angle, ϕ, is determined by the image size and focal length of the collimator as shown in the Fig. 2.3 and is given by :.

$$\phi = \tan^{-1} (v/2f) \qquad (2.2)$$

where v is the image size, which is 23 mm and f is the focal length of the collimating lens. Thus ϕ is approximately equal to 2.3° for our case.

All the optical components have been housed in an aluminium tube which is coated with non reflecting black paint to prevent any extra light from entering the system.

An interference filter is used to isolate the desired spectral component. The system employs a filter housing facility which has a provision for selecting one interference filter at a time in the field of view. For studying 630 nm and 777.4 nm nightglow lines, interference filters of 100 mm diameter having bandwidths of 1 nm were used to accommodate the shift of the passband of the filters due to (a) small temperature variations and (b) a small angle between the optical axis and the parallel bundle of rays coming from the edge of the field of view which is around 2.3° as shown above. The shift in wavelength of peak transmission for an angle of 2.3° can be calculated by the following equation (Barker and Yen, 1967).

$$\lambda_\theta = \lambda_{peak} [1 - (\mu_0 / \mu_e)^2 \, Sin^2\theta \,]^{1/2} \qquad (2.3)$$

Where, λ_θ is the wavelength of the peak transmission at an angle of incidence of θ, μ_0 is the refractive index in vacuum and μ_e is the effective refractive index of the filter material. Thus for an interference filter having a

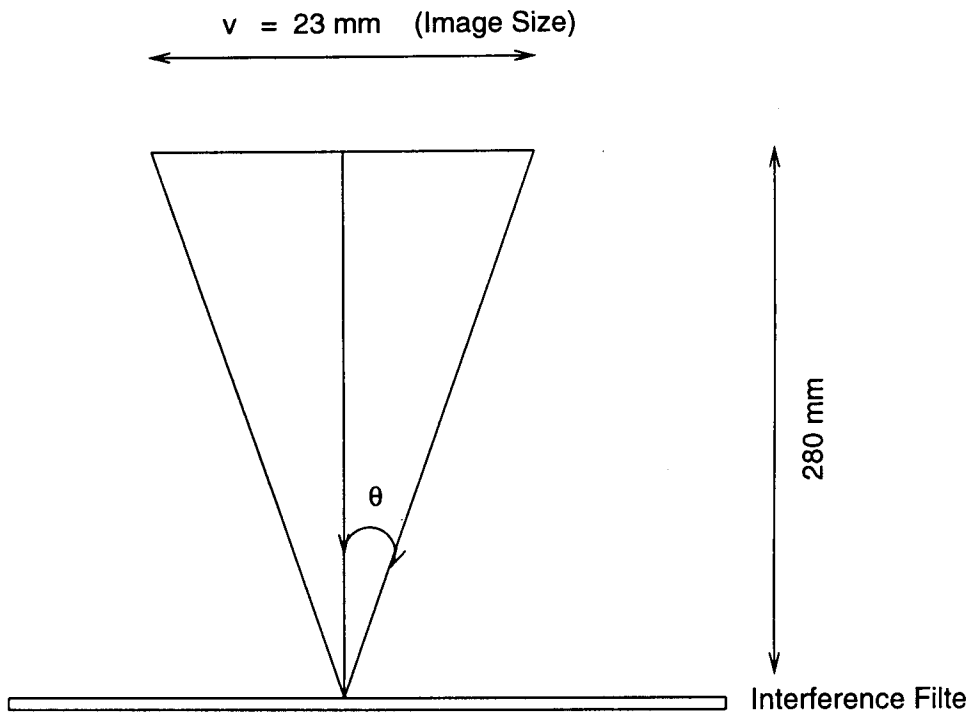

Fig 2.3 Angle between the rays coming from the edges of the collimating lens and the optic axis.

peak transmission at 630 nm and an effective refractive index of 1.5, the peak transmission will occur at 629.77 nm if the angle of incidence is 2.3. The shift in peak wavelength will be 0.23 nm. Therefore, for the rays coming from the edges of lens and making an angle ~ 2.3° with the optic axis, the shift in wavelength will be approximately 0.23 nm. Hence a bandwidth of 1 nm will be more than adequate to take care of this shift.

The spectral response of the interference filters used for the present work is shown in the Fig. 2.4. The peak transmission at 630 nm is about 70% while for 777.4 nm is around 65%.

A 280mm/f2.8 lens is used to focus the parallel beam emerging from the interference filter on to the input window of the image intensifier. This is done by using an imaging lens which is identical to the collimating lens.

The image of the sky is made at the fibre optic input window of an image intensifier (Hamamatsu Type V 1366 P). The characteristics of this type of image intensifier are summarised below:

Spectral Range	:	350 - 910 nm
Wavelength of peak response	:	600 nm
Photocathode Material	:	Multi alkali
Photocathode Effective Diameter	:	25 mm
Phosphor Screen Material	:	P - 39
Phosphor Screen Effective Diameter	:	25 mm

The spectral response of the image intensifier used for the present work is shown in Fig. 2.5. An image intensifier consists of a photocathode, electron lens, microchannel plate (MCP) which multiplies electrons, and phosphor screen which reconverts electrons into light. The operation of image intensifier can be understood from Fig. 2.6. When an optical image is focused on to the photocathode, electrons are emitted in accordance with the intensity of the input optical image. The electrons are accelerated across the cathode-to-MCP gap by a bias voltage. A high voltage (of the order of

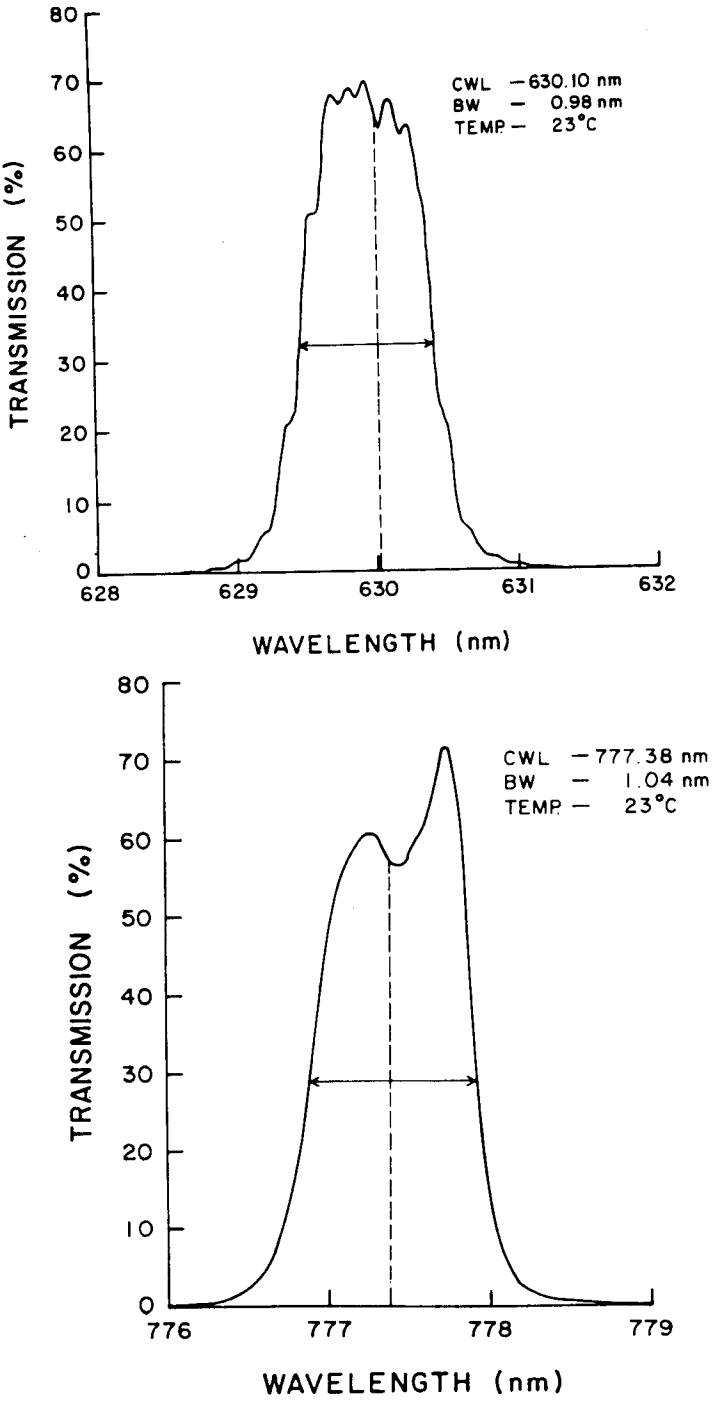

Fig. 2.4 Spectral Response of Interference Filters.

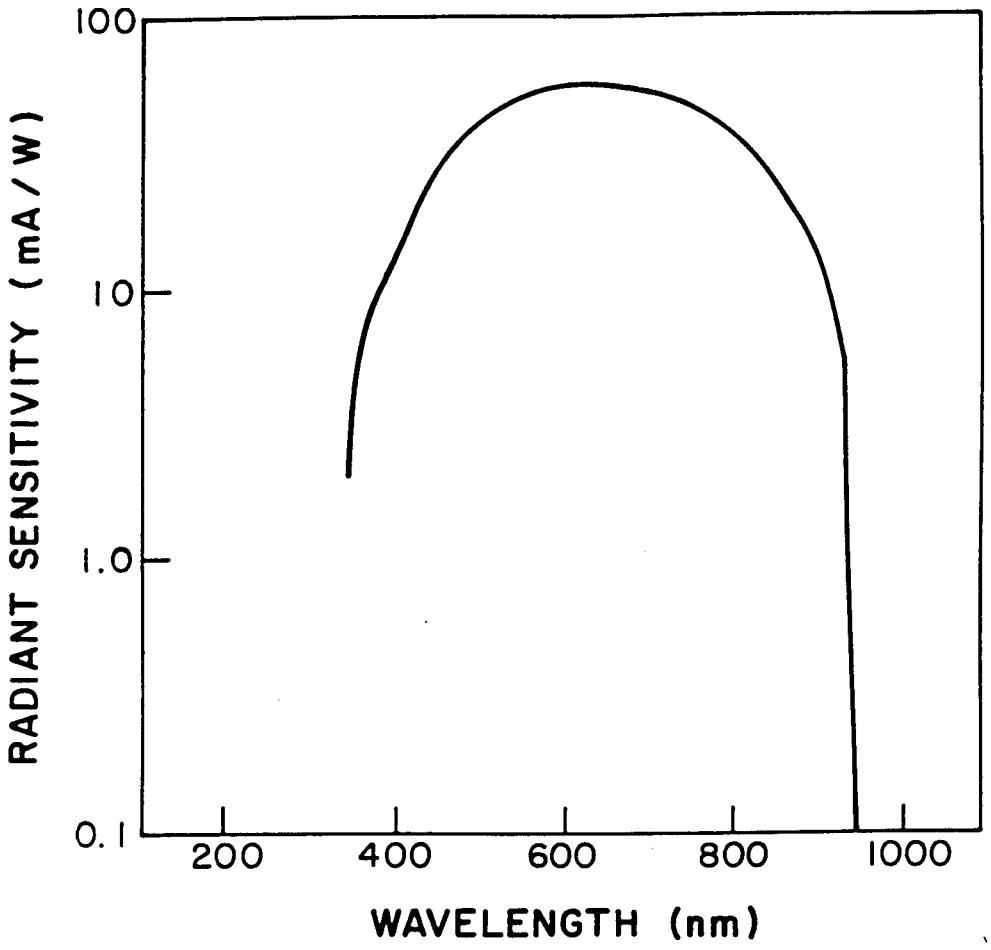

Fig. 2.5 Spectral Response of the Image Intensifier.

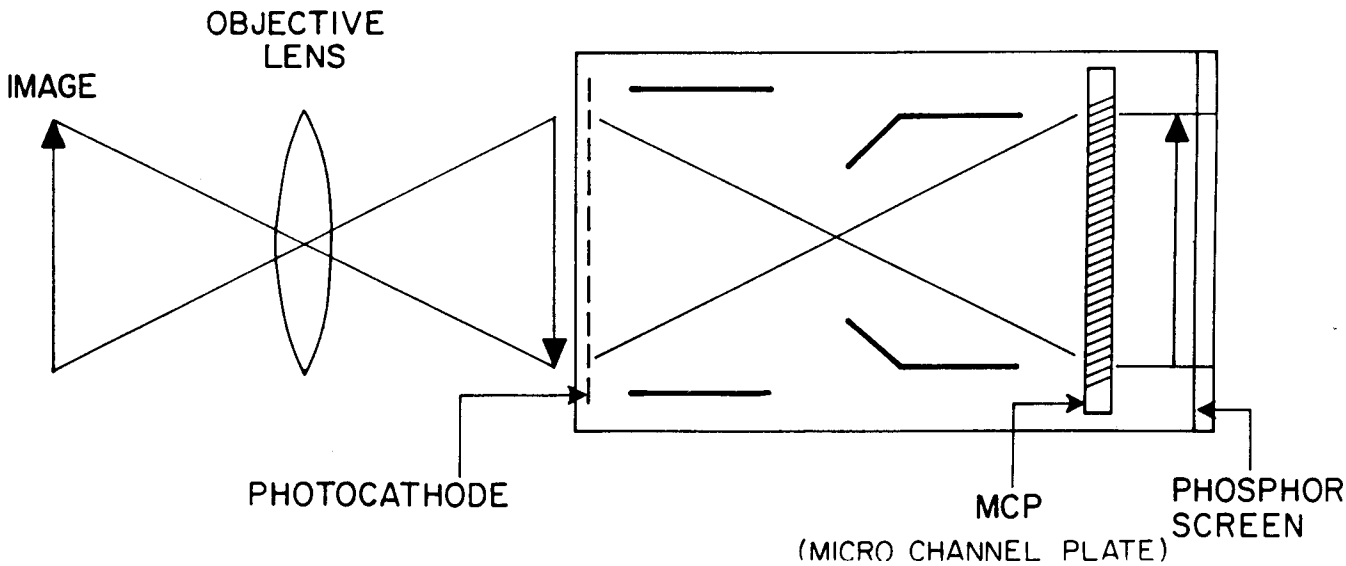

Fig.2.6 Operation of the Image Intensifier.

10 to 15 kV) is applied between the photocathode and the phosphor screen in order to accelerate the electrons which bombard the phosphor screen. The electron image is then focused on to the MCP where it is intensified, and then strikes the phosphor screen where an optical image is reproduced.

An MCP is a secondary electron multiplier consisting of an array of millions of glass capillaries (channels) fused into the form of a disk 0.48 mm thick and 25 mm in diameter. The diameter of each channel is 12 μm. When an electron enters and hits the channel wall, secondary electrons are emitted from the channel wall. These are accelerated by the potential gradient and strike the opposite wall to produce additional secondary electrons. As a result of such collisions repeated many times along the channel, a large number of electrons are produced, up to several thousand times the input number. An MCP contains approximately 1.5 million channels, each of which corresponds to a picture element and is simultaneously intensified. For the intensifier used in the present work, the result of this process is an intensification of the original incident light by a factor of approximately 40,000.

Although the image is intensified, it still needs, depending upon the natural strength of the airglow line and the image intensifier gain, to be integrated for a few tens of seconds to record the image.

For transferring the image from the output face plate of the image intensifier to the film, two standard 35 mm Nikon camera lenses are used in tandem pair. This is done since the standard camera lens are to be kept at a certain minimum distance from the image intensifier to focus the image on to the film. However, in this process, all the photons do not reach the camera resulting in significant loss of signal. To overcome this difficulty two lenses are employed before the camera. The first lens (105 mm f/1.8) is used as a collimator and the second lens (55 mm f/1.8) is used on the 35 mm Nikon camera for imaging. The final image on the film is 12 mm diameter. Kodak

tri-x panchromatic film is used and it is developed in Kodak 19b developer for getting maximum contrast.

A digitizer has been set up for the digitisation of the films. The block diagram is shown in the Fig. 2.7. It comprises of (a) light source, which is a light emitting diode LED kept at a constant voltage, (b) a condensing lens of small focal length for focusing the bundle of rays emerging from the source on to the film and also to ensure that the film is uniformly illuminated, (c) a mounting system for loading the films which are to be digitised, (d) a CCD camera which converts the transmitted light into a digital image of the size 512 X 550 x 12 bits and (e) a computer with a frame grabber.

2.3 *In Situ* Techniques

2.3.1 Introduction

There are large number of probes which have been flown on board rockets and satellites to measure the electron density and its fluctuations. Broadly all of these fall in two categories viz. the radio frequency (RF) probes and electrostatic probes. RF probes are of two types namely the impedance probe and the resonance probe. Impedance probes rely on measuring the impedance of a probe immersed in the plasma at one or more radio frequencies. When the incident frequency exceeds the gyrofrequency and the plasma frequency of the medium, the measured impedance can be interpreted in terms of the electron density and collision frequency in the medium. These probes include (a) NASA impedance probe (Jackson and Kane, 1959) where the impedance is measured by sweeping a variable capacitor and the value at which resonance occurs determines the electron density; (b) the capacitance probe (Sayers, 1963; Heikkila, 1965) where the probe forms one element of the tuned circuit whose resonance frequency is determined.

The second type of RF probe is the resonance probe wherein a RF transmitter and receiver separated by a few meters are kept on the space

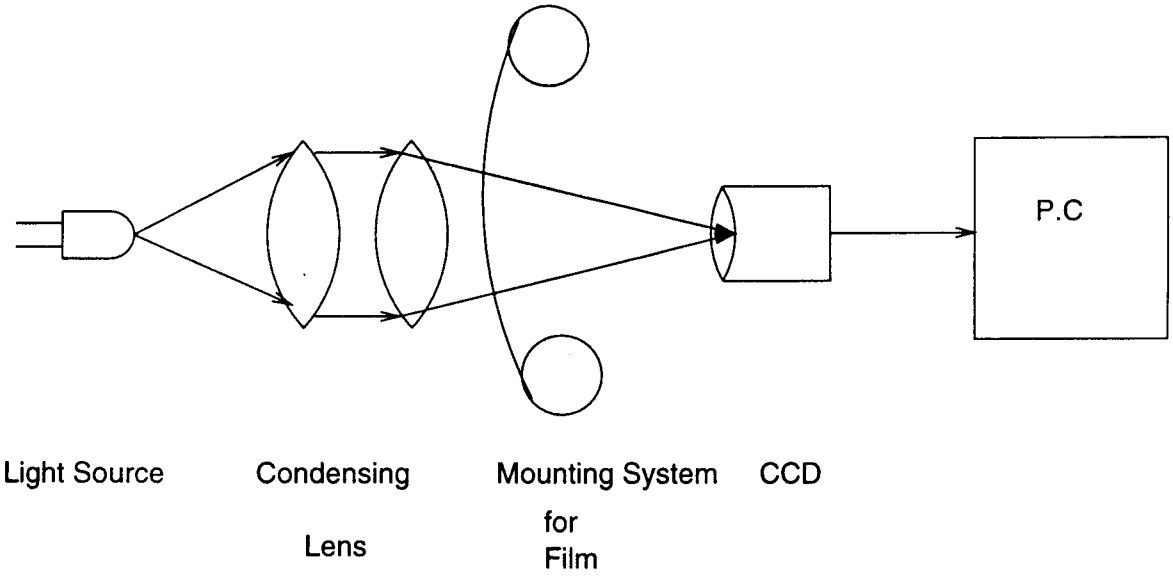

Fig. 2.7 Schematic of Image Digitization System

vehicle. The transmitter frequency is swept from approximately 0.5 MHz to 7.0 MHz for E region. The transmitted radio wave, after its passage through the ambient plasma, is received by the receiver. When the transmitted frequency matches exactly with the plasma frequency there is resonance between the transmitted radio wave and the local plasma frequency as a result of which there is an absorption of energy by the medium. This results in a dip in received signal strength enabling one to identify the local plasma frequency from which one can calculate the absolute electron density of the medium using the simple expression.

$$f_e = \frac{1}{2\pi}\sqrt{\frac{n_e e^2}{\varepsilon_0 m_e}} \qquad (2.4)$$

where,

f_e is plasma frequency in Hz

n_e is the electron density in m^{-3}

e is the electronic charge

ε_0 is the permittivity of free space (8.854×10^{-12} F/m)

m_e is the electronic mass in kg

In fact there are number of other resonances such as upper and lower hybrid frequencies. By a careful examination it is possible to isolate these resonances. But the most dominant among these is the resonance at upper hybrid frequency, f_T, which is given by, $f_T^2 = f_e^2 + f_H^2$, where f_e is the local plasma frequency and f_H is the electron gyrofrequency. Once f_T is identified, f_e can be calculated by substituting the value of f_H which can be calculated. These probes have been flown mainly for E region studies (Rao and Prakash, 1978; Heikkila et al., 1968). Under the category of electrostatic probes, Langmuir probe is the one which is used most, including in the present work. The principle and details of Langmuir probe are discussed at length in the following section with emphasis on its use on rockets.

2.3.2 Rocket-borne Langmuir Probe

Mott-Smith and Langmuir (1926) discussed the current collecting properties of a probe in a plasma from which the modern Langmuir probe (LP) derives its name. This technique was first employed for ionospheric studies in 1946 by Spencer. The basic principle of LP is the following. When a metallic probe is exposed to plasma it acquires a negative potential vis-a-vis the plasma potential. The potential thus acquired is called the 'floating' or 'wall' potential. This negative potential is created because the flux of electrons is much larger than the ion flux due to the fact the thermal velocity of electrons is much higher than those of positive ions. At floating potential the total current collected by the probe, which is the sum of electronic and ionic currents is zero. Floating potential V_f is given by

$$V_f = -\left(\frac{kT_e}{e}\right) \ln\left(\frac{j_o}{j_+}\right) \tag{2.5}$$

where k is the Boltzmann constant, T_e is the electron temperature, e is the electronic charge, j_0 (j_+) is the electron (ion) random current density. j_0 is given by

$$j_0 = \frac{n_e e v_e}{4} A \tag{2.6}$$

where v_e is the electron thermal velocity and A is the surface area of the probe.

For the F-region of ionosphere, a typical value of the floating potential will be about -0.5 volts with respect to the plasma potential. Thus when a rocket, whose outer body is made conducting and has a very large surface area, is flown it acquires a potential which is the floating potential and the same is used as reference. Now if one uses a very small probe, which could be spherical or cylindrical in shape, and bias this probe with respect to the rocket body, the probe will start collecting electronic or ionic current depending upon the bias used. Fig. 2.8. shows a typical LP current-voltage

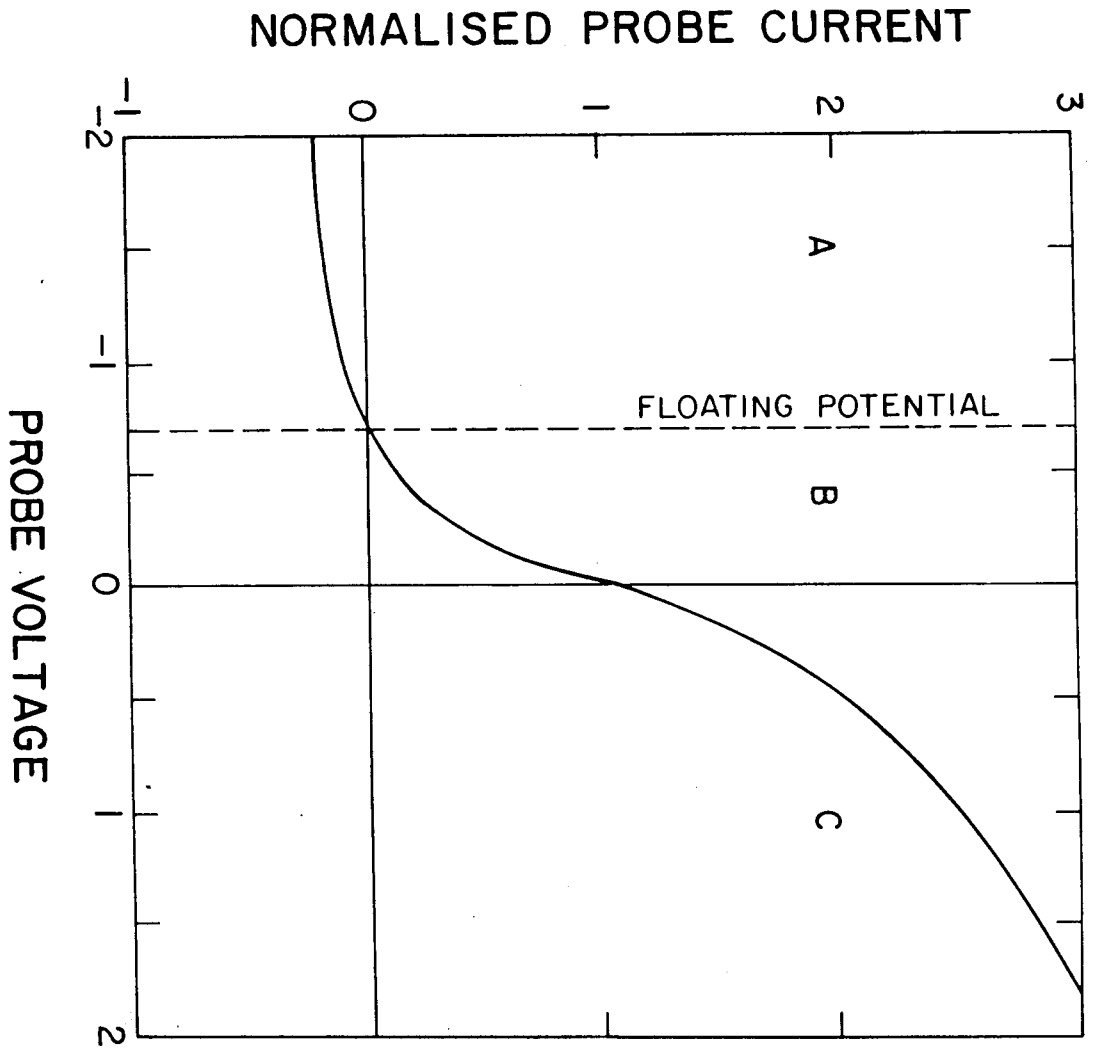

Fig.2.8 A typical Langmuir Probe I-V Characteristic curve.

characteristics. When the probe is at the floating potential, the net current collected by the probe is zero. When the probe is at plasma potential i.e. at slightly positive potential with respect to the floating potential, the current collected by the probe is entirely due to the thermal motion of the charged particles in the medium. As the average velocity of electrons is much larger than the average positive ion velocity, the probe current can be considered to be entirely due to electrons. When small negative voltages are applied to the probe, then the probe current consist of (a) a positive ion current limited by the space charge and (b) a current due to the electrons which overcome the repelling voltage of the probe. When the probe is at a positive potential with respect to plasma, positive ions are repelled and electrons are attracted towards the probe. Even a small positive voltage is sufficient to make the positive ion component of the probe current negligible compared to the electron component.

Generally, the Langmuir probe is used to determine the electron temperature and electron density. For determination of T_e the probe potential (V) has to be swept in the electron retardation region where the probe current is given by

$$j_e = j_0 \exp\left(\frac{eV}{kT_e}\right) \qquad (2.7)$$

Assuming that the electron temperature and hence the electron thermal velocity, v_e, does not change during a sweep cycle, which is typically 0.5 s or less, one can derive electron temperature from equation (2.7). For determination of electron density, the probe must be biased such that it operates in electron saturation region. It can be easily attained by biasing the probe at +4 V with respect to the floating potential.

In the two saturation regions the ion current and the electron current can be obtained by integrating the appropriate drifting Maxwellian energy distribution function over the collector surface for all energies less than the

probe potential. In the electron saturation region the electron current to a cylindrical collector is given approximately by

$$j_e = \frac{2 n_e e v_e}{\pi^{1/2}} A \left(1 + \frac{eV}{kT_e}\right)^{1/2} \qquad (2.8)$$

This expression is derived from the assumption of an infinitely long cylinder and, therefore, has an end effect correction that is usually small for typical cylindrical probe dimensions (Szuszuszczewicz and Takacs, 1979). For a small sphere (radius smaller than the Debye length), the current is given by :

$$j_e = j_0 (1 + eVKT) \qquad (2.9)$$

where j_0 is the random electron current and V is the probe voltage.

2.3.3 Langmuir Probe in the Ionosphere

Region of applicability

The preceding section discussed the theoretical background of the Langmuir probe technique. The condition for the above equations to hold in the ionosphere is determined by the criteria that the Debye length is less than the mean free path. This is necessary so that the a charged particle entering the sheath does not suffer collisions before it is captured at the probe surface. Thus, the optimum conditions for applicability of the theory are given as:

$$\gamma_p < \lambda_D < L$$

where γ_p is the probe radius, λ_D is Debye length and L is the mean free path. The mean free path for the collisions between electrons and neutral particles is about 1 cm at 85 km, decreasing rapidly with decreasing height. Negative ions which are not considered in Langmuir's theory are abundant below 85 km. Therefore 85 kms is the lower limit for the applicability of Langmuir probe theory.

The upper limit for the region of applicability is set by considerations of photoelectric effect. The photoelectric yield of a metal surface such as

tungsten, when exposed to unattenuated solar radiation is about 4 X 10^{-9} amp cm^{-3} (Hinteregger et al., 1959; Bourdeau et al., 1961). Hence the current due to photoemission would be equal to the random current density at higher altitudes than about 1000 kms under normal conditions. Thus the altitude region between 100 - 1000 kms seem to be suitable for exploration by Langmuir Probes, where it has been used extensively. Various geometries have been used, the main considerations being those of mechanical simplicity as well as minimising of the errors introduced due to the motion of the vehicle. Easier mathematical treatment of spherical and cylindrical sensors have made them more popular.

Earth's Magnetic field effect

It is known that the charged particles spiral around the magnetic field lines and diffuse along them. The effective free path for the particles is decided by the Larmor radius, $\rho = mv/eB$. In the lower ionosphere the Larmor radius is about 1 cm for electrons and is of the order of a meter for positive ions. Therefore any probe of practical dimensions will be larger than the effective free path of electrons. When the probe size is larger than the mean free path it collects more particles than can be made up by diffusion from distant regions resulting in depletion in its immediate neighbourhood. This decreases the efficiency of the probe for particle collection. Since the motion along the field line is uninhibited while motion across is inhibited the final result is a compromise in which the probe collects the electrons from regions distant along the field lines but nor far away across the lines. Electron collection is dependent in a complicated way on the probe radius, the electron temperature, the electron density and the magnetic field. Positive jon collection is however not affected by the magnetic field. It is generally believed that the magnetic field does not affect the retarding potential analysis and electron temperatures can be determined even in the presence of a magnetic field. In the retarding potential analysis one is concerned only with the high energy electrons which can overcome the

probe field. Since the magnetic field effect is less for the high energy electrons, because of the smaller Larmor radii of these electrons, the retarding-potential analysis is not considerably affected by magnetic fields.

Reference Electrode

The sweep voltage in the case of an in-situ probe is applied between two electrodes which are placed in the ambient plasma i.e. are at the floating potential. Johnson and Malter (1950) were the first to study such system theoretically. It is customary to make one of the electrodes much smaller than the other which is used as the probe and the larger one as a reference electrode. As the probe voltage is varied, the probe collects current from the medium but the potential of the reference electrode is assumed not to vary because of its large size. When the probe collects charges of one sign, it should be possible for an equal and opposite current to flow into the reference electrode. This condition is easily satisfied when the probe collects positive ions. This situation arises because of large flux of electrons reaching the probe as they have high velocity as compared to the ions. So, when the probe collects electrons an equal number of positive ions can flow into the reference electrode only if it's area is larger than the probe area by a factor equal to or greater than the ratio of the velocity of the electrons to that of the positive ions. A practical Langmuir Probe system can be treated as a single probe if the ratio of the area of the two electrodes is at least ten time j_e/j_+. This ratio, j_e/j_+, is about 170 in most of the regions of interest in the ionosphere. Typically the area available for the reference electrode is between 2×10^4 and 3×10^4 cm^2. Therefore the surface area of the probe should not be exceed 10 to 15 cm^2 if the system is to be treated as a single probe system.

Effect of Vehicle Velocity

It is known in that the average velocity of electrons is about 100 km/s which is much larger than the rocket velocity which is typically around 1.5

km/s. As the average ion velocity is comparable to the rocket velocity, the positive ion collection is affected by the vehicle velocity. The ion current to a spherical probe moving in a plasma can be written as

$$j_+ = 4 \pi r_0^2 j_{0+} Q_0(\eta_0) \tag{2.10}$$

where j_{0+} represents the random ion current in the medium, r_0 is the radius of the sheath and $Q_0(\eta_0)$ is a function of the velocity parameter η_0 given by

$$\eta_0 = \left(\frac{M_+ u_0^2}{2KT_+} \right) \tag{2.11}$$

Here M_+ is the mass of the ion and u_0 is the velocity of the probe in the medium. The form of $Q_0(\eta_0)$ was determined both theoretically and experimentally and the results were in agreement. Using these results observed positive ion currents can be corrected for vehicle motion. The effect of rocket velocity on electron current is negligible.

Effects of the wake of the vehicle

When a rocket or satellite travels with a velocity which exceeds the mean ion velocity in the medium, ions cannot penetrate into the rear of the vehicle. However this is not the case with the electrons which have large velocities. This results in a negative potential in the wake of the vehicle due to the absence of positive ions. The consequence of this is the rarefaction in the electron density distribution. The shape of the wake and the ion and electron potential distribution in it have been discussed earlier (Alpert 1965). They showed that the potential, φ, in the wake at a distance L from the rocket body is given by

$$\phi = \frac{2kT_e}{e} \log \frac{r}{L} \tag{2.12}$$

where r is radius of the rocket body. So, it is necessary for the probe to avoid the wake of the vehicle. This can be achieved by mounting the probe

at the nose tip of the rocket or by projecting it far into the medium using booms. A probe at the nose tip may enter into the wake during the descent. The effect of the probe entering into the wake would be a reduction in the electron current to it.

Effect of Vehicle Potential

When a body is placed in plasma it acquires the floating potential, v_f, at which the sum of the electron and positive ion fluxes to it is zero. This potential for a body at rest is governed by the following equation:

$$j_+ = j_0 \exp\left(-\frac{eV_f}{KT_e}\right) \tag{2.13}$$

where j_0 is the random electron current, j_+ is random positive ion current. For typical ionospheric conditions V_f ranges between -0.2 to -1.0 V. But there are spurious effects due to the motion of the body, solar radiation, the presence of fields on the moving vehicle, the earth's magnetic field and contact potentials due to dissimilar work functions of different parts of the vehicle.

It has been shown by Bourdeau and Donley, (1964) that the effect of the vehicle velocity is to modify floating potential which is given by

$$V_f = -\frac{KT_e}{e} \log\frac{v_e}{v_R} \tag{2.14}$$

where v_e is the random electron velocity, v_R represents vehicle velocity. However this does not effect the result radically. Solar radiation falling on the surface of the body gives rise to photo-emission which tends to make the vehicle acquire a positive potential at higher altitudes and also tends to increase the positive ion current to the probe. At night this effect is unimportant. The effect of the magnetic field is to give rise to an aspect sensitivity to the vehicle potential as the electron diffusion is mainly along the field lines.

Study of Electron Density Irregularities Through Langmuir Probe

Although in principle, it is possible to estimate the electron density of the medium by a Langmuir Probe, in practice it is very difficult to accurately determine the electron density. Usually, the Langmuir Probe derived values are corrected by using some simultaneous estimates such as from a resonance probe or an ionosonde. Generally a few simultaneous flights of Langmuir Probe and Resonance probes are made and a altitude dependent calibration factor is determined to correct the Langmuir Probe derive electron densities. The LP system used for the present work was calibrated (a) by using the electron density derived from the critical frequency of the E-layer as observed with an ionosonde and (b) by using the resonance probe derived absolute electron density. The calibration factor estimated for this system (Subbaraya et al., 1983) for altitude 90 to 150 km agrees fairly well with other estimates (Mechtly at al., 1967). In absence of any altitude dependent calibration factor a fixed factor of 7140 electrons cm^{-1} per μA of current is used.

For electron density irregularities one is really interested in $\delta n_e/n_e$ instead of n_e and in that case the Langmuir Probe is able to give very precise value of percentage change in electron density. The effect of calibration factor is unimportant for study of percentage change in electron density. The spatial resolution of the Langmuir Probe depends on the rocket velocity and a bandwidth of the electronics systems including the trajectory. For a typical rocket velocity of 1 km/s and a frequency response of 1 KHz for the Langmuir Probe electronics, the spatial resolution in one meter. Thus Langmuir Probe can be used to study electron density structures with scale size of 1 meter and above along the velocity vector of the rocket.

The Langmuir Probe used in the present work is essentially similar to the one used by Prakash and Subbaraya (1967), Prakash et al. (1972) and Sinha (1976). A cylindrical LP sensor of length 20 mm and diameter of 30 mm. mounted on central boom was used in the present flight.

The current collected by the LP sensor was processed in three separate channels on board to cover a very large dynamic range of electron density with a good resolution in all the three ranges. Fig. 2.9 shows the block diagram of the Langmuir Probe system which was used for study reported here. As mentioned earlier the LP sensor is a cylindrical sensor which is mounted on a central boom which is spin symmetric. A voltage generator creates the desired voltage wave form with respect to the rocket body, which as at the floating potential. Results presented in this work were obtained when the sensor was kept at a fixed potential of +4 volts with respect to the rocket body or the reference potential. Current collected by the LP sensor is fed to a current to voltage (I-V) converter which is shown in Fig. 2.10. I-V converter has four feedback resistances. When the current is smallest all the three relays (RL1, RL2, and RL3) are open and only the resistance R_1 acts as a feedback resistance and the gain of voltage amplifier is 3.36. As the current increases the gain of the voltage amplifier drops to 1.02. Likewise all the feed back resistance come in parallel one after the other and the gain keeps on changing alternatively, gives rise to following eight states of the feed back resistances

Stage	Total Feedback Resistance	Gain	Effective Feedback Resistance
1	44 MΩ	3.36	148.10 MΩ
2	44 MΩ	1.02	44.88 MΩ
3	4 MΩ	3.36	13.46 MΩ
3	4 MΩ	1.02	4.08 MΩ
5	440 KΩ	3.36	1.48 KΩ
6	440 KΩ	1.02	448.80 KΩ
7	44 KΩ	3.36	148.10 KΩ
8	44 KΩ	1.02	44.88 KΩ

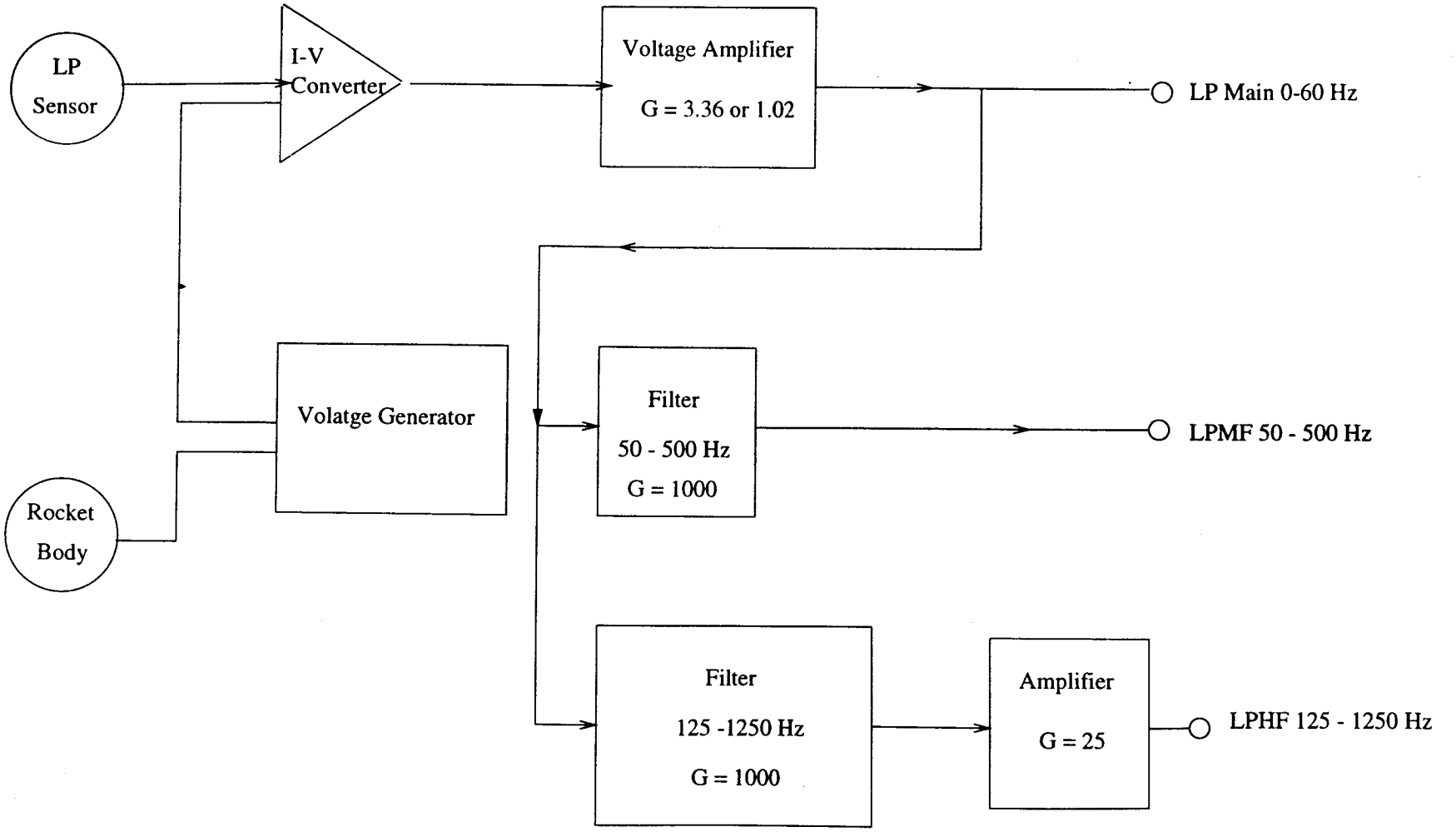

Fig. 2.9 Block diagram of Langmuir Probe used for present work.

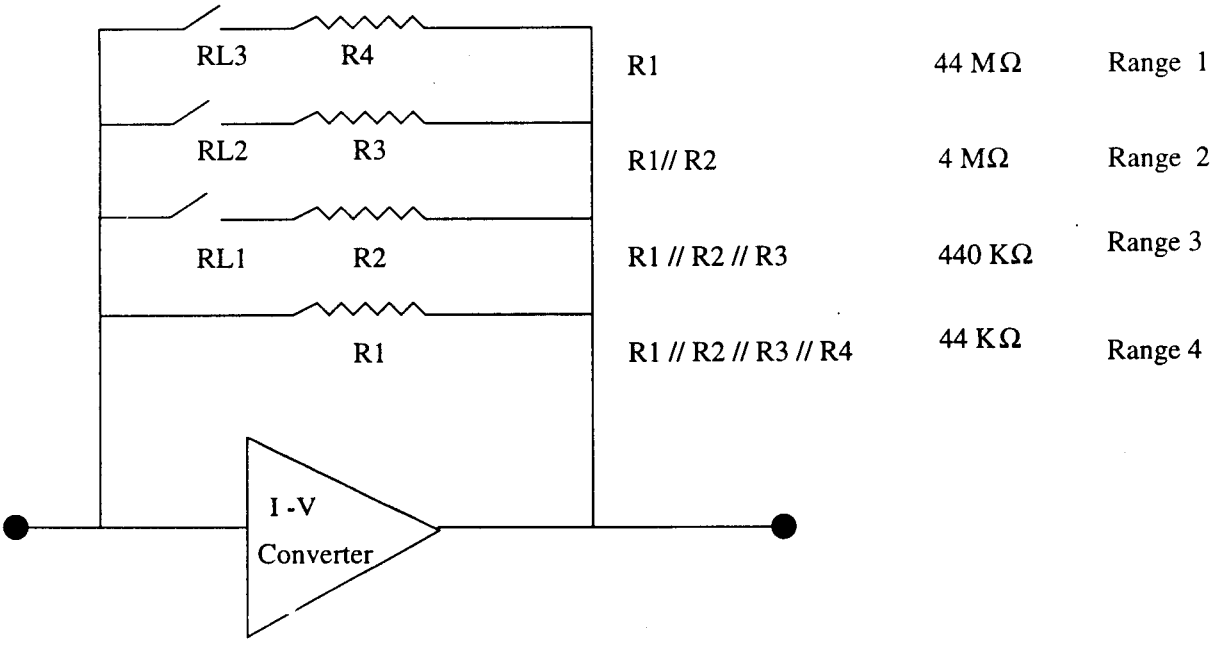

Fig. 2.10 Details of I - V Converter

The output of the voltage amplifier lies in the range of 0-5 volts and goes to 8 bit digitiser which has 255 level. Thus the smallest current which this system can measure is (5 volts)/(255X148.10 MΩ) ≈ 132.5 pA. As the leakage of the operational amplifier used (CA3140) is less than 100 pA and total noise of the electronics system is less than 50 pA, the system can very easily handle currents greater than the 150 pA.

The output of the voltage amplifier is termed as LP Main channel and is used to study fluctuations in the probe current in the frequency range DC to 60 Hz. With a typical rocket velocity of 1.2 km/s, 60 Hz corresponds to scalesize of 20 meter. As the power at smaller scalesizes drops significantly, use of two additional amplifiers is made to study the fluctuations in 50-500 Hz (24m - 2.4m) and 125 - 1250 Hz (9.6m - 0.96m) ranges.

Thus using three channels one can essentially study electron density fluctuation from very large scales down to about one meter.

Maximum detectable signal, which obviously will come in HF channel, is 0.8 mV in 5 V of main channel signal. Hence the maximum detectable power is 20log (0.8 mV/5V) = 136 db.

2.3.4 *In-Situ* Techniques of Electric Field Measurement

There are two techniques for measuring the electric fields in the ionosphere. These are (a) the Bulk Flow Technique and (b) the Langmuir Double Probe Technique. The bulk flow technique is a indirect technique to measure the electric field. Before describing the details of the Langmuir Double Probe technique, which has been used for the present study, an introduction to the bulk flow technique is given

2.3.4a Introduction

Bulk flow measurements of electric field rely on deducing the electric field from the plasma bulk flow velocity, v_b, by using the relation

$$V_b = \frac{\mathbf{E} \times \mathbf{B}}{B^2} \qquad (2.15)$$

where **E** and **B** are the electric and magnetic field vectors respectively. Bulk flow velocity of plasma can be inferred using any of the following methods: (a) artificial vapour cloud motion; (b) Doppler shift of radar signals backscattered from ionospheric irregularities; (c) Thermal ion motion; (d) Split Langmuir probe measurements on rockets or satellites.

Bulk Flow Measurements with Vapour Clouds

In this technique alkali metals like barium are released in the ionosphere from rockets during evening twilight periods. During the twilight period there is no direct sunlight at the ground but the ionosphere is illuminated by sun. When barium vapours are released by rockets they get ionised above about 140 km. After the ionisation the barium ions start drifting under the influence of the ambient electric field. The reason barium is chosen for such experiments is that the barium ions can resonantly scatter the solar radiation at wavelengths which fall in the visible part of the electromagnetic spectrum. The drifting barium ion cloud can be photographed from three ground stations to uniquely determine the bulk flow velocity of barium ion by the triangulation technique. As the drift velocity is in a direction perpendicular to the magnetic field, perpendicular electric field can be estimated from this technique. The expression for the bulk flow velocity V_b in terms of the ambient electric and magnetic fields, electrical conductivities, gyro and collision frequencies, etc. was given by Haraendel et al. (1967) and is reproduced below.

$$V_b = \frac{2}{1+\lambda}\left[\frac{EXB}{B^2} + \frac{1}{\kappa}\left(\frac{E_\perp}{B} + \frac{v_n \times B}{B}\right)\right] + \frac{\lambda - 1}{\lambda + 1} v_{n\perp} \qquad (2.16)$$

where, λ is the ratio of height integrated Pederson conductivities in the presence and in the absence of the cloud, κ is the ratio of gyration to collision frequencies of the barium ions, v_n and $v_{n\perp}$ are the neutral cloud velocity in the reference frame fixed to the earth and the component of this

velocity perpendicular to the local magnetic field direction, and E and $E_{\perp}$ are the ionospheric electric field in a frame of reference fixed to the Earth and the component of this field perpendicular to the local magnetic field direction. The major disadvantage of this technique is that electric field measurements can only be made at twilight hours.

Bulk Flow Measurements by Ionospheric Backscatter

Bulk flow velocity of plasma can also be determined by making use of the radar back scattered signals. In case of ionospheric radar the backscattered signal is either due to incoherent scattering from the thermal electrons or the coherent scattering from ionospheric irregularities.

The incoherent backscatter radars generally use very high power. When the electrons, which are responsible for the backscattered signal, are in motion, the backscattered signal is Doppler shifted. It is possible to determine the line of sight velocity of the scatterers very accurately, without making any assumptions.

In the case of coherent backscatter radar, the backscattered signal is due to these irregularities in electron density which have wavelength equal to half the radar wavelength. The Doppler shift in the coherent backscattered signals gives the phase velocity of irregularities responsible for the backscatter. In this case the bulk flow velocity can be determined only if the relationship between the phase velocity of irregularities and the bulk flow velocity can be reliably modelled. Such relationships have been found empirically for E and F region during day as well as night (Balsley et al., 1972; Prakash and Muralikrishna, 1981; Woodman, 1970). The major disadvantages of this technique are twofold.

a) Existing facilities can generally measure only one component of the drift velocity at a given setting, after which the viewing direction must be changed to measure a second component. Thus, rather large spatial differences exist in the groups of data from which perpendicular fields

are determined and the field vector at a single point is not really measured.

b) Motions producing Doppler shifts can be caused by phenomena other than the **E X B** drifts, such as motions of the neutral atmosphere, gravity waves, fluxes into or out of the protonosphere, and plasma waves not moving with an **E X B** velocity. These result in erroneous estimates of electric field.

Bulk flow measurement from thermal ion fluxes

Since the bulk flow velocity of the ionospheric plasma is comparable to the ion thermal velocity, measurements of thermal ion fluxes can also be used to compute the bulk flow velocity from which it is possible to estimate the DC electric field. This technique involves the use of retarding potential analyser with post acceleration fields and channeltrons.

2.3.4b Langmuir Double Probe Technique

In the Langmuir Double Probe technique, two identical conductors, separated by a distance, d, which is about a few meters or more, are exposed to the plasma. The potential difference between the conductors is monitored using appropriate electronic circuitry. The ambient electric field can be computed by dividing the potential difference between the two conductors by the distance, 'd', between the conductors. At the first sight the technique looks very simple but a slightly detailed look indicates the complexities of this experiment. To have little insight into this technique one has to look into the current balance equation of isolated conductor in plasma.

When a conductor is placed in a plasma, it acquires a potential at which the sum of all currents is zero. This is illustrated by the following equation:

$$I_F + I_i + I_e = 0 \qquad (2.17)$$

where I_F is the positive current which is fed to the conductor (the reason for this will be explained later), I_e is the electronic current and I_i is the ionic current. Eq. (2.17) can be rewritten as

$$I_F + j_i A = j_e \exp\left(\frac{eV_f}{kT}\right) \tag{2.18}$$

where, where V_f is the potential of the conducting surface with respect to the nearby plasma, k is Boltzman constant. From this one can calculate the potential reached by a conductor in the plasma which is given by :

$$V_f = \frac{kT}{e} Ln\left[\left(\frac{m_e}{m_i}\right)^{1/2} + \frac{I_p}{Ane\left(kT/2\pi m_e\right)^{1/2}}\right] \tag{2.19}$$

where, m_i and m_e are the ion and electron masses, n is the density of the plasma, and A is the surface area of the conducting body. The value of V_f in the ionosphere, in absence of non-thermal particles, is typically about -1 V.

The mechanism of potential difference technique can be understood by considering the electron energy diagram of the pair of separated conductors placed in the plasma and connected through a resistance, R, representing the input impedance of the differential amplifier (shown in Fig. 2.11). The electron energy at distances far away from either conductor depends on the electric field in the ionosphere. The difference of plasma potentials at the two conductors is E' d, where E' is the electric field strength and d is the distance between of the two conductors. The electrons experience the effect of the conductor within a distance of the order of Debye length from the conductor. At its surface, the maximum potential energy is reached and then the potential decreases as the surface of the conductor is penetrated with the potential becoming equal to that of the electrons inside the conductor. The electrons inside the two conductors are at different potentials because of the current I, flowing through the resistance, R, connecting the two conducting bodies. Since this current flows on to one conductor and away from the other, the surfaces of the two

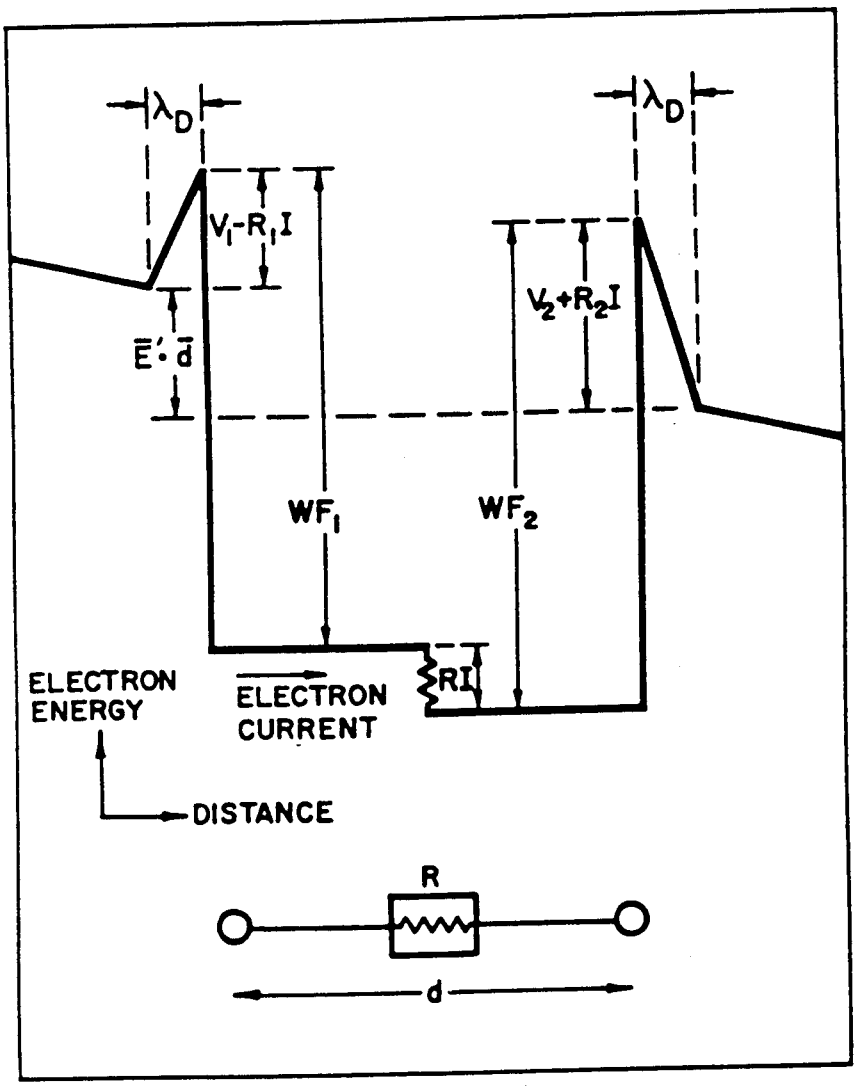

Fig. 2.11 Electron potential energy as a function of position near a Langmuir double probe.

conductors are not at the same potentials with respect to the nearby plasma. The potential of the surface of either conductor with respect to its nearby plasma can be computed from the current balance equation. In a linear approximation the effect of this current is to change the potential of the surface of either conductor by an amount R_1 I where

$$R_1 = \frac{dV}{dI} = \frac{(2\pi m_e kT)^{1/2}}{Ane^2} \exp - \left(\frac{eV}{kT}\right) \qquad (2.20)$$

Thus, the potential of the surface of one of the conductor is V_1 -R_1 I, where R_1 is sheath resistance. Summing the terms of the potential energy diagram, one obtains

$$RI = \frac{\mathbf{E'd} + (V_1 - V_2) + (WF_2 - WF_1)}{1 + (R_1/R) + (R_2/R)} \qquad (2.21)$$

where RI is the potential difference measured by the differential voltmeter, (WF_1 -WF_2) is the difference in the work functions of the two conductors, or their contact potential difference and V_1, V_2 are the potential across the sheath around the conductors. The importance of various terms in the above equation is briefly explained below.

E'.d term

The observed electric field (E') in a moving frame of reference can be transformed to the Earth's fixed frame of reference, using the relation,

$$\mathbf{E'} = \mathbf{E} + \mathbf{V} \times \mathbf{B}$$

where **E** represents field in fixed frame of reference and **V** X **B** results from the motion of the conductors across the magnetic field, B. Thus, for deducing the electric field in the earth frame of reference it is essential to perform vector subtraction. Performance of the vector subtraction requires accurate knowledge of the vehicle orientation and trajectory. V X B is typically 30 mV/m for rockets moving with a velocity of 1 km/s, while

perpendicular ionospheric electric fields are typically 10-100 mV/m at high latitudes and 1 mV/m at low latitudes.

The magnitude and shape of the V X B component along the distance vector, d, depends upon the relative position of the sensors with respect to the spin axis of the rocket.

a) Sensors deployed parallel to the spin axis:-

In this case, the induced field varies with the rocket velocity and its coning angle, when the spin axis is normal to the magnetic filed. Typically, the coning period of F-region rockets is more than 10 s and the change in rocket velocity is less than 1% per second in this duration. Therefore, this term manifest as a dc shift for electric field fluctuations with periods of the order of a few seconds and less. However, if the spin axis is inclined from the vertical by few degrees than V X B term will manifest itself as a sine wave with electric field fluctuations superimposed on it.

b) Sensors deployed perpendicular to the spin axis:-

In this case, the V X B term appears as a sinusoidal variation and the ambient field can be deduced by taking into account the amplitude of sinusoidal signal.

Sheath Potential Difference or (V_1 -V_2) term

The sheath potential drop, V_1, i.e. the potential difference between the surface of the sphere and the nearby plasma can be obtained by the current balance equation discussed earlier.

Electric field measurements are perturbed if the currents of the two conductors are different. If the potentials of the two conductors change by same amount, then there is no net effect in the (V_1 -V_2) term. Non zero differences of sheath potentials may arise from anisotropies of plasma which causes the floating potentials of the two conductors to differ. To

reduce such errors, the conductors are made spherically or cylindrically symmetric and are mounted symmetrically with respect to each other and as well as with the vehicle.

The Contact Potential or (WF_1-WF_2) Term

The (WF_1-WF_2) term originates when the average work functions of the sensors with respect to the nearby plasma are not equal. This term manifest itself as a DC shift resulting from the constant contact potential difference, developed between the sensors. Thus, the potential difference generated between the conductors deployed perpendicular to the spin axis consists of a sine wave due to V X B effect and the DC shift resulting from the difference in work functions of the two conductors. This effect can be eliminated by analysing only the signal produced by the external field since this signal oscillates sinusoidally at the payload spin rate. Non uniformities in the coating of the sensors generates an AC signal as the sensor spins in the anisotropic ionosphere, affecting the AC field measurements. The effect of this term can be minimised by applying a uniform coating to the sensors to keep the contact potential uniform.

The Sheath Resistance Term

The sheath resistance terms in the denominator result mainly from the resistance of the medium to the return flow of current that previously passed through the electronics. The sheath resistance, R_1 or R_2 surrounding the conductor is given by

$$R_1 = \frac{dV_1}{dI} = \frac{kT/e}{I + Ane\sqrt{kT/2\pi m_i}} \qquad (2.22)$$

This equation for V_1 shows that as the current I is increased the potential drop V_1 becomes less negative and hence sheath resistance R_1 decreases. The main advantage of reducing the sheath resistance is that the input impedance of the difference amplifier can be reduced which results in an

improved frequency response of the conductors for an AC electric field measurements. This is done by keeping the bias current to the conductors larger than the ion current. The denominator in the above can essentially be made unity by reducing the plasma sheath resistances (R_1 and R_2) to less than a mega ohm and by making the input impedance of the difference amplifier a few tens of mega ohm. This can be achieved by feeding a small current to the sensors.

2.4 Radio Techniques

Various radio techniques have contributed to the understanding of ionospheric phenomena. The principle of few techniques which have been used in the present work are discussed briefly here.

Ionosonde

The principle of ionosonde is based on the transmission of radio pulse vertically and measuring the time elapsed before the echo is received. The height is found from the time delay of the echo, assuming that the pulse travels at the speed of light. In ionosonde, a pulsed transmitter and a receiver are swept synchronously in frequency, and the delay time is recorded as a function of radio frequency. Ionosondes operate over frequencies in the range of 1 - 20 MHz and rely on the fact that the radio signal is reflected when its frequency f matches with the local plasma frequency f_p, where

$$f_p = (2\pi)^{-1} (n\, e^2/m_e\varepsilon_0)^{1/2} \quad \approx \quad 9000\ \sqrt{n}\ \text{Hz} \qquad (2.23)$$

where n is the plasma density in cm^{-3}. As the peak plasma density in the ionosphere is of the order of 10^6 cm^{-3}, $f_p \leq 12$ MHz. Thus the vertically transmitted frequencies greater than the plasma frequency penetrate the ionosphere. Hence ground-based ionosondes yield no information above the height of the peak on the F-region plasma density. This limitation of ground based ionosondes and lack of information of topside is overcome by making use of topside sounder onboard satellites and as well as with the

incoherent scatter radar techniques. The incoherent scatter radar technique is based on the fact that an upwardly propagating radiowave of higher frequency than the plasma frequency will be weakly reradiated by the free electrons in the ionosphere. This weak incoherent or Thompson scattering provides small but measurable return signals for a probing radar beam which contains information about various ionospheric parameters like (a) electron density, which is proportional to the area of the Doppler signal and typically observable upto 1000 km, (b) the ion acoustic velocity contained in the width of the spectrum or from the position of the peak, (c) ion temperature can be derived from ion acoustic velocity (d) ratio between electron temperature and ion temperature can be inferred from the shape of the spectrum, (e) large scale drift of the ionospheric plasma from the observed Doppler shift of the entire spectrum, (f) Rosenbluth and Rostoker, (1962) inferred differential drifts of electrons and ions from the different heights of the up - down shifted spectral wings.

Scintillations

The scintillation method is used to study the ionosphere by measuring the fluctuations of radio signal due to its traversal through an irregular medium. When the ionosphere contains irregularities of plasma density, phase fluctuations build up across the wave front. As the wave propagates away from the ionosphere, phase mixing occurs and fluctuations in amplitude develop. In the weak-scattering, thin-screen approximation, the medium is replaced by a plane surface along which the phase of the radio wave fluctuations is replaced by a plane surface along which the phase of the radio wave fluctuates but the amplitude remains constant. As the wave propagates beyond the screen, fluctuations in amplitude develop, due to interference effects. Thus if $P_\phi (k_x, k_y)$ is the power spectrum of the phase fluctuations in the wave emerging from an irregularity layer and $P_I(k_x, k_y)$ be the power spectrum of the intensity fluctuations in the received signal, then

$$P_\phi (k_x, k_y) = 2\pi(r_e\lambda)^2 (L \sec \psi) P_N(k_x, k_y, k_z = 0 \qquad (2.24)$$

$$P_I(k_x,k_y) = 4 \sin^2[(k_x^2 + k_y^2)/k_f^2] P\varphi(k_x, k_y) \quad (2.25)$$

where $k_f^2 = 4\pi/Lz$, λ is the wavelength of the incident wave, z is the distance from the source to the observation point, ψ is the angle between the ray path and the vertical at the point where the ray path intercepts the screen, r_e is the classical electron radius which is about 10-15 m, L is the thickness of the irregularity layer, and $P_N(k_x, k_y, k_z = 0)$ is the two dimensional wave number power spectrum in the electron density fluctuations in the plane perpendicular to the k vector of the incident radio wave. Scintillations of the radio beacons transmitted from a geostationary satellite offers a simple way of continuously monitoring the sub-kilometre scale size irregularities associated with equatorial spread F.

Phase and amplitude scintillation measurements are extremely useful when taken in conjunction with other in-situ and optical measurements.

CHAPTER 3

MULTIWAVELENGTH OPTICAL IMAGING OF PLASMA DEPLETIONS FROM SHAR

A unique feature which plays a major role in the physics of ESF phenomenon is the plasma 'depletion or bubble'. These are localised depletions in plasma density with spatial dimensions of the order of ten to few hundred kilometres in the direction transverse to the magnetic field. Such large scale structures correspond to the outer scale of the ESF irregularity spectrum. As the outer scale of ESF structures is considered to govern the subsequent development and characteristics of the irregularity spectrum, a full description of plasma bubble can lead to the better understanding of ESF process.

Plasma bubbles were first discovered as 'ion density bite-outs' by Hanson and Sanatini (1973), using in-situ satellite borne probes. These localised, irregular depletions in ion density were subsequently studied using in-situ techniques by others (McClure et al., 1977; Benson and Brinton, 1983; Singh et al., 1997a, 1997b). These depletions are magnetic field aligned (Tsunoda, 1980), extending to the base of the F region, with ion density decreases up to about 3 orders of magnitudes. These depletions

convect upwards at large velocities through the F layer peak to the topside ionosphere, reaching altitudes as high as 1200 km or more (Woodman and LaHoz, 1976; McClure et al., 1977; Burke et al., 1979). The plasma inside bubbles has been found to have velocities both perpendicular and parallel to the earth's magnetic field (Mendillo and Baumbgardner, 1982; Hanson and Bamgboye, 1984; Aggson et al., 1992). The post-sunset equatorial F-layer can become unstable under the influence of any disturbance produced by gravity waves, neutral winds or some other source and can generate plasma irregularities through Rayleigh-Taylor Instability (RTI). Steep plasma density gradients produced by the primary long wavelength Rayleigh-Taylor mode, create conditions which leads to the hierarchy of plasma instabilities giving rise to smaller scale irregularities (Haerendal, 1974; Ossakow, 1981; Huang and Kelley, 1996a, b). A brief description of two key mechanisms, which are known to be responsible for the generation of ESF irregularities, is given below.

3.1 Physical Mechanism of Rayleigh-Taylor Instability

Dungey (1956) first proposed the gravitational Rayleigh Taylor (R-T) instability as the process driving ESF. This R-T instability occurs when heavier fluid is supported by the lighter fluid. This condition is satisfied in the presence of a fluid density gradient which is antiparallel to gravity. In plasma, R-T instability can occur because the magnetic field acts as a lighter fluid supporting the plasma which acts as a heavier fluid. The mechanism of R-T instability can be understood by considering the electrodynamic equation for the plasma:

$$\rho_j \frac{dV_j}{dt} = \nabla p_j + \rho_j + \frac{q_j \rho_j}{M}\left(E + V_j \times B\right) + \sum_{\substack{j \\ j \neq k}} \rho_j \nu_{jk}(V_j - V_k) \quad (3.1)$$

where ρ_j is the mass density, p_j is the pressure, V_j is the velocity, q_j is the charge of the jth species, E and B are the electric and magnetic fields. The plasma constituents are assumed to be in velocity equilibrium with the

existing force fields. This assumption is valid as the response of the plasma constituents to changing forces occurs very rapidly i.e. $dV_j/dt \approx 0$. The acceleration term of the above equation is $\sim V_j/\tau$ or V_j^2/L where τ is the response time to the external forces and L is the distance for the velocity change. The Lornetz term is of the order of $V_j\Omega_j$, where Ω_j is the gyrofrequency ($q_j B/M_j$) and frictional term is $\approx V_j\nu_j$. As long as $\tau >> \Omega_j^{-1}$ or ν_j^{-1}, the acceleration term can be neglected. In F region, this term is negligible when macroscopic dynamics are considered.

Thus the steady state fluid velocity of each species can be written by setting the time derivative to zero:

$$0 = \nabla p_j + n_j k_B T + q_j M_j \left(E + V_j \times B\right) - \sum_{\substack{k \\ j \neq k}} n_j M_j \nu_{jk} \left(V_j - V_k\right) \quad (3.2)$$

Here E is the electric field measured in the earth-fixed co-ordinate system. The electric field measured in the frame of reference moving with neutral flow velocity, U, is given by $E' = E + U \times B$. Transforming the above equation in the neutral frame of reference and using $V_j' = V_j - U$, the above equation becomes

$$0 = k_B T_j \nabla n + n M_j g + n q_j E' + n q_j \left(V_j' \times B\right) - n M_j \nu_{jn} V_j' \quad (3.3)$$

Dividing by $nM_j\nu_j$ and re-arranging the terms containing velocity to one side, the equation becomes,

$$V_j' - \kappa_j \left(V_j' \times \hat{B}\right) = -D_j \frac{\nabla n}{n} + b_j E' + \left(\frac{D_j}{H_j}\right) \hat{g} \quad (3.4)$$

where $\hat{B}$ is a unit vector in the direction of magnetic field, $\hat{g}$ is in direction of gravity and $\kappa_j = \Omega_j/\nu_j = q_j B/M_j\nu_{jn}$, D_j is the diffusion coefficient ($k_B T_j/M_j\nu_{jn}$), b_j is the mobility ($q_j/M_j\nu_{jn}$), and H_j is the scale height ($k_B T_j/M_j g$). When collision frequency is large ($\kappa_j << 1$), then the first term on the LHS dominates and

$$\mathbf{V_j'} = -D_j\frac{\nabla n}{n} + b_j E' + \left(\frac{D_j}{H_j}\right)\hat{g} \qquad (3.5)$$

Thus, the velocity $V_j' = W_j'$, the fluid velocity, which would arise in an unmagnetized plasma, results in motion parallel to the forces for collisional plasma.

Similarly, for intermediate values of κ, the velocity in the direction parallel to **B** is $V_j' = W_j'$. In the direction orthogonal to **B**, the velocity can be determined from

$$V_j' \times \hat{B} - \kappa_j \left(V_j' \times \hat{B}\right) X \hat{B} = W_j' \times \hat{B} \qquad (3.6)$$

Defining $\left(V_j' \times \hat{B}\right) \times \hat{B} = V_\perp$ and $\left(W_j' \times \hat{B}\right) \times \hat{B} = W'_\perp$, and arranging the terms,

$$V_\perp = \frac{W_\perp}{1 + k_j^2} + \frac{k_j}{1 + \kappa_j^2}\left(W_\perp \times \hat{B}\right) \qquad (3.7)$$

For the electrons κ_e is large, so that the second term in the above equation dominates and the velocity of electrons can be expressed as :

$$V_e = \frac{E \times B}{B^2} - \left(\frac{m}{eB^2}\right)(g \times B) + \left(k_B T / eB^2 n\right)(\nabla n \times B) \qquad (3.8)$$

In the F region $\kappa_i >> 1$, for the ions but not large enough to ignore the first term as for the electrons,

$$V_i = \left(\frac{b_i}{\kappa_i^2}\right) E + \frac{g}{\nu_{in}\kappa_i^2} - \left(\frac{D_i}{\kappa_i^2}\right)\frac{\nabla n}{n} + \frac{\mathbf{E} \times \mathbf{B}}{\mathbf{B}^2} - \left(m/eB^2\right)(\mathbf{g} \times \mathbf{B}) + \left(k_B T / eB^2 n\right)(\nabla \mathbf{n} \times \mathbf{B}) \qquad (3.9)$$

As the electron mass is small, g × B term in the equation for V_e can be ignored. Similarly, in the equations for ions, the second and third term can

be dropped as $\kappa_i >> 1$. Since $\mathbf{E} \times \mathbf{B}$ term is identical for ions and electrons, it does not give rise to current and J is given by :

$$\mathbf{J} = ne(\mathbf{V}_i - \mathbf{V}_e)$$

$$\mathbf{J} = \sigma_p \mathbf{E} + \left(\frac{ne}{\Omega_i}\right)\mathbf{g} \times \hat{\mathbf{B}} - \left(\frac{k_B}{B^2}\right)(T_i + T_e)(\nabla n \times \mathbf{B}) \qquad (3.10)$$

Thus the gravitational current flows even in a collisional plasma while the electric field term exists only if $\sigma_p \neq 0$, i.e. in a partially collisional plasma. For a pure R-T case, considering only the second term i.e. the gravitational term, for a vertically stratified equatorial F layer under the effect of gravity only, a net current flows in the x direction with magnitude,

$$J_x = \frac{nMg}{B} \qquad (3.11)$$

Since the gravitational term is proportional to mass, ions move faster than the electrons. This differential motion results in divergence and accumulation of charges on the edges of the small initial perturbation. As a result, perturbation electric fields δE develop in such a way that they cause an upward $\delta\mathbf{E} \times \mathbf{B}$ drift of the ions and electrons in the region of plasma depletion and a downward drift in the region where the density is enhanced as shown in Fig. 3.1. Thus the lower density plasma is taken upward and vice versa creating a larger perturbation and the system becomes unstable. The linear growth rate has been computed by linearising the continuity equation, linear momentum and current conservation equation (Haerendal 1974; Ossakow et al., 1979; Hanson et al., 1986) and is expressed as

$$\gamma_g = \frac{g}{L\nu_{in}} \qquad (3.12)$$

where L is the inverse gradient scale length expressed as:

$$L = \left(\frac{1}{n_0}\frac{dn_0}{dz}\right)^{-1} \qquad (3.13)$$

The growth rate of the instability must be faster than the life time of the ions $(1/\nu_R)$ otherwise the ions would be lost by recombination process.

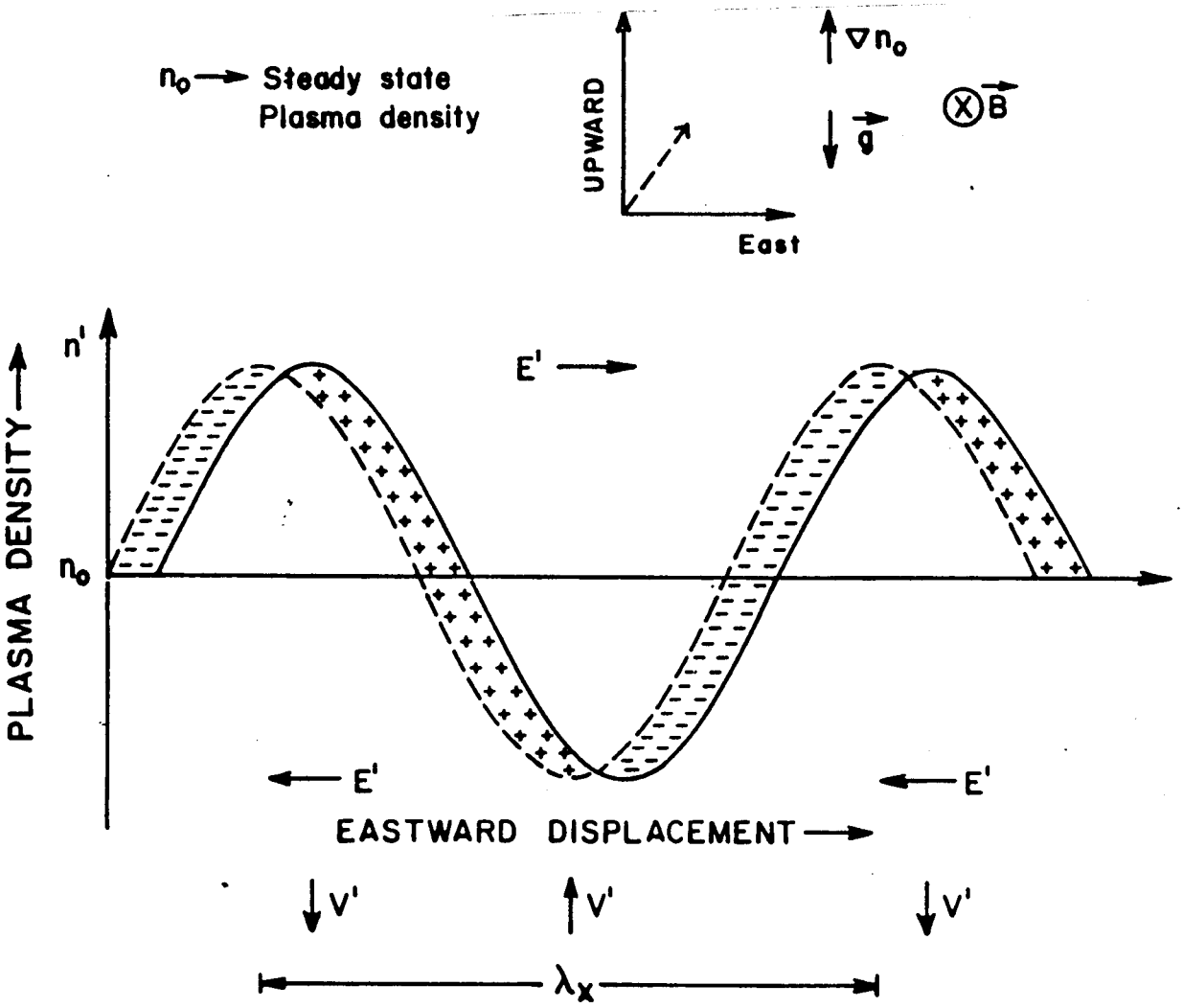

Fig.3.1 Physical mechanism of Rayleigh-Taylor instability. The solid and dashed line shows the ion and electron densities. Regions of excess ions and electrons are represented by positive and negative signs respectively.

This instability has **k** $\perp$ **B** and is also called as 'flute instability'.

3.2 Mechanism of Gradient Drift (E X B) Instability

It is known that the steep density gradients created by the primary R-T instability make conditions favourable for other plasma instabilities to generate smaller scale irregularities (Haerendal, 1974; Ossakow, 1981). In the F region, the gradient drift instability occurs whenever the direction of electric field is such that the E $\times$ B drift is parallel to the background plasma density gradient ∇n. The mechanism can be explained by considering the Pederson mobilities of ions and electrons in the F region which is expressed as $1/(eB)\ (\nu/\Omega)$ where ν is the collision frequency and Ω is the gyrofrequency. Thus, forces in the Pederson direction are opposite in direction for electrons and ions. During the night time, since ν_{in}/Ω_i ($\sim 2.7 \times 10^{-3}$) > ν_{en}/Ω_e ($\sim 2.5 \times 10^{-5}$), charge separation occurs as ions move faster than the electrons in the Pederson direction. This differential motion results in regions of excess ions and electrons in such a way that polarisation electric fields are developed to maintain charge neutrality conditions. In the presence of a sinusoidal perturbation, these polarisation drifts are directed eastward and westward alternately in the trough and the crest region which give rise to upward and downward drift. The downward drift brings plasma from the denser region which gets accumulated in the crest region while the plasma is taken away by the upward polarisation drift in the trough region as shown in Fig. 3.2. This causes the amplitude of the perturbation to grow. The linear growth rate of this instability at the F region altitudes is given by the expression:

$$\gamma_E = \frac{E_0}{BL} \qquad (3.14)$$

where E_0 and B are the magnitudes of ambient zonal electric and the earth's magnetic fields respectively.

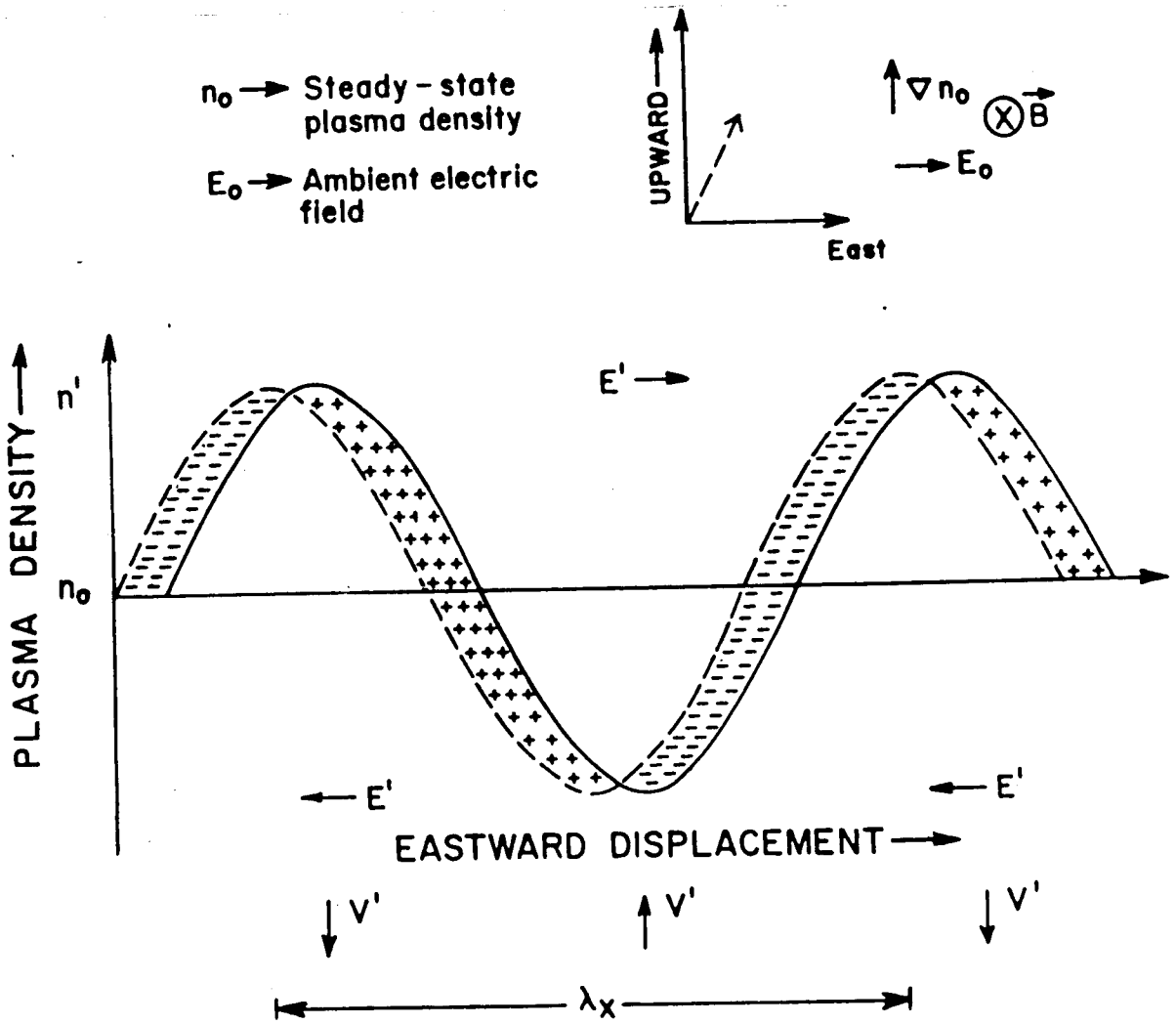

Fig.3.2 Picture demostrating the physical mechanism of E × B instability with the same notation as in Fig.3.1.

The planetary scale electric fields in the F region of the ionosphere are directed upward and eastward during daytime and reverse their polarity within one to two hours after local sunset (Woodman, 1970). Under these conditions the gradient drift instability in the F region can occur in the presence of either the zonal electric field with vertical plasma density gradient or vertical electric field with zonal plasma density gradient. During night time, the bottomside of the F layer is characterised by the presence of steep vertical density gradients and hence zonal electric fields can contribute to the development of primary instability process. As mentioned before, steep plasma density gradients are created in the zonal direction due to the action of primary instability mechanisms and so the vertical electric field can result in the development of secondary instabilities.

It is worth noting that the conditions which determine the growth rate of the gradient drift instability in the E and F regions are different. This is attributed to the fact that the collision frequency of ions exceeds their gyrofrequency in the E region while in the F region they drift essentially in the Hall direction along with electrons. In the E region this instability occurs when the direction of electric field E is parallel to the background plasma density gradient. Simon (1963) invoked this instability to explain the low frequency fluctuations seen in laboratory plasma discharges. Later on, attempts were made to explain E region irregularities using this instability process (Maeda et al., 1963; Tsuda et al., 1966; Whitehead, 1967, 1968; Sato et al., 1968; Fejer et al., 1975; Sudan et al., 1973). The mechanism was extended to explain ESF irregularities (Martyn, 1959b; Reid, 1968; Cunnold, 1969).

3.3 Airglow Emissions used in the present study of Plasma Depletions

Plasma depletions seen in the optical images are the optical signatures of plasma bubbles which are generated through R-T process during the postsunset time at the bottomside of the F layer. The formation of

depleted regions in low latitude ionosphere has been the subject of a number of observational (Weber et al., 1978; Mendillo and Baumgardner, 1982; Rohrbaugh et al., 1989; Sinha et al., 1991; Mukherjee et al., 1993; Sahai et al., 1994a; Sinha et al., 1996; Mendillo et al., 1997a, b; Taylor et al., 1997; Tinsley et al., 1997) and theoretical (Zalesak et al., 1982; Anderson and Mendillo, 1983; Sekar et al., 1997) studies. As these plasma bubbles are regions of localised, irregular depletions in electron density, they are associated with reduced airglow intensity as compared to the surrounding regions. The morphology and the dynamics of these field aligned transequatorial ionospheric plasma depletions can be monitored through observations of the intensities of various ionospheric airglow emissions.

Atomic oxygen emissions, which arise from F-region recombination processes, can be used as diagnostic tools to study large scale F-region irregularities. The OI emissions at 777.4 nm and 630 nm are particularly suitable for ground based mapping of these irregularities. McClure et al. (1977), indicated that the part of the vertical ionospheric motions, responsible for the 630 nm airglow maps of VanZandt and Peterson (1968), was due to ionospheric processes associated with the plumes and bubbles of ionospheric irregularities. Weber et al. (1978), and Moore and Weber (1981) used an airborne TV imaging system to demonstrate that 630 nm and 777.4 nm emissions originating from the equatorial evening ionosphere could be used to obtain all-sky airglow maps of F-region plasma depletions.

3.3.1 Mechanism of 630 nm Emission

The 630 nm airglow line is emitted by $O(^1D)$ atoms which are produced by the dissociative recombination of O_2^+ with electrons during night time. Study of the creation and destruction of the metastable oxygen atom, $O(^1D)$, became important since the identification of the 630 nm emission in the nightglow spectrum. The early studies of the processes by which this state is excited have been reviewed by Chamberlain (1961) and Noxon (1968). The principal thermospheric sources of $O(^1D)$ atoms are discussed below (Hays et al., 1978).

Electron Impact

Ground state atomic oxygen, $O(^3P)$, may be excited to the ^1D state as a result of collisions with electrons of energy greater than 1.96 eV, by both hot thermals and photoelectrons (Dalgarno and Walker, 1964; Wallace and McElroy, 1966).

$$O(^3P) + e\,(E > 1.96\ eV) \rightarrow O(^1D) + e \qquad (3.15)$$

Rees et al. (1967) evaluated the excitation rate by hot thermal electrons. Non-thermal photoelectrons and secondary electrons also produce $O(^1D)$ during the random walk energy degradation processes which lead to thermalization process (Fournier and Nagy, 1965).

Photodissociation

The Photodissociation in the Schumann-Runge continuum (150 nm - 175 nm) of molecular oxygen (Noxon and Johanson, 1972) also contribute to the production of $O(^1D)$ state by,

$$O_2(X^3\Sigma_g^-) + h\nu \rightarrow O(^1D) + O(^3P) \qquad (3.16)$$

The cross sections for this process are well known (Metzer and Cook, 1964; Hudson, 1971) and thus the rate of $O(^1D)$ production by this process can be determined if the solar flux is known.

Dissociative Recombination

The classical night-time source of $O(^1D)$ is dissociative recombination which is given below:

$$O^+_2(X^2\Pi_g) + e \xrightarrow{\alpha} O(^1D) + O(^3P) + 5\ eV \qquad (3.17)$$

This process is of little significance in the sunlit atmosphere. The O^+_2 ions are formed as a part of the night time decay of ionisation via the initial ion-atom exchange reaction that converts O^+ ions to O^+_2 as given below:

$$O^+ + O_2 \xrightarrow{\gamma} O^+_2 + O \qquad (3.18)$$

where the rate coefficient $\gamma \approx 2 \times 10^{-11}$ cm^3s^{-1} and $\alpha \approx 1.9 \times 10^{-7}(T_e/300)^{-0.5}$ cm^3s^{-1} (Banks and Kockarts, 1973). It can be seen that the later process being slower than the former one, governs the overall rate of the reaction. Tinsley and Bittencourt (1975), showed that the column emission rate, J_{630}, due to dissociative recombination, is given by

$$J_{630} = \int \left(\frac{K A_{630} \gamma_1 n(O_2) n(O^+) \, dz}{A(1 + dz/A)} \right) \qquad (3.19)$$

where $n(O_2)$ is the molecular oxygen density, $n(O^+)$ is the atomic oxygen ion density, γ_1 is the reaction rate coefficient for the dissociative recombination of O_2^+, K is the quantum efficiency (i.e. the fraction of ^1D excited states produced per dissociative recombination of O_2^+), A and A_{630} represent the Einstein coefficients for transition from the ^1D state to ground state and for transition leading to the 630 nm emission respectively, and dz is the altitude dependent quenching coefficient.

Thus this line arises from reactions between F-region plasma (O^+, e^-) and the neutral atmosphere (O_2, N_2). The exponential decrease of N_2 and O_2 with altitude causes the red line emission profile to be influenced strongly by the plasma below the F-region peak, as well as the height of that peak. At higher altitudes the concentration of neutrals is less and at lower altitudes the concentration of electrons is less. So, the bulk emission originates from a layer located around 250 km having a thickness of about 50 km as the optimum number of neutrals and electrons are present around this altitude.

Destruction of $O(^1D)$: Quenching and Radiation

Airglow emission at 630 nm arise when the oxygen, $O(^1D)$ state is destroyed either by quenching or radiation processes:

(a) Spontaneous radiation :

$$O(^1D) \rightarrow O(3P) + h\nu \qquad (3.20)$$

(b) Quenching on O_2 and N_2,

$$O(^1D) + O_2 \rightarrow O(^3P) + O_2 \quad (3.21)$$

$$O(^1D) + N_2 \rightarrow O(^3P) + N_2 \quad (3.22)$$

The rate of O_2 quenching is of the same order of magnitude as N_2, but the concentration of O_2 is only about 0.1 times that of N_2.

3.3.2 Mechanism of 777.4 nm Emission

The 777.4 nm emission was first observed by Weil and Joseph (1970) and it results mainly from the radiative recombination of O^+ and electrons in the ionospheric F-region. The excitation mechanism for OI emissions due to radiative recombination was first suggested by Hanson (1969).

$$O^+ + e \rightarrow O(4p\ ^3P, 3p\ ^5P, 3p\ ^3P) + h\nu \quad (3.23)$$

The transitions and corresponding lines are ($3s\ ^3S^0$ - $4p\ ^3P$) at 436.8 nm, ($3s\ ^5S^0$ - $3p\ ^5P$) at 777.4 nm and ($3s\ ^3S^0$ - $3p\ ^3P$) at 844.6 nm. As can be seen from the above equation, emission at 777.4 nm is dominated by plasma densities in the topside ionosphere, where most of the total electron content (TEC) resides.

A small contribution to this emission also comes from the ion-ion recombination reaction (Knudson, 1970; Tinsley et al., 1973)

$$O^+ + O^- \rightarrow O + O \quad (3.24)$$

The production of O^- ions is through the radiative attachment reaction

$$O + e^- \rightarrow O^- + h\nu \quad (3.25)$$

which is followed by mutual neutralisation with O^+ ions leaving one or both the oxygen atoms in an excited state, which can then decay or cascade to the ground state in one or more transitions (Oslen et al., 1971). Knudson (1970), estimated the concentration of negative ions in the night time F_2 ionosphere and found it to be a small fraction of the electron concentration, (< 1% of [e]). Hanson (1970), compared the contribution of radiative recombination and oxygen ion-ion neutralisation mechanism and concluded

that radiative recombination should always be dominant. Tinsley et al. (1973), showed that the radiative recombination is the major source for the 777.4 nm emission in the tropical region and that the column emission rate, J_{7774}, due to this process, is given by

$$J_{777.4} = \int \alpha_{777.4} \left[n(e)\right]^2 dz \qquad (3.26)$$

where $\alpha_{777.4}$ is the partial rate coefficient for radiative recombination, n(e) is the electron density, and z denotes the altitude. Therefore, neglecting the small contribution from the ion-ion recombination, the observed 777.4 nm emission is a function of the integrated $[n(e)]^2$, and hence the maximum contribution comes from F_2 peak.

This emission is a very good indicator of the F_2 region electron density. This was shown by Tinsley and Bittencourt (1975) by considering the ratio of vertical column emission rate of radiative recombination process and dissociative recombination. They showed that for electron density estimation the above ratio should have (a) the numerator containing the column emission rate of an atomic oxygen radiative recombination emission (such as OI 905 - to 910 Å continuum, OI 7774 Å or OI 4368 Å) and (b) the denominator containing the column emission rate of an atomic oxygen emission from dissociative recombination, like [OI] 6300 Å, 6364 Å, 2972 Å, or 5577 Å, if F region component can be separated from E region component.

The airglow emissions at 630 nm and 777.4 nm have been used in the present study for studying various properties of plasma depletions.

3.4 Observations of Plasma Depletions

The optical imaging system was operated from SHAR (14° N, 80° E, 5.5° N, dip latitude) from January to March 1993 in order to photograph ionospheric plasma depletions. During this period, ground based ionosonde was operated from SHAR. The VHF scintillations were also recorded at

Ahmedabad, SHAR and Waltair using the 244 MHz beacon onboard the satellite FLEETSTAT (73° E). A second campaign was conducted from January to April, 1997, from SHAR. Attempts were made to operate the system during 1994 to 1996 but very low solar activity coupled with bad weather did not permit any significant data set from SHAR.

The airglow viewing geometry as seen by the instrument operated from SHAR is shown in Fig. 3.3. The magnetic field line geometry was obtained using a model magnetic field represented by spherical harmonic coefficients. The thick line in this figure represents the 630 nm emission line located around 250 km. With a 180° field of view, the system can see plasma depletions up to a dip latitude of 30° N near the northern edge and upto 17° S dip latitude near the southern edge which correspond to field lines passing through 2000 km and about 700 km, respectively above the dip equator. The north-south extent covered by this system is around 3650 km and that along east-west direction is approximately 3575 km.

As the intensity of the airglow emissions are very weak, exposure times of 30 s was used to record 630 nm images and 120 s exposure was required for 777.4 nm images. Longer exposures for 777.4 nm were required as the intensity of this radiation is $\approx$ 4-5 times smaller than 630 nm emission.

3.5 Procedure of Optical Data Analysis

All the images obtained by the system were digitised using CCD-based digitising system. During the first campaign the digitisation resulted in 512 $\times$ 512 array of 8 bits. However, for the images obtained during 1997 period, a higher resolution digitising CCD camera system was used. This produced 512 $\times$ 550 array of 12 bits. Since the airglow depletions are embedded in the background, it is necessary to eliminate the background in order to enhance the depletion. This involves following methodology.

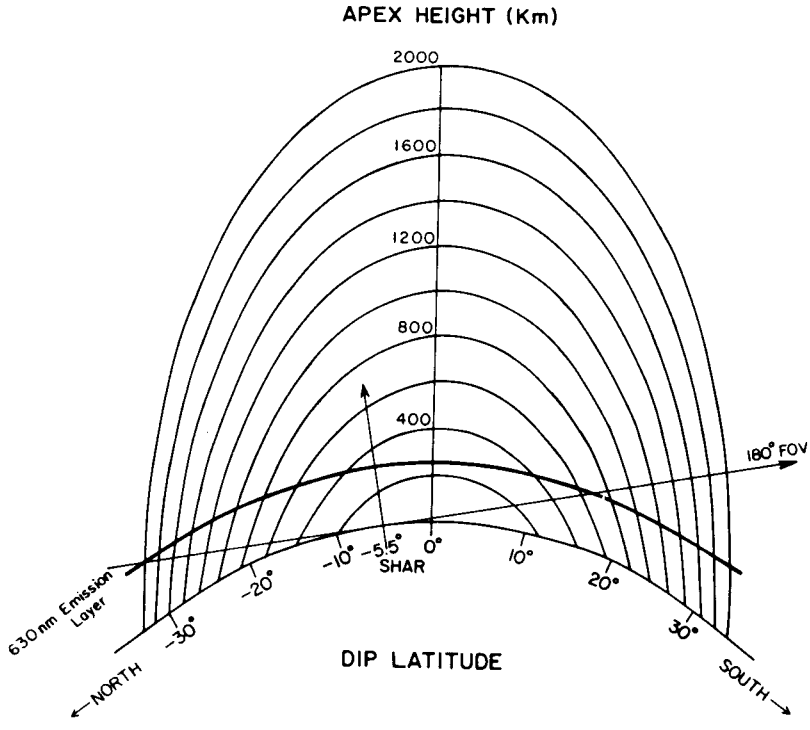

Fig 3.3 Airglow viewing geometry from SHAR.

Using the light source and condensing lens system employed for digitisation of the image, a number of frames were exposed with film without data in the film carrier. These frames represented flat field frame. An average of 10 such flat field frames was taken to generate the master flat field frame for the CCD camera employed for digitising. Before taking the actual picture, the fish eye lens was covered and 30, 60 and 120 s exposures were taken for removal of the noise of the image intensifier. All the frames having same exposure time were averaged and a master averaged frame was generated for that exposure time. The data frames were then normalised with the master flat field frame to remove the non-uniformities of the illumination of the digitising system. For a given exposure time, the frame which was obtained by closing the fish eye lens cover, was subtracted from individual data frames to remove the effect of image intensifier noise. Thus a series of data frames were obtained for a particular exposure time. Next, all these frames were averaged to generate a final frame. This final frame was subtracted from the data frames to remove all the stationary features such as the station illumination, building lights, etc. and thus enhancing the non-stationary features such as the plasma depletions.

The entire procedure of analysis starting from, the exposing of film, developing and fixing it, digitisation, removal of image intensifier and background noise, flat field and image processing was identical for all images shown here except that for the 1997 campaign a 12-bit digitising system was used. The colours introduced are the false colours and these have been employed to improve the viewing of the image. As no calibration with the standard source was performed, the airglow intensities of all the images are in relative units. The images having similar colours can be inter compared.

3.6 Results

3.6.1 Airglow Depletions and Scintillations

Strong spread F echoes were seen on the ionograms recorded from SHAR on February 21, 1993. Very clear plasma depletions were also observed on the same night using our Multi Wavelength All Sky Imaging System, MAIS. The 630.0 nm airglow images obtained on 21/22 February 1993 nights are shown in the Fig. 3.4a and b. The centre of the image represents zenith over SHAR. The image at 2256 hrs shows the presence of one fully developed plasma depletion (almost overhead at SHAR) and one very weak depletion on the western side. The yellow regions indicate small airglow intensity (and hence low plasma density) whereas the blue regions indicate the highest density. The other shades represent intermediate intensities. At 2316 hrs LT the first depletion has moved eastward, the weaker depletion has intensified and moved slightly eastward and a third depletion has just started forming on the western horizon. At 2346 hrs LT, all the depletions have intensified and moved eastward. Another interesting feature seen in this image is the flanking of depletion on both eastern and western side, by regions of enhanced airglow. At 0001 hrs LT, the depletions have weakened very much. But the depletions started becoming more pronounced at 0006 hrs LT and 0016 hrs LT. Beyond 0016 hrs LT the depletions became very weak.

Similarly, Fig. 3.4c shows the 777.4 nm airglow images obtained on the same night. Here dark violet bands represent more airglow intensity. White regions indicate regions of less airglow intensity and hence represent plasma depletions. Weaker depletions are seen around 2318 hrs LT and 2323 hrs LT which are observed to drift eastward. Around 2343 hrs LT the depletions are flanked by enhanced regions of airglow which becomes weaker later on as shown in Fig. 3.4b.

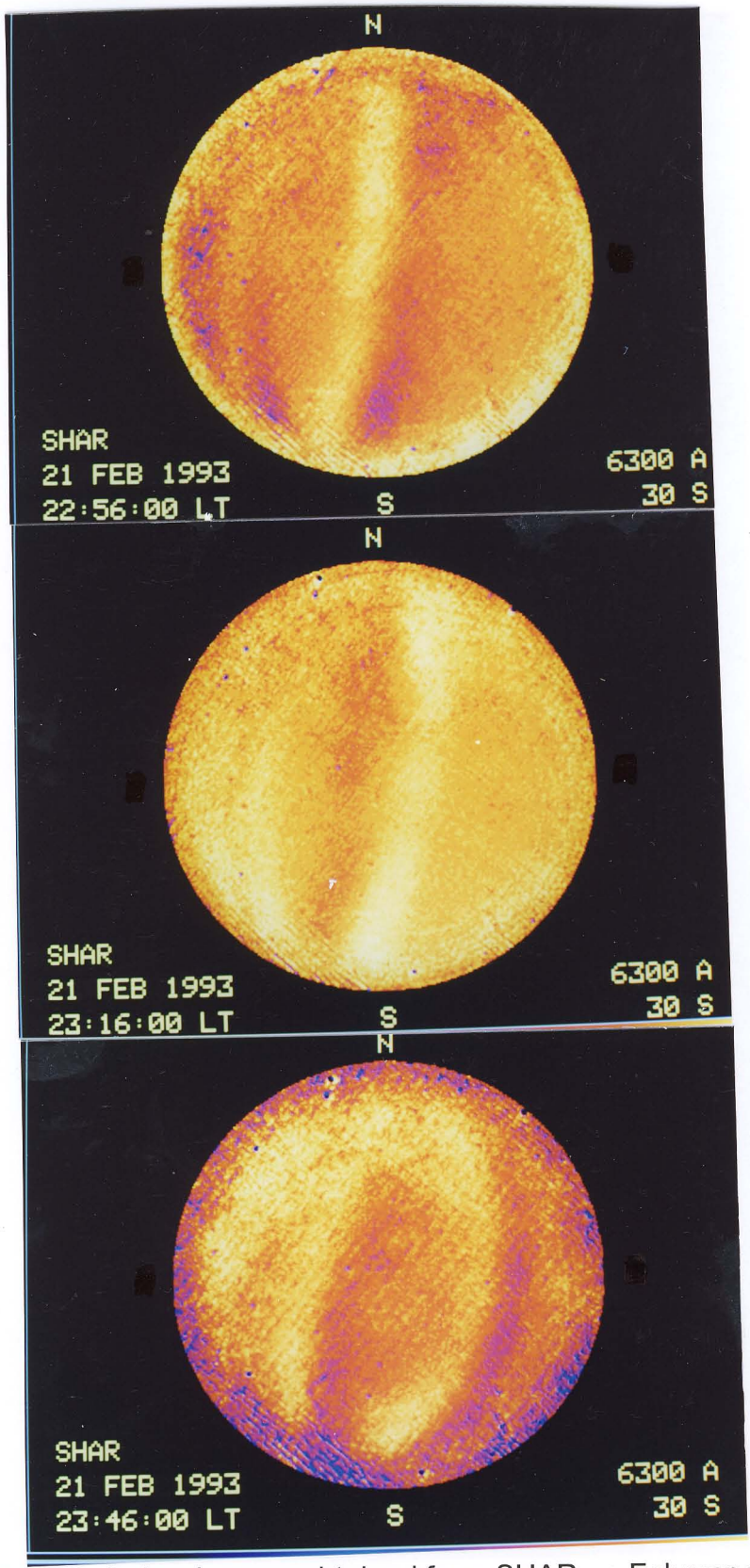

Fig. 3.4a 630 nm airglow images obtained from SHAR on February 21, 1993.

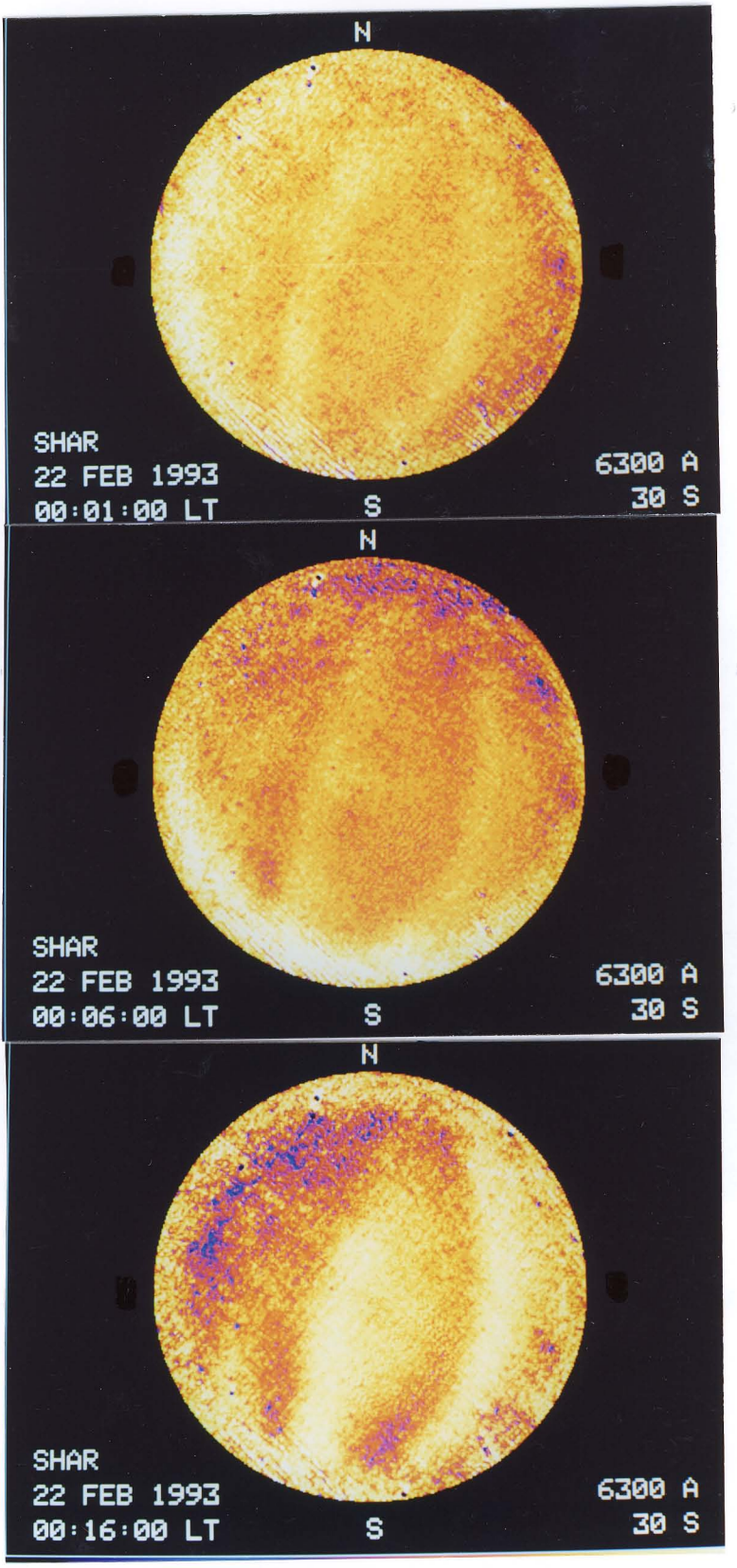

Fig. 3.4b 630 nm airglow images obtained from SHAR on February 21, 1993.

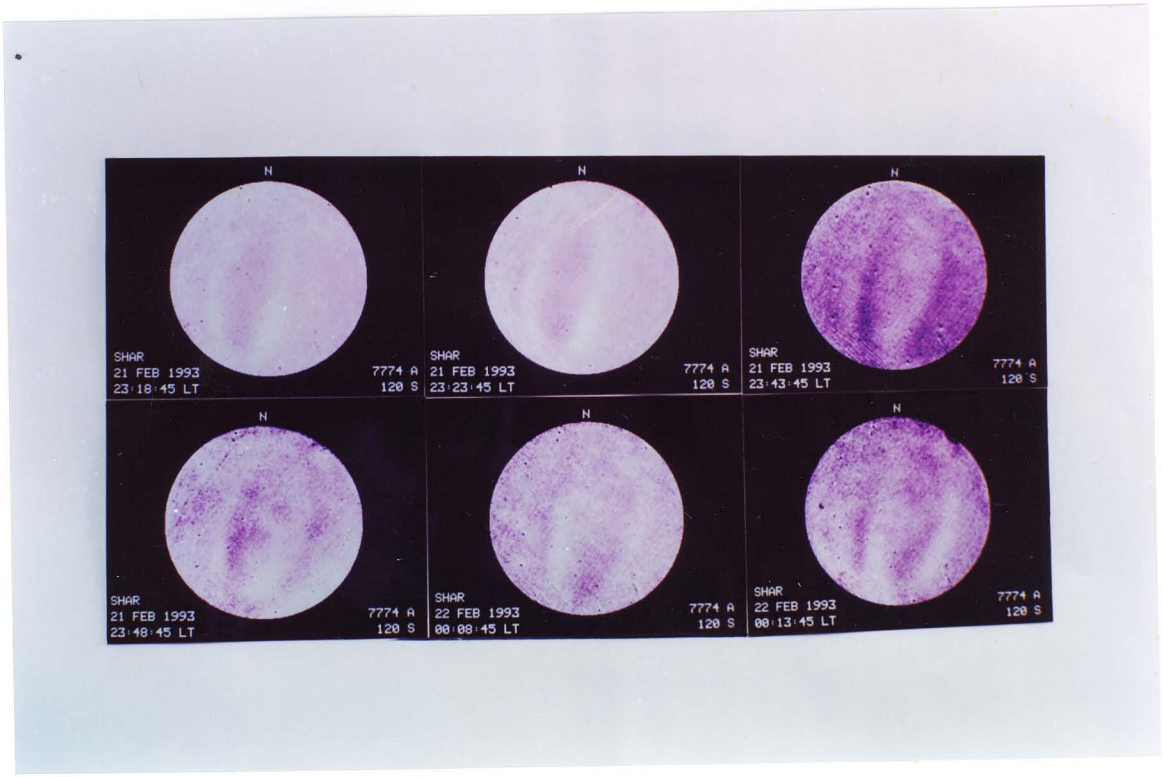

Fig. 3.4c 777.4 nm airglow images obtained from SHAR on February 21, 1993.

The spread F as seen on the ionograms occurred in three distinct patches during this night. First signatures of spreading of F-layer trace during this night were seen at 1900 hrs LT with h'F, the minimum virtual height of F layer, at 330 km as shown in Fig. 3.5. Spreading became more evident in the ionogram of 1930 hrs LT. Strong spread F echoes appeared in the ionograms of 2000 hrs LT. Here the spreading was seen in two altitude regions. One between 310 and 390 km corresponding to overhead echoes, while the other between 430 and 500 km corresponding to oblique echoes appearing from a patch situated in the east or west of the ionosonde. By 2015 hrs LT the two groups of echoes merged into single region of echoes which was present till 2115 hrs LT. The spreading is considerably weakened at 2145 hrs LT and completely absent at 2200 hrs LT. The F-layer descended gradually with h'F of 230 km at 2130 hrs LT.

The second patch of spread F occurred between 2230 and 2330 hrs LT. In this case two additional traces are noticed at 2230 hrs LT which develop into moderate spread F in subsequent ionograms. Spreading in the main trace has disappeared at 2330 hrs LT. However, another trace corresponding to oblique echoes is seen which disappears by midnight. The third patch occurred between 0045 and 0230 hrs LT.

The nocturnal variations of the h'F and vertical drift, V_z, deduced from the rate of change in h'F are shown in the Fig. 3.6. The evening height rise in h'F lifts the F layer base to nearly 340 km at 1900 hrs LT. The layer descends to 310 km by 2000 hrs LT, but again rises for a short duration to 330 km. A rapid descent from 330 km to 225 km is seen between 2015 and 2130 hrs LT. The h'F remains at around 220 km between 2200 and 0400 hrs LT. The vertical drift, V_z, is upward before 1900 hrs LT with a maximum velocity ≈ 30 ms^{-1}. From 1915 to 2130 hrs LT it is downward, except at 2015 hrs LT, with a maximum downward velocity ≈ 50 ms^{-1} at 2130 hrs LT. Later in the night, there are no significant vertical motions.

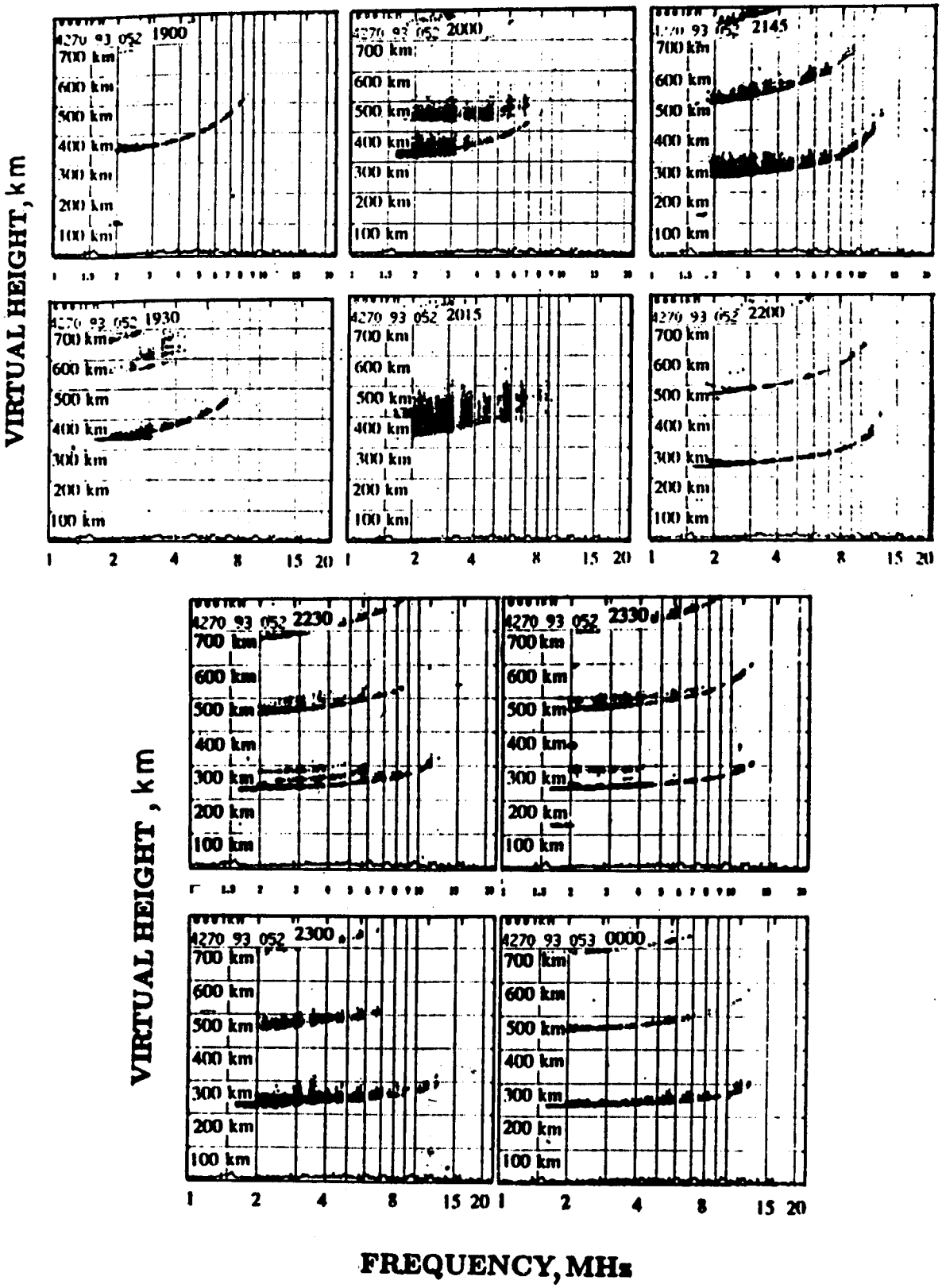

Fig.3.5 Sequence of ionograms taken at SHAR (14°N, 80°E,dip 14°N) at 1900, 1930, 2000, 2015, 2145, 2200, 2230, 2330, 2300, 0000 hrs LT on February 21, 1993.

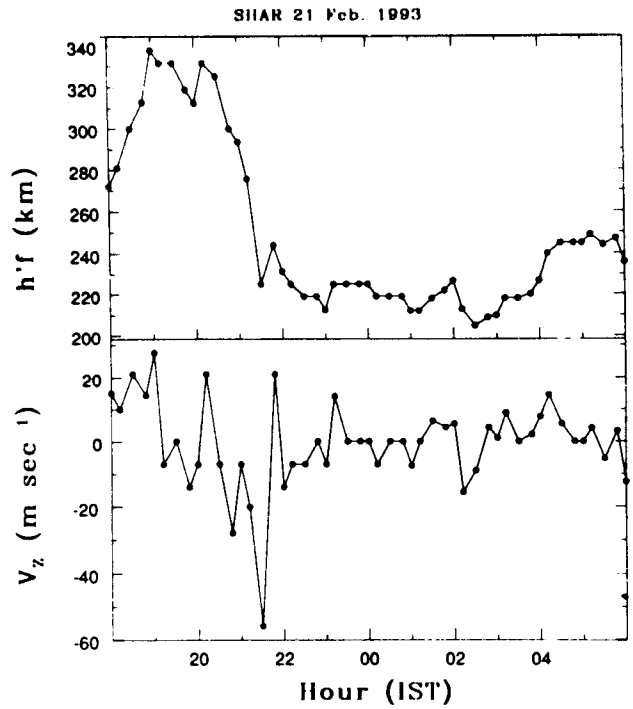

Fig.3.6 Nocturnal variations of h'F (top panel) and the vertical velocity of the F-layer, V_z (bottom panel) deduced from the rate of change in h'F over SHAR on February 21, 1993. Positive (negative) values of V_z indicate upward (downward) motion.

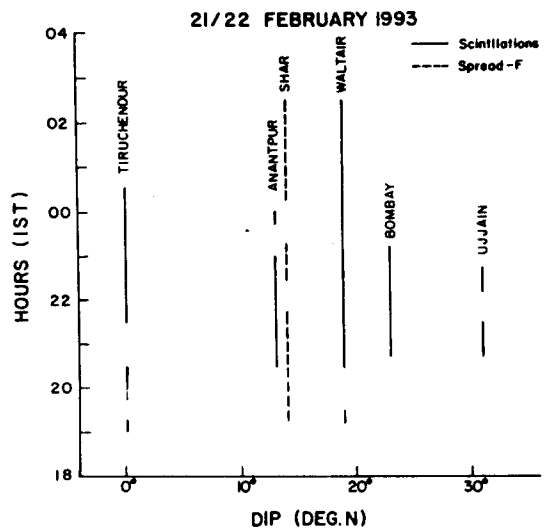

Fig.3.7 Durations for which scintillations were observed at Tiruchendur, Anatpur, Waltair, Bombay and Ujjain on the night of February 21, 1993. Dashed line shows the duration of spread F at SHAR. Dip angle of sub-ionospheric point at 400 km above these stations are plotted on the x-axis.

The VHF scintillations occurring during this night were recorded at SHAR, Ahmedabad and Waltair using the 244 MHz beacon on board the satellite FLEETSTAT (73°E). Scintillations were also recorded at a number of stations in India as part of the All India Co-ordinated Programme on Ionosphere-Thermosphere. Occurrence of scintillations at a few selected stations is shown in Fig. 3.7. Here the duration of scintillations recorded over these stations are plotted at the dip angle of the sub-ionospheric point corresponding to 400 km altitude. Scintillations were observed over Tiruchendur (8.3°N, 78.1°E, dip 0.6°S), situated near the magnetic equator, in three distinct patches between 1900 and 0030 hrs LT. Two patches of scintillations were also observed at Anantpur (14.7°N, 77.6°E, dip 15.5°N) between 2030 and 0000 hrs and over Waltair (17.7°N, 83.3°E, dip 21.4°), between 1915 and 0230 hrs LT. Scintillations were also seen at Bombay (19°N, 73°E, dip 25.7°), situated south of the anomaly crest region, in three patches between 2100 and 2315 hrs LT. However, in the anomaly crest region while there were no scintillations or spread F noticed over Ahmedabad (23°N, 72.4°E, dip 33.8°), there were scintillation recorded in two patches between 2015 and 2215 hrs LT over Ujjain (23.2°N, 75.8°E, dip 33.9°) which is situated at the same latitude as Ahmedabad but few degrees east in longitude. Thus, the occurrence of scintillations up to the anomaly crest region shows that the very large scales features, namely the plasma depletions as well as smaller scales extend right up to these regions.

3.6.2 Drifts of Plasma Depletions

The observed plasma depletions displayed eastward motions throughout the night. As discussed earlier, eastward thermospheric winds cause eastward plasma drift through F-region dynamo mechanism. Thus the background plasma, airglow depletions, and ESF irregularities all drift with essentially the same zonal speed. An attempt was made to determine the eastward velocity of these depletions from the series of 630 nm images. For this purpose, the images were scanned in the east-west direction through

zenith to obtain a cross-section of the brightness pattern for each depletion from which the spatial shifts were determined. Velocities were found to lie between 40 and 120 ms^{-1} in the eastward direction as seen in the Fig. 3.8. Also plotted in this figure are the eastward velocities of the irregularities obtained from other location for comparison with our data. The dotted line shows zonal velocities of airglow depletions obtained during MISETA campaign (Mendillo et al., 1997a) from Arequipa, Peru (16.5° S, 72° W) which agrees closely with the values obtained from Fejer (1991) drift model which are shown as thick solid line. The dashed line in the figure displays the eastward velocity obtained using Faraday rotation (TEC) fluctuations registered at C. Paulista on GOES 3 VHF beacon (Abdu et al., 1985). They showed TEC fluctuations to be the manifestations of plasma bubble dynamics in the equatorial ionosphere, since they are strongly correlated with range type spread F and amplitude scintillations. The different scale sizes producing TEC fluctuations are expected to drift with the same east-west velocity, since they are colocated within a plasma depletion (Tsunoda and Towle, 1979; Szuszczewicz et al., 1980; Basu et al., 1978). It can be seen from the figure that the decrease in irregularity velocity with respect to the local time over SHAR is consistent with the trend seen at C. Paulista and Arequipa, Peru. However, the drift velocities obtained from our data are slightly higher than those observed at Arequipa, Peru (16.5° S, 72° W) and are smaller than those observed at C. Paulista (22° S, 45° W). This might be a manifestation of possible existence of a latitudinal variation in the zonal velocities which when projected in the equatorial plane would manifest as shear in the velocity. Abdu et al. (1985) reached the same conclusion by comparing zonal velocities obtained from TEC fluctuations with those derived from Jicamarca radar (Fejer et al., 1981) and VHF scintillations over Natal (Yeh et al., 1981). It is interesting to note that the westward tilts of the plasma bubbles were interpreted in terms of negative shears in the eastward plasma drift at the dip equator which results from its latitudinal

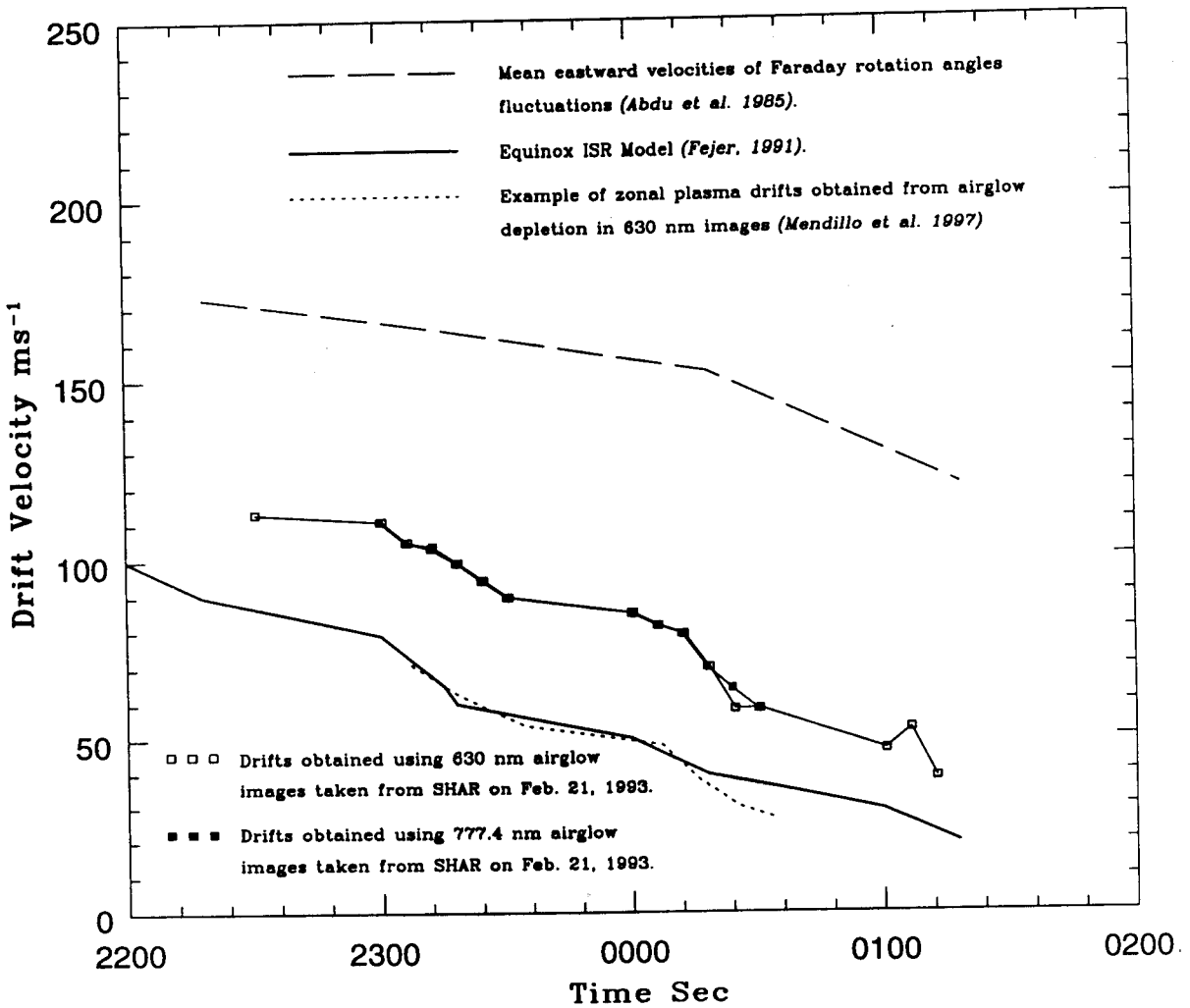

Fig.3.8 Eastward drift speed of plasma depletions

variation (Woodman and LaHoz, 1976; Tsunoda, 1981; Weber et al., 1980; Anderson and Mendillo, 1983).

Eastward velocities of drifting patches of irregularities observed are found to be in range of 100 - 150 ms^{-1} by Koparkar and Rastogi (1985) who monitored the scintillations of SIRIO and FLEETSTAT satellite signals simultaneously over Bombay. Mendillo and Baumgardner (1982) presented local time variation of eastward drift velocities of 630 nm airglow depletion patches over Ascension Island (7.5° S) that decreased from 190 ms^{-1} to 80 ms^{-1} at 0100 hrs LT. Taylor et al. (1997) found the drift motions of the depletions to be approximately 80 - 100 ms^{-1} eastward prior to local midnight and reduced to a minimum of 30 - 50 ms^{-1} in the morning hours. There was no indication of drift reversal in our data which has been observed by Weber et al. (1978) and Taylor et al. (1997). Taylor et al. (1997) suggested this to be related to the reversals in the F region dynamo winds, possibly due to impulsive magnetic activity earlier in the evenings.

3.6.3 Degree of Depletions, Brightness Pattern, and Tilts of the Plasma Depletions

The images obtained on the nights of February 14, 1993 and February 17, 1993 display a transient phenomenon where an increase in airglow intensity or brightness is observed. Fig. 3.9a, b, and c shows the 630 nm images obtained on 14 February 1993 at 2116, 2126, 2136, 2141, 2246 and 2257 hrs LT. Black regions represents low airglow intensity, white regions represent high airglow intensity and purple represents intermediate intensity. At 2116 hrs LT two depletions are clearly seen, one on the western side and the other on the eastern side. At 2126 hrs LT all the three depletions have moved eastwards and the depletion on the eastern side has weakened. The central depletion is enhanced and is flanked on both sides by very extended regions of large airglow intensity. At 2136 and 2141 hrs LT the enhancements around both depletions have increased. Around 2246 hrs LT the enhancement around the western depletion has become less

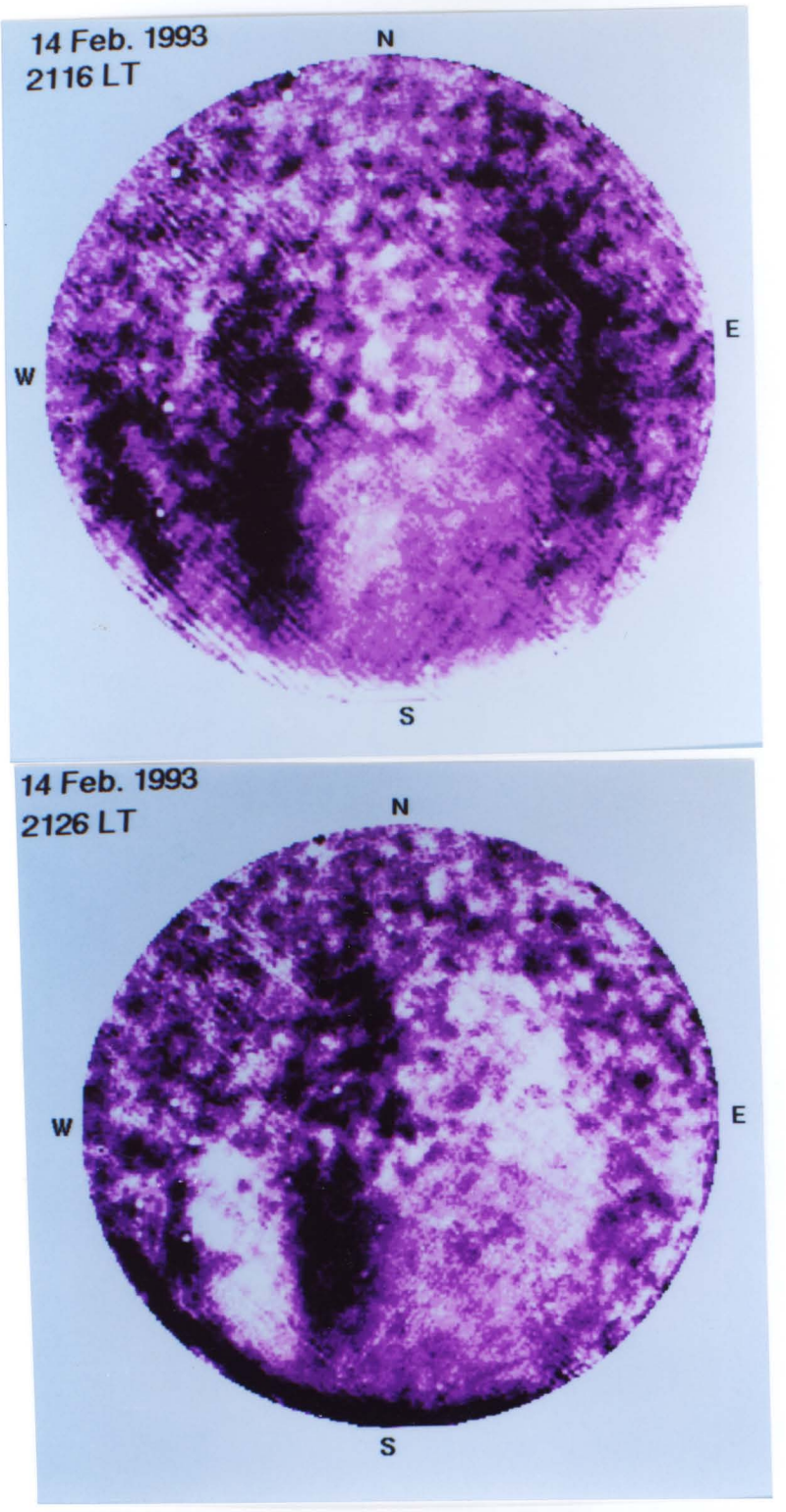

Fig. 3.9a Sequence of 630 nm airglow images taken from SHAR showing brightness pattern on February 14, 1993.

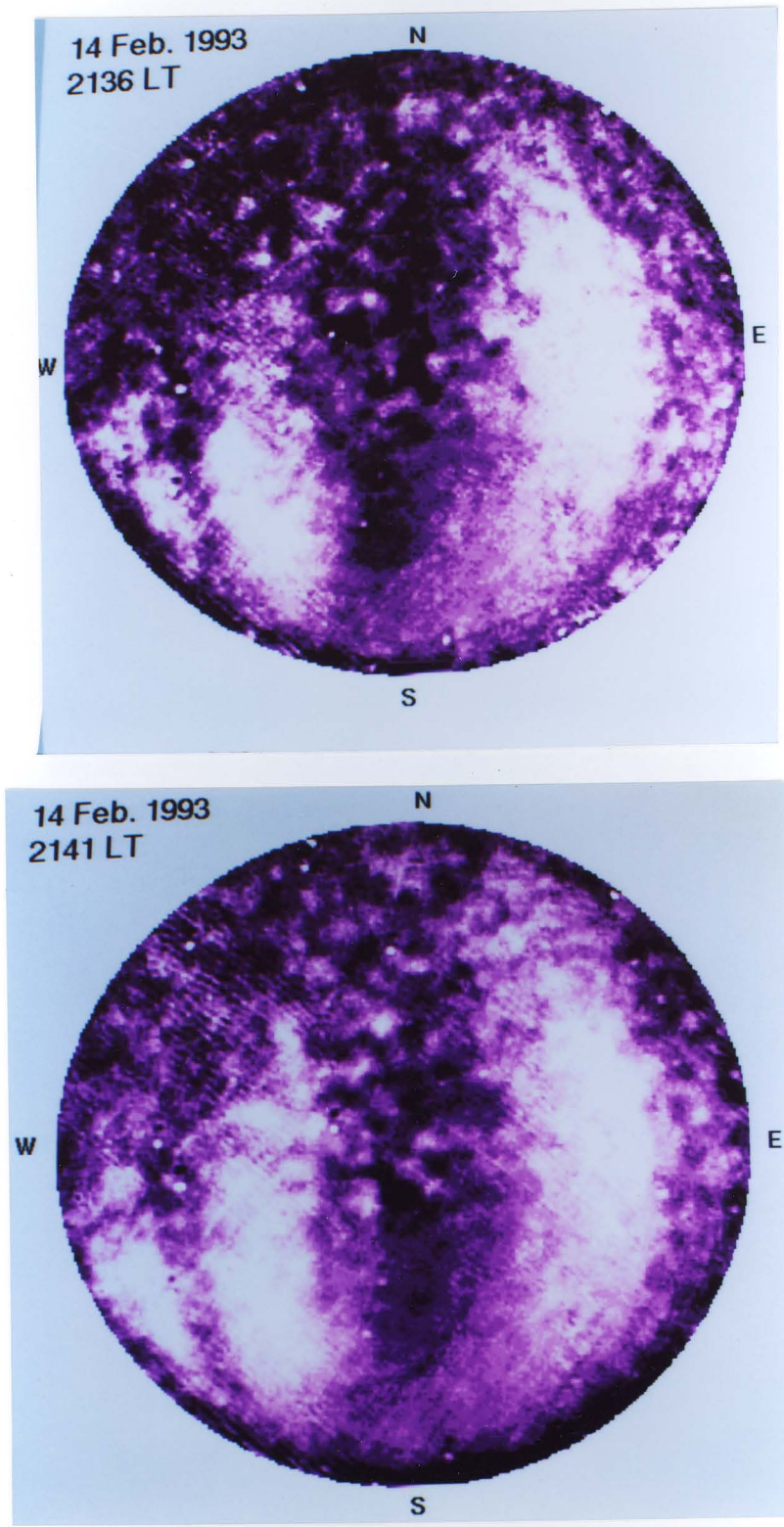

Fig. 3.9b Sequence of 630 nm airglow images taken from SHAR showing brightness pattern on February 14, 1993.

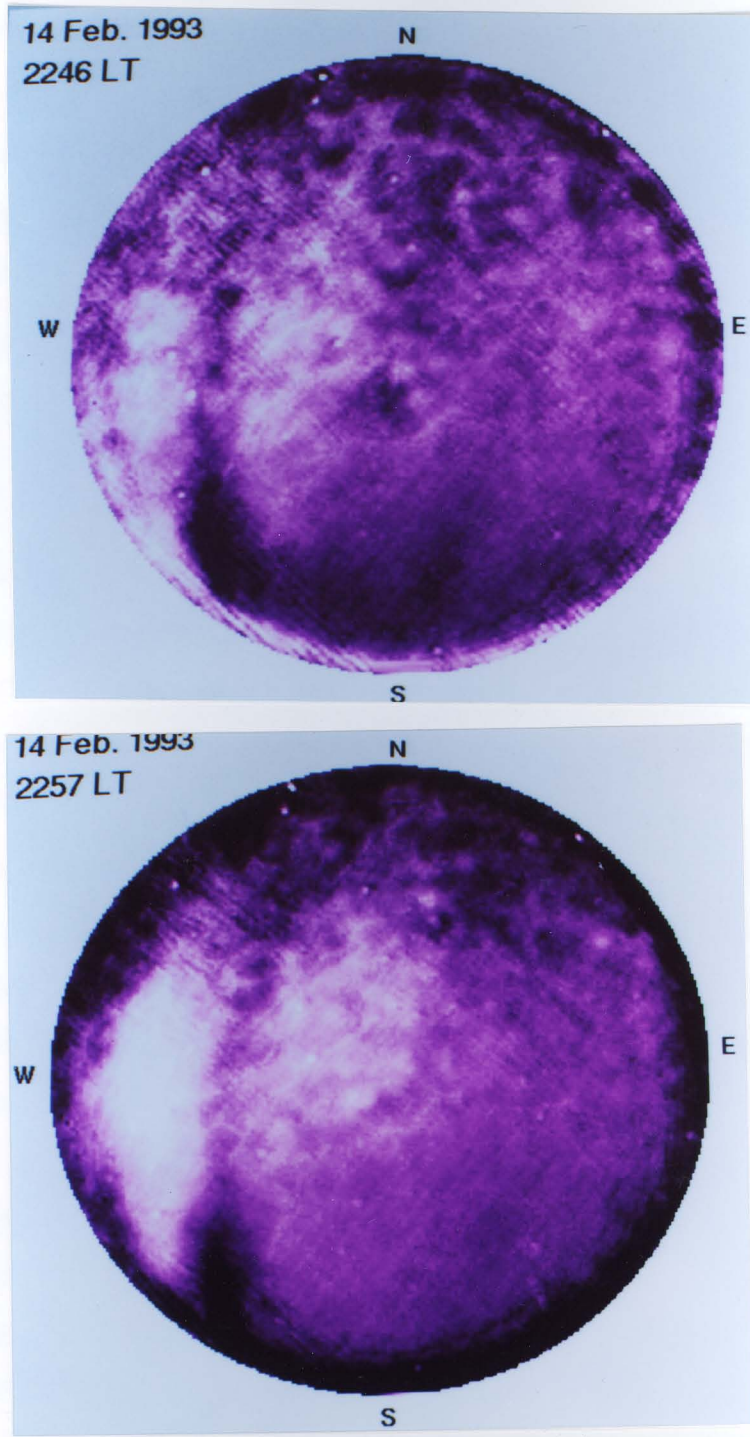

Fig. 3.9c Sequence of 630 nm airglow images taken from SHAR showing brightness pattern on February 14, 1993.

pronounced. At 2257 hrs although the depletion has weakened, the enhancements on both sides have become prominent again. But even in these cases of very extended depletions, there is enhancement on both sides which can be very clearly seen at 2216, 2221, and 2226 hrs LT.

Fig. 3.9d shows the development and movement of plasma depletions on yet another night of 17 February 1993. Unlike the image shown earlier the depletions obtained on the night of 17 February 1993 are very much extended in the east-west direction.

The images shown in Figs. 3.9 were analysed further. As discussed earlier, the images obtained in 1993 were stored in 512 × 512 × 8 bit format. In order to estimate various parameters of depletions like (a) the exact location of depletions and enhancements, (b) degree of depletions (c) detailed structures on both the walls, (d) exact E-W extent of the depletions (e) inter depletion distance, eight pixel about the 256th pixel were averaged for each pixel in the horizontal direction. This gave the variation of airglow intensity (in relative units) in the zonal direction along the centre of the image at the zenith.

These scans of the images at the zenith have revealed various parameters related to the enhancements which can be seen in Fig. 3.10. Enhancements are seen at 2126 hrs LT on the night of February 14, 1993. Around 2136 hrs LT, one enhancement is observed on the north-east side of the image where the increase in the airglow intensity relative to the background is ≈ 80%. This enhancement is characterised by a zonal extent of width nearly 770 km. A second one is seen on south west side and in this case the relative increase in airglow intensity is about 50% with an east-west spread of approximately 630 km. These two enhancements are separated by ≈ 1160 km. The enhancement seen on the left side appears to drift with velocity of 230 m/s while that on the right side drifts with ≈ 115 m/s. By 2141 hrs LT, the intensity of enhancement increases. The relative intensity of the enhancement seen on the south-west side of the image increases to 98%

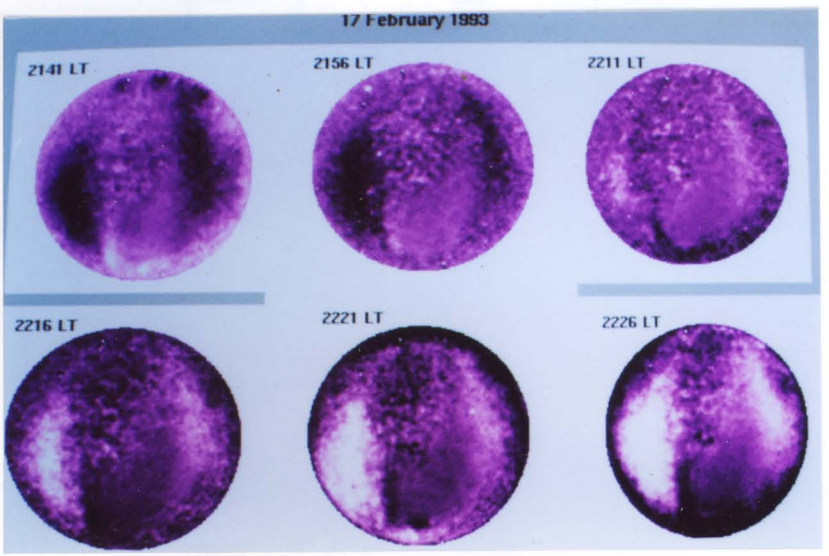

Fig. 3.9d Sequence of 630 nm airglow images taken from SHAR showing brightness pattern on February 17, 1993.

SHAR February 14, 1993

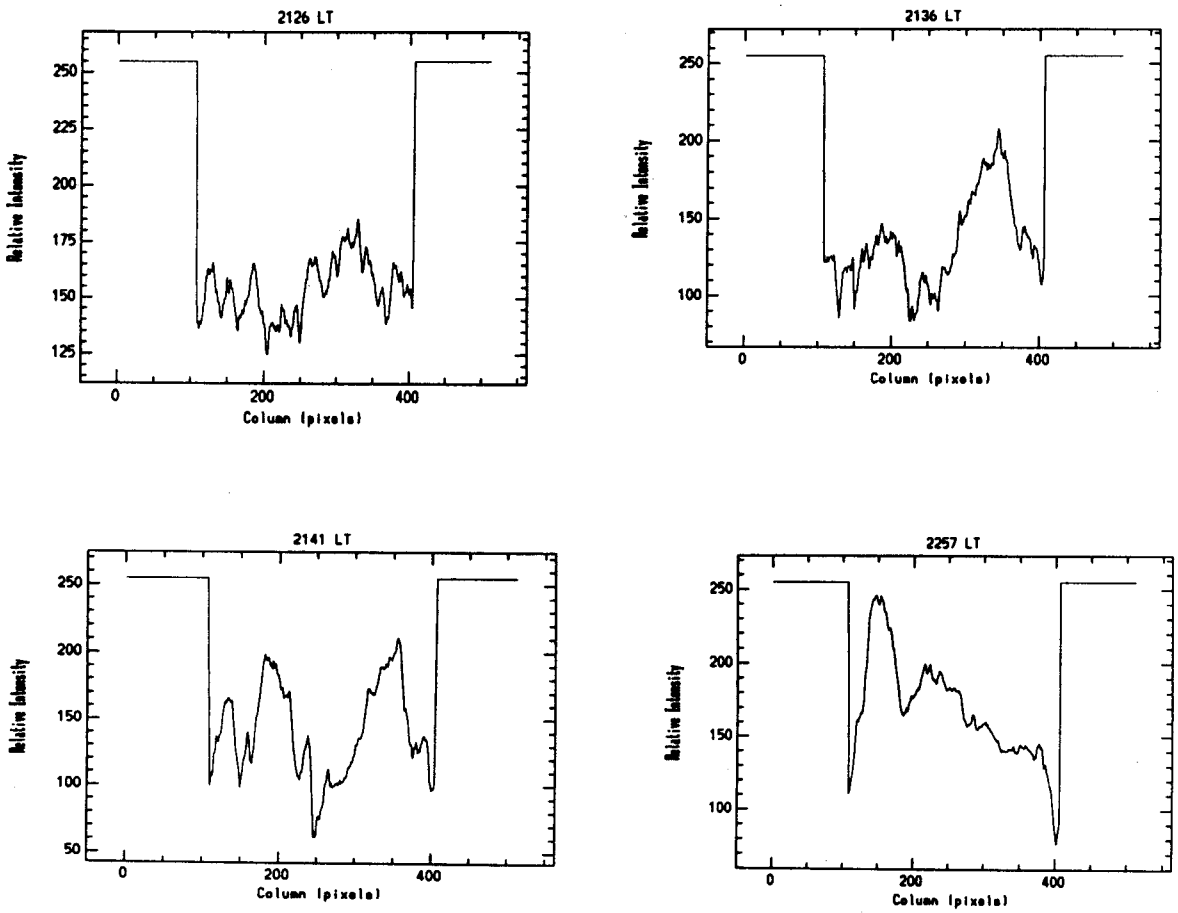

Fig.3.10 East-west scan at zenith of the 630 nm airglow images showing enhancements in airglow intensity.

while the enhancement on the north-east side increases to 83%. The east-west extent of the enhancements occurring on the south-west and north-east side of the image increases to 700 km and 1050 km respectively and are separated by 980 km. The average velocity of these airglow enhancement is 172.5 m/s which remains same by 2152 hrs LT. These enhancements finally disappear from the field of view (FOV) by about 2201 hrs LT. A sudden enhancement in airglow intensity is seen again around 2257 hrs LT.

Fig. 3.11 show a similar increase in airglow intensity as seen on the night of February 17, 1993. The relative increases in the intensity with respect to background at around 2216 hrs LT is 57% and 50% each having a spatial extent of 700 km in the zonal direction. The distance between these two enhancements is ≈1325 km. By 2221 hrs LT, the intensities of enhancements are ≈ 40% and 30% and are characterised by an east-west extent of 730 and 625 km respectively, separated by 1290 km. The enhancement seen around 2216 hrs LT is observed to drift with a velocity of 233 m/s which decreases to 116 m/s by 2226 hrs LT. An increase in degree of enhancement is noticed at around 2226 hrs LT wherein the relative airglow intensity increases to 85% and 70%. The zonal width is ≈ 945 km and 630 km respectively and are separated by about 1260 km.

Multiple depletions seen in the airglow images are found to have varying degree of depletions i.e. they are characterised by a range of depletion depths. One of the interesting observations is that the east-west extent of the bubbles varies with the depletion depth. Shallower bubbles appear to be associated with smaller zonal width as compared to steep bubbles. For example, on the night of February 17, 1993, two depletions were observed at around 2141 hrs LT wherein the relative decrease in the airglow with respect to background is 60% and 44%. These depletions are characterised by a zonal extent of 768 km and 560 km respectively. By 2156

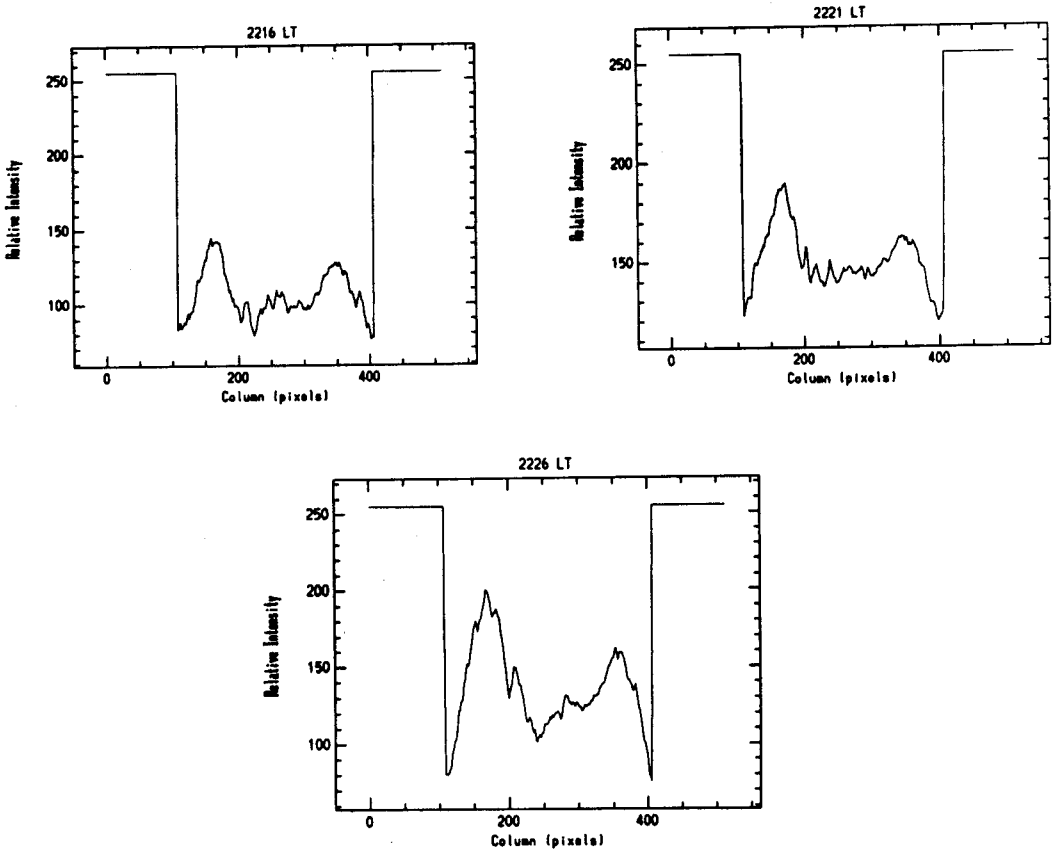

Fig.3.11 East-west scan at zenith of 630 nm images obtained on 17 Feb. 1993 showing examples of increase in airglow intensity.

hrs LT, the depth of depletions changes to 68% and 30% and the corresponding east-west extent to 910 km and 450 km, respectively. Deeper bubbles with degree of depletions as high as 98% were observed on the night of February 14, 1993. Bubbles with depth nearly equal to 33%, 18%, 15% and 77% were observed to be associated with widths of 210 km, 175 km, 105 km, and 875 km in the zonal direction. These features are summarised in the Table. 3.1.

Table 3.1 Degree of depletion and width of the depletions in the zonal direction for the images obtained on 14 and 17 February 1993.

Time	**Degree of depletion (%)**				**Width of Depletion (km)**			
Feb. 17, 1993	(i)	(ii)	(iii)	(iv)	(i)	(ii)	(iii)	(iv)
2146	38	9			700	210		
2151	60	27	44		770	140	560	
2156	68	30			910	670		
Feb. 14, 1993								
2106	33	18	15	77	210	175	105	875
2111	26	31	17	85	175	525	175	980
2136	50	45	80		175	100	420	
2251	18	56			385	1500		

Table 3.1 shows few examples where bubbles having high degree of depletions are observed to be associated with larger depletion widths as compared to shallower bubbles. This is probably the manifestation of the fact that deeper bubbles characterised by large amplitudes represent well developed irregularities while shallower bubbles depict weaker irregularities.

A very interesting feature noticed from the images is the eastward tilt of the plasma depletions which varies between 10-15° with the geomagnetic

equator as shown in Fig. 3.4 These tilts are seen in the images which have been obtained using both 630 and 777.4 nm emission lines. Similar features are noticed in the images obtained during other nights.

Initial results from airborne measurements conducted within a few degrees, of the magnetic equator (Weber et al., 1978; Buchau et al., 1978) revealed that depletions were N-S aligned close to the equator but a skewness was observed for depletions ends extending far from the equator.

In the subsequent study (Weber at al. 1980), from the region above and to the north of Ascension Island (7.9° S, 14.4° W, dip lat. 16° S) observed westward tilts near the poleward ends of the depletions. Later on, ground based studies using all sky imaging system (Mendillo and Baumgardner, 1982; Mendillo and Tyler, 1983) showed that the depletions observed from Ascension Island display westward tilts which seems to be the optical manifestation of the westward tilts of the plumes recorded by incoherent scatter radar (Woodman and LaHoz, 1976; Tsunoda, 1980) and by in-situ probes (McClure et al., 1977).

Woodman and LaHoz (1976) proposed that an eastward neutral wind blowing through a depleted region will polarise the depletion so that it drifts eastward with velocity less than the ambient E × B eastward drift. Thus, relative to the background ionosphere, the bubbles drift westward as they rise which accounts for the westward tilts of the plumes. Simulation studies by Zalesak et al. (1982) showed westward tilts of the bubbles to be due to the assumed decrease of the flux-tube integrated Pederson conductivity above $h_{max}(F_2)$ with increasing altitude. This decrease leads to a shear in eastward plasma drift which is responsible for the westward tilt of the simulated bubble structure. An alternative mechanism was suggested by Anderson and Mendillo (1983). Modelling studies by them indicate that westward tilts are associated with eastward plasma drifts that decrease with altitude above F_2 peak and this shear results from an altitudinal decrease in zonal wind.

It is known that the eastward zonal wind results in the development of vertically downward polarisation electric fields, through F region dynamo, which in turn causes F region plasma drift (Rishbeth, 1971; Heelis et al., 1974). Thus, an increase in zonal wind with altitude will result in an increase in the eastward plasma drift with altitude. Haerendal (1980), deduced westward plasma flow in the lower F region which reverses to eastward at higher levels, from vapour cloud release experiments, whereas radar measurements of plasma irregularities by Kudeki et al. (1981) and Tsunoda et al. (1981) have shown positive shears, velocity increasing with altitude. Eastward tilts seen in our data suggest that tilts might be associated with the variation of plasma drifts with altitude, thus supporting the mechanism proposed by Anderson and Mendillo (1983). This is further strengthened by the evidence of the existence of positive shears in the zonal winds with altitude which have been obtained using barium vapour release method during the onset time of ESF (Raghavarao et al., 1987; Sridharan et al., 1997). Ionisation hole campaign (Sridharan et al., 1997) conducted from SHAR on February 19, 1993, revealed that zonal winds exhibit a positive shear of 2.2 ms^{-1} km^{-1} as displayed in Fig. 3.12a. Optical imaging results obtained during the same night but at the later time from SHAR display eastward tilts, shown in Fig. 3.12b, suggesting the existence of altitudinal increase in plasma drifts. In Fig. 3.12b, depletions are seen as light yellow regions surrounded by enhanced regions shown as dark blue bands.

3.6.4 Walls of Plasma Depletions:

A very interesting feature which has emerged from the east-west scan across the plasma depletions observed in our data is the presence of small scale perturbations on both the eastern and the western walls of the depletions as seen in Fig. 3.10. Weber et al. (1978), reported only western walls to be unstable. They used an airborne all-sky spectrophotometer and an ionosonde to show that 630 nm airglow depletions in the night-time equatorial ionosphere result from local elevations in the bottomside of the F

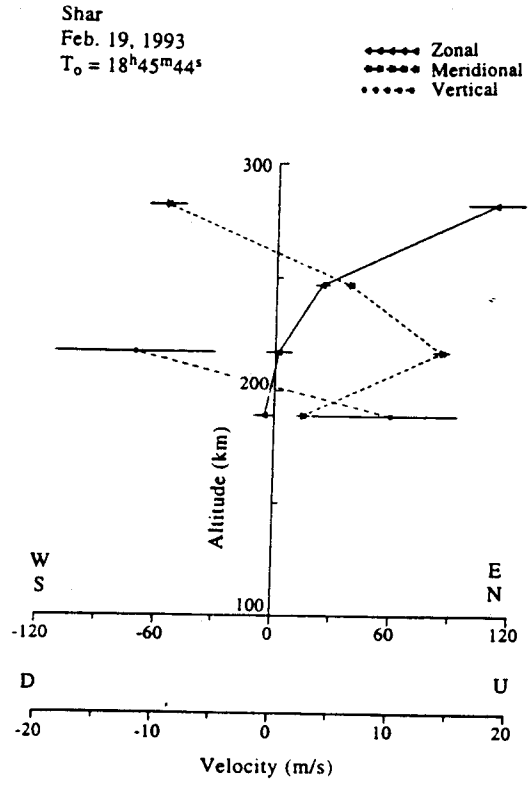

Fig. 3.12a Altitude profiles of zonal (eastward positive), meridional (northward positive) and vertical (upward positive) at the onset time of ESF on February 19, 1993.

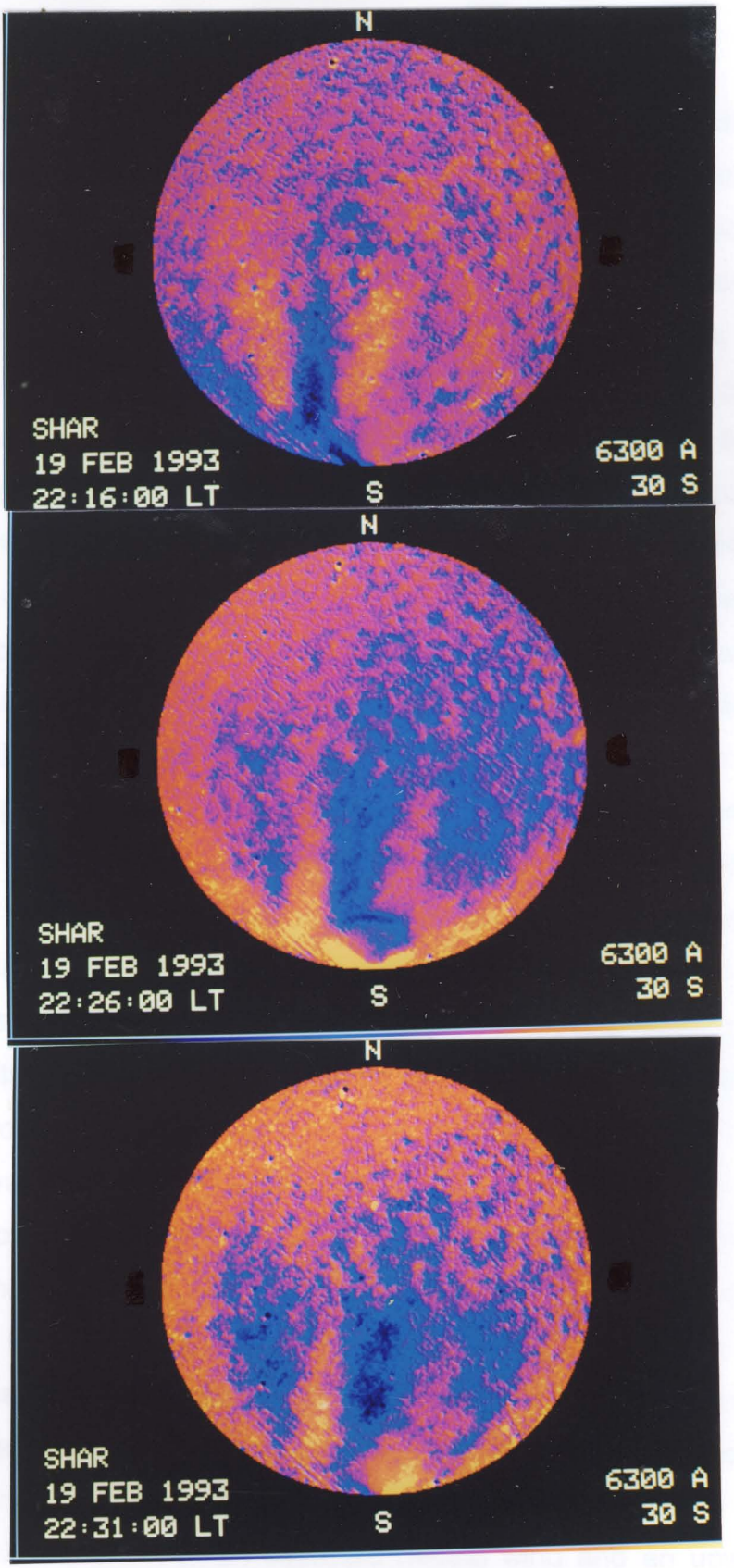

Fig. 3.12b 630 nm airglow images taken during 'Ionisation Hole' campaign conducted from SHAR on Feb. 19, 1993. Dark blue regions indicate enhanced airglow intensity and light yellow regions represent less intensity and hence plasma depletions.

layer. Tsunoda (1981), showed that the plumes are colocated with bubbles and develop where bottomside backscatter is locally elevated in altitude by about 30 to 60 km with stronger backscatter occurring on the west side of local elevation. He suggested that an eastward neutral wind can produce this E-W asymmetry of the bottomside backscatter strength. This was explained by considering the linear growth rates for determining the gross spatial distribution of irregularity strength as shown in Fig. 3.13. The linear growth rate is proportional to the component of the electron density gradient that is in the direction of the velocity vector. The figure shows the electron density contour of an altitude modulated F layer. The linear growth rates for three different cases is also shown along with the corresponding backscatter strength which is assumed to be strongest where the largest growth rate is anticipated leading to the largest amplitude field aligned irregularities. For the case of an upward moving F layer, the velocity vector is directed upward and growth rate is maximum in the region where electron density gradient is directed upward i.e. in the centre and outside the region C and C' as seen in the figure. Similarly for a F layer at high altitude, growth rate due to R-T instability shows similar variation as for an upward moving layer since equivalent gravitational velocity is upward. It has been mentioned earlier that an eastward neutral wind generates vertically downward electric field producing eastward plasma drift. Rishbeth (1971) showed theoretically that the degree of coupling between F region plasma and the neutral wind depends upon the ability of the E region to short circuit the polarisation field. Thus, because of finite conductivity of E region during night time, the eastward plasma drift lags behind the neutral wind velocity (Woodman, 1972). Therefore, in the neutral wind frame of reference the plasma drifts westwards which is equivalent to an upward directed electric field in that frame. The combined effect of an eastward neutral wind and an upward moving (or high) F layer results in a plasma drift velocity vector which is directed upward and westward in the frame of reference of neutral wind. As this velocity vector is closely aligned with electron density gradients in the

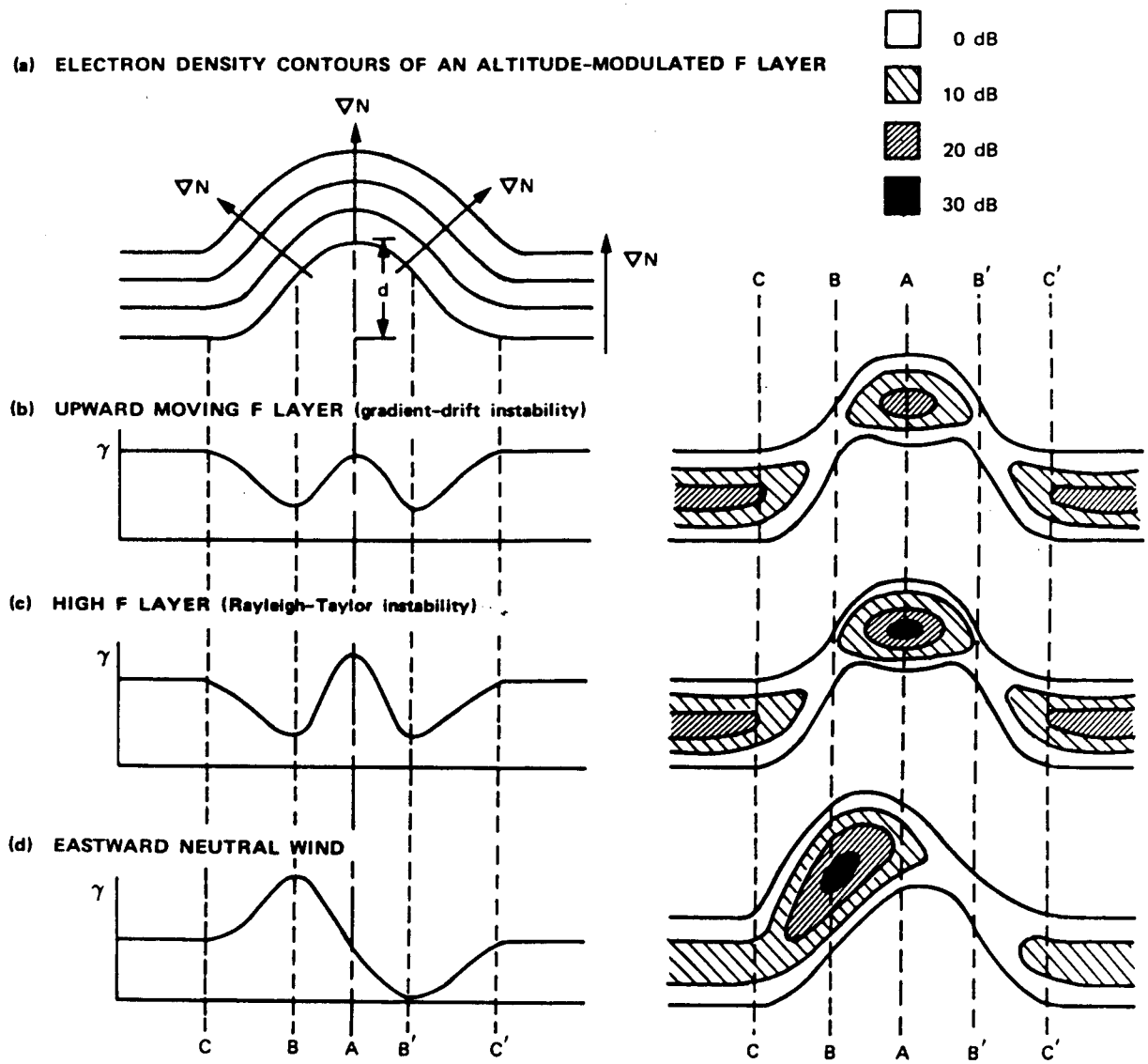

Fig.3.13 Spatial distribution of growth rate and backscatter strength produced by (a) electron density contours of an altitude modulated F layer, (b) an upward moving F layer, (c) a high F layer, and (d) an eastward neutral wind (After *Tsunoda, 1981*).

west wall, it results in the maximum growth rate on the west wall of the elevated region and hence strong backscatter strength.

Numerical simulation work by Zalesak et al. (1982) indicated the existence of two primary regions of electron density steepening which can generate secondary instabilities. These regions as identified in their modelling studies were the west wall of the bubble at low altitudes (below 370 km) and the east wall of the bubble at higher altitudes i.e. above 370 km, where the largest growth rate for gradient drift and gravitational R-T instability occurs as verified by local stability analysis.

We conjecture that the structures on the eastern wall can be accounted by considering steep plasma density gradients in the horizontal direction which result from the action of the primary R-T instability (Haerendal, 1974). The eastern side of the depletion is characterised by the presence of steep electron density gradients in the eastward direction. As discussed earlier, during night time the zonal neutral wind produces vertically downward polarisation electric field which results in the $\mathbf{E} \times \mathbf{B}$ plasma drift in the eastward direction. Thus, $\mathbf{E} \times \mathbf{B}$ drift is parallel to the direction of horizontal gradients, both pointing in the eastward direction. Hence, the conditions are conducive for gradient drift instability to operate on the steep horizontal gradients, thus making the eastern wall unstable.

3.7 Discussion

The distance between adjacent depletions, the inter depletion distance (IDD), is representative of the scale size of the altitude modulated F layer which, in turn, can throw light on the source responsible for the modulation of the bottomside F layer. IDD is found to vary between 100 km to about 950 km. Plumes observed in the RTI maps of radar (Tsunoda and White, 1981; Tsunoda et al., 1982; Tsunoda, 1983; Kelley et al., 1986; Hysell et al., 1990) correspond to bubbles that are usually generated from near the crest of large scale upwellings. The primary plume spacing is about 400 - 600 km, and the secondary plume spacing is 50 - 100 km. However, it

is to be noted that the plume spacing is derived by assuming the mean horizontal plasma drift speed. IDD inferred from airglow images in the present study are more realistic as the images are the snapshots giving the instantaneous picture. The separation between the adjacent depletions suggest that gravity waves might be the seeding agency for generating such large scale structures (Hysell et al., 1990). F-region gravity wave airglow signatures were imaged at Arecibo (18° N, 65° W, dec. ≈ 11° W) for the first time (Nottingham et al., 1994; Miller et al., 1994; Mendillo et al., 1997b). Singh et al. (1997a) presented examples of plasma bubble development from wavy ion density structures in the bottomside F layer using Atmosphere Explorer E data. The wavy structures mostly had east-west wavelengths of 150-800 km with a exception of 3000 km in one case. They found that in a fully developed equatorial spread F case, east-west wavelengths varying between 0.5 km to 690 km occurred simultaneously. They presented observations showing that the spacing between bubble patches appeared to be determined by the wavelengths present in the precursor wave structure.

It has been mentioned earlier that 630 nm emission originates from the bottomside of the F layer and airglow depletions in 630 nm line are associated with bottomside structures in the F layer (Weber et al., 1978). Thus the 3-D surface maps of the airglow images provide a unique way for studying the altitude modulation of the bottomside F layer. 3-D surface maps of the images taken on 5 March 1997 and 6 March 1997 display prominent differences. Fig. 3.14a, b show images obtained on these nights where the dark bands represent regions of reduced airglow intensity and hence depletions in electron density. Fig. 3.15 to Fig. 3.17 show the 3-D surface maps of the airglow images where the depletions are seen to have steep edges. The bottom panel of the Fig. 3.15 and Fig. 3.16 show the contour plots where a part of the image around the depletion was analysed in details. The top and right sides of these plots point towards northern and eastward directions, respectively. From the total image size of 512 × 550, a

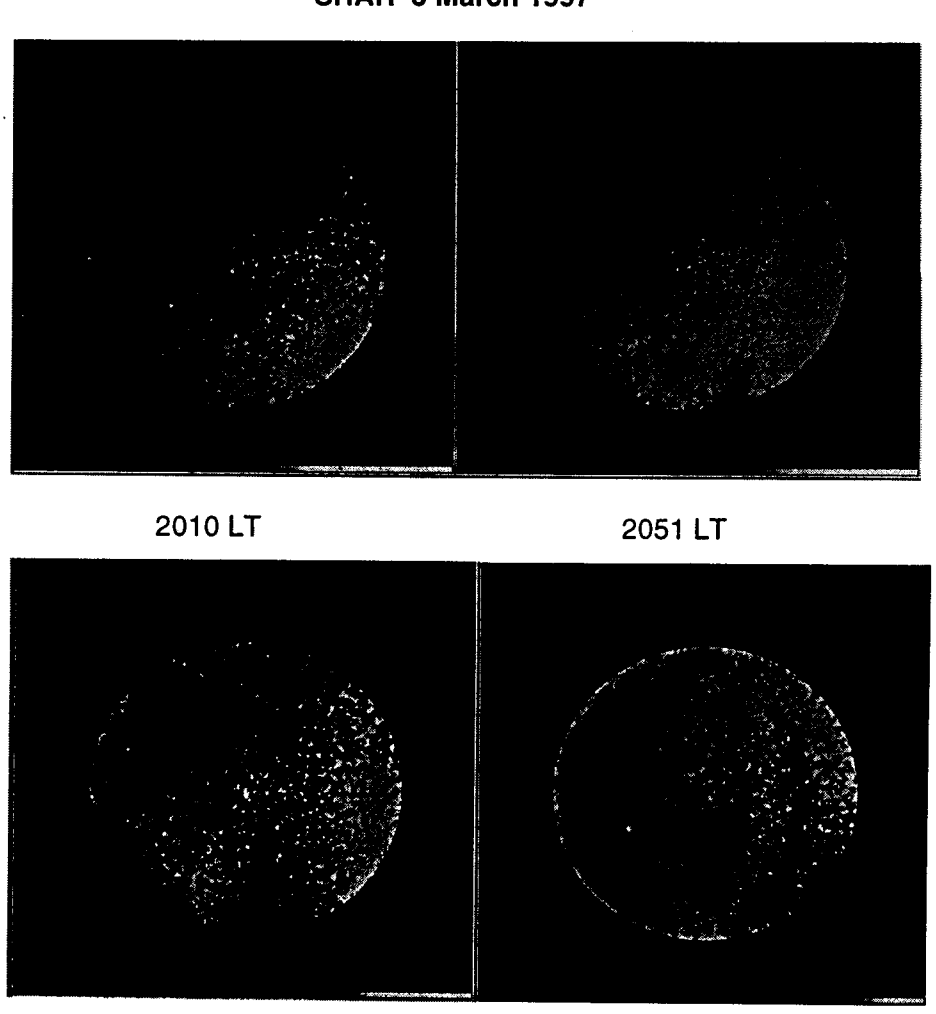

Fig. 3.14a Images obtained on 5 March 1997. Dark bands represent depletions in electron density.

SHAR 6 March 1997

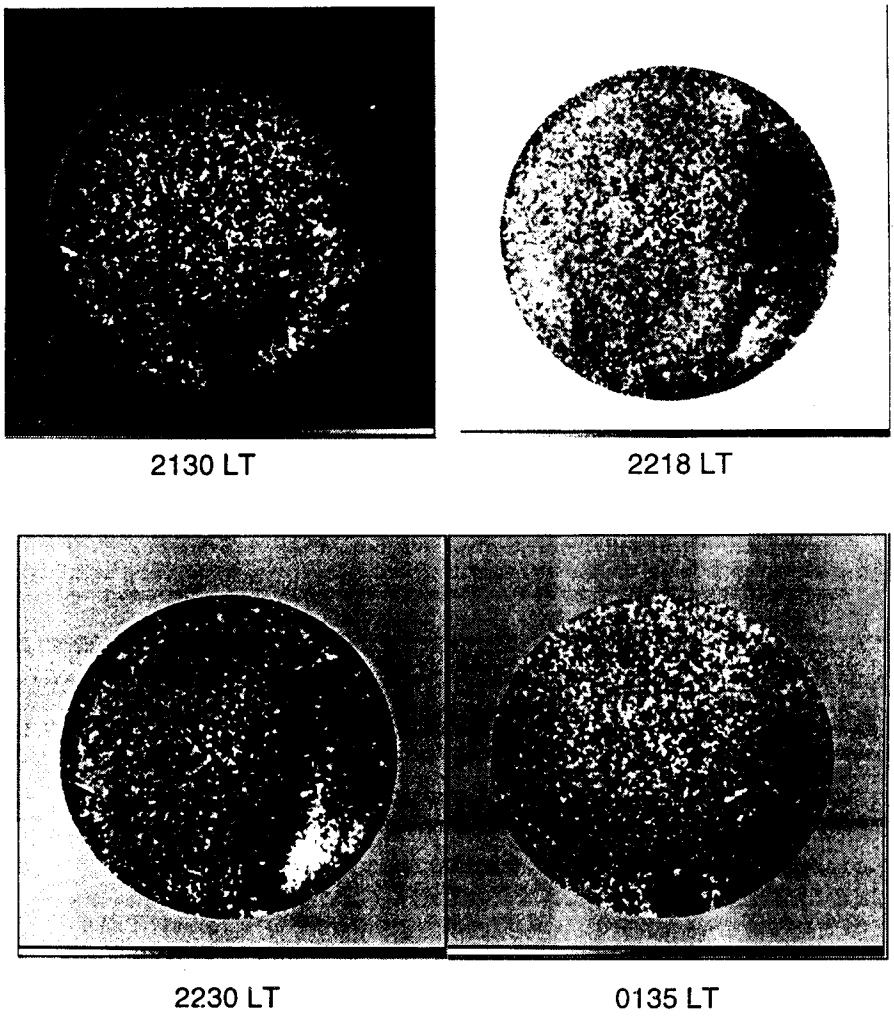

Fig.3.14b Images obtained on 6 March 1997 from SHAR. Dark bands are plasma depletions showing brigtness pattern around 2230 LT.

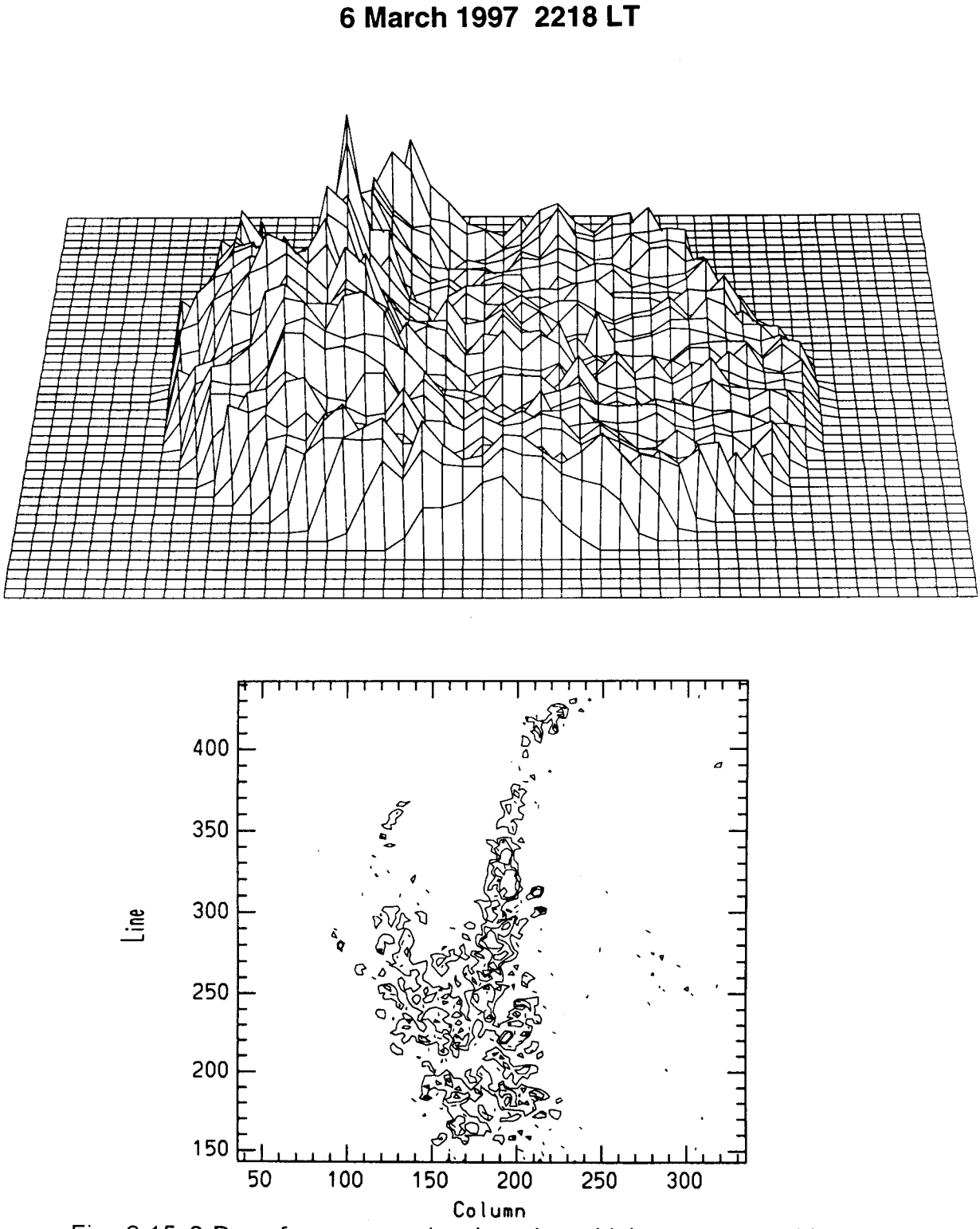

Fig. 3.15 3-D surface maps showing sinusoidal structures and contours plots showing tilts of depletions seen on 6 March 1997.

6 March 1997 2230 LT

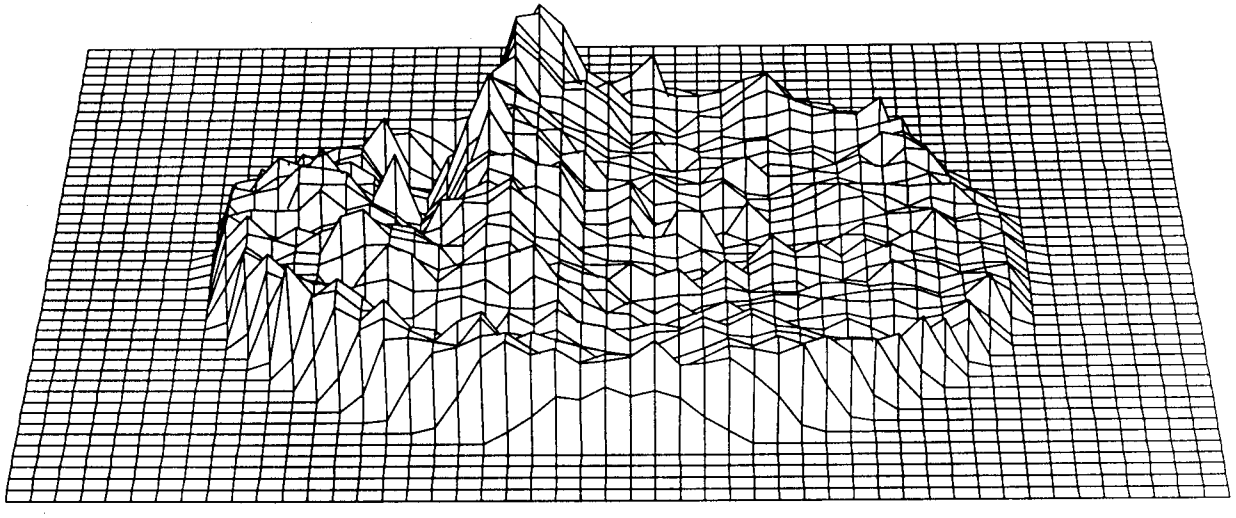

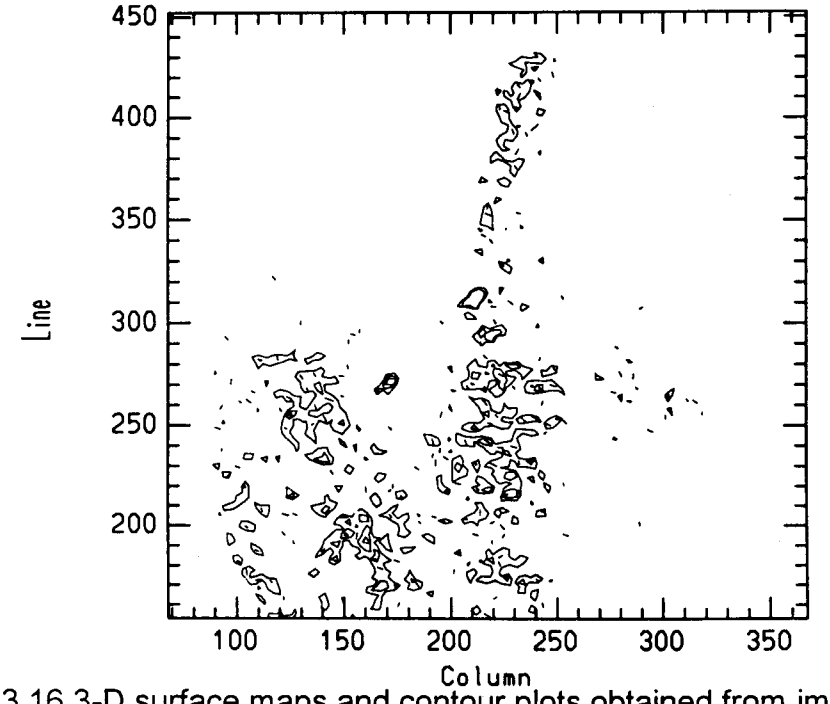

Fig.3.16 3-D surface maps and contour plots obtained from images taken on 6 March, 1997.

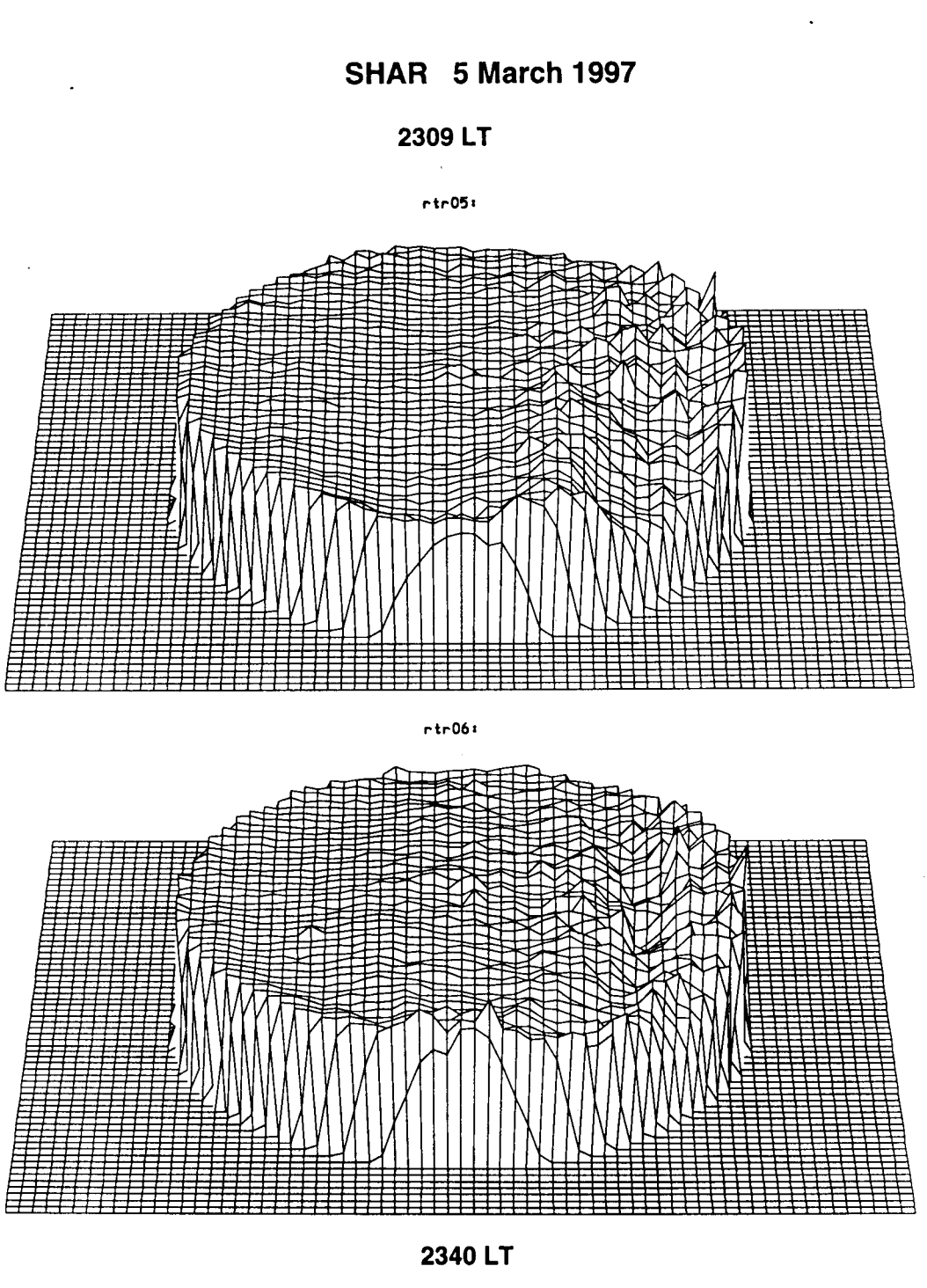

Fig. 3.17 3-D surface maps of 630 nm airglow images taken on 5 March 1997.

subset of 350 × 450 was selected. The contours of the images (minimum values) shows the orientation of the depletions very clearly. The tilts of the depletions seen in the images obtained in 1993 have been discussed earlier. One of the noticeable features seen in Fig. 3.15 and Fig. 3.16 is the presence of sinusoidal structures in the 630 nm airglow images which were obtained on 6 March 1997. However, no such perturbations are seen in Fig. 3.17 which are the 3-D surface maps of the images obtained on 5 March 1997. The scale size of the sinusoidal structures seen on 6 March 1997 varies between 900 and 1500 km. The most promising candidate responsible for seeding of such large scale structures appears to be atmospheric gravity waves. F region gravity waves have been detected for decades using various radio diagnostics to sense their presence as travelling ionospheric disturbances (TIDs). Similarly, periodic variations in photometer and FPI signatures have long been attributed to variations in airglow chemistry associated with gravity wave motions (Roach, 1961; Hines 1964). Röttger (1973, 1976, 1978) used a transequatorial radio propagation technique to characterise the wavelike properties of ESF structures and found that the east-west spacing of ESF patches was ≈ 380 km. He argued that the spatially resonant gravity wave mechanism of Whitehead (1971) and Beer (1973) is responsible for the organisation of F region ionisation into large scale wave like ionisation. Klostermeyer (1978) made a non-linear calculation of the effect of spatial resonance and concluded that gravity waves could indeed organise the F layer plasma into large scale horizontally modulated contours. Moreover, the R-T growth rate is quite small ($\sim 10^{-4}$ s^{-1}), and growth rate from electron density variations due to thermal fluctuations may not be quick enough to account for the rapid development of large scale irregularities after sunset.

The presence of large scale sinusoidal structures as seen in the 3-D surface plots on the night of 6 March 1997 suggests that these structures are probably associated with gravity waves. It is observed that on this night strong depletions occur as compared to the preceding night which also shows the absence of such large scale perturbations in the 3-D surface plots. This suggests that the variability in the nature of the plasma

depletions on these nights could possibly be the result of the variability of gravity waves.

It was seen that transient features such as the airglow enhancements were observed on few nights. This feature appears both in the south-west and north-east of zenith and is seen to drift eastward, exiting from north east side of zenith. Recently 'brightness wave' was reported during MISETA campaign (Mendillo et al., 1997a) which appeared as transient airglow structures seen in the airglow images recorded at Arequipa, Peru (16.4° S). These were interpreted in terms of an anomaly associated with the thermal behaviour of the upper atmosphere. Mendillo et al. (1997a, 1997b) concluded that the brightness waves results from airglow produced by poleward winds generated by midnight pressure bulge (MTM).

CHAPTER 4

RESULTS OF *IN-SITU* ELECTRON DENSITY MEASUREMENTS FROM SHAR

This chapter deals with the results of the electron density measurements in the F region over SHAR (13° 42′ N, 80° 14′ E, dip 14° N), a low latitude station in India. The electron density measurements were made by using a Langmuir Probe (LP) onboard two RH-560 rockets of the Indian Space Research Organisation, ISRO.

RH-560 is a two stage solid propellant, spin stabilised rocket with a nominal apogee of approximately 350 km with a payload carrying capacity of about 90 kg. Two RH-560 rockets were launched for studying electron density irregularities (a) during fully developed phase of equatorial spread F (ESF) and (b) at the onset time of ESF. Before discussing the results from these two flights, a brief summary of major earlier rocket results is given below, to present these results in proper perspective.

4.1 Summary of the Earlier *In-situ* Work on Electron Density Irregularities

A NASA Javelian rocket was launched on Nov. 18, 1973, from Natal, Brazil, during equatorial spread F conditions (Kelley et al., 1976). This rocket experiment along with a 50 MHz radar results, provided the first evidence that the regions of depleted plasma density rise due to buoyancy forces and attain altitudes far above the region unstable to the R-T

mechanism. This partly explained the high altitude spread F, observed by Farley et al. (1970), in terms of primary instability operating below the peak in F region electron density. Costa and Kelley (1978) analysed the bottomside electron density data obtained from the same flight and found that the steepened coherent structures exhibited a shallow spectra, with $k^{-2.0}$ power law behaviour in intermediate (10 km > λ > 100 m) and transitional (100 m > λ > 10 m) scales instead of a turbulent cascade of structures. Similar k^{-2} power law scaling was observed by Dyson et al. (1974) using AE satellite data, by Morse at al (1977) in the Equion experiment and also by Kelley and Mozer (1972) using the electric field data. Costa and Kelley (1978) found that sharp density gradients (scale length, L, < 100 m) could destabilise collisional drift waves, given a model ion collision frequency profile.

Rino et al. (1981) discussed the fixed-bias Langmuir probe derived density power spectra obtained from Plumex-I rocket launched from Kwajalein Atoll (9.4° N, 167.45° E). A fully developed spread F in decay phase was encountered during this experiment. They found that for electron density irregularities with scalesizes ranging between 5 km and 500 m, the spectral index (n) ranged between -1.2 and -2.5. However, for irregularities with scalesizes between 50 m and 500 m , steep spectra was observed with n lying between -2.3 and -3.4 for altitudes less than 370 km. For altitudes greater than 370 km, shallow spectra with n ranging between -1.2 and - 2.6 were seen. The break in spectrum observed near 500 m is a typical dimension for the finger like striations that have been observed to develop in barium clouds (Keskinen et al., 1980). The break is evident in data obtained from the vicinity of F peak and is represented by n flatter than -2 for smaller wavenumbers and much steeper than -2 for greater wavenumbers. Keskinen et al. (1981) discussed one dimensional bottomside irregularity spectra exhibiting a spectral slope of -2.5 over scalesize range of 1 km to tens of meters and developed a computational model of R-T instability that supported the experimental results.

Kelley et al. (1982) studied Plumex data of electron density as well as electric field fluctuations in different wavelength regimes. They found that

density spectra exhibited k^{-2} behaviour at long wavelengths and became steeper for $\lambda < 100$ m with n around -4.5 or -5. This spectral form was observed for altitudes exceeding 280 km. However, below 280 km, k^{-2} spectral behaviour was observed for scalesizes up to about 20 m. Power spectra of electric field irregularities displayed Boltzmann relationship for $\lambda < 100$ m. This was explained in terms of drift waves operating at altitudes above some collisional cut off which was around 280 km. It was suggested that the classical diffusion might also be responsible for a Boltzmann like relationship between the density and electric field.

Barium-Strontium vapour release experiments conducted from SHAR, India, (Raghavarao et al., 1984; Raghavarao et al., 1987), showed the presence of spatial gradients in electric field around an altitude of 194 km at the time of onset of ESF caused by neutral winds and shears in them. Significant vertical winds were also detected at the time of onset time of ESF.

Two sounding rockets instrumented with RF probes and electric field double probes, launched as a part of Condor experiment from Punta Lobos (12.3° S, 76° W, 0.85° N dip), Peru, investigated spread F depletions. LaBelle et al. (1986), discussed the density and electric field spectra obtained during the Condor campaign. The condor density fluctuation spectra display a break at a wavelength near 100 m, identical to that found in the PLUMEX experiment (Kelley et al., 1982). Their results are consistent with the previous conjecture that drift waves only exist above 300 km altitude. However, during the Condor experiment, spread F turbulence was not observed below 280 km owing to high altitude of F layer. By dividing the spectra into regions where linear GRT growth is positive (the injection band) and negative (the dissipation band) and then performing an energy balance, they argued that classical ambipolar diffusion accounted for the necessary dissipation for spectra measured at low altitudes. For high altitude spectra, an anomalous diffusion which is two orders of magnitude stronger than ambipolar diffusion, D_a, is needed implying the existence of electrostatic waves. Statistical arguments indicated that anomalous diffusivity was implied by the measured spectral forms and that this diffusivity was not related to coherent steepening. Thus, diffusion due to wave particle interactions and small scale drift wave transport seemed likely.

Prakash et al. (1991) studied ESF irregularities using RH-560 rockets instrumented with Langmuir Probes launched from SHAR, India. They found that the relationship between n and mean integrated spectral power, P_T, (in 20 m to 200 m scalesize range) can be represented by a Gaussian function and that the altitude variation of n normalised with respect to P_T displayed that the nature of spectral index remains same between 230 km and the apogee of the rocket, which was 332 km. This is at variance with the observation that 280 km is the threshold altitude for the steep drift wave type of spectra to a shallower spectra. These results are summarised in the form of Table 4.1 and Table 4.2.

Table 4.1 Summary of previous rocket results from American and Pacific sectors.

Year	Place	Remarks
1973	Natal, Brazil (Kelley et al., 1976)	Rise of density depletions to higher altitudes.
1973	Natal, Brazil (Costa and Kelley, 1978)	Presence of coherent steepened structures in the bottom side, responsible for k^{-2} power law behaviour for 10 m $< \lambda <$ 10 km.
1979	Kwajalien Atoll (PLUMEX-I) (i) Rino et al., 1981	a) 10 km $<\lambda<$100m, $P \propto k^{-2}$. b) Spectral break near $\lambda \sim$ 500m, For 50$< \lambda \sim$ 500m occurring for altitudes < 370 km.
	(ii) Kelley, 1982b	a) For Alt > 280 km For $\lambda <$ 100 m, n = -4.5 For $\lambda >$ 100 m, n = -2.0 b) Alt < 280 km, $\lambda >$ 20 m, n = -2.0
1983	Punta Lobos, Peru Condor Experiment. LaBelle et al., (1986)	a) No turbulence below 280 km, Higher altitude of F layer. b) For n_e spectra, For $\lambda >$ 100 m, n = -2.0 For $\lambda <$ 100 m, n = -4.5 c) E_H spectrum : For $\lambda >$ 100 m, $\delta E \propto \delta n_e/n$ For $\lambda <$ 100 m, $(\delta E)^2 \propto (\delta n/n)^2 k^{-2}$.
1990	Kwajalein Atoll Hysell et al., (1994)	a) Presence of steepened structures. b) n_e spectra: For $\lambda >$80-100 m, n = -2.0, For $\lambda <$80 - 100 m, n = -4.5 c) E_v & $E_H \propto \delta n/n$ at $\lambda >$ 300 m but at shorter scales, $(\delta E)^2 \propto (\delta n/n)^2 k^{-2}$.

Table 4.2 Summary of previous rocket results from the Indian sector.

Year	Place	Remarks
1981	SHAR (Raghavarao et al., 1984)	a) Spatial gradients in EF at the onset of ESF around an altitude of 194 km, caused by neutral winds and shears in them. b) Evidence of divergence in the plasma motion, which possibly generates a plasma hole during the onset of ESF.
1982	SHAR (Raghavarao et al., 1987)	a) Confirmation of large scale gradients in EF at the onset of ESF around 200 km. b) Presence of significant vertical winds at the onset time.
1982	SHAR (Prakash et al., 1991)	a) Fluctuations with $\lambda \approx$ few tens of kms present below 150 km. Smooth profile observed between 150 km and base of the F region. b) For $20 < \lambda < 200$ m, spectral index lies between -1.5 and -4.6.

4.2 Results of the Rocket Flight at the Time of Onset of ESF (Present Work)

As a part of 'Ionisation hole' campaign, two RH-560 rockets were launched from SHAR to investigate the ionospheric conditions at the onset time of ESF. During the campaign complementary ground based experiments were operated from different locations spread over the country. The prediction of ESF was required well before its onset, so that the rocket flight could be conducted during the onset time. A OI 630 mm dayglow photometer operated from Waltair (17.7° N; 83.3° E;10.5° N dip lat.), which could predict the occurrence of ESF a few hours prior to its observation in ionograms (Sridharan et al., 1994), was used for this purpose. It has been shown (Sridharan et al., 1992; Pallam Raju et al., 1996) that dayglow photometer can be used to infer the strength of the Equatorial Ionisation Anomaly (EIA). By separating out the contribution of the EIA from the OI 630 nm dayglow measurement, a prediction of ESF occurrence was made on 19 Feb. 1993 (Sridharan et al., 1997).

A RH-560 rocket was launched from SHAR on 19 February 1993 at 1915 hrs LT during the onset time of ESF as a part of 'Ionisation hole' campaign. Electron density measurements were made using a Langmuir probe sensor with a hemispherical shape. The sensor, having 40 mm diameter, was mounted on a small boom which was located slightly away from the centre of the top deck and was parallel to the spin axis. The LP sensor was connected to the electronics package by means of a shielded cable. The sensor potential was swept from -2 V to +4 V with fixed time delays at the two extrema of the sweep. The negative potential enables positive ion density measurements to be made while the positive extreme provides electron density measurements and the sweep can be used for calculating the electron temperature. Above 100 km altitude, the sweep waveform was automatically altered with the help of a telecommand. Fig. 4.1 shows the exact nature of the sweep waveforms which were applied to the LP sensor upto and beyond 100 seconds from the launch. In the present work, only the observation with fix positive bias of +4 volts will be discussed.

The ionospheric conditions during this flight were monitored by ionosonde at SHAR. The ionograms revealed that the base of the F layer was around 270 km at 1815 hrs LT and rose up to 375 km by 1915 hrs LT. The spread in the returned signal started appearing around 1910 hrs LT, was well developed by 1945 hrs LT and was seen through out the night as shown in Fig. 4.2.

VHF scintillations were recorded during this campaign using a radio beacon on board FLEETSTAT satellite (73°E) at 244 MHz. The duration of occurrence of VHF scintillations which are caused by the presence of sub-kilometre scalesize structures is shown in the Fig. 4.3. Iyer and Chandra (1993) discussed the details of the occurrence of scintillations during the whole period of February-March 1993: a special campaign of scintillation network of All India Co-ordinated Programme on Ionosphere-Thermosphere Studies (AICPITS). It can be seen from the Fig. 4.3 that the duration and the occurrence pattern of scintillations varies at different locations. At

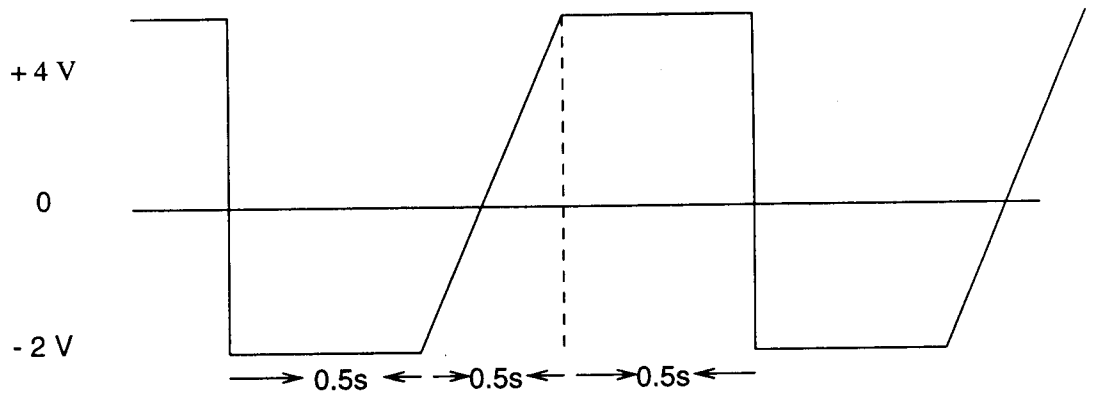

Sweep Waveform upto 100 s,

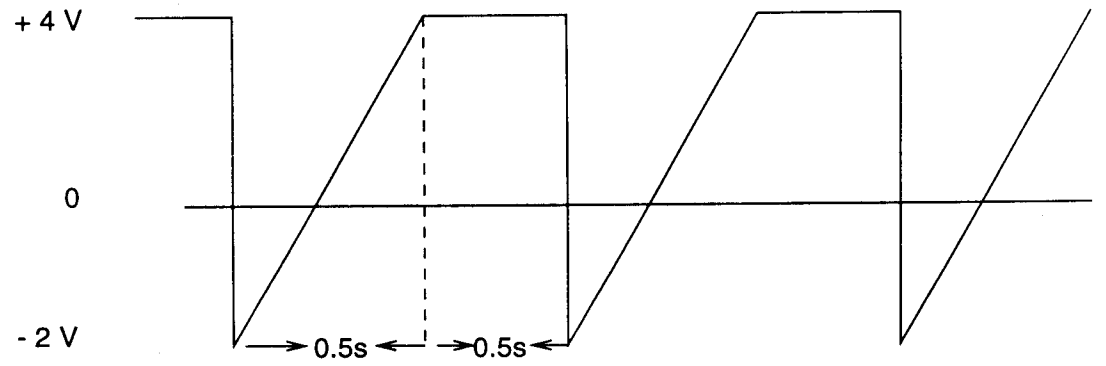

Sweep Waveform after 100 s.

Fig. 4.1 Sweep Waveform Applied to the LP Sensor.

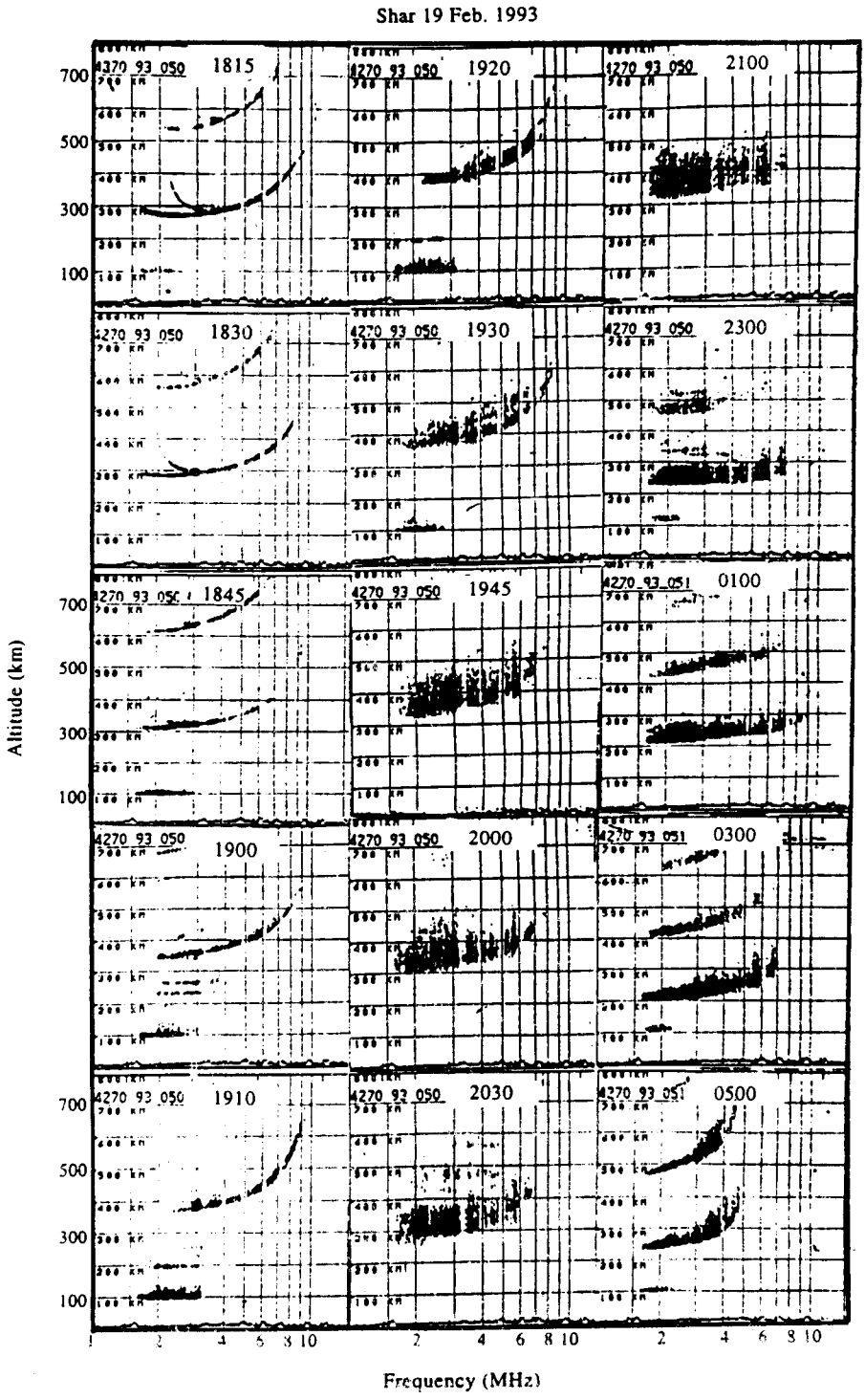

Fig. 4.2 Ionograms obtained during the night of rocket flight conducted from SHAR on 19 February 1993

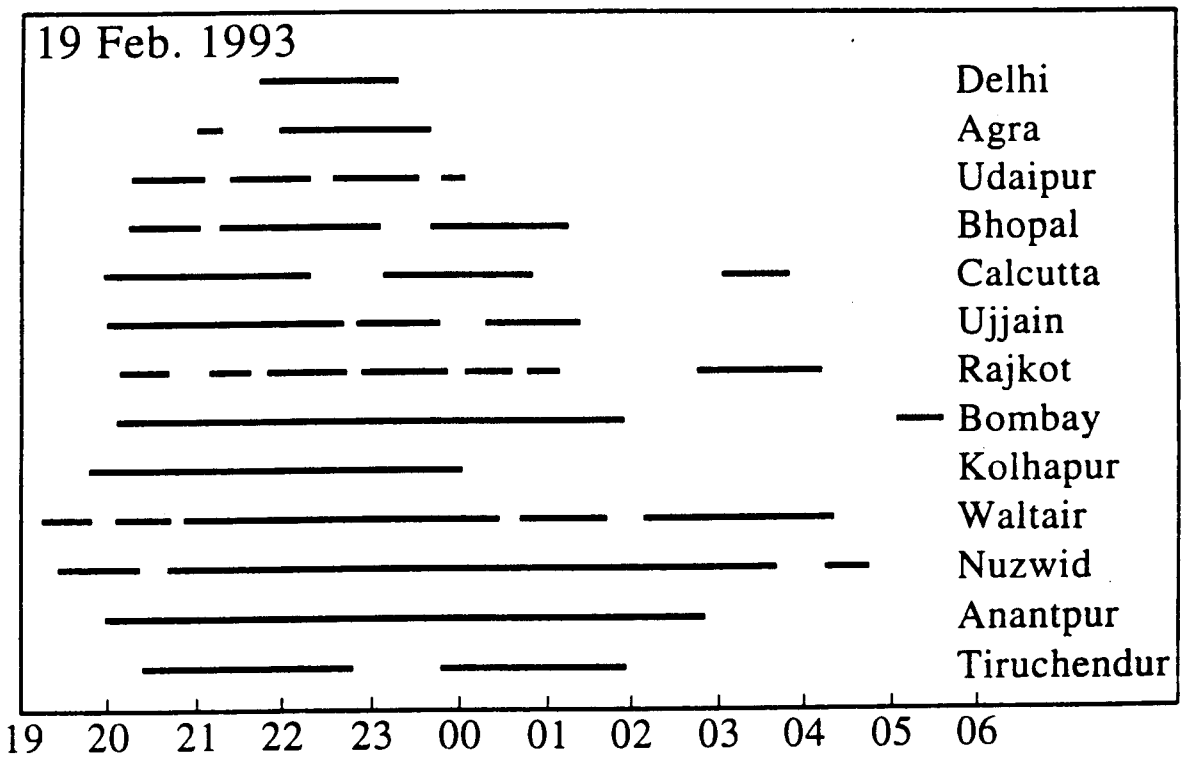

Fig. 4.3 Duration of occurrences of VHF scintillations from a chain of ground based stations receiving the beacon signal at 244 MHz transmitted by the Fleetstat satellite (Chandra et al. 1997).

Tiruchendur (8°E, 77°W), near the magnetic equator, the scintillations occurred in two patches, one during 2015-2245 hrs LT and another during 2345-0200 hrs LT. At Anantpur (7° N dip lat.), scintillations are seen in a single patch from 2000-0300 hrs LT. At Nuzwid (10° N dip lat.) and Waltair (17.7° N; 83.3° E;10.5°N dip lat.) they commenced around 1915 hrs LT and lasted, until 0500 hrs LT, with intermittent breaks. However, at Kolhapur situated in the western part of India and at nearly the same magnetic latitude (~ 10°N dip lat.), the scintillations occurred only for a short duration (2000-0000 hrs LT), whereas at Bombay (11.5°N dip lat.) the duration was significantly longer (2000-0200 hrs LT). One of the interesting observations is the occurrence of scintillations at Bombay during the pre-sunrise period. For the stations located in the crest region of the EIA, i.e. Rajkot (16°N dip lat.), Ujjain (16.8°N dip lat.), Bhopal (16.7°N dip lat.) and Calcutta (15.8°N dip lat.), scintillations occurred between 2000-0100 hrs LT in three patches. It is observed that the duration of the scintillations reduces considerably northwards. An interesting feature is that the duration of the scintillations is longest over Waltair (17.7° N; 83.3° E;10.5°N dip lat.) and Nuzwid (10° N dip lat.), and not over the dip equator.

The electron density profile obtained during the ascent of the rocket at the onset time of ESF, conducted from SHAR on February 19, 1993 is shown in Fig. 4.4. As the descent data was a bit noisy, only ascent data is presented. As the LP sensor in this flight was mounted slightly away from the centre, the electron density profile exhibited spin modulation. It is well known that this is due to the fact that when the LP mounting is off centred, the surface area offered by the sensor for electron collection is different as the rocket spins. This would manifest in the form of a sinusoidal signal i.e. a sine wave of spin frequency will be superimposed on the signal measured by the LP without affecting the nature of irregularities if they are present in the medium. It is to be noted that the LP flown in this flight was very sensitive and similar to the ones used in the earlier flights conducted from

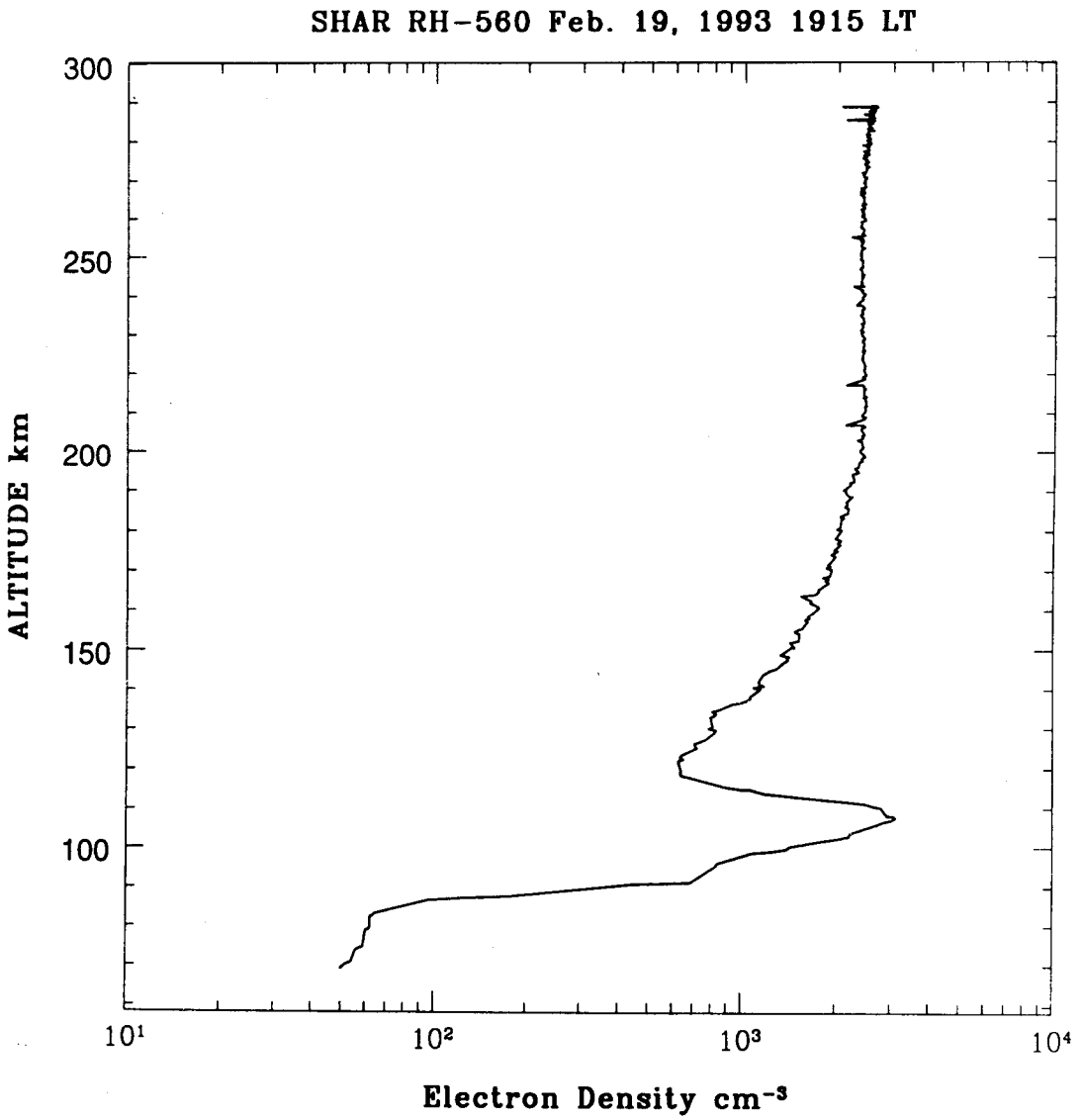

Fig. 4.4 Electron density profile obtained during the ascent of thr rocket flight conducted at the onset time of ESF.

SHAR (Sinha, 1976; Sinha and Prakash, 1995) which detected weak irregularities.

The LP started measuring the current from about 50 s after the launch until the splash down which occurred at 1924 hrs LT. As the mounting of the LP sensor was off-centre, the probe current exhibited the expected spin modulation. For the retrieval of the electron density, only the peak current value was considered during each spin cycle. It is observed that the electron density started increasing very sharply from about 85 km to about 93 km altitude range, then relatively slowly upto about 110 km. Above 110 km the electron density decreased upto about 122 km and beyond 122 km, the density started increasing in a gradual fashion reaching a value of about 2.5 x 10^3 cm^{-3} at apogee. Apart from some small fluctuations (< 15% of the ambient density), the region above 122 km does not show any major structure. However, a mass spectrometer, which was flown for the first time, revealed ion density fluctuations in the altitude range of 250-290 km (Sridharan et al., 1997).

Thus there is a clear cut discrepancy in the measurements made by LP and the mass spectrometer. The irregularities observed by the mass spectrometer are in NO^+, O_2^+ and O^+. These irregularities were observed in a region of practically zero vertical density gradient region, in which irregularities are not supposed to be produced by mechanism such as RTI. However, numerical simulation work (Sekar et al., 1997) attempted to explain the irregularities observed only by the mass spectrometer. Their work revealed that the altitude variation of the recombination coefficient and the vertical polarisation velocity due to fringe fields associated with the plasma bubble at the base of the F layer change the polarity of the vertical plasma density gradients in the lower F region. They discussed that the penetration of the fringe fields is mainly responsible for the development of zonal density gradients which plays a crucial role in the secondary plasma instabilities resulting in the generation of kilometre scalesize irregularities in the vertical direction. However, these simulations results provide the possibility of the generation of irregularities exactly over the magnetic dip

equator, whereas the irregularities which the mass spectrometer appears to have detected were over a low latitude station SHAR (13° 42′ N, 80° 14 E, dip 14° N). Thus, the electron density profile at the time of onset of ESF, does not show presence of irregularities of any significance.

4.3 Results of the Rocket Flight During Fully Developed ESF Conditions (Present Work)

A RH-560 rocket equipped with LP and a pair of double probes was launched to measure simultaneously the electron density and the electric field fluctuations on 4 October 1988 at 2132 hrs LT during a well developed phase of ESF.

4.3.1 Flight Details

The arrangement of sensors on this flight is shown in Fig. 4.5. A cylindrical LP having diameter 35 mm and length 20 mm with a fixed positive bias of 4 volts was used to measure the current in the electron saturation regime. The LP sensor was mounted on a thin deployable central boom of about 25 mm diameter which was fixed on the top deck of the rocket concentric with its spin axis. The sensor was made of brass and was gold plated. The current collected by the sensor was processed onboard in three different frequency bands (a) DC - 200 Hz (b) 50 - 500 Hz, and (c) 125 - 1250 Hz. This was done to accommodate the large dynamic range of irregularity amplitude associated with a large scalesize range viz. from a few tens of kilometres to a fraction of meter.

Two pairs of the double probes were used to measure the fluctuations in the electric field along and perpendicular to the spin axis of the rocket which was off the vertical direction by a few degrees. One pair of double probes with a separation of 1 m was mounted on the central deployable boom, which was along the spin axis of the rocket, and measured the electric field fluctuations in a direction very close to the vertical. The other pair separated by approximately 2.4 m was mounted by

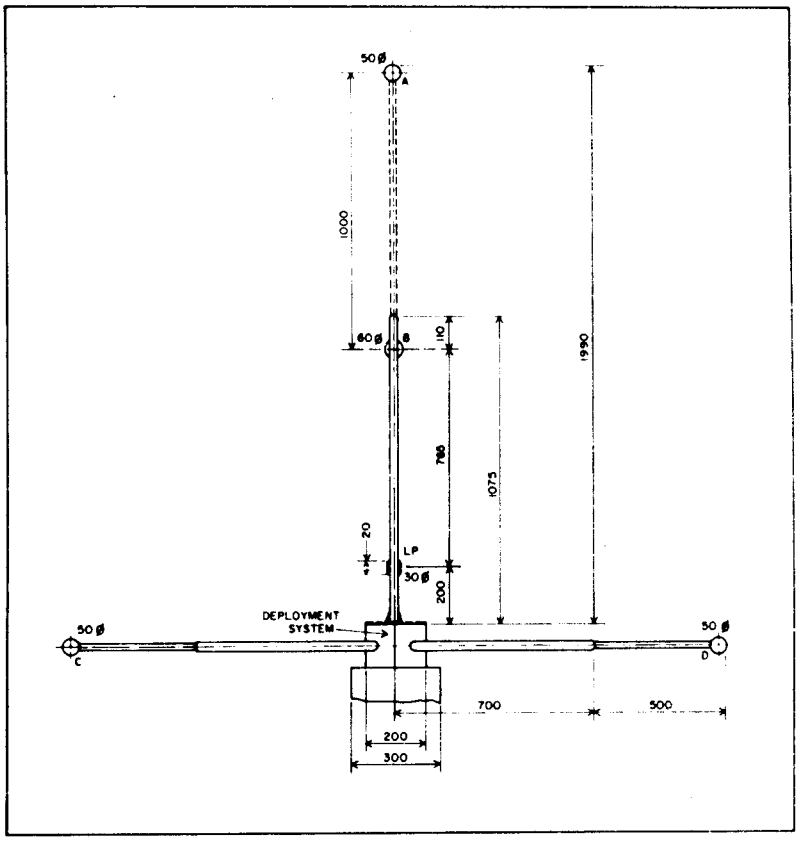

Fig. 4.5 Schematic of the arrangement of LP and double probe system carried on RH-560 rocket launched from SHAR on 8 October 1988.

using two deployable side-booms along a direction perpendicular to the spin axis to measure the fluctuations in the electric field in a direction close to the horizontal. A set of two filters in the frequency ranges (DC - 100 Hz and 50 - 500 Hz) were used on-board to measure electric field fluctuations. The rocket, which was launched due east of the SHAR launch station with an elevation of 81.25° and azimuth of approximately 82°, attained an apogee of 348 km. The trajectory of the rocket is shown in the Fig. 4.6.

The Langmuir probes used on both the above mentioned flights were the ones described by Prakash and Subbaraya, (1967), Prakash et al. (1972), and Sinha (1976). The LP electronics was capable of measuring a large dynamic range of current, from 1 nA to 100 μA. The frequency response of LP system was more than a few KHz enabling the measurement of vertical structures in electron density with scales as small as one meter. In order to handle the large dynamic range of the current, a current to voltage converter with an eight stage feedback resistance was employed. The probe current was converted into electron density using a fixed calibration factor of 7140 e/cm^{-3}/μA (Sinha and Prakash, 1995). As the amplitude of small scale irregularities ($\lambda \sim 1$ m) is many orders of magnitude smaller than that of the large scale irregularities ($\lambda \sim 300$ m), the LP current was analysed onboard in four different frequency bands suitably covering the large scalesize range.

4.3.2 Ionospheric Conditions During the Rocket Flight

The launch time of RH-560 rocket on 4th October 1988 (during fully developed ESF conditions) was decided by continuously monitoring the ionospheric conditions using a KEL ionosonde at SHAR. It is known that the F-layer altitude and the vertical movement play important roles in the growth of the irregularities associated with the ESF phenomena. Chandra et al. (1997) studied the correlation of spread-F with the post-sunset rise of the

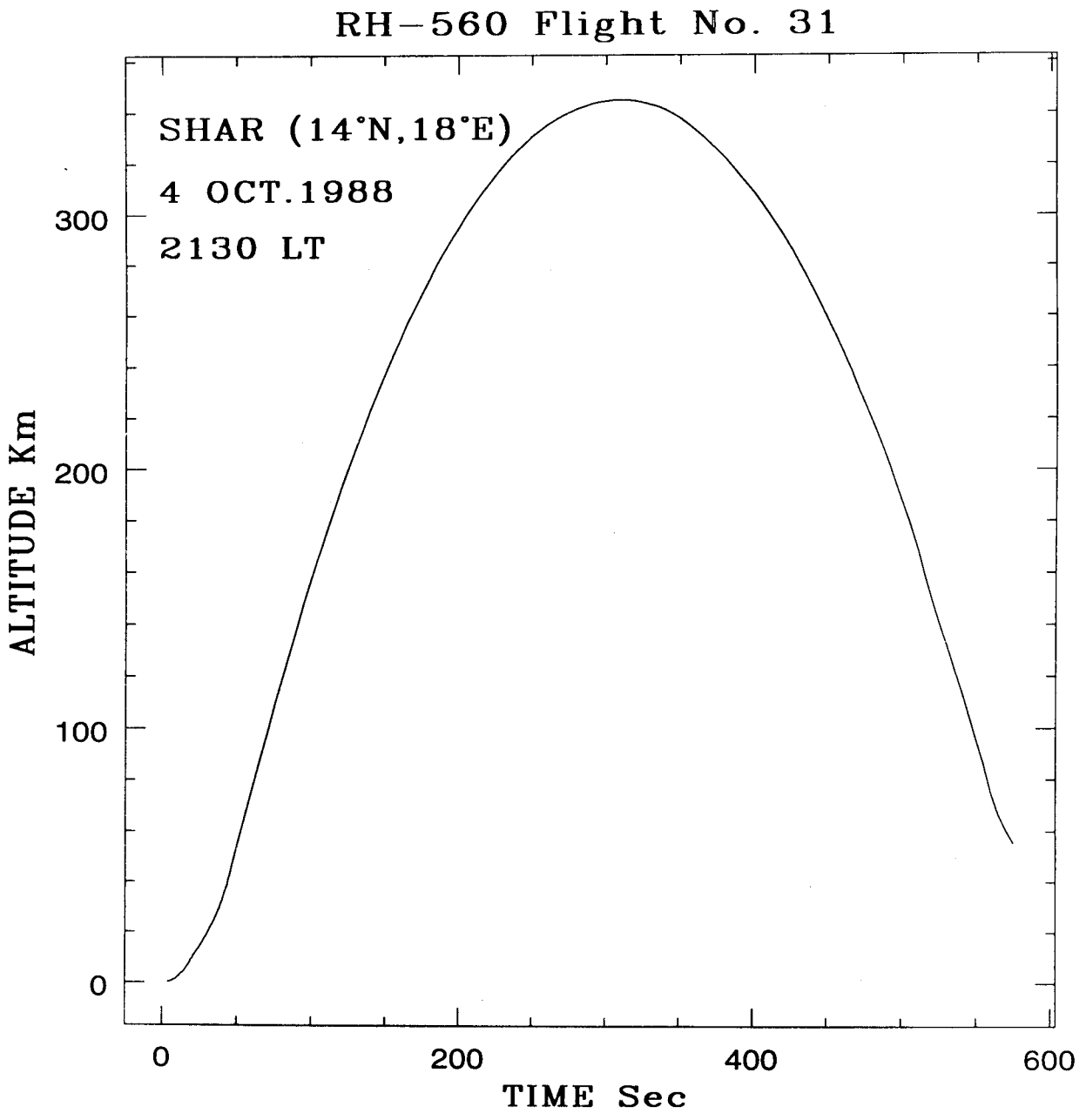

Fig. 4.6 Trajectory of RH-560 rocket launched on Oct. 4, 1988 from SHAR

F - layer using quarter hourly values of h'F from the ionograms. They found that (a) ESF occurred for at least a few hours on the nights when h'F rose to 350 km or more and (b) the reversal of electric field as inferred from h'F variations occurred earlier (around 1900 hrs LT) on non-spread F days. The ionograms recorded on 4 October 1988 are shown in Fig. 4.7. It can be seen that the first traces of ESF echoes occurred around 1855 hrs LT, with h'F value of about 375 km. Spread F was fully developed with strong echoes seen over the frequency range of 1.6 - 7.0 MHz around 1930 hrs LT. This would have been the ideal time for the rocket flight but due to the limitations of the RH-560 rocket which had a predicted apogee of about 350 km, rocket launch was planned when F layer started descending to lower altitudes. The base of the F region had come down to 250 km at 2015 hrs LT, but due to bad weather conditions, the rocket launch was further postponed for later time. The F layer rose again with h'F more than 300 km at 2100 hrs LT and also a strong blanketing type of sporadic E (E_s) developed. The F layer descended later to 250 km around 2130 hrs LT and this was the time when the rocket was launched. A strong blanketing type of E_s was seen at this time at around 105 km altitude, with five multiple echoes, which completely obscured F layer echoes below 3.5 MHz. However, spread F echoes were seen at frequencies above 3.5 MHz. The presence of such large number of multiple echoes shows that the Es layer was very thin.

The variation of the height of the F layer is shown in the Fig. 4.8,: the time of the rocket launch is also marked. From the successive ionograms the vertical drift velocity was inferred and large vertical velocities were seen with maximum values close to about 70 m/s. The vertical velocity at the time of the rocket launch was about 20 m/s downward and it shows two dominant periodicities, one having a period of 60 - 70 min and the other around 15 min. Chandra et al. (1997) suggested that such oscillatory features in h'F data might possibly be due to the large scale gravity waves in the neutral atmosphere. Kelley et al. (1981) used the phase difference between the motions over Jicamarca and Huancayo to estimate the wavelength

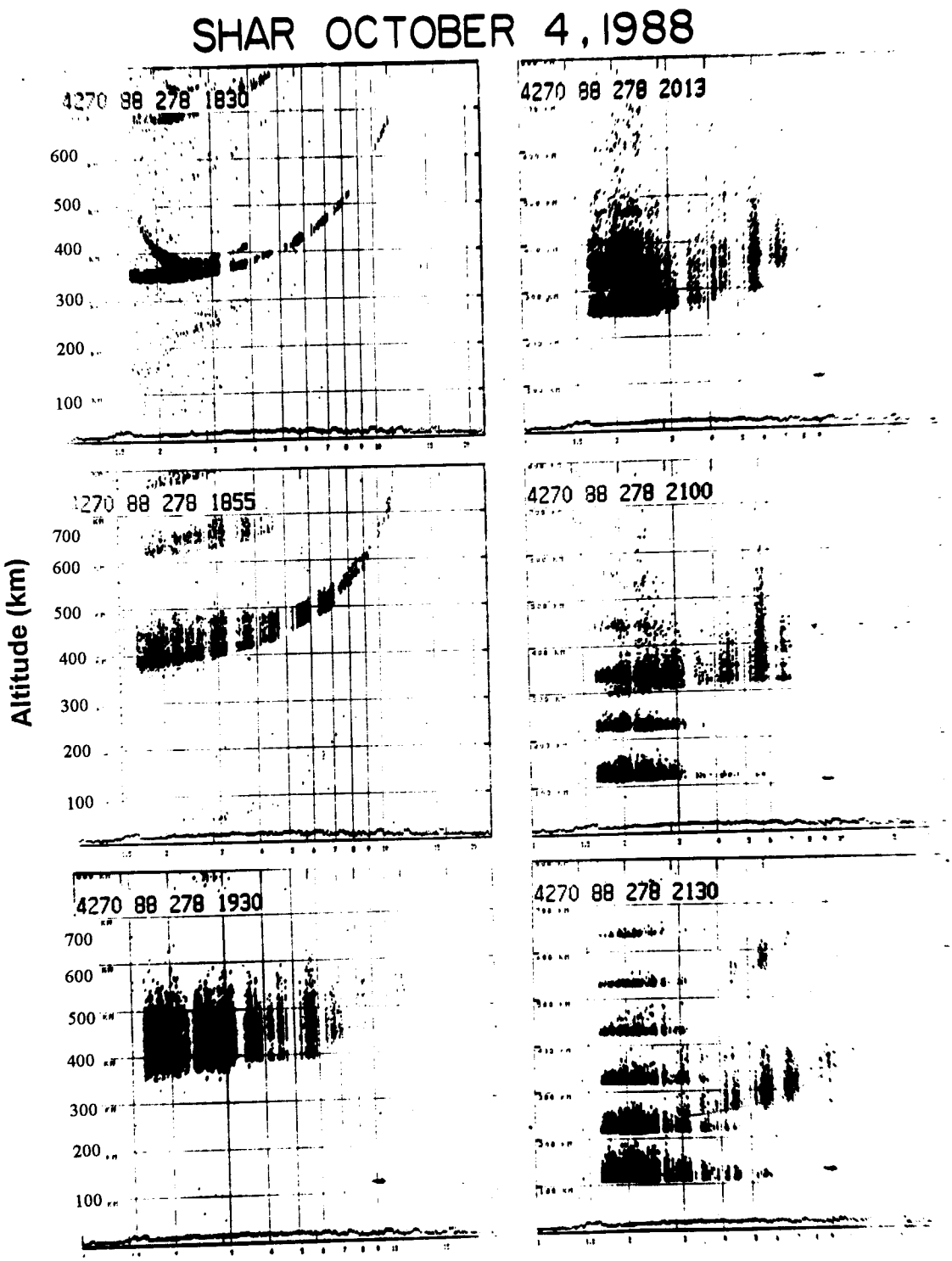

Fig. 4.7 Ionograms over SHAR at 1830, 1855, 1930, 2013, 2100 and 2130 hr LT during the night of the rocket launch on 4 October 1988.

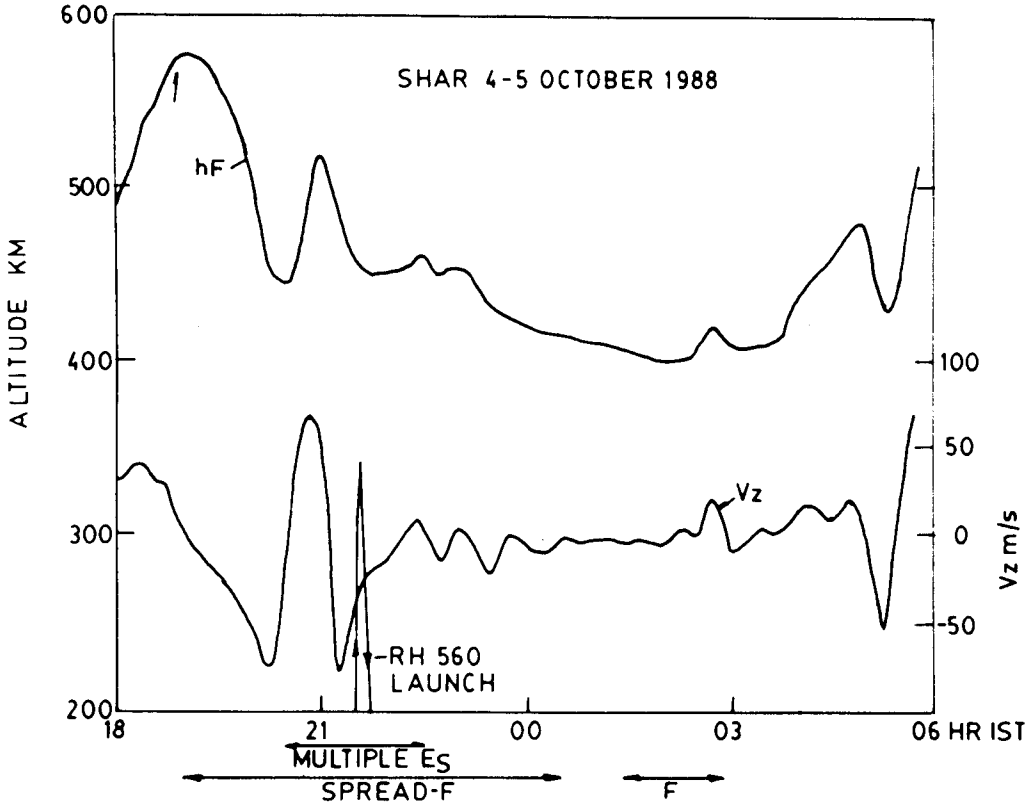

Fig. 4.8 Variations of h'F (upper curve) and the vertical drift velocity (lower curve) with time during the night of rocket flight. The RH-560 trajectory is also depicted. Durations of spread F and sporadic E are also marked in the figure (Chandra et al. 1997).

associated with the observed wave in the zonal direction (λ) using the following expression

$$dy = (n + \varphi/360)\ \lambda \qquad (4.1)$$

where dy is the zonal separation between the two stations, φ is the phase difference and n is an integer. Chandra et al. (1997) estimated the zonal wavelength using h'F data from Thumba and SHAR to be about 660 km, 220 km and 132 km for n = 0, 1 and 2, respectively. However, the scalesize is restricted by the lower wavelength cut off in the region where the relevant gravity waves might be present. Comparisons of the zonal wavelengths observed over Thumba and SHAR with those observed by Kelley et al. (1981) over Jicamarca and Huancayo indicates that the wavelengths are similar over the globe (Chandra et al., 1997).

4.3.3 Scintillations during the Rocket Flight (October 4, 1988)

A 136.1 MHz receiver to record VHF scintillations using the radio beacon onboard the geostationary satellite ETS - II (130° E) was used for studying ESF irregularities (Chandra et al., 1992; Chandra et al., 1997). A 12 element Yagi antenna with an estimated gain of 15 dB and beam width of approximately 30° was used. Analog data were recorded using a variable speed paper chart recorder and the digital data were recorded on audio cassettes using a microprocessor based recorder, with a sampling rate of 10 Hz in block sizes of 100 s each. The digital data were analysed to compute the scintillation index S_4 which is the normalised RMS value of the intensity fluctuations. The sub-ionospheric point for the ETS-II satellite to the receiver ray path, at 400 km altitude, was located approximately 2.0° E and 0.5° south of SHAR. Therefore, the scintillations recorded over SHAR can be related to the ionospheric irregularities located approximately 220 km towards the east. Power spectra were also computed using a standard FFT routine. The range of the temporal scintillation spectra was limited to 5 Hz on the higher frequency side and to the Fresnel cut-off ($\sqrt{\lambda_z z}$) on the lower frequency

side, where λ_z is the wavelength of radio-beacon and z is the altitude at which irregularities are located. With a irregularity drift velocity of about 100 ms^{-1}, a sample at 5 Hz corresponds to the lower scalesize range of 20 m. For the irregularity height of 300 - 400 km, the Fresnel size turns out to be 800 - 900 m. Thus the spectral estimates can be made from about 800 m to 20 m. The spectral slopes were computed from 0.3 to 3.0 Hz corresponding to irregularities with scalesizes in the range of 300 m - 30 m

During the night of 4 October 1988, the appearance of scintillations commenced around 1845 hrs LT and lasted till 0400 hrs LT. Detailed analysis of the scintillation data during this night has been reported by Chandra et al. (1992). An example of the chart recording around the flight time is shown in the Fig. 4.9 which displays a high fading rate, with 48 fades/min. The temporal variation of the scintillation data during the period 1851 - 0100 hrs LT is shown in the Fig. 4.10. The S_4 index varied between 0.2 and 0.4, with quasi - periodic fluctuations of dominant periodicities around 70 min and 15 min. Assuming the power law dependence of the type $P(f) \propto f^{-p}$, the spectral index, p, was calculated and its temporal variation is also shown in the Fig. 4.10. The spectral index is seen to vary between 3 and 5 with fluctuations of periodicities similar to those observed in the temporal variation of h'F, S_4 and p (Chandra et al., 1997).

4.3.4 Features of the Electron Density Profile

The electron density variation with altitude i.e. (n_e-h) profile, during a fully developed ESF condition, obtained by using a RH-560 rocket launched on 4th October 1988, is displayed in Fig. 4.11. The solid line shows the variation of electron density obtained during the rocket ascent and dashed line indicates electron density during the rocket descent. The profile exhibits irregularities in three different patches occurring between 165-175 km, 210 - 260 km and 295 - 330 km region. It also reveals two distinct layers in the E region, one located around 105 km and the other around 130 km. These layers are present both during ascent and descent of the rocket flight. The

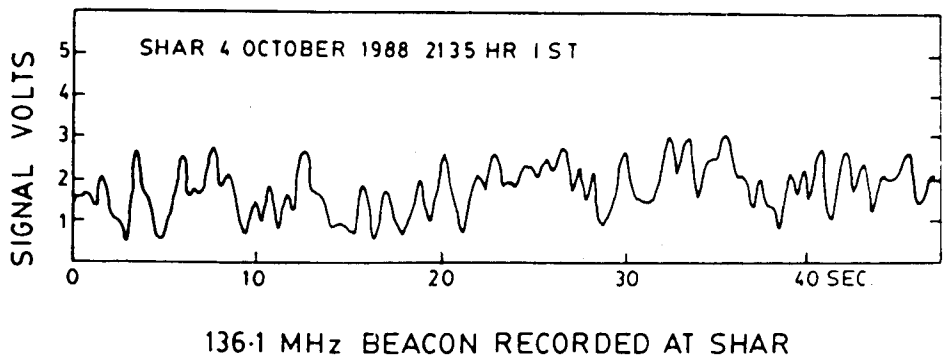

Fig. 4.9 Example of scintillation recorded over SHAR near the time of the rocket launch on 4 October 1988 (Chandra et al. 1997).

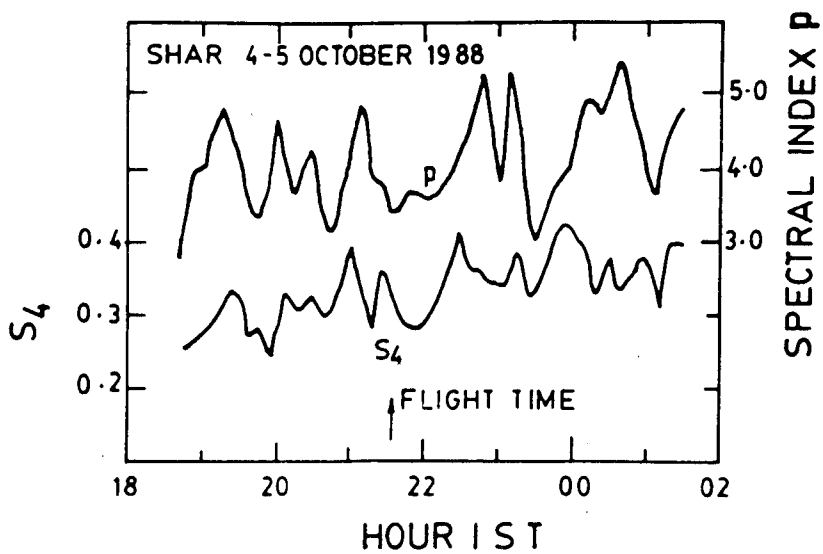

Fig. 4.10 Time variations of the scintillation index S4 (lower curve) and the spectral index p, obtained from the temporal scintillation spectra (upper curve) during the night of the rocket launch.

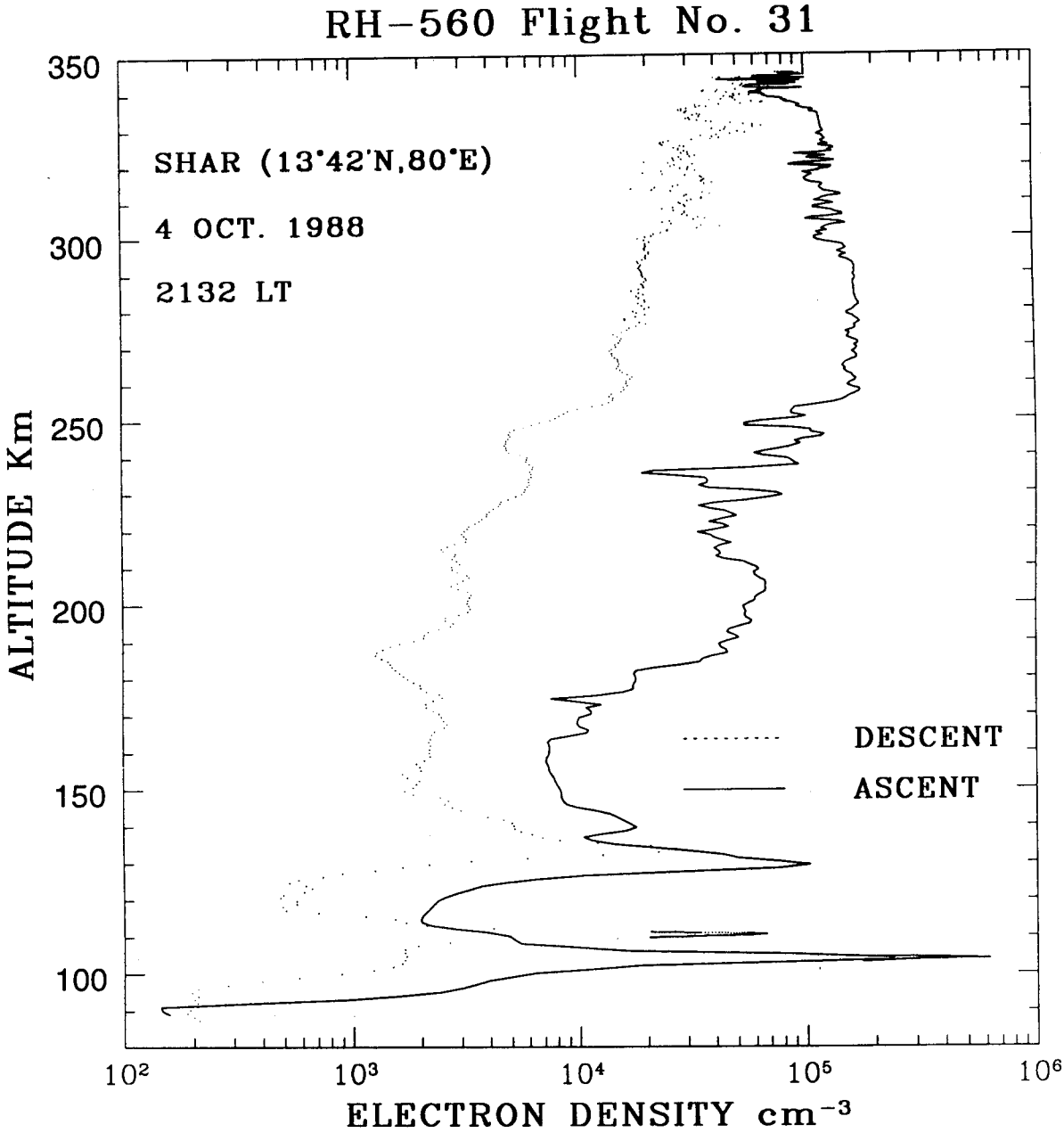

Fig.4.11 Variation of electron density with altitude during ascent and descent of RH-560 rocket launched from SHAR on 4 October 1988 during fully developed spread F.

electron density values during the descent are smaller than the ascent values by an order of magnitude.

The region below 150 km displayed large scale structures with vertical scalesizes varying between 15 to 20 km where the electron density varied by a factor of about 50. Similar structures were observed during the descent also around the same altitude range which indicates the presence of horizontal gradients of the order of few hundred of kilometres. Such large increase of density (by a factor of 50) has not been reported so far. Earlier rocket flights from SHAR (Prakash et al., 1991) showed number of large scale structures in the region 100 - 150 km with vertical scalesizes as large as 25 km but the density increase was only by a factor of 20. E region flight from Thumba by Prakash et al. (1970) revealed the presence of structures with scalesize of 5 - 10 km in the altitude range of 90 - 130 km, but in these structures also the density increase was only by a factor of 10 or so.

A very interesting feature seen in the n_e-h profile is the occurrence of irregularities in the F-region valley, above 150 km upto the base of the F region. This region is characterised by the presence of structures with wavelengths up to about 10 km. The electron density in them varied by a factor of 1.5 around 170 km. Around 180 km, n_e-h profile shows an increase in electron density by a factor of 2.3 in 4.5 km. Very large scale structure with vertical scale size of about 39 km is also seen in this region which extends down to about 150 km. Small scale structures with half wavelength of 3 km and less are also seen in the n_e-h profile in 165 - 180 km region superimposed on large scale fluctuations. These small scale fluctuations may be the result of cascade process of the larger scale structures.

Fluctuations in the scalesize 0.1 - 2.0 km (intermediate range) are quite prominent above 200 km altitude region. A depletion in electron density is observed around 236 km during the ascent in which electron density decreases by a factor of 3. A similar depletion is observed during the descent also but it is located around 245 km. Another significant decrease in electron density is seen around 175 km during the ascent and

the corresponding structure during the descent is seen around 187 km. The presence of these two structures at different altitudes during the ascent and descent indicate the presence of horizontal gradients in the electron density distribution. As shown in Fig. 4.12 the horizontal separation between the ascent and descent at 180 km and 240 km is 273 km and 230 km, respectively. Assuming a night-time zonal plasma drift of 150 ms^{-1}, the depletions encountered during the rocket ascent and descent cannot be the same. This shows the presence of large scale horizontal gradients and appears to be a manifestation of E-W cut of a plasma bubble in the rocket data. It is observed that the horizontal electron density gradients are larger than the vertical ones. Similar horizontal gradients were observed by McClure et al. (1977) in AE satellite data. Recently, Gdalevich et al. (1998) reported the presence of horizontal gradients in plasma density using a cylindrical Langmuir probe in the rocket experiment 'Vertical-10', which they attributed to large scale disturbances propagating as IGWs in the upper atmosphere.

As the vertical electron density gradients play a very important role in the generation of irregularities, these were calculated from the electron density profile. Density gradient scale length, L (L^{-1} = dn/dh (1/n)), were calculated for a vertical extent of 2 km. Such L values were calculated every 50 m. Fig. 4.13 shows the percentage occurrence of gradients, sharper than an arbitrarily assumed L^{-1} value of 0.75 Km^{-1}) which are shown as horizontal bars along with n_e-h profile. It is seen that percentage occurrence of steepest gradients is maximum (~ 80%) around 236 km and near apogee i.e. around 345 km and these are colocated with strong irregularities occurring in the same altitude range. Base of the F layer is located around 255 km and the bottomside of the F layer is characterised by L ≈ 7.6 km where electron density increases by a factor of 6.1 in 10 km altitude extent. Between 260 - 280 km altitude region, where vertical gradients over 20 km altitude extent are almost zero, a patch of small amplitude irregularity is

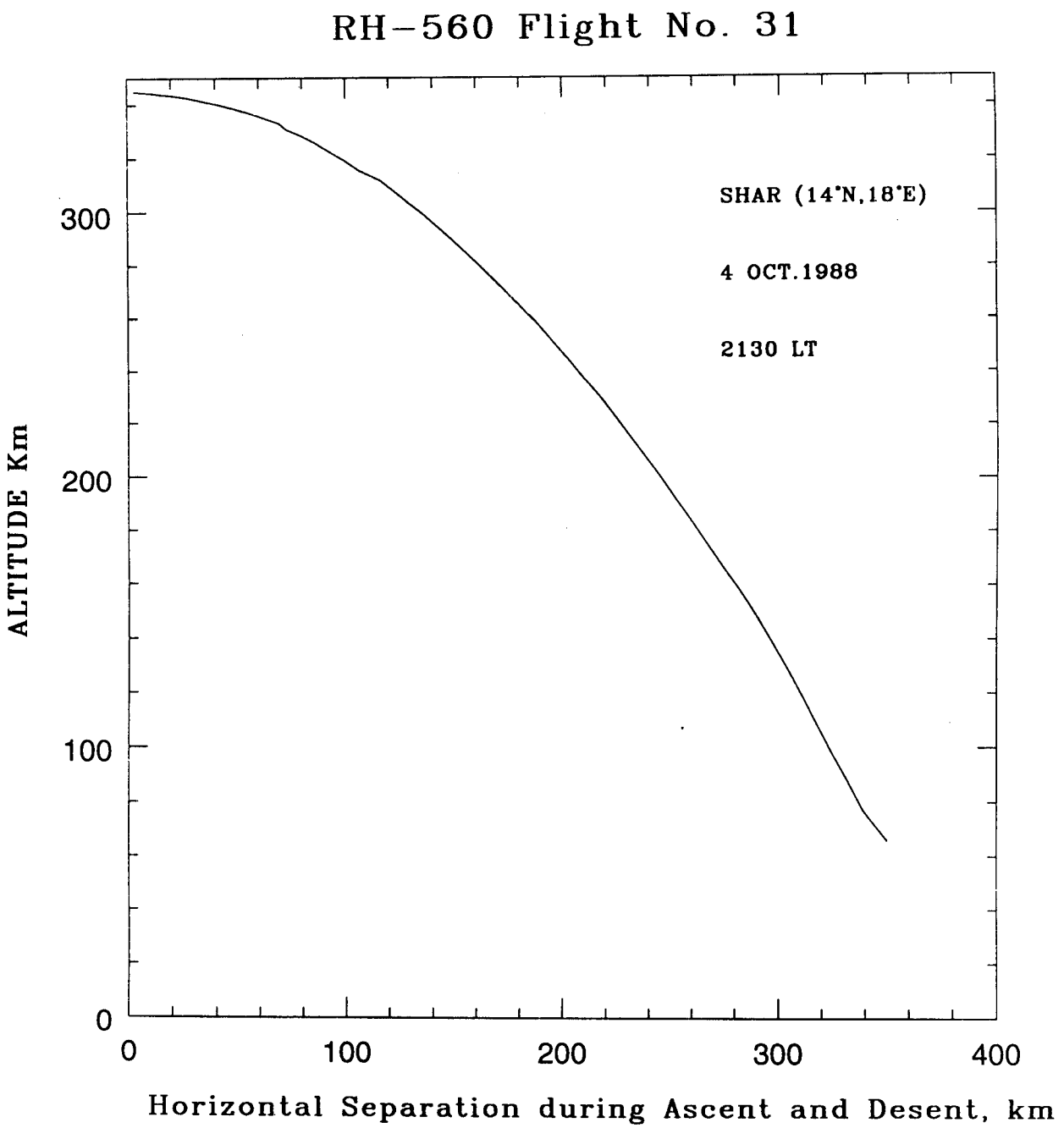

Fig. 4.12 Horizontal distance between the upleg and the downleg position of rocket launched on 4 October 1988, from SHAR

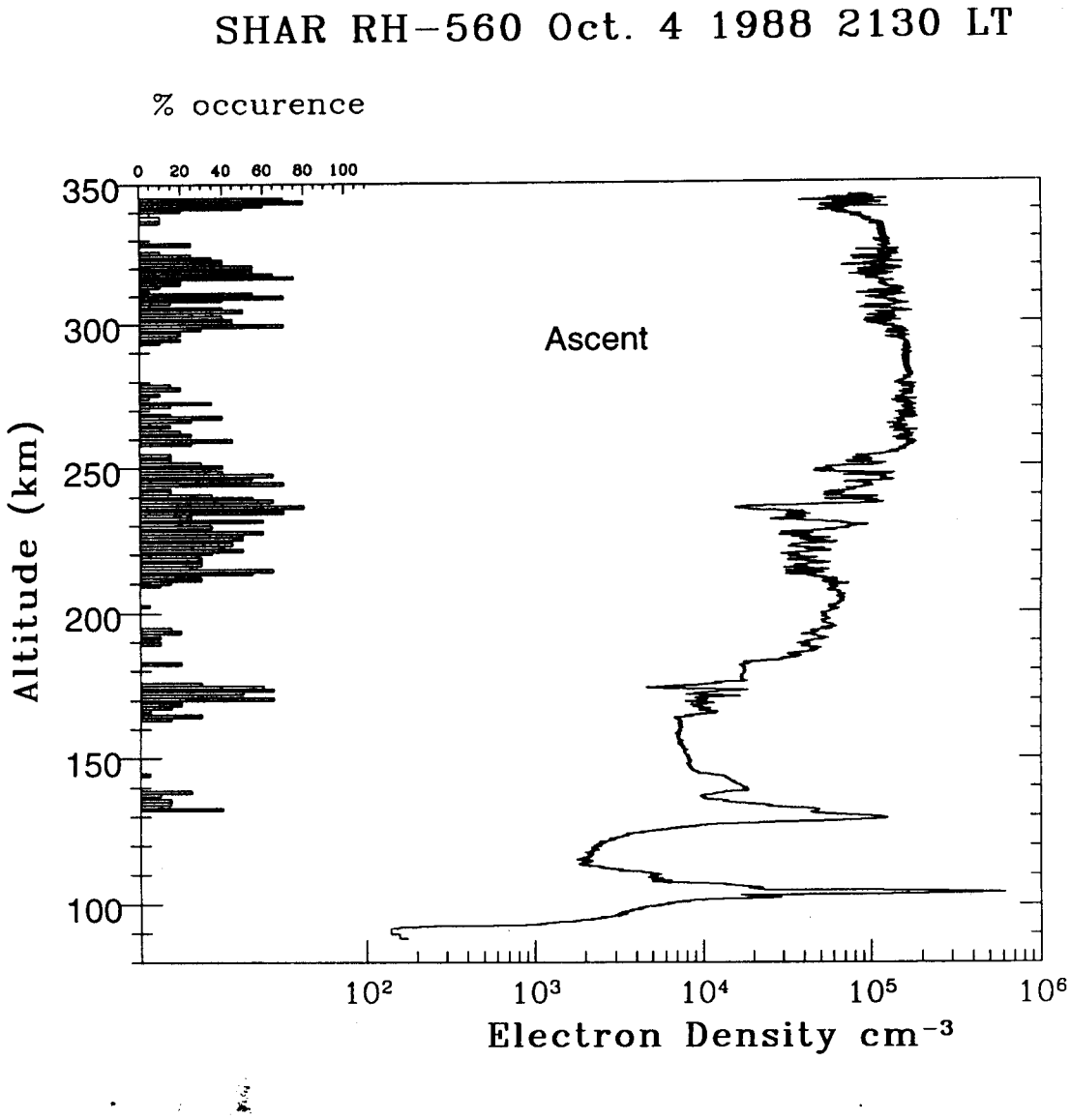

Fig. 4.13 Horizontal bar shows the % occurrence of steep gradients (L^{-1} sharper than 0.75 km^{-1}) along with the density profile during the ascent.

observed followed by a region of smooth profile. Another patch of irregularity is seen above 280 km which extends upto about 330 km.

4.3.5 Effective Growth Rate Estimation

It is believed that the primary driving process for intermediate scale wavelengths is Generalised Rayleigh-Taylor (GRT) instability (Dungey, 1956; Hudson and Kennel, 1975; Scannapieco and Ossakow, 1976; Keskinen et al., 1981; Zalesak et al., 1982). The expression for growth rate by GRT instability includes gravitational (Kelley et al., 1981), electric field as well as the neutral winds terms. It has been discussed earlier that the gravitational term is unstable whenever g has a component anti-parallel to the density gradient and local linear growth rate (γ_g) is given by = $g/\nu_{in}L$, where ν_{in} is the ion-neutral collision frequency and L is the gradient scale length. The electric field is destabilising when $E \times B$ is parallel to ∇n_e, with the local linear growth rate due to the electric field (γ_E) given by $\gamma_E = E/BL$. γ_E is less than γ_g for altitudes $\geq$ 300 km. Thus for an upward directed gradient, the eastward electric field during the post-sunset period can make the bottomside of the F region unstable. In the presence of winds and electric fields, the current density is $\sigma E'$, where $E' = E + U \times B$ and σ is conductivity. As the large scale neutral wind is primarily eastward at sunset (Sipler and Biondi, 1978), $(U \times B) \times B$ is also horizontal and hence cannot have a component parallel to ∇n if the ionosphere is vertically stratified. Hence neutral winds (U) contribute only when the ionosphere is tilted. Since the layer changes height during the course of any given night, there is a possibility that the layers can be tilted with respect to vertical. Sekar and Raghavarao (1987) studied the role of vertical winds on the R-T instability using the linear theory for growth rate of collisional R-T instability mechanism. They found out that the effects of vertically downward winds can be more effective than the gravitational term in generating instability in the altitude region of 200 - 300 km. The effective linear growth rate γ_g for the irregularities generated through GRT instability including vertical winds can be written as:

$$\gamma_g = \frac{E\cos\alpha}{BL} + \frac{g\cos\alpha}{\nu_{in} L} + \frac{U\sin\alpha}{L} + \frac{W}{L} + \nu_R \qquad (4.2)$$

where W is the vertical wind, α is the tilt of the ionosphere and ν_R is the recombination coefficient.

As mentioned before, electron density irregularities with intermediate scales are seen above 200 km in the n_e-h profile. For making an estimate of the linear growth rate, gradients have been calculated over 4 km by smoothening the profile using 4 km running average. Downward vertical winds in the range of 10 - 25 m/s have been reported in literature (Raghavarao et al., 1984, 1987; Sridharan et al., 1997). So, vertically downward wind of magnitude 20 m/s has been used for the calculation of γ_g. Electric field has been estimated from the movement of F layer as seen in the ionosonde data. As mentioned before, at the time of this flight, the F layer was moving downward with velocity approximately 20 m/s which corresponds to westward electric field of about 0.8 mV/m. Zonal winds have been assumed to be 100 m/s. ν_R has been taken from McFarland et al. (1973) and ν_{in} has been computed using the expression $\nu_{in} \approx 2.4 \times 10^{-11} M^{-1/2} n_n$ where n_n is the neutral density and M is the mean molecular weight of the neutrals and ions (Kelley, 1989). These neutral parameters have been taken from Mass Spectrometer Incoherent Scatter (MSIS-86) model. The estimated γ_g for the n_e-h profile obtained on 4 October, 1988 is shown in Fig. 4.14. Also shown in the last panel of this figure is the percentage amplitude of irregularities with scale sizes (200 m - 2 km). The middle panel displays the smoothened profile (obtained by taking 4 km running average) for viewing large scale structures and it shows strong kinks in electron density around 235 km and 245 km with lack of large scale perturbations between 250 to 290 km. However smaller kinks are observed between 292 - 320 km altitude region. It is clearly seen from the last panel of the Fig. 4.14 that the amplitude of intermediate scale irregularities is maximum (6%) around 232 km around which the smoothened profile exhibits the largest kink and at other altitudes, the growth rate of irregularities is appreciable

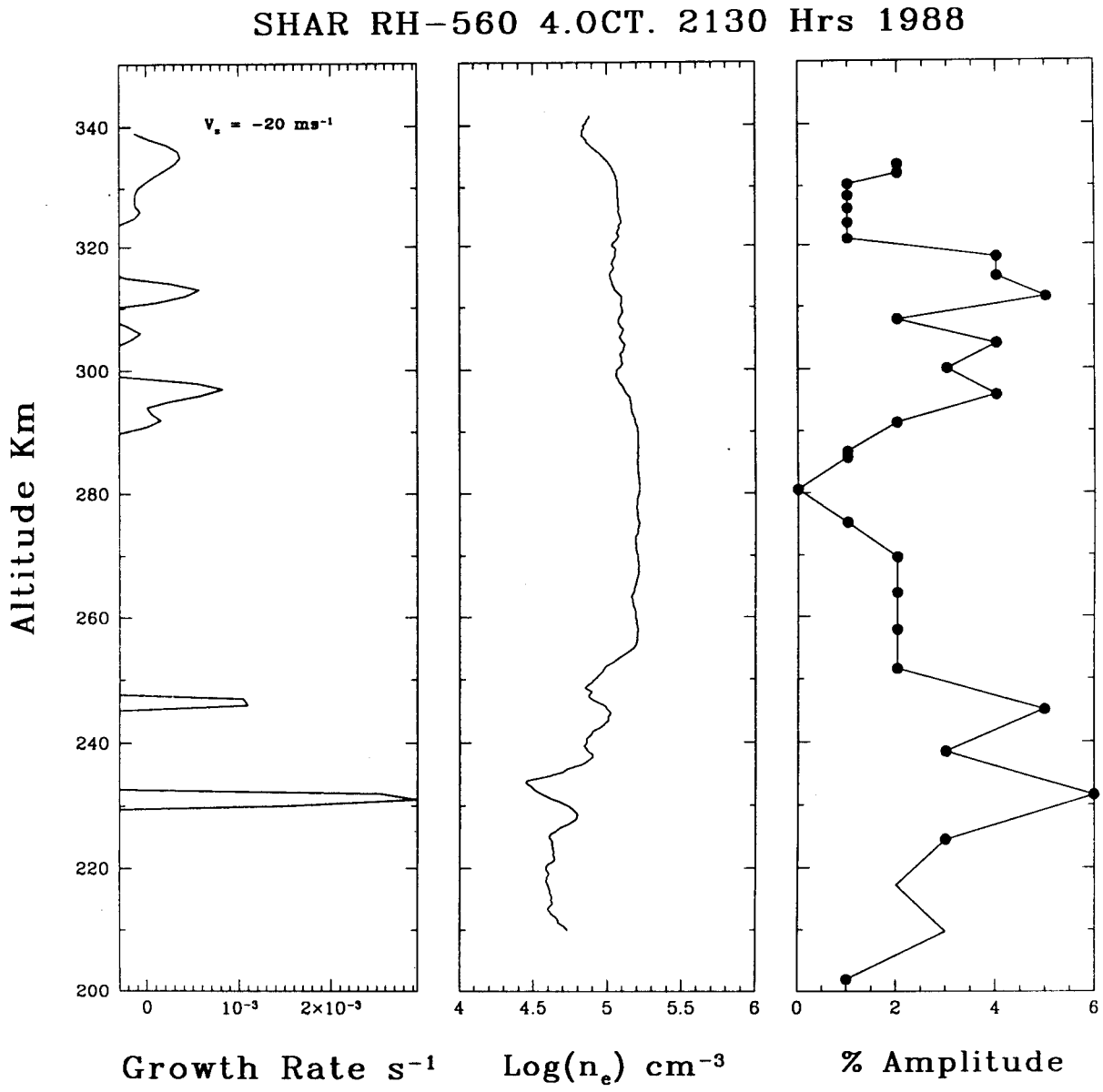

Fig. 4.14 The variation of linear growth rate for the irregularities generated through GRT instability shown in the first panel; middle panel shows the profile obtained by taking 4 km running average and the last panel displays the % amplitude of irregularities in the intermediate scale.

where the larger scale irregularities (λ ~ 200m -- 2 km) have more amplitude. This is in agreement with the consensus that hierarchy of processes operate where large scale irregularities can give rise to smaller scale irregularities (Haraendel, 1974). It is observed that the effective growth rate is maximum ($\gamma_g \approx 2.9 \times 10^{-3}$ s^{-1}) around 232 km which coincides with the region where the profile displays strong irregularities. It is seen that γ_g is positive at the altitudes where the amplitude is appreciable supporting the belief that they are produced by GRTI mechanism.

The relationship between γ_g and gradients has also been investigated. It is seen from the Fig. 4.15 that the growth rate is positive only when the gradients are negative both at lower and higher altitudes. At lower altitudes ν_{in} is more and so Gravitational Rayleigh - Taylor Instability will be less dominating than the electric fields and winds in contrast to the higher altitudes. The direction of electric field inferred from the motion of the F layer is westward which is conducive for the growth of gradient drift instability if gradients are negative. Thus it appears that during this flight, gradient drift instability might be playing a dominant role in generation of irregularities in the intermediate scales both at lower and as well as at higher altitudes.

4.3.6 Spectral Analysis of the Irregularities

As discussed before, n_e-h profile exhibited irregularities at a number of altitude ranges. The nature of the plasma turbulence in these altitudes can be investigated by the technique of spectral analysis. Since spread F irregularities are known to be highly field aligned, the turbulence is effectively two dimensional. If the rocket moves through the medium at a velocity exceeding the phase velocity of any of the waves comprising the turbulence, then for at least short periods of time the turbulence can be treated as frozen in the medium. In such a case, the time series observed by the rocket probe corresponds to a spatial waveform in the plasma along the rocket trajectory. The temporal Fourier transform of the rocket probe data corresponds to a one dimensional spatial Fourier transform of the

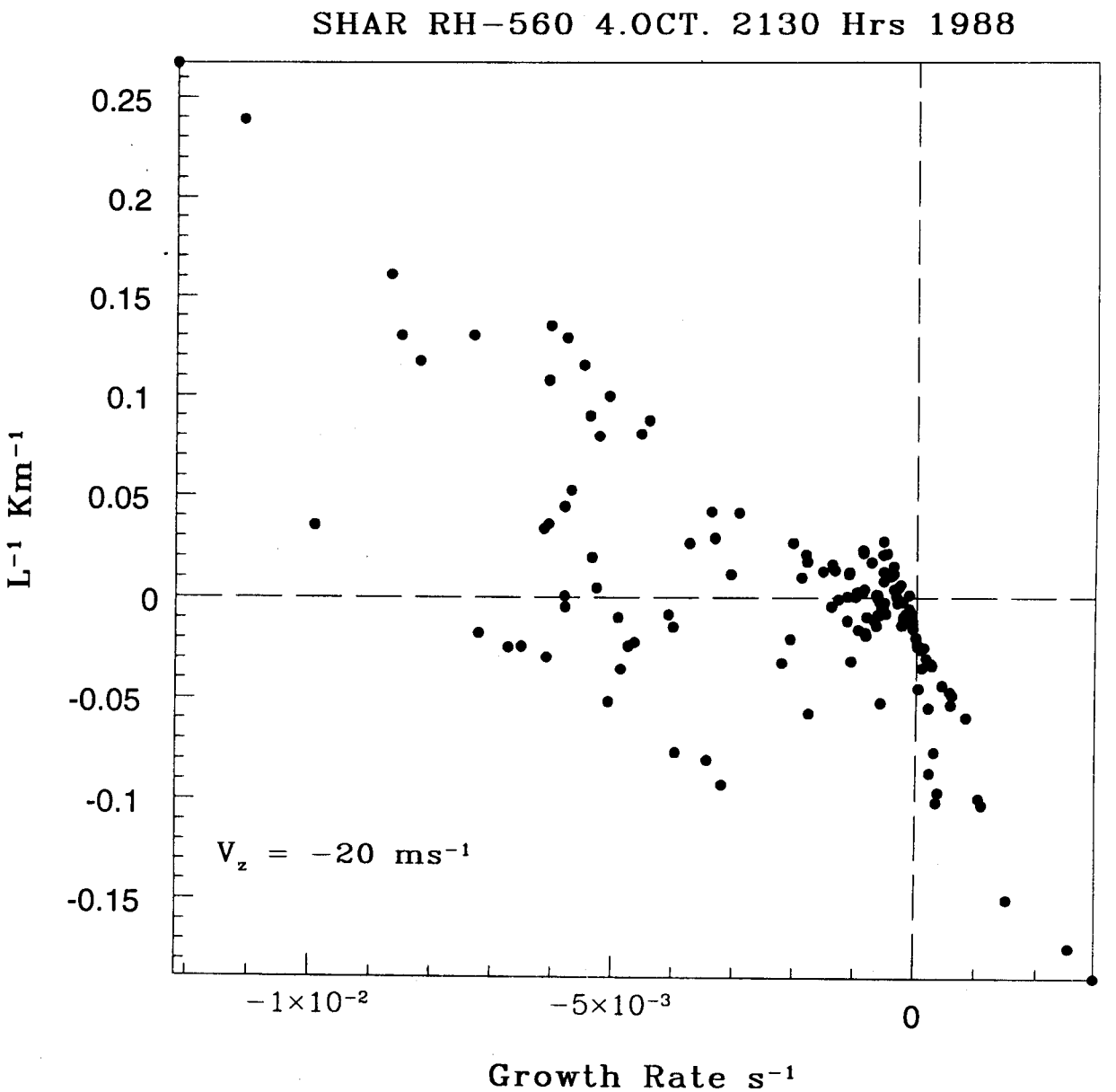

Fig. 4.15 The relationship between linear GRT growth rate and inverse gradient scale length.

plasma turbulence. The frequency and power of the Fourier transform are related to the spatial wave number by $k= 2\pi f/V_{rocket}$ (Costa and Kelley, 1978). Most of the theoretical and experimental studies of the spectrum of spread F irregularities concentrate on certain subranges in wavenumber space for which the power spectral density follows a power law $P(k) \propto k^n$, where P(k) is the power associated with a wavenumber k, and n is the spectral index. The rocket borne probe effectively integrates over one dimension of k, thus giving one dimensional spectrum. The spectral index, n, of the electron density irregularities observed in various altitude ranges was computed using the power law mentioned above.

As discussed earlier, the current collected by the LP sensor was processed in three different channels: (a) Main channel (DC - 60 Hz), (b) MF channel (50 - 500 Hz) and (c) HF channel (25 - 1250 Hz). This was done to study the nature of irregularities occurring in different wavelength regimes. For studying irregularities in the scalesize range of 100 m - 1 km, data from dc channel was used. Data from MF and HF channel was used for studying the smaller scale size fluctuations. The Fast Fourier Transform (FFT) technique was used to compute the power spectrum of these irregularities. Power spectrum was computed for a data length of about 2 seconds using cosine Hanning window. Since the data is in rocket frame of reference, it is necessary to transform it in the earth's frame of reference to interpret the results in term of existing theories. However, this requires the knowledge of the phase velocity of the irregularities as discussed by Fedricks and Coronoti (1976) and Temerin (1979). The spectra discussed here are in the rocket frame of reference due to the lack of information about the phase velocity.

As described earlier that the n_e-h profile displayed irregularities in three different patches. Power spectral analysis of the electron density irregularities occurring in the altitude range of 165 - 175 km showed the presence of fluctuations with vertical scale size varying from 15 m to 1 km. The power spectral index was computed by fitting a straight line to the power spectrum of the irregularities. The power spectra obtained from low altitude region (165 - 175 km) are shown in the Fig. 4.16. It was observed

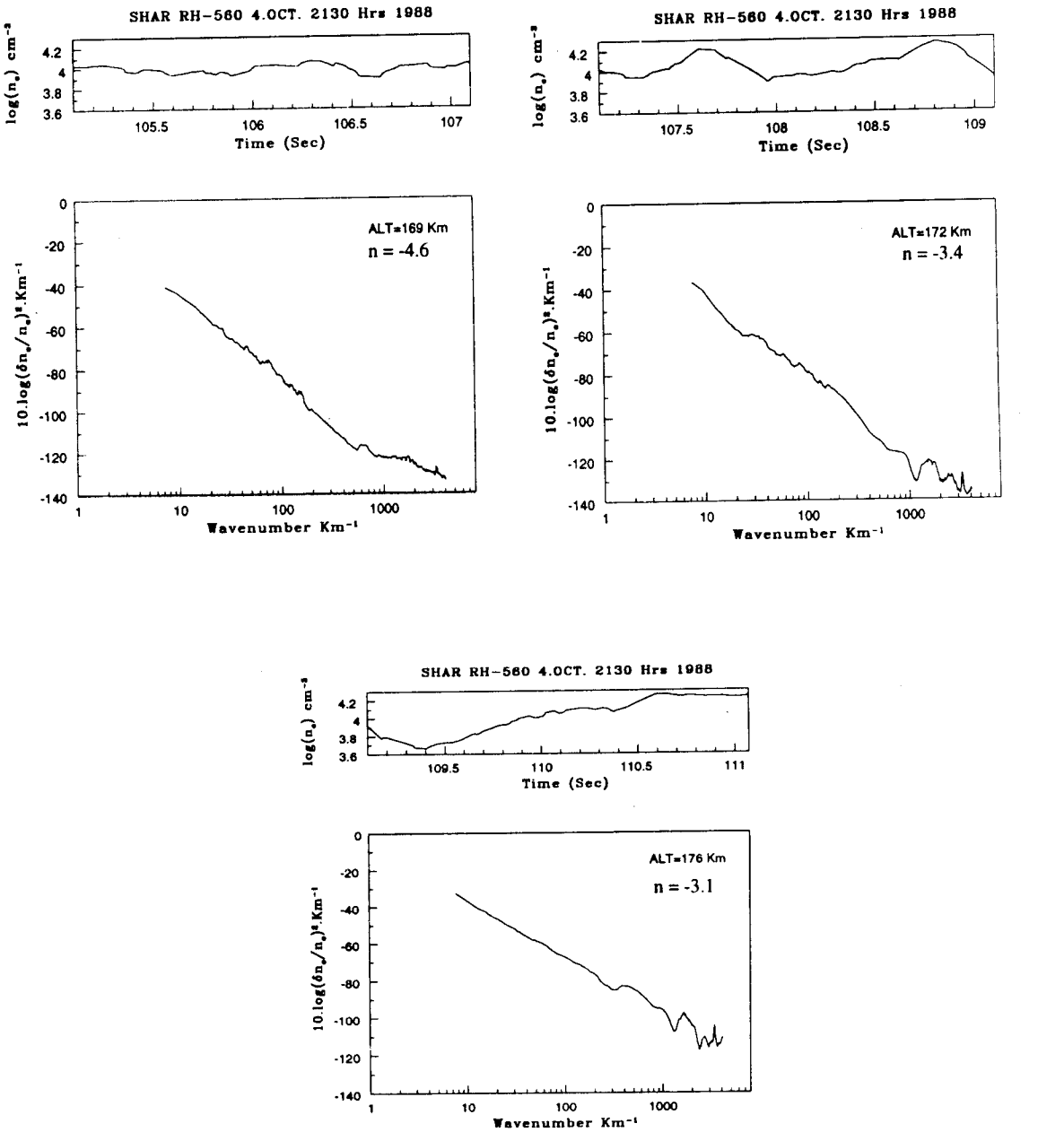

Fig. 4.16 Electron Density variation (log scale) and power spectrum of irregularities at 169, 172 and 176 km altitude regions.

that these irregularities exhibited steep power spectral index which flattened with increasing altitudes. At lower altitudes growth rate of irregularities due to gravitational R-T instability would be small owing to high ion-neutral collision frequencies. Such steep spectra cannot be explained by GDI. As the power spectra of the irregularities in this altitude region has not been reported earlier, this is a interesting feature and it appears that some new mechanism has to be invoked for explaining such steep spectra. Another interesting feature noticed in these spectra is a change in the nature of slope occurring at small scale sizes. Around the altitude of 169 km, a change in spectral behaviour is evident at $\lambda \sim 12$ m ($k = 523.3$ km^{-1}) i.e. for $\lambda < 12$ m spectrum becomes shallower. Around 172 km there is a slight indication of change in the spectral form near $\lambda \sim 10$ m ($k = 628$ km^{-1}). Similarly around 176 km, a shallower spectrum is observed for $\lambda < 6$ m ($k = 1046.6$ km^{-1}) as shown in Fig. 4.16. Thus the noticeable feature observed in the spectra obtained from this altitude region is that the wavelength at which break in the spectrum occurs, shifts to lower wavelength side with increase in altitude.

There is a marked difference in the power law behaviour of the structures observed above 200 km altitude as compared to the lower altitude region. Irregularities in the scale size range of 100 m to 2 km were observed in 210 - 260 km (Fig. 4.17) and 290 - 330 km (Fig. 4.18) altitude regions. The spectral index of these irregularities lies between -1.5 ± 0.5. These values agree with the earlier observations (Rino et al., 1981; Kelley et al., 1982). Irregularities in the transitional scale sizes ($10 \text{ m} \leq \lambda \leq 100$ m) display power spectral index ranging between -2.5 and -4.5. In the altitude region of 210 - 245 km, fluctuations in this wavelength regime exhibit steep spectral index with n values being approximately -4.0 ± 0.5 and a relatively shallower spectrum with n ranging between -2.5 and -3.5 is seen between 240 km and 260 km. It is observed that at lower altitudes, a break in spectrum is observed near $\lambda \approx 30$ m where the spectrum steepens.

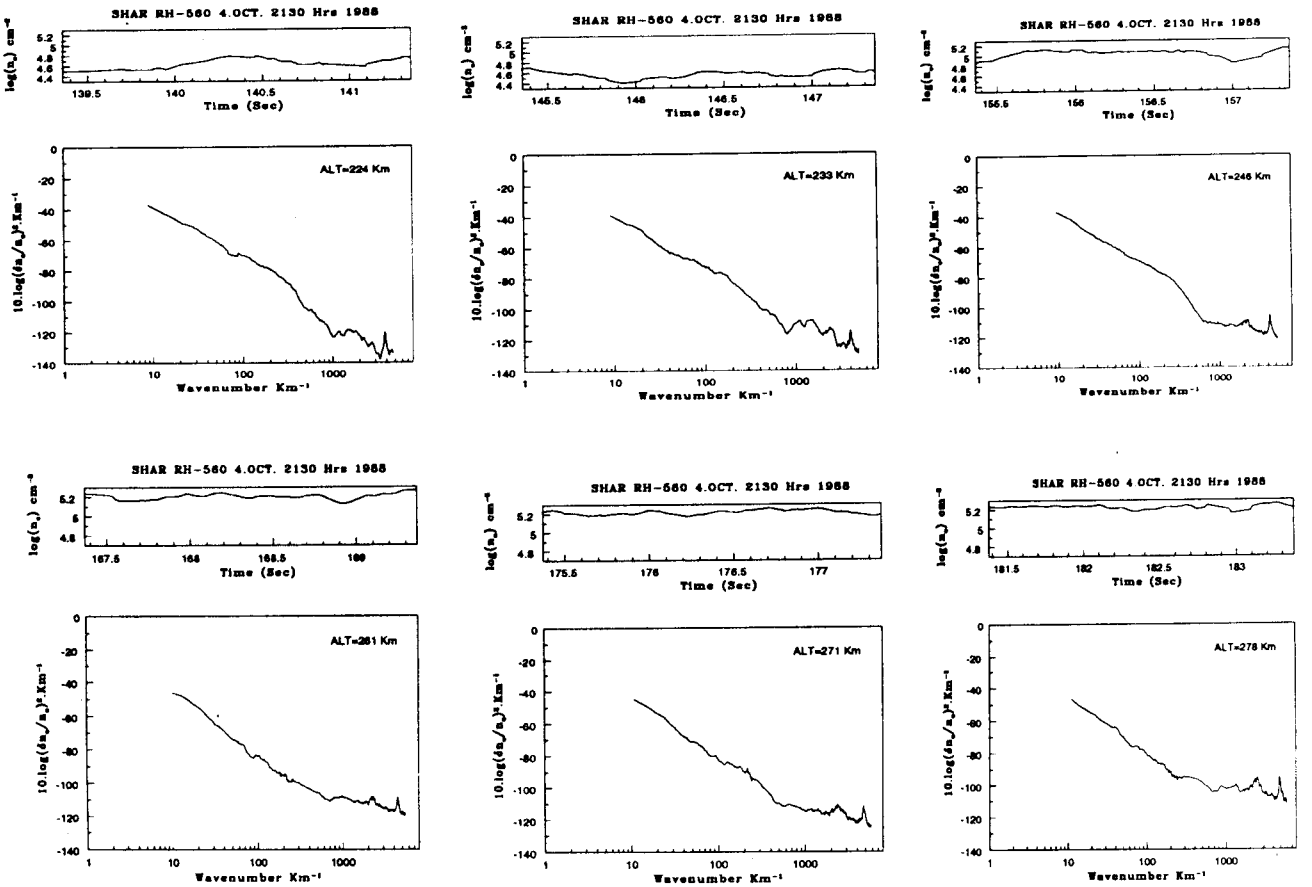

Fig. 4.17 Electron Density Varaition (log scale) and power spectrum of irregularities at 224, 233, 246, 261, 271 and 278 km.

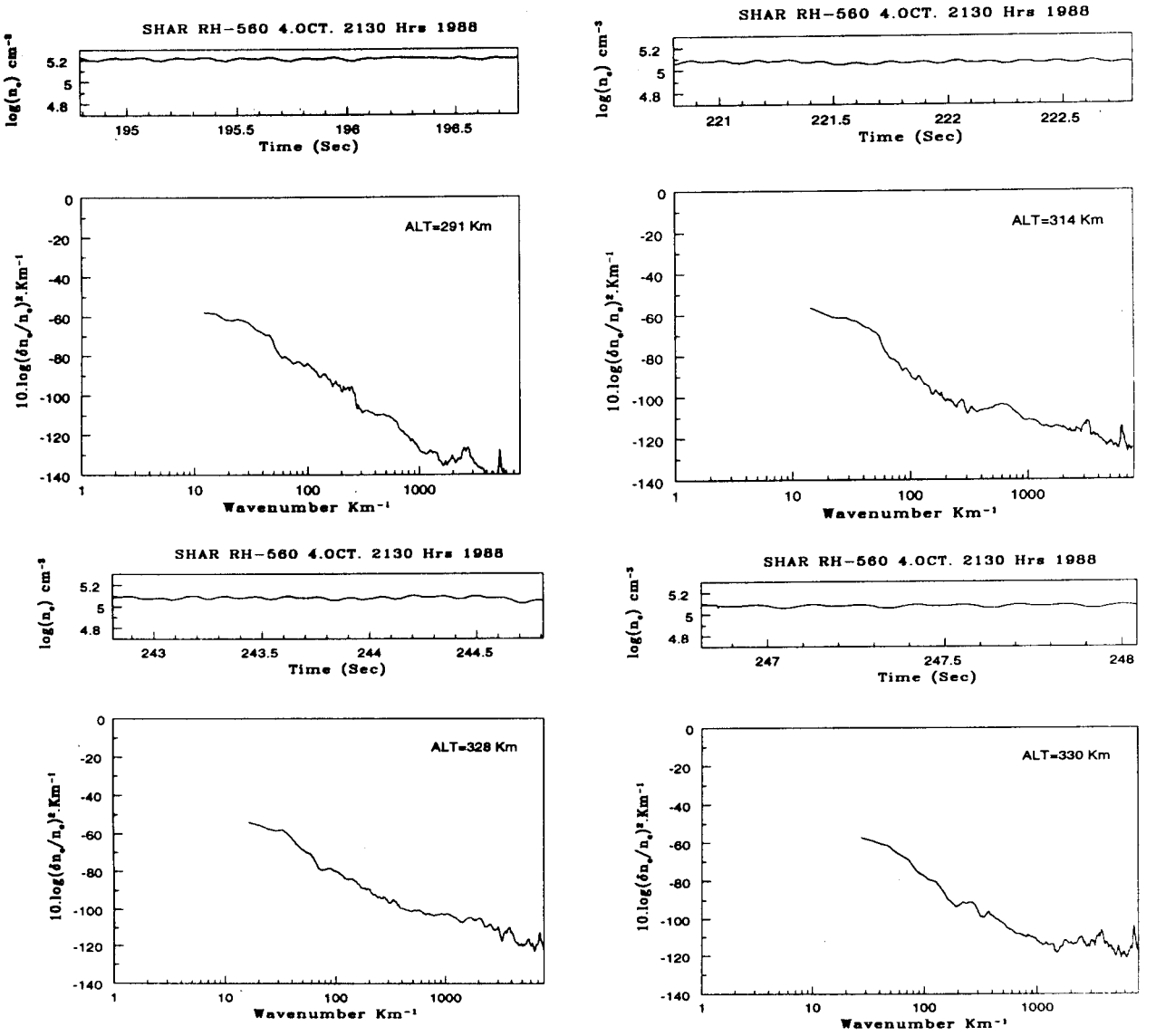

Fig. 4.18 Electron density variation (log scale) and power spectrum of irregularities at 291, 314, 328 and 330 km.

In 290 - 330 km region, the irregularities in the transitional scales display shallower spectrum at 290 km and become steeper upwards where the perturbation levels are high. As seen in Fig. 4.17 and Fig. 4.18, there is no indication of break in the spectrum at higher altitudes within transitional scale. Rino et al. (1981) observed that in the high density, highly structured region (below 370 km), the spectral regime for λ between 10 km - 10 m developed a distinct break near 500 m. For $\lambda > 500$ m shallow power law spectral index was observed. At higher altitudes where less intense fluctuations occurred, a single power law with k^{-2} behaviour characterised the spectral density function over the entire spectral regime. Thus it seems that the evolution of spectra in the transitional scales depends on the turbulence strength. When perturbations are strong, steeper spectra are observed in the transitional scales. For $\lambda < 10$ m, there is an indication of the spectrum becoming shallower both at higher and lower altitudes. PLUMEX data (Kelley et al., 1982) revealed irregularities which satisfied $P \propto k^{-2}$ type of power law for long wavelengths but a break in the spectrum was observed near $\lambda \sim 100$ m with n between -4.5 and -5.0. However, exception to this spectral form occurred at low altitudes (< 280 km) where the spectrum displayed shallow index ($n \sim -2$) scaling down to $\lambda \sim 20$ m. This change in the spectral behaviour was explained in terms of drift waves which are collisionally damped at lower altitudes. However, Prakash et al. (1991) observed spectral indices ranging between 1.6 - 4.7 in the transitional scale regime. Their results did not suggest the existence of altitude dependence of spectral index. Results from CONDOR experiment (LaBelle et al., 1986) showed steep spectra in this wavelength regime at higher altitudes as the data was available from high altitudes only. It is interesting that our results display steep spectra at low altitudes and a break is noticed around 30 m. It appears that turbulence strength affects the shape of the spectrum in the transitional regime. The wavelength at which the transition from shallow to steep spectra occurs at the lower altitudes (210 - 260 km) ranges between 26 - 30 m. It is seen that this wavelength tends to decrease with altitude, the rate of decrease determined from the slope of the best fit is around -9.6 m per kilometres.

4.4 Discussion

Irregularities occurring in the F-region valley are relatively unexplored. Woodman and LaHoz (1976) first identified valley region irregularities below the main plumes in the RTI radar maps obtained from Jicamarca. Vickrey et al. (!984) studied the electron density irregularities occurring in the F region valley which were obtained from fixed bias LP flown on two rockets launched from Natal, Brazil (Kelley et al., 1976, 1979; Costa and Kelley, 1978) and from Kwajalein Atoll (Szuszczewicz et al., 1980; Rino et al., 1981; Kelley et al., 1982). During these two flights quasi-sinusoidal fluctuations in the F_1 layer valley (170 to 200 km) were observed where the local zero order vertical plasma density gradient nearly vanishes. They showed that the spectra in this region displayed peaks at wavelengths of 700 to 1400 m (Fig. 4.19a). They proposed a simple steady state theory to explain the formation of structures in the F_1 layer valley region. They suggested that the valley irregularities were the 'images' of instabilities driven by the GRT instability operating on the bottomside F layer at the equator. This theory predicted a scalesize dependent effective diffusion process in the F region that may dominate over classical cross field diffusion at kilometre scalesizes. However, the fluctuations observed in our data in the valley region display very steep spectra and there is no indication of peaks at smaller wavelengths. The theoretically calculated spectrum, shown in the Fig. 4.19b, for the valley region irregularities as discussed by Vickrey et al. (1984), seems to be quite different from our results. This indicates that the valley region irregularities observed in our data are not the image striations of irregularities occurring elsewhere along the magnetic field line.

As mentioned before, very large scale structure with vertical scalesize of about 39 km is also seen in the valley region which extends down to about 150 km. It is interesting to note that the earlier observations of electron density from SHAR revealed a smooth density profile in this region (Prakash et al., 1991). The presence of such large scale structures in

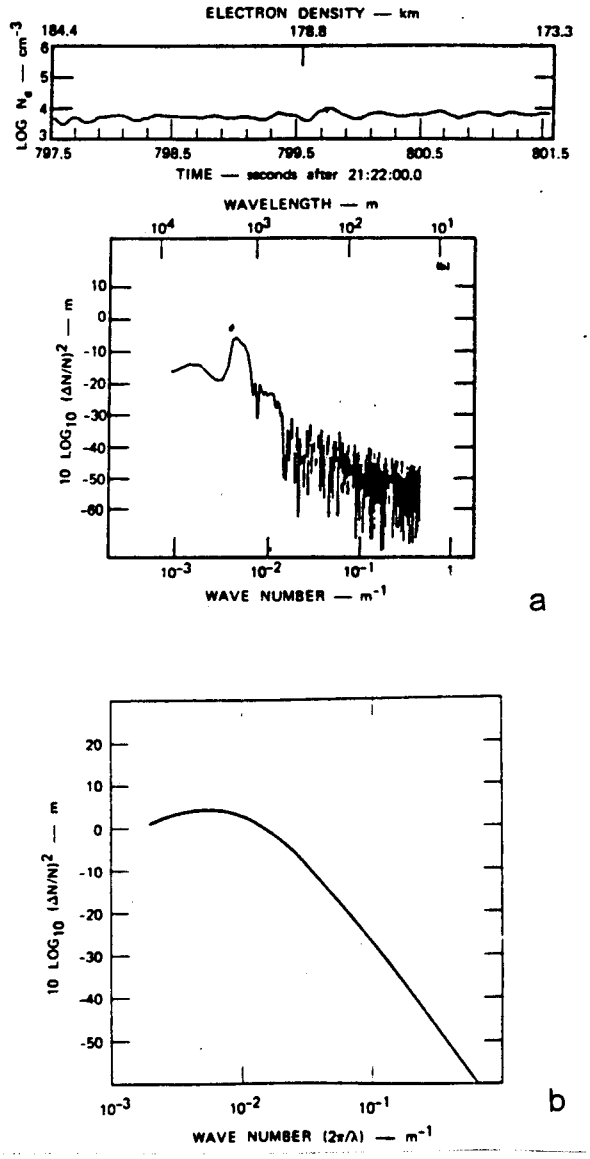

Fig. 4.19 (a) Waveform and spectrum of irregularities observed between 173 and 184 km altitude obtained from the downleg of the rocket launched from Natal, Brazil, on 18 November, 1973; (b) Theoretically calculated steady state spectrum for image formation proposed by Vickrey et al. (1984).

our data suggest that gravity waves might be playing a dominant role in generating irregularities in this region. Horizontal motions obtained from 25 sodium cloud vapour release experiments were examined in the altitude range from 70 - 190 km by Kochanski (1964). The weakest vertical wind shear, in the 70 - 190 km altitude range, were observed in a quiescent region occurring between 140 - 190 km altitude range. This region was characterised by variations with half wavelengths of 20 -25 km in only few cases. This agrees well with the theory of the internal gravity waves (Hines 1960) which permits only long modes in this region. Hydrodynamic considerations allow a wide spectrum of these waves at any altitude above 50 km but certain modes are removed by viscous dissipation, reflection and hydromagnetic viscosity. As a consequence, the dominant modes attain their maximum amplitude in the E region and only a portion of the waves reaches the base of the F layer. At 90 km the empirically found vertical wavelength of the dominant modes is 12 km, horizontal wavelength around 600 km, and time scale of the motion is about 1 - 2 hrs. The theory does not specify dominant modes but sets lowest permissible limits: vertical wavelength over 1 km are allowed at heights near 100 km and over 80 km at the altitude 180 km. Horizontal motions are predominant and vertical motions are estimated to be less than 10% of horizontal components. Prakash (1996) invoked a new mechanism for the production of seed irregularities in the base of the F region large enough to trigger ESF. This results from the transmission of perturbation electric fields to F region altitudes which in turn are generated through E region electron density irregularities. Numerical simulation work by Sekar et al. (1997) has shown that the fringe fields associated with the bubbles can map down to lower altitudes and can produce irregularities at the base of the F region over the magnetic dip equator.

4.5 Summary

A highly structured profile was observed using rocket borne Langmuir Probe during fully developed spread F conditions on 4 October, 1988. Following features were seen during the flight:

1) Irregularities in electron density were observed below the base, at the base and above the base of the F region which was seen to be located around 255 km. Large scale structures with vertical scale sizes varying up to 20 km were present below 150 km region. Earlier rocket flights from SHAR (Prakash et al., 1991) showed number of large scale structures in the region 100 - 150 km with vertical scale sizes as large as 25 km. Fluctuations in the altitude range of 90 - 130 km were also seen in the rocket flights conducted from Thumba. But the increase of density by a factor as large as 50, as observed on the flight conducted on 4 October 1988 reported here, is a new observation. Such large increases have not been observed earlier.

2) One of the most interesting feature of the profile is the occurrence of a patch of irregularity between 165 - 175 km altitude range. Fluctuations with wavelength as large as 10 km are observed in this region. Very large structure with vertical scale size of about 39 km is also seen in this region between 150 km to about 210 km. Earlier flights from SHAR revealed a relatively quiescent region between 150 km up to the base of the F region. The presence of such large scale structures in our data suggest that gravity waves might be playing a dominant role in generating irregularities in this region. This is consistent with the theory of the internal gravity waves (Hines, 1960) which allows only long modes in this region, smaller scales being removed by viscous dissipation, reflection and hydromagnetic viscosity.

3) Electron density irregularities in the scale size range of 15 m to 1 km were quite prominent in altitude range of 165 - 175 km. Power spectral analysis of the perturbations occurring in this altitude region displayed

steep spectral index ranging between -4.6 to -3.1. The growth rate of the irregularities produced through Gravitational Rayleigh-Taylor instability would be negative in this region due to high ion-neutral collision frequencies. Moreover Gradient Drift Instability cannot give rise to such steep spectra. The spectral behaviour of these irregularities cannot be explained by the images striation theory proposed by Vickrey et al. (1984). Thus it appears that some new mechanism has to be invoked for explaining such steep spectra occurring in this altitude region.

4) Electron density irregularities in the intermediate scale size range (0.1 - 10 km) are seen very prominently in the 210 - 250 and 295 - 320 km altitude regions. These structures are likely to be generated through Generalised Rayleigh-Taylor Instability (GRTI). Calculations of effective linear growth rate of GRTI using typical values of observed vertical wind of 20 m/s were made. The relationship between gradients and the effective growth rate (γ_g) was investigated. It was found that γ_g was positive both at the lower and the higher altitudes only when the gradients were negative. It is known that the electric fields are destabilising when the E X B drift is parallel to ∇n. Since the F layer was descending, at the time of flight the ambient electric field must be westward. During this flight, westward electric field seems to be dominating than the gravity and vertically downward wind in producing irregularities both at lower and higher altitudes.

5) Power spectral analysis of the electron density irregularities in the scalesize range of 100 m to 1 km observed in 210 - 255 km altitude range and 290 - 330 km regions displayed spectral index of the order - 1.5 $\pm$ 0.5. Earlier studies have displayed shallow spectral indices (Rino et al., 1981; Kelley et al., 1982). In 210 - 255 km region, the irregularities in the transitional regime (10 m - 100 m) display a break in the spectrum around 30 m. In 290 - 330 km region, the irregularities in the transitional scales display shallow spectrum at 290 km and becomes steeper upwards. It is interesting to note that the region between 210 - 245 km is

characterised by large perturbations level. It seems that the evolution of spectra in the transitional regime depends on the turbulence strength. For $\lambda < 10$ m, there is an indication of the spectrum becoming shallower both at lower and higher altitudes.

CHAPTER 5

IN-SITU ELECTRIC FIELD MEASUREMENTS DURING SPREAD F

5.1 Rocket - Borne Double Probe System

This chapter discusses the first *in-situ* measurements of electric field fluctuations made during the fully developed spread-F conditions from a low latitude station, SHAR (13° 42′ N, 80° 14′ E, dip 14° N), India. These observations were made simultaneously with electron density measurements discussed in the previous chapter. The double probe system flown on RH-560 rocket on October 4, 1988 was essentially similar to that discussed by Pal et al. (1983) and Pal (1985). As mentioned earlier, vertical electric field measurements were made by a pair of cylindrical sensors mounted on a boom extended in front of the rocket along its spin axis. The cylindrical shape of the sensors was chosen for following reasons: (a) It has been discussed in Chapter 2 that the reduction in the ion current improves the sensor performance. For a cylindrical sensor mounted concentrically on a thin boom, the ion current can be reduced by insulating it from the top side as the ion current is mainly collected from the front surface of a moving sensor, (b) the projected area of a sphere, in a direction perpendicular to the spin axis, is less than that of a cylinder of diameter and height equal to the diameter of the sphere. Thus the effective area for the collection of electron current is more for a cylindrical sensor. This increase in the

effective area of the sensor results in a reduced sensor impedance which improves the frequency response of the double probe system. The side sensors, which were deployed perpendicular to the spin axis, for the determination of horizontal electric field, could not be made cylindrical for mechanical reasons.

A constant current of about 90 nA was fed to each of the electric field sensors to reduce the sheath resistance. Significance of low sheath resistance has been discussed in Chapter 2. To reduce the contact potential asymmetry on the sensor surface, a uniform coating of aquadag was applied to each sensor.

Fig. 5.1 shows a simplified block diagram of the electric field double probe system. Band pass filters were used to study the small scalesize irregularities. Data were separated into two channels (a) 0-100 Hz for studying large scale structures and (b) 50 - 500 Hz, for studying medium scale structures. The pass band in the latter frequency range corresponded to irregularities with scalesizes in the range of 30 m to 3 m for a rocket moving with a velocity of about 1.5 kms^{-1}. An extra gain of about 30 was given to the signals during filtering process. Vertical electric field fluctuations were measured by a pair of double probe separated by 1 m along the spin axis and electric field perturbations normal to the spin axis were determined by a pair of double probe separated by 2.4 m. If the wavelength of an electrostatic wave is shorter than the separation distance between the electrodes than the full electric field potential $-\mathbf{E}.\mathbf{d}$ is not measured (Fejer and Kelley, 1980).

5.2 V x B Induced Field

As mentioned earlier, the V x B induced field arises due to the motion of the double probe system across the geomagnetic field B. An estimation of the magnitude of this term has been made along the spin axis of the rocket and also across it during the course of the rocket flight. If φ is the dip angle

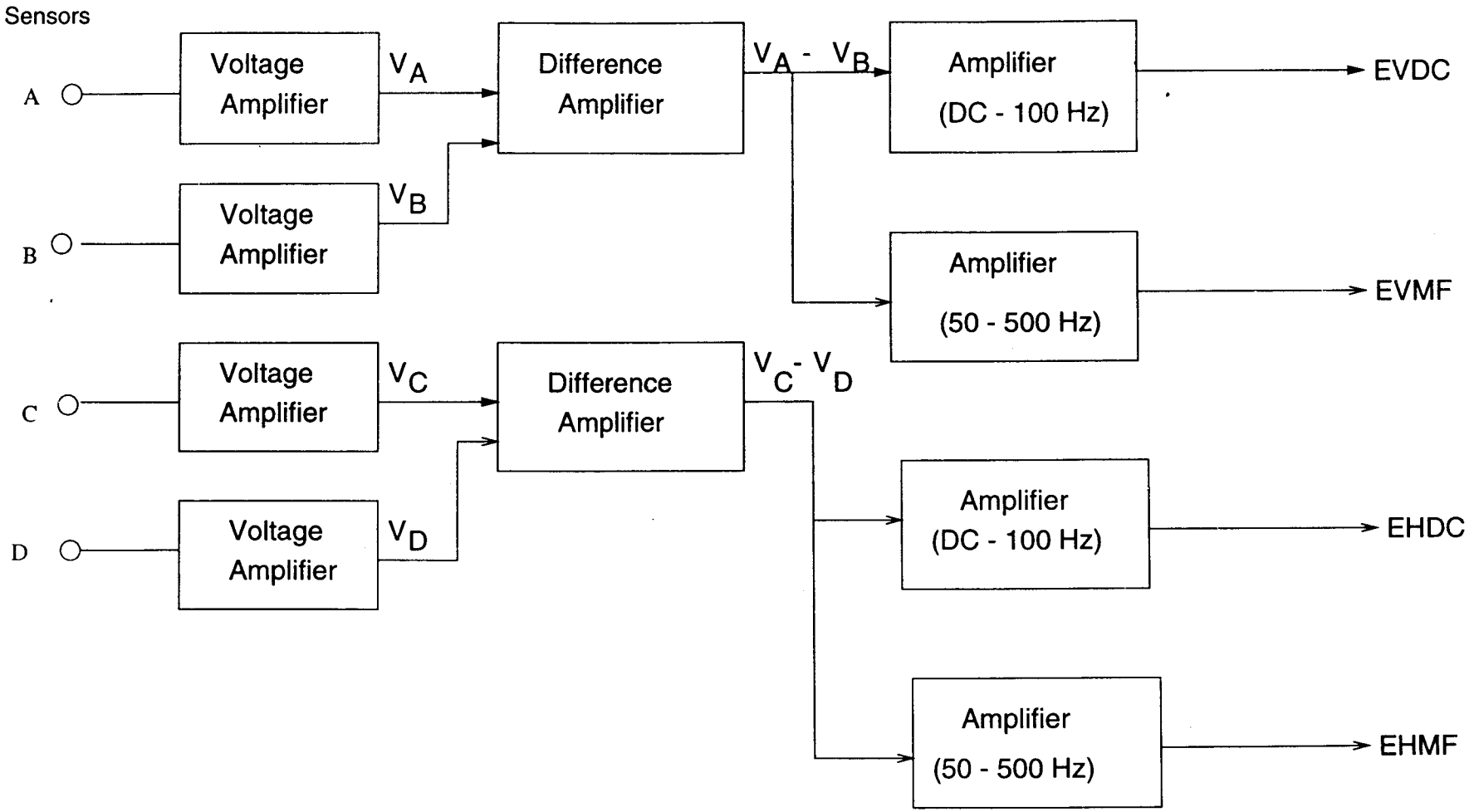

Fig. 5.1 Schematic of Electric Field Probe

of the location of the rocket at any instant and φ' is the angle which the velocity vector makes with the geomagnetic North i.e. azimuth of the rocket, then the induced field along the spin axis and perpendicular to it are given by :

$$\Phi_I = B\sqrt{V_v^2 + V_H^2}\,\sin(\varphi + \varphi')\cos\left[\tan^{-1}\left(\frac{V_v}{V_H}\right) \pm \theta\right] \qquad (5.2)$$

$$\Phi_\perp = B\sqrt{V_v^2 + V_H^2}\,\sin(\varphi + \varphi')\sin\left[\tan^{-1}\left(\frac{V_v}{V_H}\right) \pm \theta\right] \qquad (5.3)$$

where θ is the angle between the rocket spin axis and the vertical, V_v and V_H are the vertical and horizontal components of the rocket velocity respectively, B is the earth's magnetic field as shown in the Fig. 5.2. Here the plus sign is applicable during ascent and the minus sign during descent. Fig. 5.3 and 5.4 show the V x B component induced across and along the spin axis for different values of the rocket orientation angle θ. It can be seen from these figures that (a) as θ increases, the induced field during ascent and descent also increases and (b) the difference between the V x B component during the upleg and the downleg motion of the rocket is more for the component of the induced field across the rocket spin axis as compared to that induced along it.

5.3 On Board Data Handling with SDS

As discussed above, the V x B induced field in the low latitude equatorial F region is ~ 20 - 40 mV/m depending on the velocity of the rocket and the angle between the spin axis and the vertical. This poses serious problem in the determination of the ionospheric electric fields which are typically 1 mV/m. The slowly varying contact potential of the sensor gives rise to slowly changing potential. To eliminate the dc and slowly changing voltage from the potential difference measured by the axial (A - B) and the side (C - D) sensors, a Suitable DC Subtractor (SDS) system was used, so that the ac fluctuations of smaller amplitude embedded in it can be

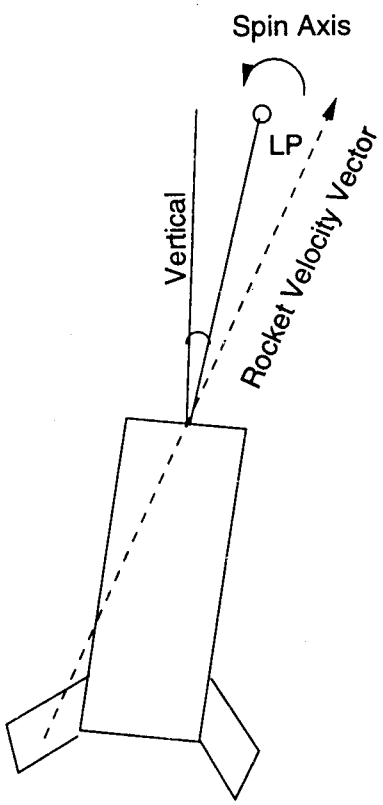

Fig.5.2 Attitude of the rocket during ascent.

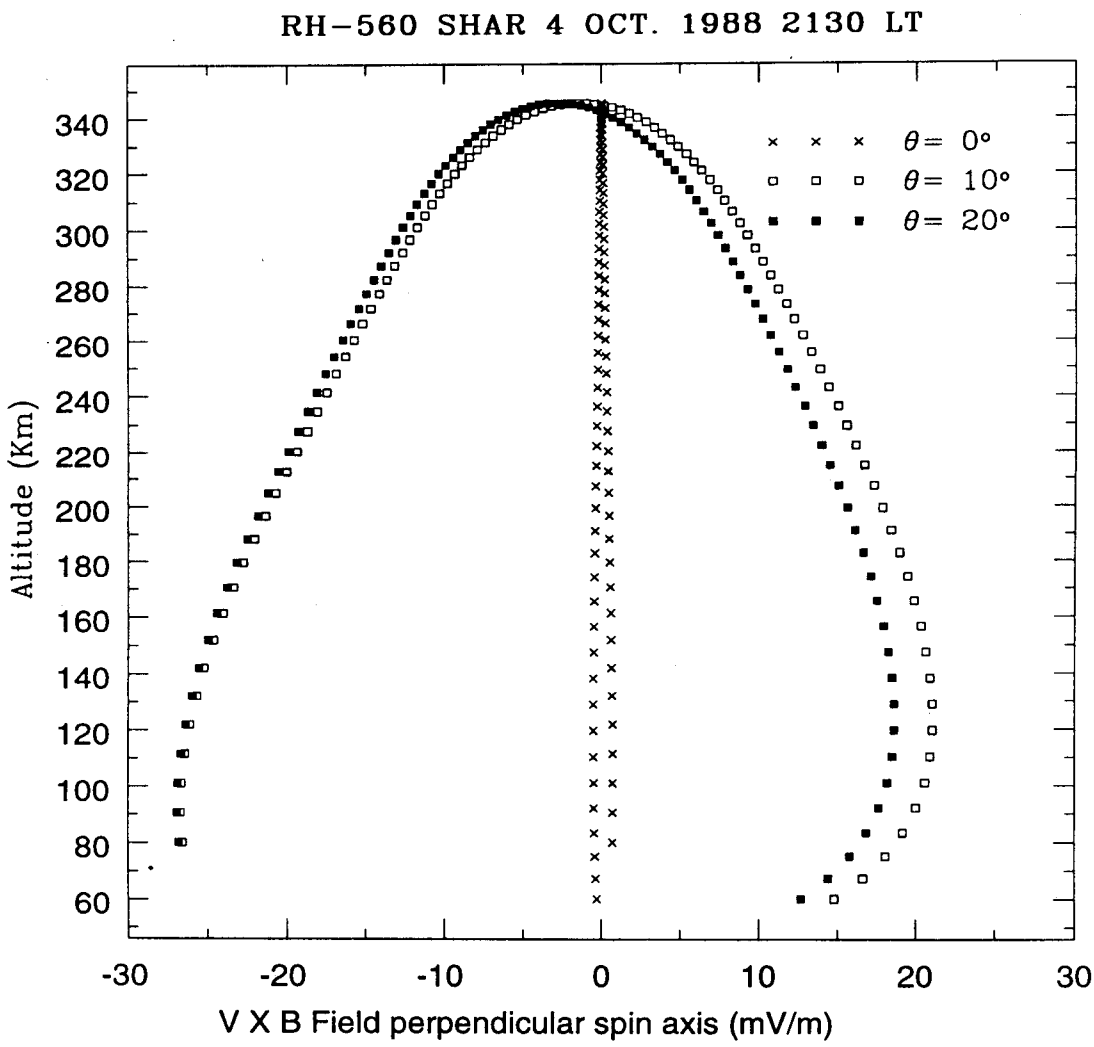

Fig. 5.3 Induced Electric field due to V x B effect across the rocket spin axis for different inclination of spin axis with respect to the vertical.

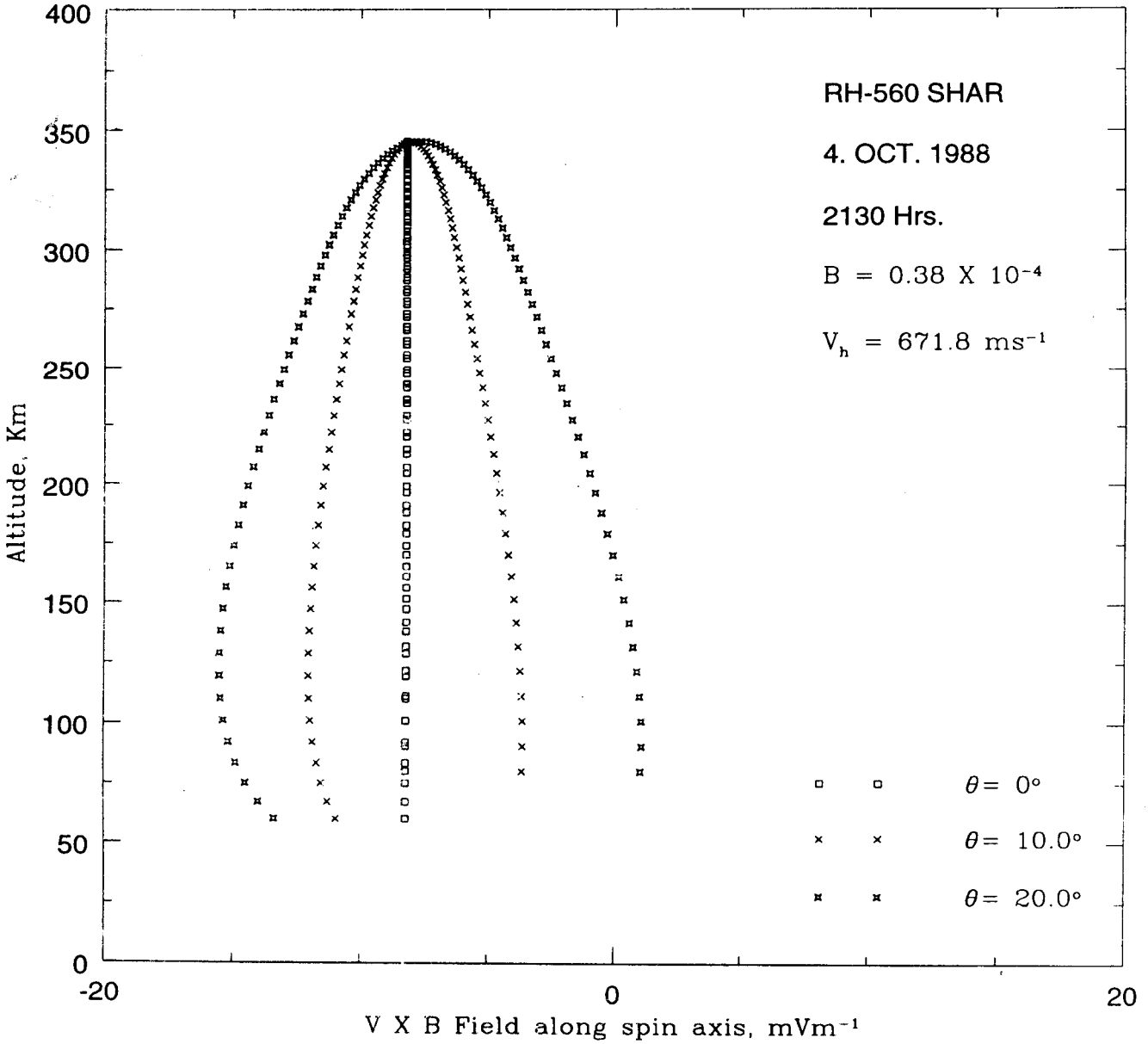

Fig. 5.4 Electric field induced due to V x B effect in the direction parallel to the rocket spin axis for various angles between the spin axis and the vertical.

amplified. To achieve the accuracy required for these measurements, extra gain was necessary. The principle of SDS operation is as follows.

The signal is amplified at the input stage in a preamplifier, with a predecided gain and the output is monitored with a window comparator to detect the upper and lower limits of the signal. During the course of the flight, whenever the change in the dc component of input signal becomes large enough to bring the output signal to one extreme end of the telemetry channel, a digital counter either counts up or down. As a result, a predecided voltage step is either subtracted from or added to the input signal, to bring the output within the limits of the telemetry channel. Information about the voltage step is also telemetered to the ground in the form of dc level.

Determination of Electric Field

The electric field component parallel to the spin axis (E_v') of the rocket was determined by dividing the potential difference between the axial sensors by the separation between them. As discussed above, the primary function of SDS was to enhance the ac fluctuations superimposed on dc field. Since the dc switchings that are introduced by SDS circuit incorporated in the payload were telemetered to ground, a new data series was generated by adding or subtracting appropriate dc shift to the data. The new series gave the actual potential difference measured between the sensors A and B. The resultant was then divided by the separation between the sensors to obtain the electric field component in the vertical direction. Similarly the potential difference between the side sensors was obtained by adding or subtracting the dc output from the SDS data. This can be understood by the block diagram shown in Fig. 5.5. Here X represent the output of the operational amplifier which gives the potential difference between the sensors (A - B) or (C - D) which is amplified by the gain of preamplifier, N. This is passed through the comparator unit and if it does not lie between 0 and 5 volts which represents the two extremes for the signal,

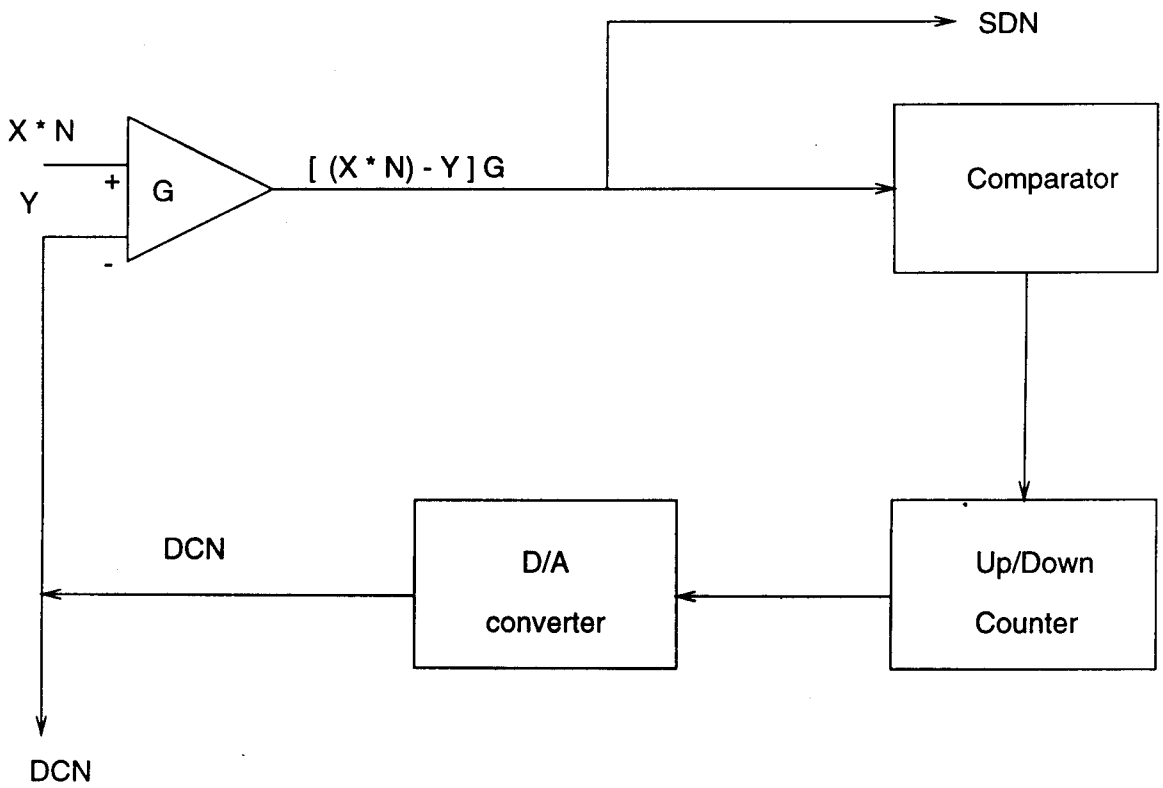

Fig.5.5 Schematic of Suitable DC Subtractor.

the counter is triggered. This is followed by the subtraction or addition of the signal by a step constant (which is ~ 1.2 in this case) resulting in the output Y. The whole process can be written in the form of the equation:

$$G^*(X \times N - Y) = SDN \tag{5.3}$$

where Y = DCN x k, k being a step constant. thus,

$$X \times N = SDN/G + DCN \times K \tag{5.4}$$

$$X = SDN/(G \times N) + DCN \times k/N \tag{5.5}$$

The values of G and N were adjusted by visual inspection of the data to obtain smoothly joined data set. Here G is the gain of the difference amplifier (~ 20 in this case), SDN and DCN represent the two channels telemetered to the ground which were used for retrieval of the potential difference between the sensors.

5.4 Procedure of Analysis of the Electric Field Data

The raw data series obtained by the above methodology exhibited a sinusoidal variation corresponding to the spin rate of the rocket which was approximately 3.5 Hz. This can be seen in the Fig. 5.6. For studying the nature of structures, it was necessary to remove the spin modulation from the data. As mentioned before the inclination of the spin axis of the rocket was approximately 9° from the vertical and was fairly stable in space with a precession angle of about $\pm 10^\circ$. Hence, E_v' measured along the spin axis would be very close to the vertical electric field quite well. The V x B effect was removed by taking the running average of about 10 seconds of data and then subtracting the smoothened signal from the original data. In order to eliminate the spin modulation for viewing large scale structures ($\lambda > 400$ m), a low pass filter (cut off frequency at 3 Hz) was applied. Another alternative method was also used for removal of the spin modulation. In this method a sine wave having same amplitude as the original data and which is π degree out of phase with it was subtracted from the raw data, the effect is shown in Fig. 5.7 (a, b).

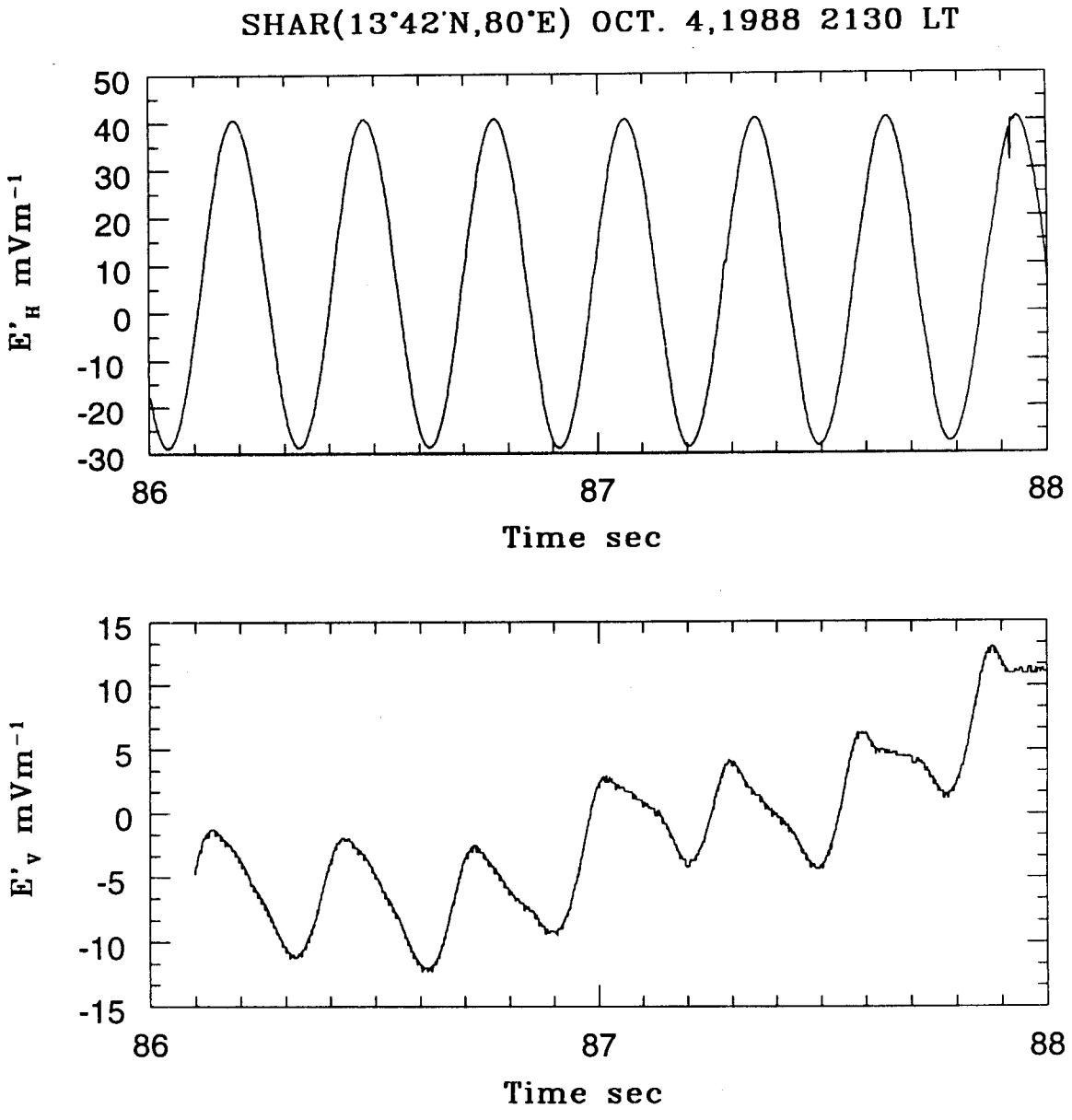

Fig. 5.6 Sample of electric field data showing the effect of spin modulation both across and along the spin axis.

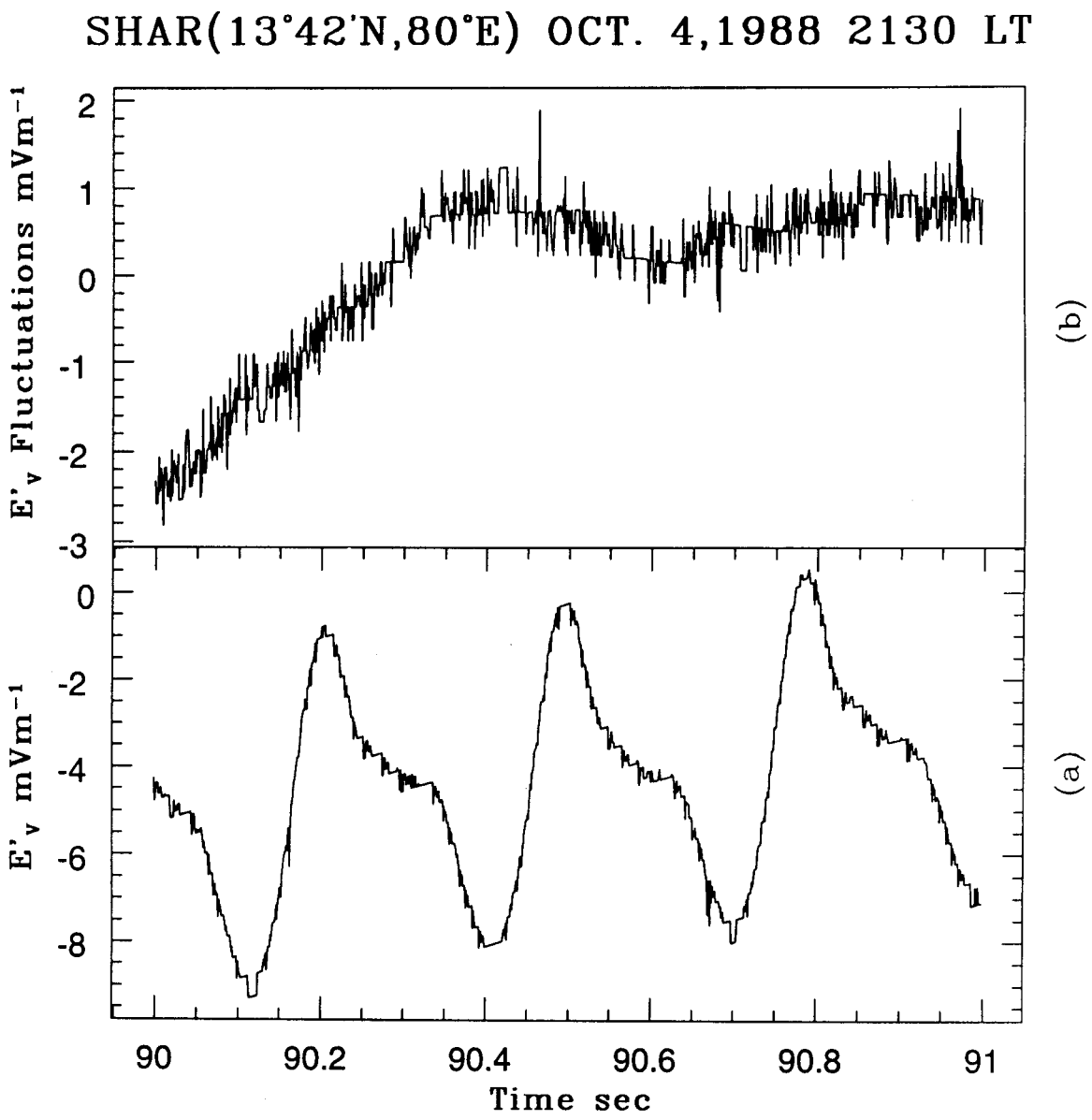

Fig.5.7 (a) Electric field fluctuations superimposed on the sinusoidal wave due to spin effect, (b) Residual data after removing the spin effect by subtracting a sine wave which is 180 degree out of phase with the original series.

E_H' which represents the electric field component perpendicular to the spin axis of the rocket is derived from the potential difference between the sensors C and D. The raw data exhibits the sinusoidal variation corresponding to the spin frequency of the rocket with a dc shift which may be due to the slowly changing contact potential of the side sensors. The dc shift was eliminated by taking average of 2 seconds of data set and subtracting it from the corresponding original data set. To remove the spin modulation effect, procedure used in the case of E_v' of subtracting a sine wave of identical amplitude as the original data series and phase shifted by π degrees was adopted. When the angle between the distance vector, d, representing the separation of the side sensors and geomagnetic field lines becomes less than 30° , then there would be significant disturbance to the sensors due to their interaction with the rocket body and the axial boom via the geomagnetic field lines. Therefore only the values occurring within $\pm 15^\circ$ of the peak were used for analysis. To identify the peaks, following method was adopted. The raw data was smoothened by taking 7 point running average, corresponding to 7 ms of data interval (10.5 m assuming rocket velocity to be $\approx$ 1.5 km/s) and then gradients were calculated over that period. At the peaks, gradients reverse their sign i.e. switch from positive to negative values or vice versa. The time, t, corresponding to the peaks was determined and the E_H' values were obtained by taking the average of $t \pm 0.02$ seconds of data to consider the data within an angle of $\pm 15^\circ$ with respect to the horizontal. This corresponds to the E-W position of the sensor. As during each spin cycle the polarity of the potential difference measured by the sensors is reversed as the position of the side sensor is interchanged, the absolute values of the peak values were used for the determination of E_H'.

5.5 Results

5.5.1 E_v' Measurements

As discussed before, E_v' representing the component of electric field measured along the spin axis is inferred from the potential difference between the sensors A and B. Fig. 5.8 shows the fluctuations in E_v' occurring in various altitude regions. It is observed that around 165 km, structures with half wavelength of about 7 km are present. Smaller scale perturbations superimposed on these large scale structures are also present. Around 175 km, structure with amplitude around 12 mV/m is seen. Structure with amplitude near 5 mV/m and with half wavelength approximately 5 km is observed around 183 km. The amplitude of irregularities observed between 210 - 260 km altitude region is smaller than those seen at the lower altitudes. The maximum amplitude of irregularities in this region is around 4 mV/m. Around 230 km altitude region, structure with half wavelength of about 5 km and amplitude around 4 mV/m is seen. Between 236 km to 239 km, structures with scalesizes varying between 0.5 - 1.5 km and with amplitudes as large as 3.5 mV/m are seen. Around 245 km, perturbations with scalesize around 2.8 km and amplitude around 1.9 mV/m are observed. Fluctuations with scalesize around 2.8 km and amplitude nearly 2.5 mV/m are seen around 247 km. Between 260 - 280 km altitude region, small scale irregularities with amplitude around 1 mV/m are evident. A relatively smooth region is observed between 280 - 290 km. A patch of irregularity in E_V' is seen between 292 - 330 km altitude region. Perturbations with scalesize around 1.4 km are seen between 292 and 295 km with amplitude as large as 2.8 mV/m.

5.5.2 E_H' Measurements

Fig. 5.9 shows the raw data as well as the moving average calculated for different data lengths as discussed in the figure caption, for viewing various scales occurring in E_H' profile with altitude. As the spin rate is

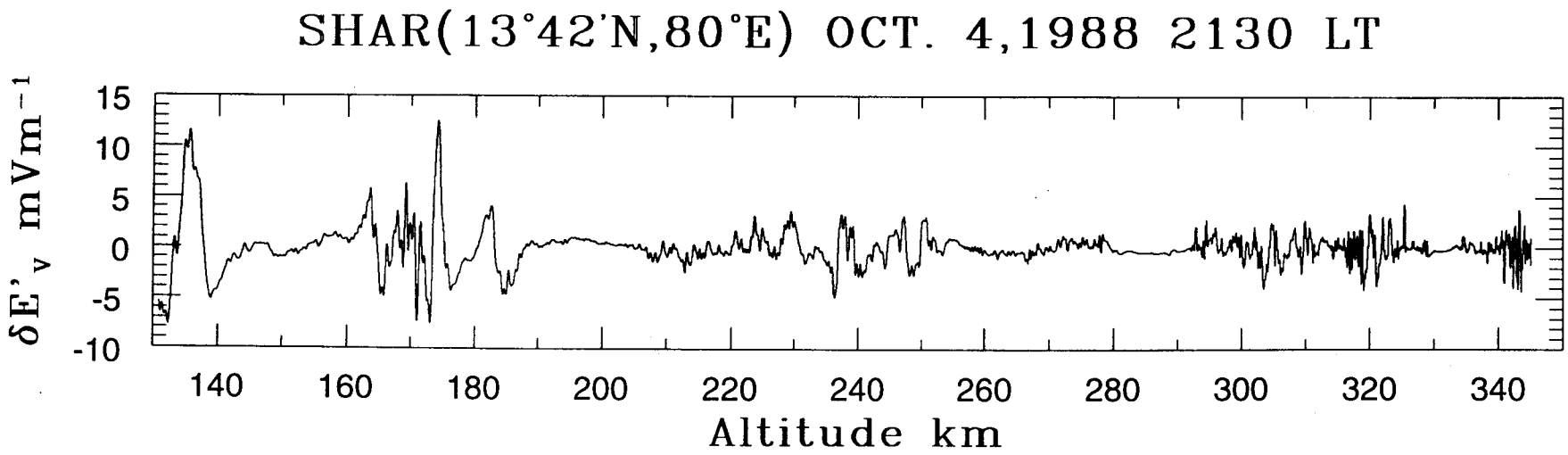

Fig. 5.8 Electric field fluctuations in the vertical direction.

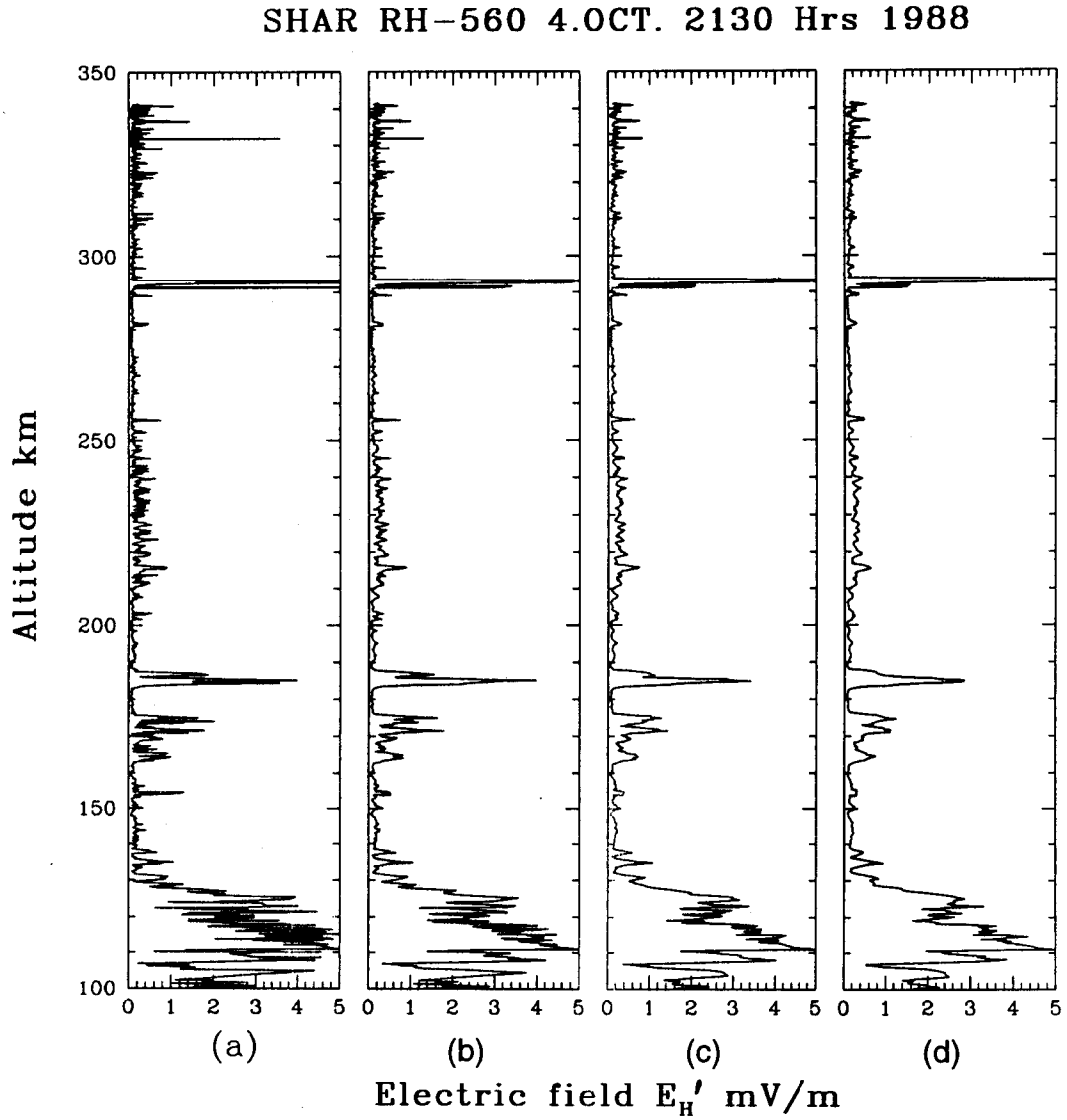

Fig.5.9 Variation of horizontal electric field with altitude (a) raw data, (b), (c) and (d) represent the moving average taken for 3, 5, and 7 points for viweing structures with scalesizes > 750 m, 1250 m and 1750 m respectively.

around 3.5 Hz, and since the values around the peak have been considered, the variation of the horizontal electric field E_H' with altitude is available every 215 km. Hence the vertical structure of E_H' with $\lambda > 215$ m can be studied. It is observed that between 100 - 130 km large perturbations with values as high as 5 mV/m are present. Between 160 - 170 km, a patch of irregularity is seen with values of E_H' lying between 0.7 - 2 mV/m. High values of E_H' ranging between 2 - 4 mV/m are seen between 184 - 188 km altitude region. It is to be noted that in this altitude region, E_V' exhibits a drop from 4 mV/m to -5 mV/m. At around 165 km, irregularities with scalesize around 2.7 km and amplitude around 0.7 mV/m are seen. E_H' fluctuations with half wavelength nearly equal to 5.5 km and amplitude around 1.4 mV/m are seen at about 172 km. Around 185 km, perturbation in E_H' values with amplitudes as high as 4 mV/m and scalesize around 3.6 km are observed. Weak fluctuations in E_H' are evident between 210 - 255 km altitude region, where the maximum value observed is around 0.9 mV/m. Around 215 km, fluctuations in E_H' having scalesize around 1.8 km and amplitude nearly equal to 0.7 mV/m are observed. At high altitudes i.e. around 292 km, the amplitude of E_H' fluctuations goes upto 7.7 mV/m and are characterised by scalesize approximately 1 km. Around 332 km, fluctuations in E_H' of around 4 mV/m are present. Between 295 - 332 km, weak irregularities with values less than 0.6 mV/m are seen.

It is known that the zonal electric field gives rise to the vertical electrodynamic drift given by the expression

$$V_z = E \times B/B^2 \qquad (5.6)$$

where E is the zonal field, B is the earth's magnetic field. As the spin axis of the rocket is inclined by about 8.8° with respect to vertical and the dip angle at SHAR is around 14° N, the vertical electrodynamic drift is given by $V = E \cos(8.8^\circ)/B\cos(14^\circ)$. Here E is the electric field measured across the rocket spin axis.

The vertical electrodynamic drift obtained by using the above expression is shown in Fig. 5.10. Since the ac field is measured, the drift is indicative of motion of the irregularities. As mentioned in the previous chapter, at the time of the rocket launch i.e. around 2130 hrs LT, the ionograms recorded at SHAR showed that the F layer was drifting downward indicating that the ambient field was westward. Between 100 - 130 km altitude region, V_z as high as 130 m/s is observed. Around 185 km, $V_z \approx 100$ m/s is seen and high values of $V_z \approx 250$ m/s are observed around 292 km. Between 165 to 175 km altitude region, V_z as high as 50 m/s are seen and in the 210 - 260 km altitude extent V_z lies between 2 - 20 m/s. The maximum velocity observed between 260 - 280 km region is around 7 m/s. The base of the F layer located around 255 km is seen to drift downward with $V_z \approx 19$ m/s. This matches closely with the velocity calculated using rate of change of h'F inferred from ionograms which is ≈ 20 m/s.

Miller et al. (1986) deduced the thermospheric meridional wind from ionospheric h_mF_2 data. Later on, Krishna Murthy et al. (1990) derived the meridional winds near the magnetic equator directly from h'F data at two equatorial stations situated nearly on the same magnetic meridian. The vertical drift V can be written as

$$V = V_z \cos I - U \cos I \sin I - W_D \sin^2 I \qquad (5.7)$$

where U is the meridional neutral wind in the northward direction, W_D is the plasma drift due to diffusion, V_D represents vertical E X B drift. Rishbeth et al. (1978) showed that a southward (northward) neutral wind pushes the ionisation up (down) along the field lines. Vertical drift obtained from the ionograms i.e. using $\Delta h'F/\Delta t$, is the sum of true vertical drift and the apparent vertical drift due to the chemical loss given by βH (Subbarao and Krishna Murthy, 1983), where β is the attachment coefficient and H is the ionisation scale height. Thus,

$$V = V_{ion} - \beta L \qquad (5.8)$$

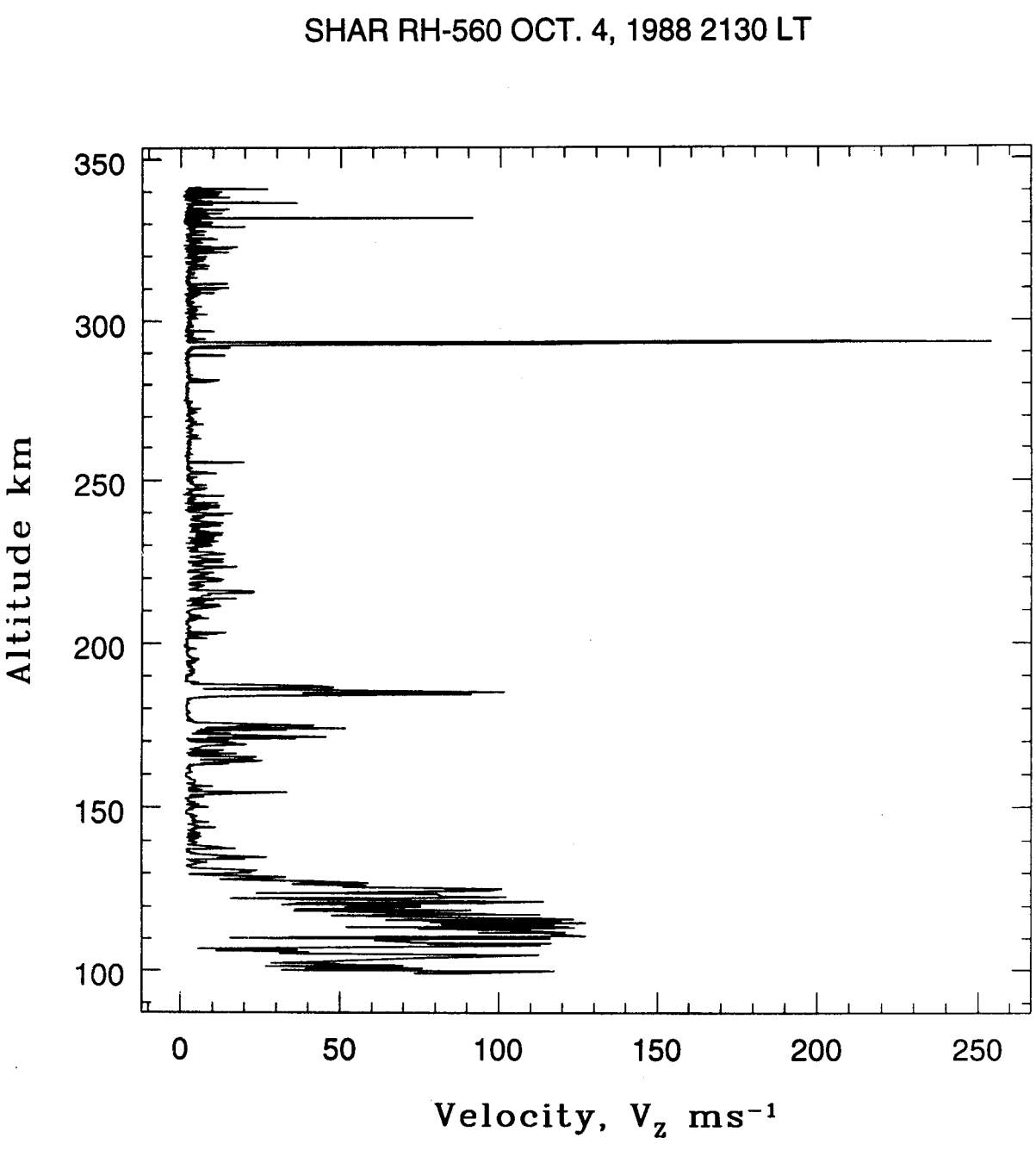

Fig.5.10 Variation of vertical velocity with altitude calculated from the horizontal electric field data.

where β has been taken from Anderson and Rusch (1980), V_{ion} is the velocity inferred from ionograms using h'F data which is around 20 m/s downwards, L is the gradient scale length, $W_D = g/\nu_{in}$ (Rishbeth et al., 1978), where neutral parameters for determining ν_{in} have been calculated using MSIS-86 model. At the base of the F layer located around 255 km, L is approximately 3.3 X 10^2 m. Thus, the neutral meridional wind at the base of the F layer can be evaluated using the expression:

$$U = V_Z/\sin I - V/\cos I \sin I - W_D \tan I \qquad (5.9)$$

Substituting the values of V_Z, V, and W_D, observed at the base of the F layer, the meridional wind at the base of the F layer is estimated to be 78 m/s in the northward direction.

5.5.3 Correlation Study between Electron Density and Electric Field Irregularities

As mentioned in Chapter 4, electron density irregularities were observed in three different patches occurring between 165 - 175 km, 210 - 255 km and 290 - 330 km altitude regions. It is observed that the fluctuations in E_V' and E_H' are colocated with the electron density irregularities as seen in Fig. 5.11. One of the remarkable features during this flight is the simultaneous occurrence of irregularities below the base of the F-region, at the base, and as well as above the base. This provided a unique opportunity for studying the nature of electron density and electric field irregularities at different altitude region simultaneously. This was done by performing the correlation studies between n_e and E_V' and n_e and E_H' for every 10 km of data sets. This study showed that the large scale irregularities in n_e and E_V' seen below the base of the F region i.e. around 160 - 175 km, exhibit strong anti-correlation. However fluctuations in n_e and E_H' display poor anti-correlation. Around 165 km, the correlation coefficient between δn_e and $\delta E_V'$ is around -0.76 while that between δn_e and $\delta E_H'$ is about -0.2. Similarly, around 175 km, fluctuations in δn_e and $\delta E_V'$ display

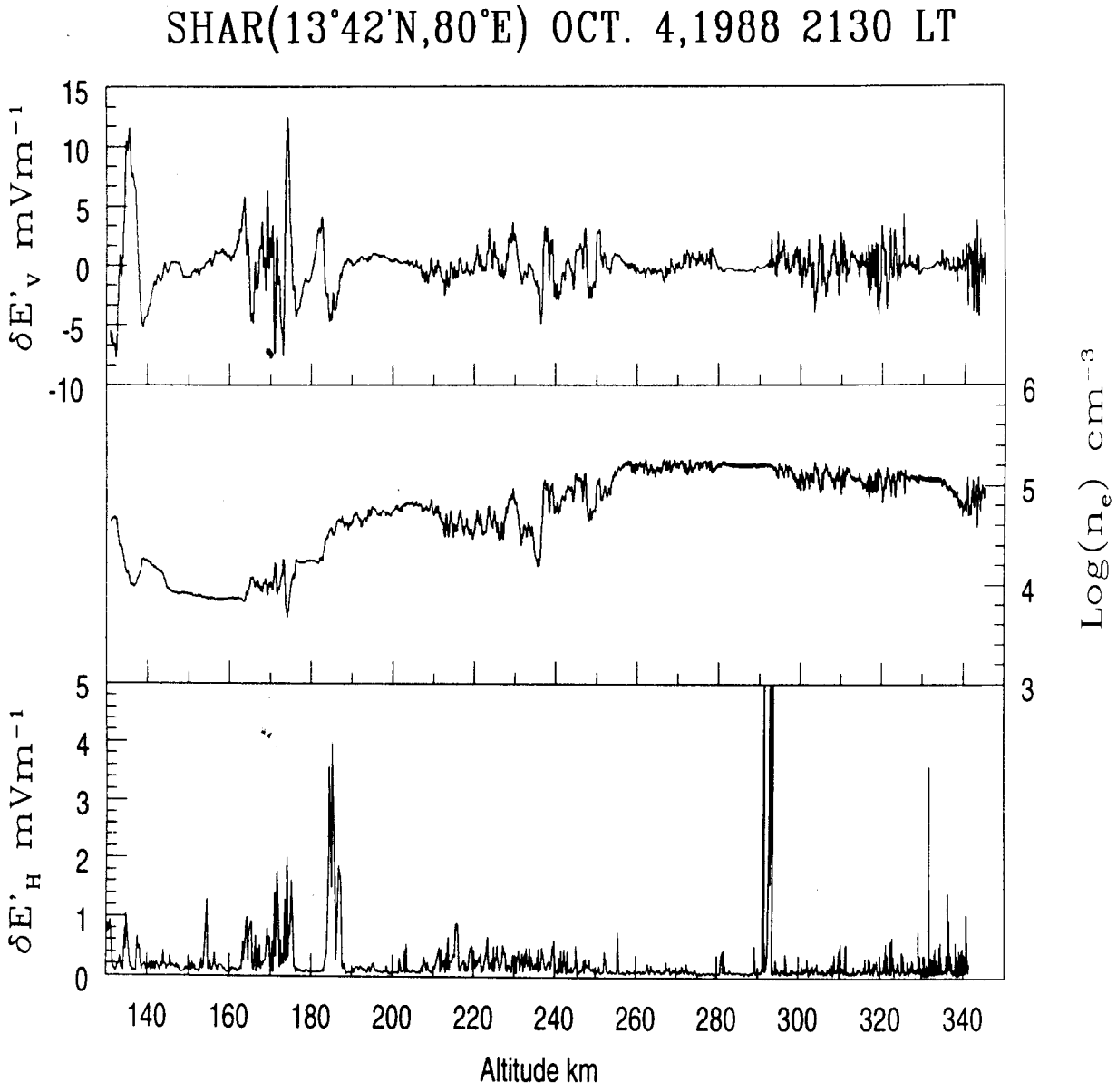

Fig.5.11 Horizontal electric field, electron density and vertical electric field perturbations during the ascent of the rocket showing the simultaneous occurrence of irregularities.

correlation coefficient equal to -0.83 and that between δn_e and $\delta E_H'$ is nearly -0.54 as shown in Fig. 5.12.

A very interesting feature is observed in 210 - 255 km altitude range. The relationship between electric field and electron density irregularities observed in this region show a different trend. In this region electron density fluctuations are strongly correlated with $\delta E_V'$ while with $\delta E_H'$ they display poor correlation. Very strong correlation is seen between δn_e and $\delta E_V'$ around 245 km with correlation coefficient $\approx$ 0.9. An example can be seen in Fig. 5.13. This trend of correlation changes to anti-correlation at higher altitudes i.e. for irregularities occurring above the base of the F layer. Around 305 km, a high correlation coefficient with value $\approx$ 0.92 is observed for δn_e and $\delta E_V'$. But the fluctuation in E_H' display poor anti-correlation. The variation of correlation coefficient between the electric field and electron density calculated for every 10 km of data sets along with the percentage amplitude of irregularities in the intermediate scales is shown in Fig. 5.14. Hysell et al. (1994) observed irregularities in n_e and electric field simultaneously and found that $\delta E_H' \propto -\delta n$ on large scales. They also observed that the large scale features in vertical electric field are also anti-correlated with δn although not so clearly as observed in the E_H'. This observation is in contrast to our measurements. The observation of strong correlation seen around the base of the F layer, where the large amplitude irregularities occur, is very interesting. Charge neutrality condition imposes the restriction that the current in the F region be divergence free. As the F region currents lie principally in the x direction, J_x must be nearly continuos. When the density and Pederson conductivity are non-uniform, polarisation charges accumulate at horizontal density gradients giving rise to horizontal electric field in such a way that $\nabla.J = 0$. Thus $E_H' \propto -\delta n$. Hysell et al.(1994) attributed the anti-correlation between δE_V and δn to the eastward neutral wind which drives the current in the vertical direction and produces vertical polarisation field which might be responsible for the production of plasma irregularities (Tsunoda et al., 1982).

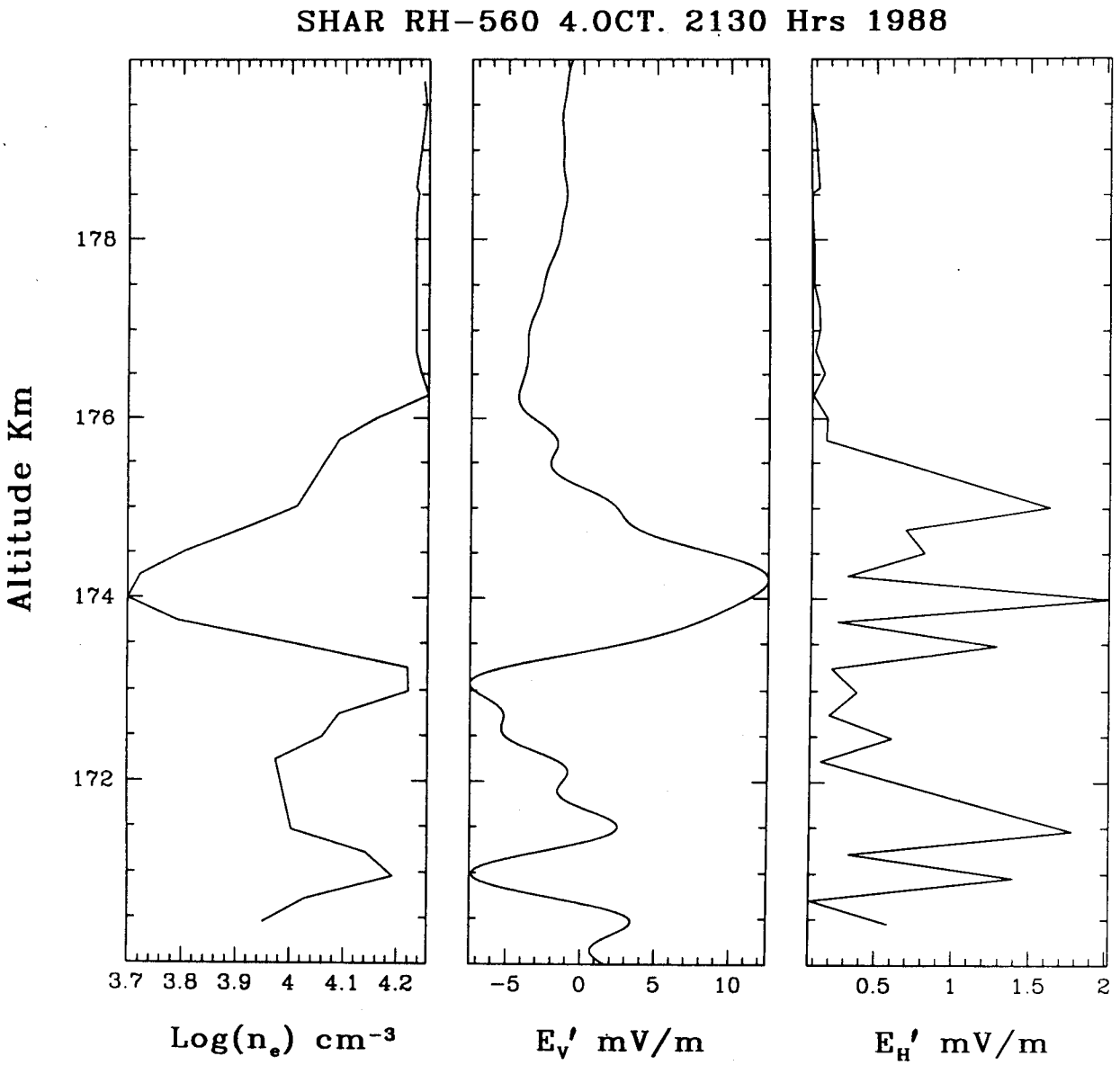

Fig.5.12 Electron density and electric field fluctuations in 170-180 km altitude region displaying anti-correlation between them.

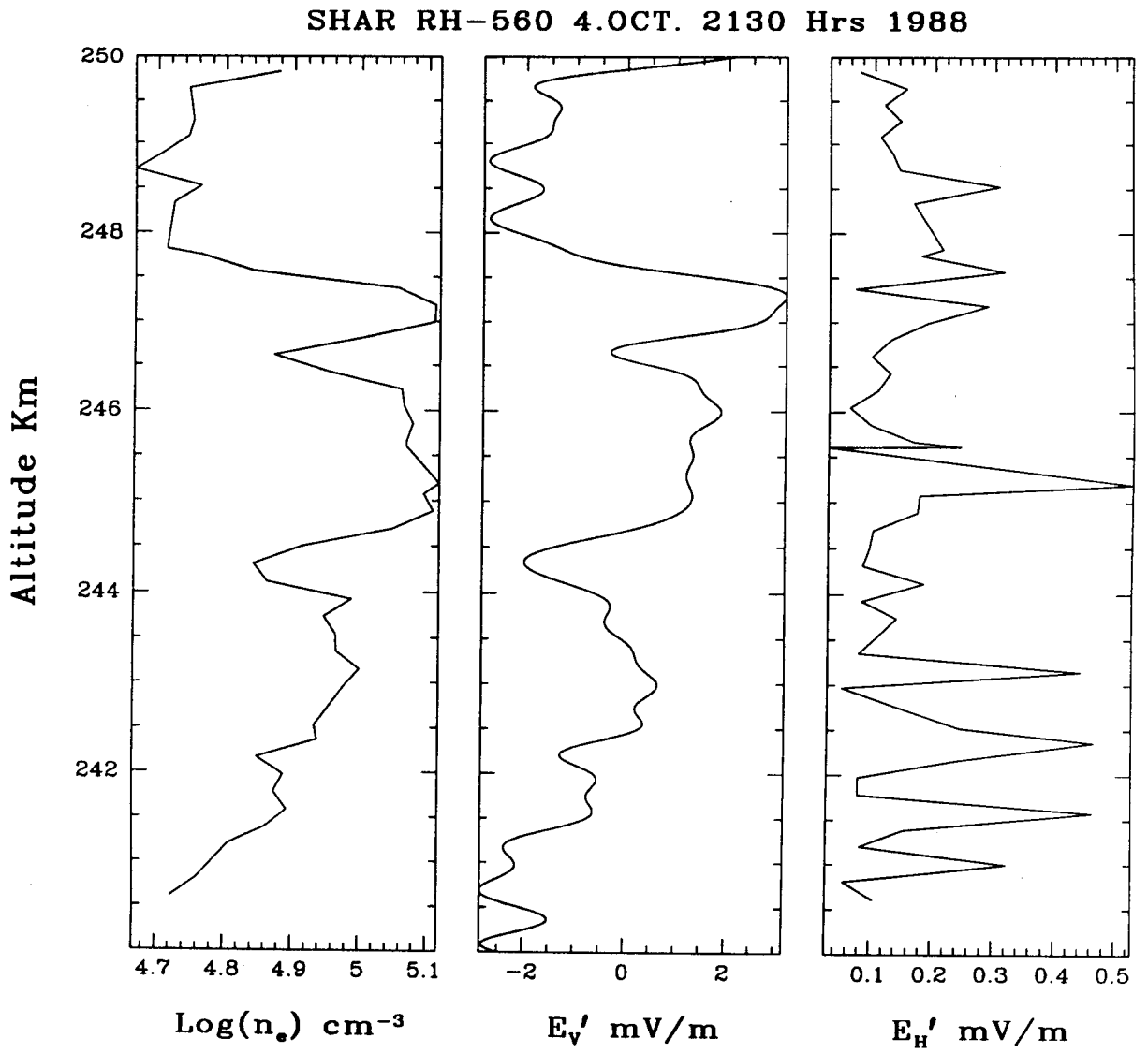

Fig.5.13 Figure showing the correlation between electric field and electron density fluctuations.

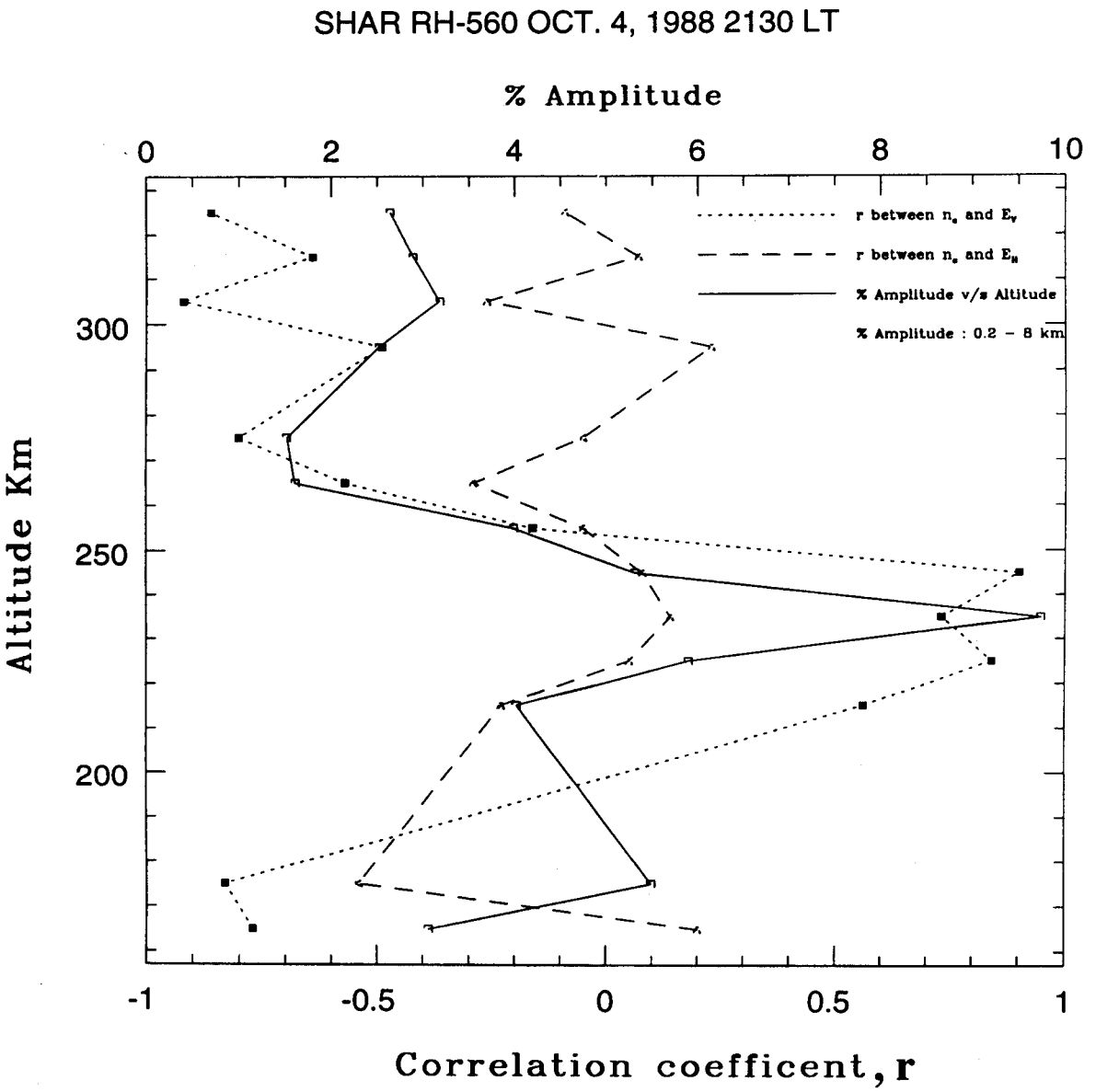

Fig.5.14 Variation of (a) correlation coefficient, r, with altitude between electric field and electron density computed every 10 km and (b) the % amplitude of electron density fluctuations in 0.2 - 8 km scalesize range with altitude.

The E_V measurement seems to contain strong high frequency components which are evident in the form of intense spikes. At the altitudes where weak irregularities occur, smaller spikes are observed. It is seen that the magnitude of the spikes is large in the region where strong irregularities are observed i.e. around the base of the F layer (210 - 255 km). Strong spikes with magnitudes exceeding 5 mV/m are observed between 220 - 230 km as seen in the Fig. 5.15 and Fig. 5.16. However E_H' does not exhibit intense spikes as observed in the vertical direction.

At some altitudes saw-tooth structures are evident both in E_H' and n_e. However E_V' profile does not exhibit such structures. It is seen that saw-tooth structures are observed only when the amplitude of electron density structures is weak except on few occasions when saw-tooth structures are seen only in E_H' and not in n_e. The shape of saw-tooth structures is different in n_e and E_H' profile e.g. if the increase in n_e is much faster than the decrease, the converse is true for E_H'. The nature of the shapes of the saw-tooth structures is different in the lower ($\approx$ 165 km) and upper altitudes (290 - 330 km). At lower altitudes (~ 164 km) the increase in n_e is much faster than its decrease whereas for E_H' decrease is much faster than its increase. Around 163 km, E_H' decreases by a factor of nearly 2 to 7 as seen in Fig. 5.17. There appears to be a threshold for E_H' for generation of these saw-tooth structures. In the lower altitude regions these are seen if E_H' is greater than 0.6 mV/m where as in the upper region (290 - 300 km) the threshold appears to be about 8 mV/m as seen in Fig. 5.18. Hysell at al (1994) reported saw-tooth structures in electron density depletions where right side was more steep and concluded that there is a preferential direction for plasma steepening. However, the nature of saw-tooth structures in our data suggests that the plasma steepening can occur in any direction and the plasma steepening does not necessarily operate so as to increase $\partial n/\partial z$, where z is upwards.

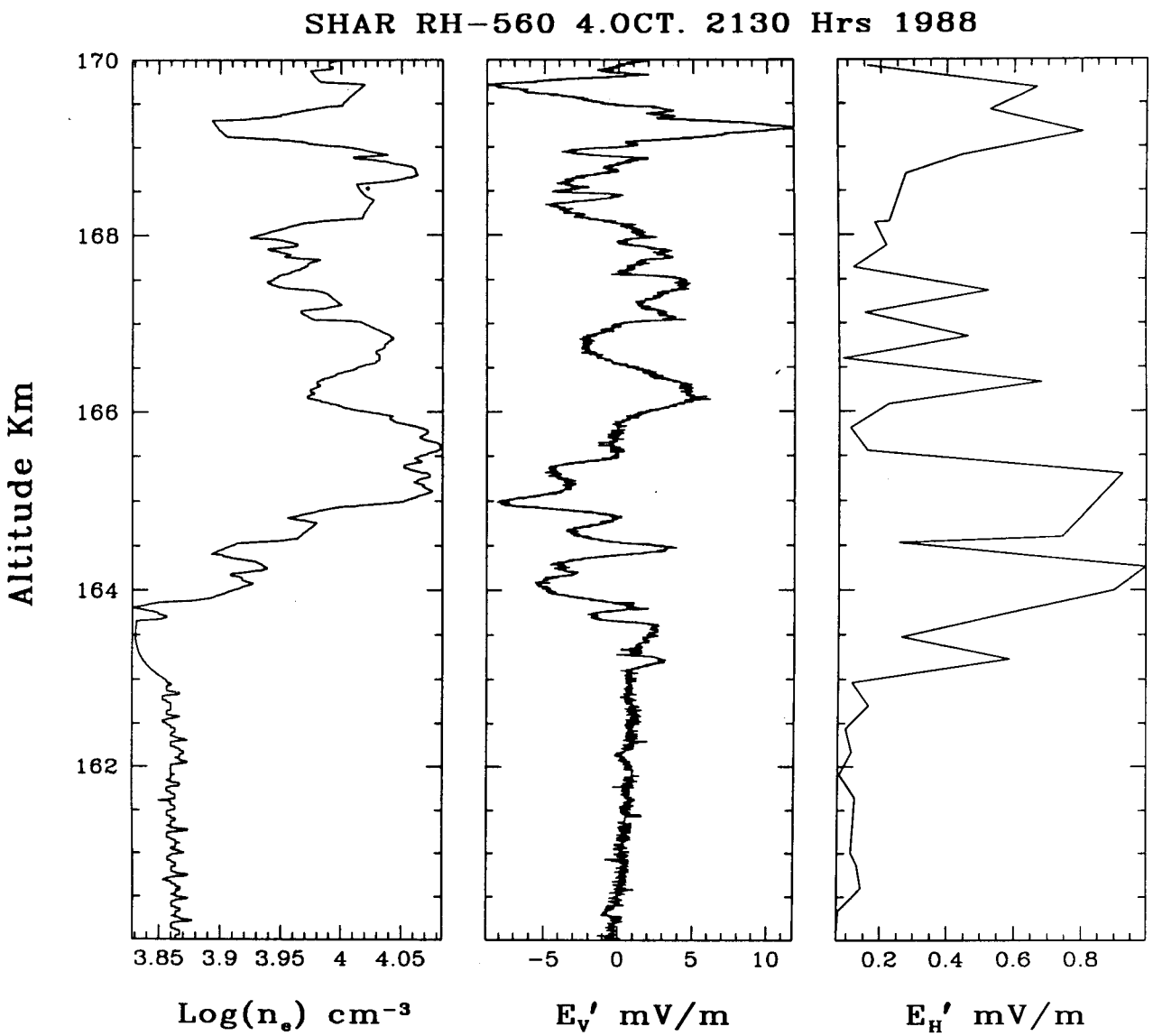

Fig.5.15 Variation of electron density, E_V' and E_H' with altitude showing the presence of high frequency components in the vertical electric field fluctuations only.

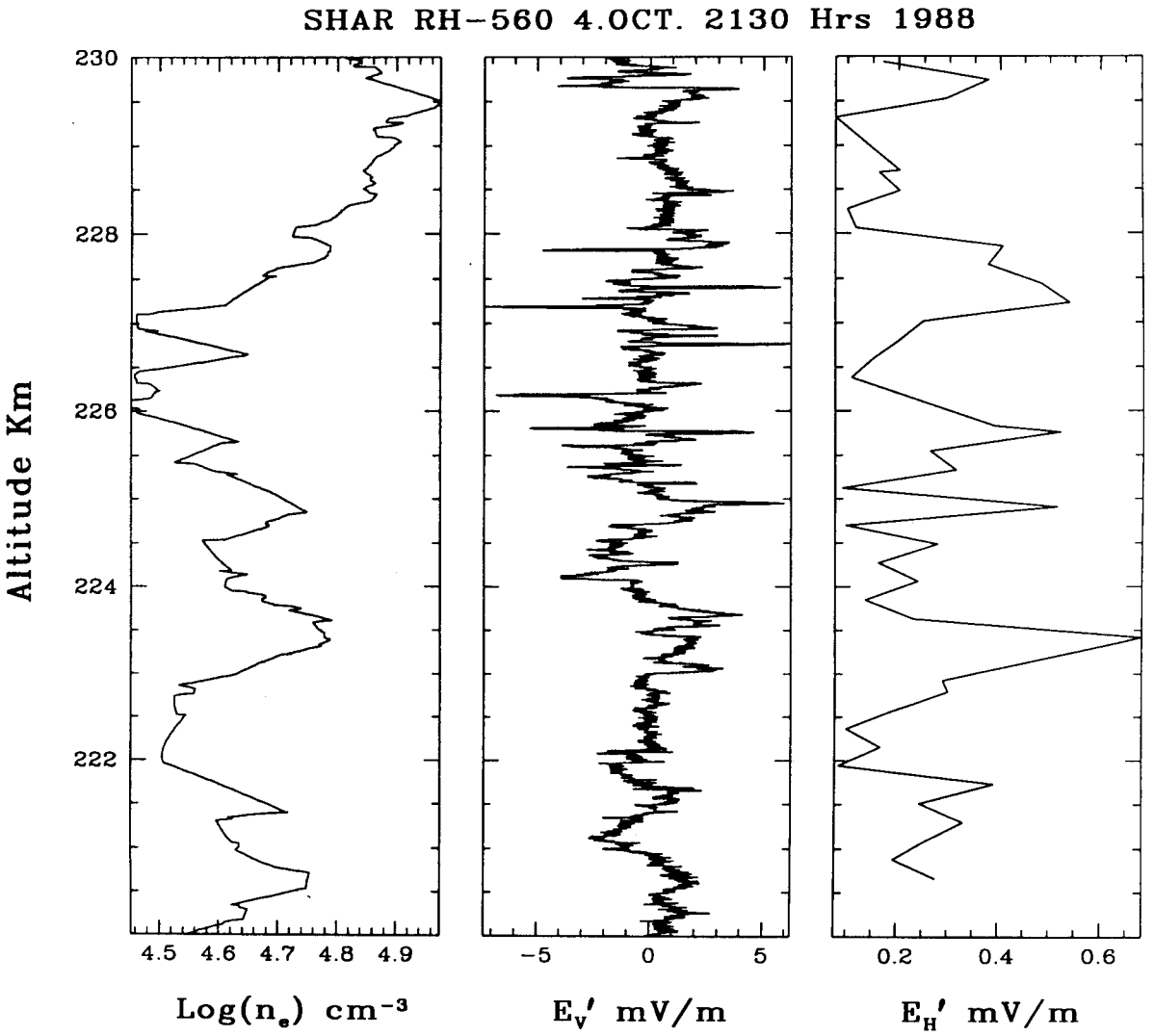

Fig. 5.16 Variation of fluctuations in electron density, vertical electric field and horizontal electric field with altitude. This figure shows that magnitude of high frequency component increases in the region where strong electron density irregularities occur.

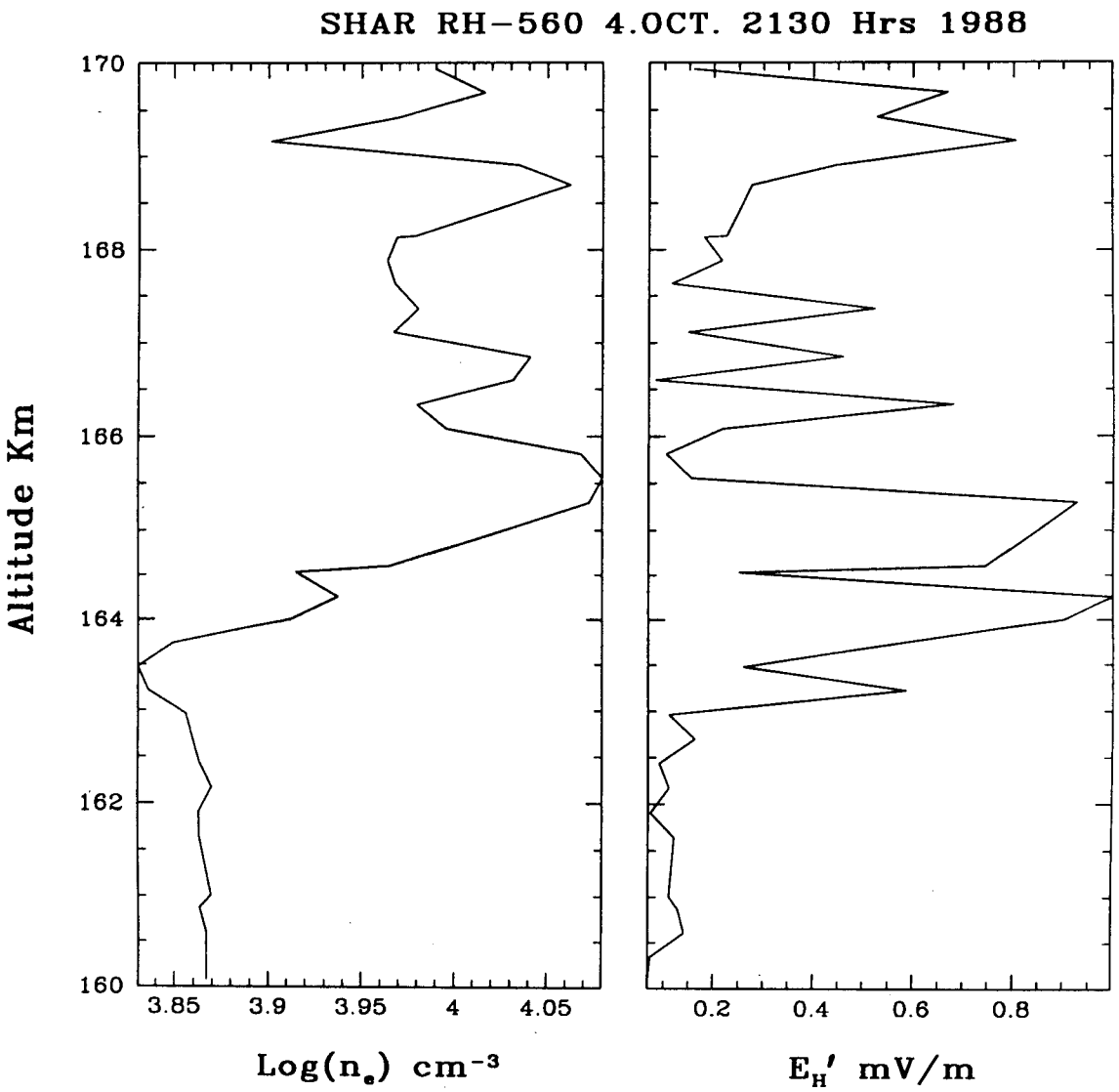

Fig.5.17 Example of saw-tooth structures in electron density and horizontal electric field profile in lower altitude region.

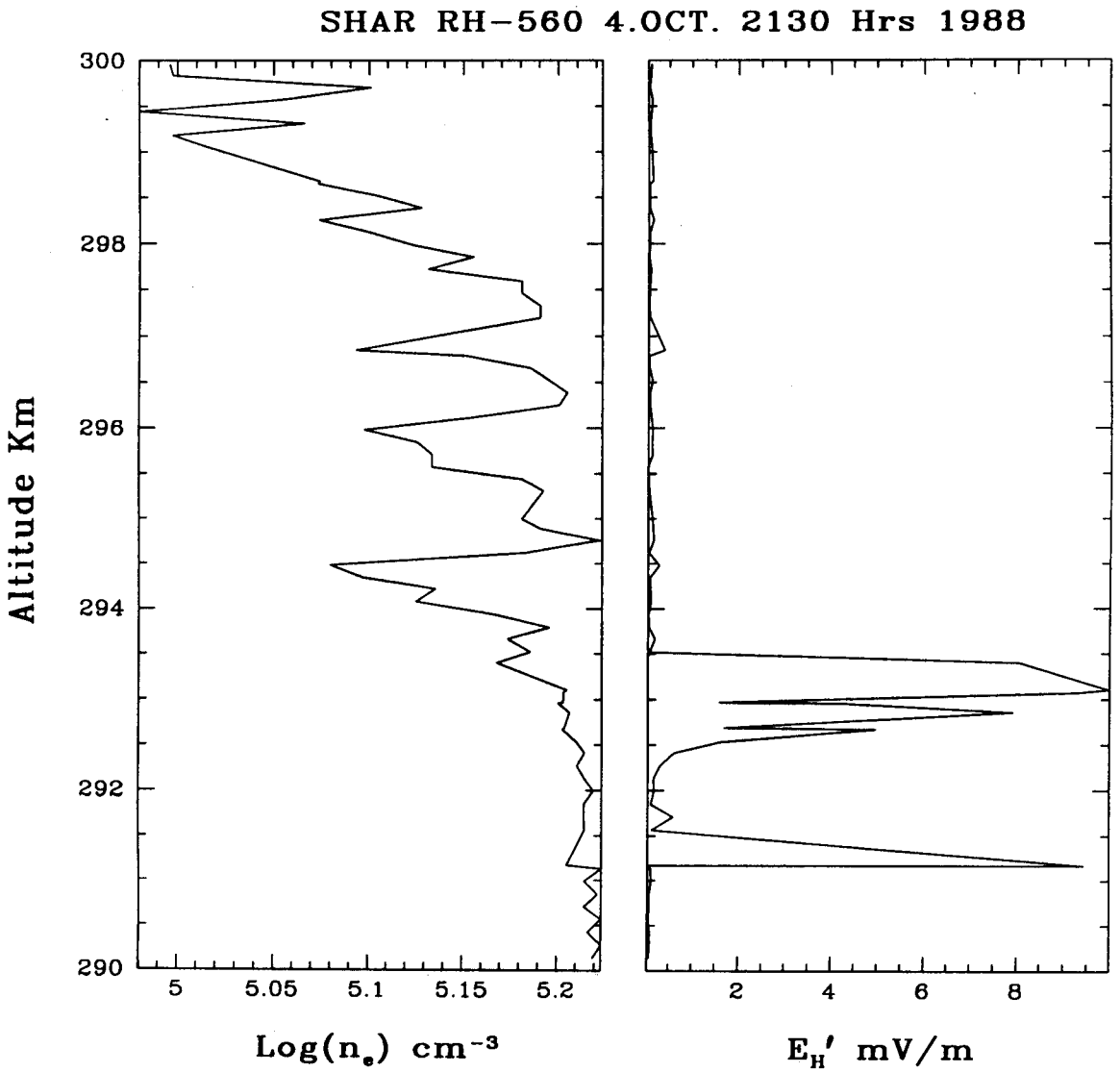

Fig.5.18 Example of saw-tooth structures at higher altitude of opposite character than those observed at lower altitude as shown in Fig.5.17.

5.5.4 Power Spectral Analysis of Irregularities

It is known that the relationship between electron density irregularities and electric field fluctuations serves as an important clue to the plasma instabilities and processes acting during spread F as has been discussed in Chapter 1.

To study the spectral nature of irregularities in E_H' and E_V', a composite spectra of scalesizes ranging from very large to about one meter was obtained. This was accomplished by making use of dc (0 - 100 Hz) channel data and mid frequency (MF) channel data having frequency response between 50 - 500 Hz. As the amplitude of the small scale irregularities is small, additional gains of 75 and 25 were used to amplify the amplitude of these smaller scale structures. Visual inspection of the data was performed for selecting the times of low gain and high gain periods. Since the amplitude saturated during most of the high gain period, data sets corresponding to low gain period were considered for spectral analysis. For obtaining the composite spectra, MF channel data was normalised with respect to the DC channel data at 60 Hz. The normalisation was performed by taking 7 point running average of DC channel data and then fitting a least square best fit line to the data set. Similarly, MF data was smoothened by taking 5 point moving average and then the power obtained at 60 Hz from MF data was normalised to that obtained by DC channel data. Power spectra of the irregularities was obtained for 2 seconds of data set of DC channel and the corresponding MF channel data.

The composite spectra E_V' and E_H' thus obtained are shown in Fig. 5.19 and 5.20 for a few selected altitude regions. From these spectra the spectral indices have been calculated for intermediate, transitional and short scalesize ranges and the same are tabulated below.

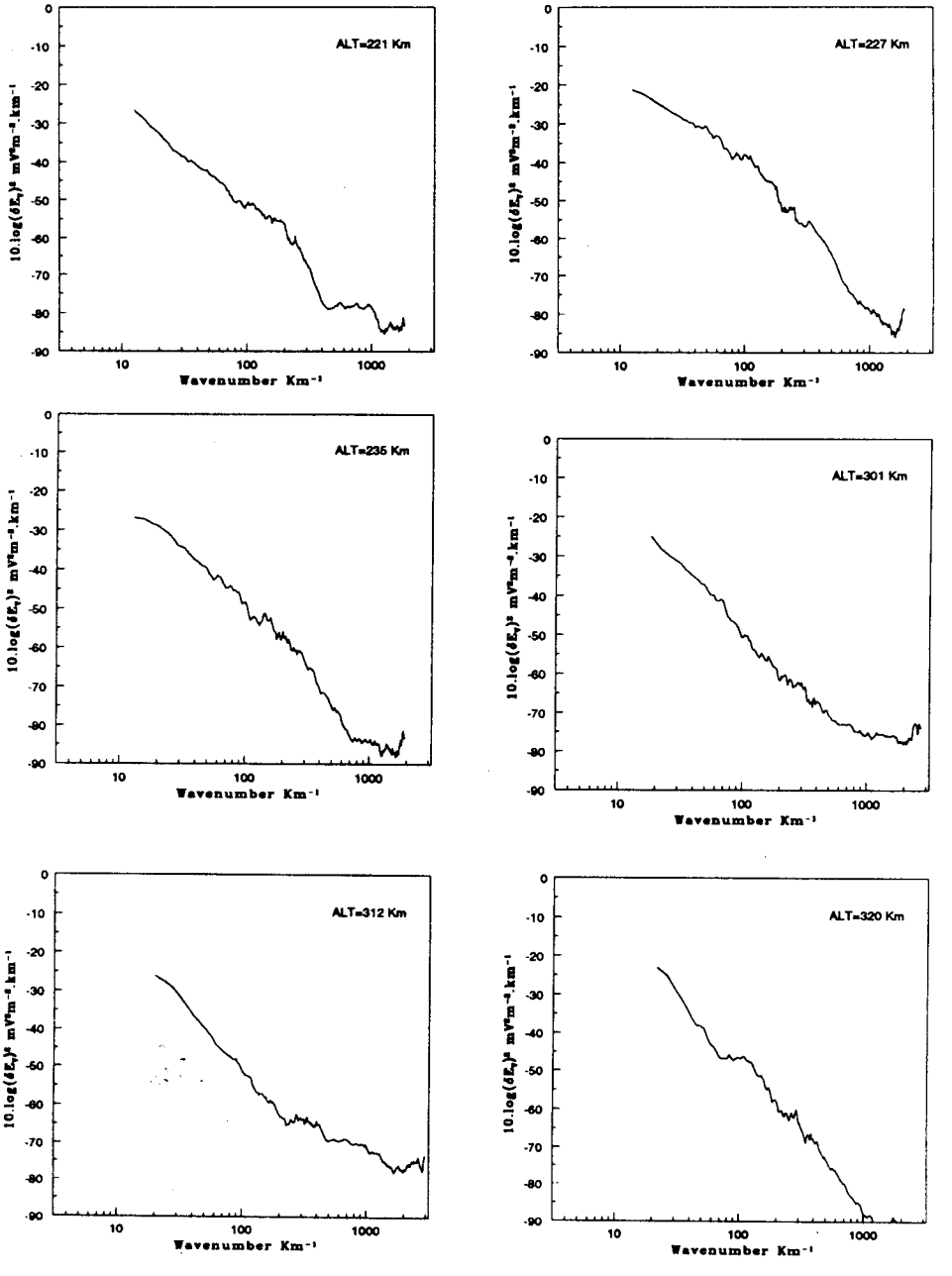

Fig.5.19 Power spectra of vertical electric field fluctuations at 221 km, 235 km, 301 km, 312 km and 320 km.

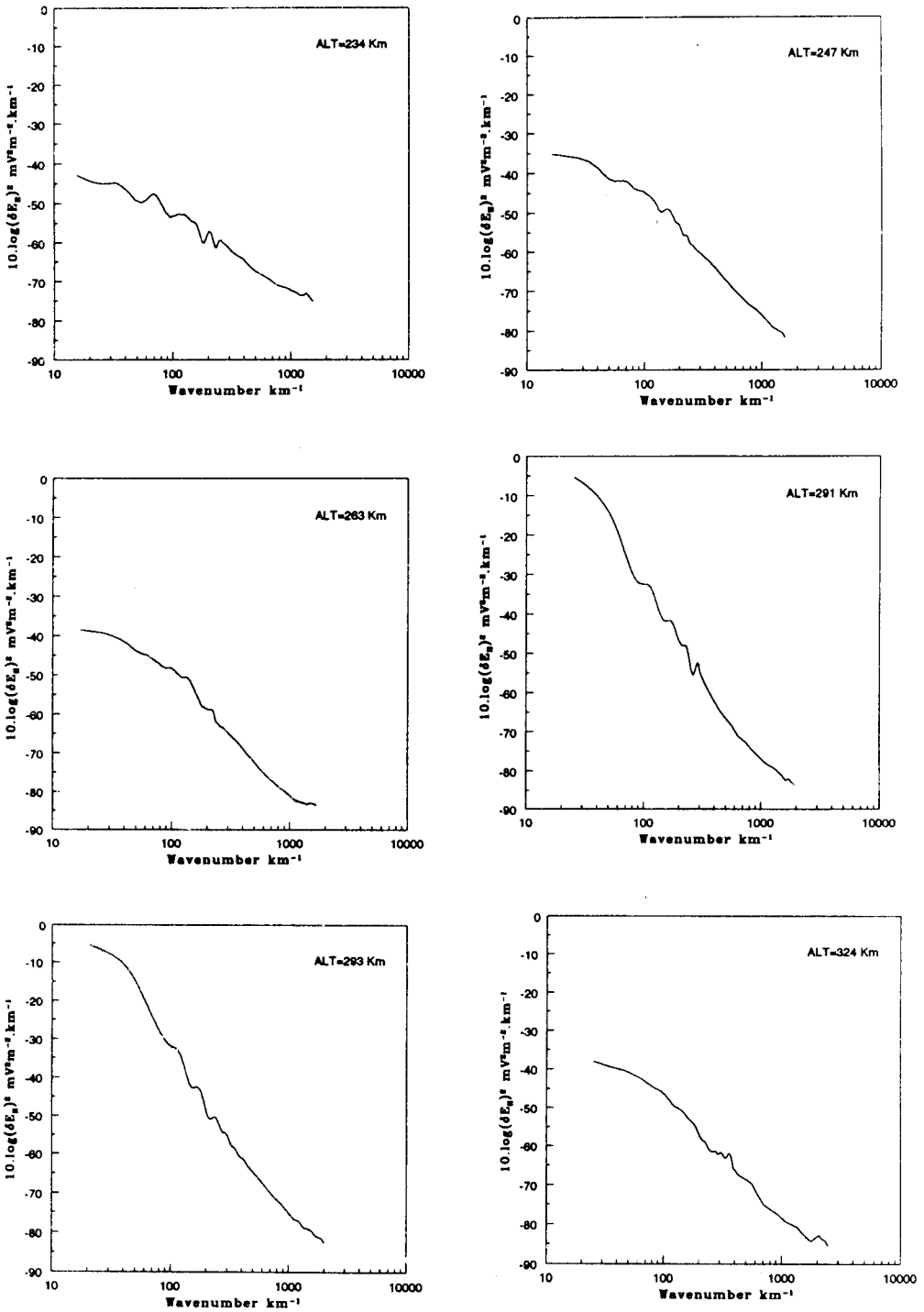

Fig.5.20 Power spectra of electric field fluctuations across the spin axis 234 km, 247 km, 263 km, 291 km, 293 km and 324 km.

Table 5.1 Spectra of $\delta E_H'$ fluctuations.

Altitude km	λ (100 m-1 km)	λ (10-100 m)	λ (< 10 m)
210-255	-1.2 ± 0.5	-3.0 ± 0.9	-1.8 ± 0.8
290-330	-1.2 ± 0.5	-2.5 ± 1.4	-2.5 ± 1.4

Table 5.2 Spectra of $\delta E_V'$ fluctuations

Altitude (km)	λ (100 m-1 km)	λ (10 m-100 m)	λ (< 10 m)
210 - 255	-1.2 ± 0.7	-3 ± 0.9	-2.5 ±1.4
290 - 330	-1.2 ± 0.8	-2.5 ±1.4	-1.6 ± 1.4

It is observed that the irregularities in E_V' and E_H' occurring in the intermediate scales (λ ~ 100 m - 1 km) display shallow spectral indices both in the lower (210 - 255 km) and higher altitude (290 - 330 km) region. The spectral index for E_V' fluctuations is ~ -1.2 ± 0.8 while for E_H', it is around -1.2 ± 0.5. It has been mentioned earlier in Chapter 4 that electron density irregularities exhibit shallow spectral indices for intermediate scales ranging between -1 and -2. This supports the contention that the irregularities in the intermediate scales are generated through GRTI mechanism.

The irregularities in the transitional scales (λ ~ 10 m - 100 m) display spectra with spectral indices around -3 ± 0.9 for both E_V' and E_H' in 210 - 255 km altitude region. However, the electron density irregularities in the transitional scales, in this region display steeper spectrum with spectral index ranging between -2.5 and -5. In the higher altitude region (290 - 330 km), the electric field spectrum display spectral index around -2.5 ± 1.4 and electron density display spectral indices in the range -2.5 and -4.5.

Irregularities in E_V' occurring in 165 - 175 km altitude region exhibit steep spectra. Around 165 km, fluctuations with λ ~ 40 m - 1 km can be

represented by a single power spectral index nearly equal to -4.09. There is an indication of a break in spectrum near 40 m, i e. for scalesize < 40 m, spectrum becomes shallower. Around 169 km, electric field irregularities with λ > 11 m display spectra with spectral index ~ 3.6 and for short wavelength, the nature of the spectrum changes. Irregularities occurring near 172 km with λ > 32 m follow power law with spectral index ~ 3.28. For smaller scales it becomes shallower. Around 176 km, strong irregularities are seen which display spectral index around -3.3. A break in spectrum is observed around λ ~ 9 m where it becomes shallower. It is interesting to note that E_V' and electron density spectra display nearly the same spectra. This is probably the manifestation of the fact that electron density and vertical electric field irregularities display either strong correlation or anti-correlation as discussed in Section 5.5.3.

The nature of the spectra observed around the base of the F layer is markedly different from the spectra observed at the higher altitudes. Around 256 km, the spectra of E_V' steepens near λ ~ 75 m and there is an indication of the spectrum becoming shallower for λ < 36 m. At about 221 km, spectra becomes steep near λ ~ 33 m and around 15 m it changes to a shallower spectra. Thus the nature of the spectra is highly variable and may be partly due to the temporal variations of irregularities. In the region 260 - 280 km, where the amplitude of irregularities is weak, the spectrum merges with the noise level determined by telemetry for λ < 13 m. At higher altitudes, around 309 km spectrum display shallow behaviour for λ > 104 m and becomes steeper between 10 and 104 m. For λ < 10 m, there is an indication of the spectrum becoming shallower.

5.6 Discussion

It was observed that the irregularities in electric field and electron density displayed the anti-correlation between 165 - 175 km and 290 - 320 km altitude regions. This is expected due to generation of polarisation electric fields which develop to maintain divergence free conditions as

discussed earlier. However, a very interesting phenomenon is observed between 210 - 255 km altitude region where electric field and electron density display strong correlation. This can be understood by considering the motion of charged particles in the directions perpendicular to B, which can be expressed, using the equations for conservation of momentum (Kelley, 1989) as given below.

$$0 = -k_B T_j (\partial n/\partial x) + n q_j E_x + n q_j V_{jy} B - n M_j \nu_{jn} V_{jx} \quad (5.10)$$

$$0 = -k_B T_j (\partial n/\partial y) + n q_j E_y + n q_j V_{jx} B - n M_j \nu_{jn} V_{jy} \quad (5.11)$$

where M_j refers to the mass of the ion species, $V_{jx,y}$ is the velocity of the plasma constituents, B is in the z direction. From the above equations, V_{jx} and V_{jy} can be written as:

$$V_{jx}\left(1+\frac{q_j^{\,2}B^2}{M_j^{\,2}\nu_{jn}^{\,2}}\right)=\frac{-k_BT_j}{M_j\nu_{jn}}\frac{1}{n}\frac{\partial n}{\partial x}+\frac{q_j}{M_j\nu_{jn}}E_x-\frac{q_jBk_BT_j}{M_j^{\,2}\nu_{jn}^{\,2}}\frac{1}{n}\frac{\partial n}{\partial y}+\frac{q_jB}{M_j^{\,2}\nu_{jn}^{\,2}}E_y$$

$$V_{jy}\left(1+\frac{q_j^{\,2}B^2}{M_j^{\,2}\nu_{jn}^{\,2}}\right)=\frac{-k_BT_j}{M_j\nu_{jn}}\frac{1}{n}\frac{\partial n}{\partial y}+\frac{q_j}{M_j\nu_{jn}}E_y-\frac{q_jBk_BT_j}{M_j^{\,2}\nu_{jn}^{\,2}}\frac{1}{n}\frac{\partial n}{\partial x}+\frac{q_jB}{M_j^{\,2}\nu_{jn}^{\,2}}E_x$$

Since, the E x B drift and the diamagnetic drift velocities can be written as

$$\mathbf{V}_{Ej} = \mathbf{E} \times \mathbf{B}/B^2, \qquad \mathbf{V}_{Dj} = -\frac{k_B T_j}{q_j B^2 n}\nabla n \times \mathbf{B} \quad (5.12)$$

The equation for the perpendicular velocity can be combined and written as

$$V_{j\perp}\left(1+\frac{q_j^{\,2}B^2}{M_j^{\,2}\nu_{jn}^{\,2}}\right)=\frac{-k_BT_j}{M_j\nu_{jn}}\nabla_\perp n+\frac{q_j}{M_j\nu_{jn}}\mathbf{E}_\perp-\frac{q_jB^2}{M_j^{\,2}\nu_{jn}^{\,2}}\mathbf{V}_D+\frac{q_j^{\,2}B^2}{M_j^{\,2}\nu_{jn}^{\,2}}\mathbf{V}_E$$

Defining the perpendicular diffusion coefficient for the motion antiparallel to a density gradient by an expression of the form $V = -D(\nabla n/n)$,

$$D_{j\perp} = \frac{k_B T_j}{M_j \nu_{jn}} \frac{1}{\left(1 + \dfrac{\Omega_j^{\,2}}{\nu_{jn}^{\,2}}\right)} \quad (5.13)$$

In the F region, gyrofrequencies are much greater than the collision frequencies, therefore the above expression is reduced to:

$$D_{j\perp} = \frac{k_B T_j}{M_j}\left(\frac{\nu_{jn}}{\Omega_{jn}^{\ 2}}\right) \qquad (5.14)$$

The perpendicular diffusion coefficient of species j can be written as

$$D_{j\perp} = r_j^{\ 2}\,\nu_j \qquad (5.15)$$

where,ν_j represents the collision frequency, r_j is the gyroradius which is expressed as

$$r_j^{\ 2} = \left(k_B T_j / M_j\right)^{1/2}\,\Omega_j^{\ -1} \qquad (5.16)$$

Since r_j is much larger for ions than for electrons, the ions tend to diffuse more rapidly down a density gradient which exists perpendicular to the magnetic field than the electrons. When this occurs an electric field builds up parallel to ∇n, so the ion motion across the field lines is retarded and the electron motion is enhanced. This may be the reason for the positive correlation seen in the altitude range of 210 - 260 km in the present flight. Such process results in the diffusion of plasma structure across a magnetic field with a diffusion coefficient equal to the low electron diffusion coefficient. Kelley et al. (1982a) calculated the relative amplitude of kilometre scale structures produced at various places in auroral oval which were then allowed to convect through regions of varying E-region conductivity. Vickrey and Kelley (1982) showed that the cross field diffusion at high latitudes results in the formation of images in the E region which tend to slow diffusion process. They discussed that the image will reduce the decay of F region structure by limiting the field aligned current that would otherwise reduce the ambipolar electric field. Since it is this field which impedes ion diffusion, the formation of E region reduces the F region cross field diffusion rate. Later on, Vickrey et al. (1984) explained the

formation of irregularities below the bottomside of the F region at low latitudes on the basis of the image mechanism.

The electric field experiment carried abroad the San Macro D equatorial ionospheric satellite revealed the downdrafting motion inside depletion regions (Laakso et al., 1994). McClure et al. (1977) and Hanson and Bamgboye (1984) also reported downdrafting motion of the ionisation irregularities. Laakso et al. (1994) pointed out that both updrafting and downdrafting motions are expected on the basis of generalised gradient drift or collisional R-T instability process in the ionospheric F-region. It is known that the gravitation would result in upward plasma flow in plasma depletion regions. However, both background westward zonal electric fields and upward vertical neutral winds can cause an occurrence of downdrafting if those parameters are strong enough. They showed that as the background zonal electric field becomes westward (after ~ 2100 LT) in the equatorial ionosphere, the plasma inside the bubbles at altitude ~ 400 km and less at magnetic equator may assume a downdrafting motion (~ 100 m/s), while at higher altitudes in the same flux tube, the plasma flow remains upward. Such simultaneous occurrence of the updrafting and downdrafting plasma flow in a single bubble channel may lead to the pinching off the upper part of the depletion region from the lower altitude regions, causing the decay of a bubble or the formation of a dead bubble. Aggson et al. (1992) reported such pinched off bubbles (dead bubbles) using double probe experiment carried on board San Macro D satellite. They suggested that after approximately 15 min the type I events (live bubbles) may be pinched off from the low densities of the bottomside F region and the bubbles probably become type II events (dead bubble) which continue to drift eastward with the general background zonal plasma flow.

Laakso et al. (1994) showed that the electric field inside the bubble (E_{y1}) can be expressed by the following relation,

$$E_{y1} = E_{y0} + \left[\frac{gB}{\nu_{in}} - U_x B + E_{y0}\right]\left(\frac{n_o}{n_1} - 1\right) \quad (5.17)$$

where the subscript 0 refers to values outside of the bubble (E_{y0}, n_0) and the subscript 1 refers to values inside the bubble (E_{y1}, n_1), U_x is the zonal neutral wind. This equation indicates that the downdrafting plasma flow can occur if the background electric field is oriented westward and the gravitational term minus the neutral wind speed term is small. They observed a number of depletion regions with downdrafting velocity at altitudes below 350 km in the F region near to geomagnetic equator. They found that these bubbles were characterised by enhanced westward electric fields of several millivolts per meter corresponding to downward flow speeds of about 50 - 150 ms^{-1}. The altitude of the transition between the updrafting and downdrafting flows at the magnetic equator as a function of background zonal electric field suggested by Laakso et al. (1994). They suggested that below 350 km, the downdrafting velocities can occur if the ambient E_y is more negative than -0.4 mV/m. It was seen from the ionograms obtained from SHAR that the F layer was descending indicating that the ambient field is westward ($E_H' \sim -0.8$ mVm^{-1}) during the rocket flight pertaining to the present study. Around 292 km vertical drifts as high as 250 ms^{-1} have been observed.

Our data indicated the presence of spikes in E_v' only. This observation is consistent with those of Hysell et al. (1994). They surmised that the spikes in the E_V profile are indicative of an ambipolar electric field. As ions attempt to diffuse across steep vertical gradients, an ambipolar electric field arises to inhibit their transport and bind them to the more tightly bound electrons. Thus charge neutrality is maintained. The electric field spike is more if the density gradient is steep. This field is given by $\delta E \sim \rho^2 \Omega_i$ B/L where ρ is the ion Larmor radius, Ω_i is the ion cyclotron frequency, and L is the gradient scale length. The relative absence of intense spikes in the zonal direction suggests that the most abrupt gradients in the plasma are in the vertical direction.

CHAPTER 6

CONCLUSIONS AND SUMMARY

This chapter summarises the results of the optical imaging, Langmuir probe and double probes measurements which were conducted from low latitude station, SHAR (13°E, 82°W), India. These were carried out for the better understanding of ionisation irregularities in F-region, collectively known as spread-F irregularities. Various characteristics of the very large scale irregularities i.e. plasma depletions were studied using an all-sky optical imaging system developed at Physical Research Laboratory, India. It is known that the gravity plays a major role in generating irregularities through Rayleigh-Taylor instability. However, physics of ESF irregularities on various scales is not properly understood either experimentally or theoretically. In view of this, the simultaneous in-situ measurements of electron density and electric field were analysed for the better understanding of ESF irregularities .

Optical Imaging of Plasma Depletions

1) A very interesting feature noticed is the tilt of the depletions which is about 10-15% towards east. It is interesting to note that the magnetic declination of SHAR is approximately 2.5° W. However, this is in contrast to the earlier observations obtained using all sky imaging system (Mendillo and Baumgardner, 1982; Mendillo and Tyler, 1983) which

displayed westward tilts. These tilts were interpreted as the optical manifestation of the westward tilts of the plumes recorded by incoherent scatter radar (Woodman and LaHoz, 1976; Tsunoda, 1980) and by in-situ probes (McClure et al., 1977). Woodman and LaHoz (1976) interpreted these tilts in terms of the lag in the drift velocity of depletions with respect to background plasma caused by an eastward neutral wind. Anderson and Mendillo (1983) tried to explain the westward tilts on the basis of eastward plasma drifts that decrease with altitude above F_2 peak. We conjecture that the eastward tilts of plasma depletions seen in our data might be associated with the variation of plasma drifts with altitude. This is supported by the evidence of the existence of positive shears in the zonal winds with altitude which have been obtained by using barium vapour release method during the onset time of ESF. Recently, Ionisation hole campaign (Sridharan et al., 1997) conducted from SHAR on February 19, 1993 revealed the existence of positive shears of 2.2 ms^{-1} km^{-1} in the zonal winds. Plasma depletions obtained on the same night but at the later time display eastward tilts suggesting the existence of altitudinal increase in plasma drift over SHAR.

2) Another interesting observation is that both the eastern and the western walls of the depletions are equally unstable to small scale perturbations. Earlier observations over the American region (Weber et al., 1978) indicated only western walls to be unstable. Tsunoda (1981) suggested that the eastward neutral wind operating on the vertical gradients can make the western wall unstable. However, the structures on the eastern wall of the depletions seen in our data suggest that gradient drift instability acting on the horizontal gradients could make the eastern wall unstable.

3) Multiple depletions found in the airglow images are characterised by a varying degree of depletions. One of the novel observations is that the east-west extent of the bubbles varies with the depletion depth. Shallower bubbles appear to be associated with smaller zonal width as

compared to deeper bubbles. We suggest that this is probably the manifestation of the fact that deeper bubbles characterised by large amplitudes represent well developed irregularities while shallower bubbles are representative of weaker irregularities.

4) VHF scintillations were also recorded at SHAR using the 244 MHz beacon on board FLEETSTAT (73°E). These were also recorded at a number of stations in India as a part of the All India Co-ordinated Programme on Ionosphere-Thermosphere and were observed up to anomaly crest region. Thus, the occurrence of scintillations up to the anomaly crest region shows that the large scales features namely the plasma depletions as well as smaller scales extend right up to these regions.

5) The eastward drifts of plasma depletions have been inferred from the series of airglow images along the east-west line passing through the zenith. Drift velocities were found between 40 and 120 ms^{-1} which agrees with the drift velocities inferred from scintillations (Koparkar and Rastogi, 1985). A comparison of the irregularity velocity obtained from other locations showed that the decrease in drift with local time over SHAR is consistent with the trend seen at C. Paulista (Abdu et al., 1985) and Arequipa, Peru (Mendillo et al., 1997). However, the drift velocities obtained from our data are slightly higher than those observed at Arequipa, Peru (16.5° S, 72° W) and are smaller than the ones observed at C. Paulista (22° S, 45° W). This might be a manifestation of the existence of latitudinal variation in the zonal velocities. These were assumed in the modelling studies by Anderson and Mendilllo (1983) for explaining the tilts of bubbles.

6) The distance between adjacent depletions, the inter depletion distance (IDD), is representative of the scalesize of the altitude modulated F layer. IDD is found to vary between 100 km to about 950 km. The separation

between the adjacent depletions suggests that gravity waves might be the seeding agency for generating such large scale structures.

7) In addition to the plasma depletions, where the decrease in plasma density is very large, sinusoidal wave like perturbations of scalesizes 900 - 1500 km were also observed in 630 nm airglow images. It is to be noted that wave like structures were observed by Rottger (1973) using forward scatter technique. Such large scale structures in the bottomside of the F layer as seen in our data could also be possibly due to gravity waves.

In-situ Electron Density Measurements

As a part of 'ionisation hole' campaign, two RH-560 rockets were launched from SHAR to obtain the background thermospheric and ionospheric conditions at the onset time of ESF. The electron density profile obtained during this campaign does not show the presence of large scalesizes (λ > a few km) in the bottomside of the F layer. However, a mass spectrometer, which was flown for the first time, revealed ion density fluctuations in the altitude range of 250-290 km (Sridharan et al. 1997).

Another RH-560 rocket flight which was conducted from SHAR during fully developed spread F conditions revealed a large range of irregularities observed in patches at various altitude ranges i.e. 165-175, 210-250, 260-280 and 295-320 km. The n_e-h profile exhibited many interesting features which are given below:

1) One of the most interesting feature of the profile is the occurrence of a patch of irregularity between 165 - 175 km altitude range. The remarkable feature of the irregularities occurring in this altitude region is the presence of structures in the scalesize range of 15 m to 1 km. Power spectral analysis of these valley region irregularities exhibit steep spectral indices ranging between -3.1 to -4.6. High ion-neutral collision frequencies would make the growth rate of R-T instability in this region negative. Such steep spectra cannot be explained by gradient drift

instability. As the spectral behaviour of these valley region irregularities is markedly different from those described by Vickrey et al. (1984), it appears that fluctuations observed in our data are not the image striations of fluctuations occurring at other altitudes. Some new mechanism has to be invoked for explaining such steep spectra in this altitude region.

2) Fluctuations with wavelength as large as 10 km are observed between 150 km to about 210 km region. Very large structure with vertical scale size of about 39 km is also seen in this region. Earlier flights from SHAR revealed a relatively quiescent region between 150 km up to the base of the F region. The presence of such large scale structures in our data suggest that gravity waves might be playing a dominant role in generating irregularities in this region. This is consistent with the theory of the internal gravity waves (Hines, 1960) which allows only long modes in this region, smaller scales being removed by viscous dissipation, reflection and hydromagnetic viscosity. The other possibility for the observation of irregularities could be the transmission of irregularities via geomagnetic field lines. Recently Sekar et al. (1997) showed that the fringe fields associated with the bubbles can go down up to the base of the F layer and generate irregularities there. Small scale structures may be the result of cascade process of larger scale structures.

3) Electron density structures with vertical scalesizes varying upto 20 km were present below 150 km region. A number of large scale fluctuations with vertical scale size as large as 25 km were observed in the earlier flights from SHAR in 100 - 150 km altitude region (Prakash et al., 1991).

4) Fluctuations in the intermediate scalesize range (0.1 - 10 km) are prominent in the 210 - 250 and 295 - 320 km altitude regions. These structures are likely to be produced through Generalised Rayleigh-Taylor Instability (GRTI). Calculations of effective linear growth rate (γ_g) of GRTI using typical values of observed vertical wind of 20 m/s were made.

Investigation of the relationship between γ_g and gradients revealed that γ_g was positive both at lower and higher altitudes only when the gradients were negative. It is known that electric fields have destabilising effect when E × B drift is parallel to ∇n. During the rocket flight, the F-layer was descending, the direction of ambient field must be westward. Thus, electric field seems to be dominating than the gravity and vertically downward wind in producing irregularities both at lower and higher altitudes.]

5) Fluctuations with scalesizes in the range of 100 m to 1 km were observed in 210 - 250 km and 290 - 330 km altitude regions. The spectral Indices of these irregularities is -1.5 ± 0.5. These values agree with the earlier observations (Rino et al., 1981, Kelley et al., 1992). In 210 - 255 km region, the power spectrum display a break around 30 m. In 290 - 330 km region, the irregularities in the transitional scales display shallower spectrum at 290 km and becomes steeper upwards. Rino et al. (1981) observed that above 370 km, spectrum becomes shallower as compared to lower altitudes where perturbations levels were high. Our data shows the occurrence of large perturbations in 210 - 250 km region. It appears that the evolution of spectra in the transitional regime depends on the turbulence strength. For short wavelengths (< 10 m), there is an indication of the spectrum becoming shallower both at higher and lower altitudes.

In-situ electric Field Measurements

A RH-560 rocket launched from SHAR during fully developed spread F condition carried two pairs of double probes for electric field measurements simultaneous with the electron density measurements discussed above. It was observed that the electron density and electric field fluctuations are colocated during the rocket flight. The interesting features are listed below:

1) It is observed that large scale perturbations in $\delta E_V'$ are prominent at lower altitudes. Around 165 km, structures with vertical half wavelengths of $\approx$ 7 km are observed along with the smaller scale perturbations superimposed on them. Fluctuations with amplitude as large as 12 mV/m are seen around 175 km. The amplitude of $\delta E_V'$ irregularities observed between 210 - 260 km altitude region is smaller than those seen at the lower altitudes. The maximum amplitude of irregularities in this region is $\approx$ 4 mV/m. Between 260 - 280 km altitude region, $\delta E_V'$ irregularities with amplitude $\approx$ 1 mV/m are seen. A relatively smooth region is observed between 280 - 290 km. Between 292 and 295 km fluctuations with scalesize around 1.4 km having amplitude as large as 2.8 mV/m are seen

2) The variation of horizontal electric field with altitude exhibits a patch of irregularity between 160 - 170 km with amplitudes lying between 0.7 - 2 mV/m. High values of E_H' with values between 2 - 4 mV/m are observed in 184 - 188 km altitude region. Weak irregularities in E_H' are seen between 210 - 255 km altitude region with maximum amplitude of 0.9 mV/m. At higher altitudes i.e. around 292 km, E_H' perturbations with scalesize as large as 1 km having amplitude as high as 7.7 mV/m are observed. Weak irregularities with amplitudes less than 0.6 mV/m are seen between 295 - 332 km altitude regions.

3) $\delta E_V'$ and δn_e fluctuations are either strongly correlated or anti-correlated in various altitude regions. However, E_H' perturbations exhibit poor correlation with n_e irregularities. Around 175 km, the correlation coefficient between $\delta E_V'$ and δn_e irregularities is $\approx$ -0.8 while that between δn_e and $\delta E_H'$ fluctuations, it is $\approx$ -0.5. A very interesting feature is observed between 210 - 255 km altitude region where electron density irregularities and electric field perturbations display positive correlation. Very strong correlation is observed between δn_e and $\delta E_V'$ around 245 km with correlation coefficient $\approx$ 0.9. It is interesting to note that strong

positive correlation is seen around the base of the F layer where this trend again changes at higher altitudes where electric field irregularities exhibit anti-correlation. Around 305 km, correlation coefficient $\approx$ -0.9 is seen for δn_e and $\delta E_V'$ perturbations. Hysell et al. (1994) observed that on large scales $\delta E_H' \propto -\delta n$ while $\delta E_V'$ fluctuations were not clearly anti-correlated as in horizontal directions which is in contrast to our observations. Hysell et al. (1994) interpreted the anti-correlation as being due to charge neutrality conditions which imposes the restriction that the current in the F-region be divergence free. When the density and Pederson conductivity are non-uniform, polarisation charges accumulate at horizontal density gradients giving rise to horizontal electric field in such a way that $\nabla J = 0$ and hence, $\delta E_H' \propto -\delta n$. They attributed the anti-correlation between δn_e and $\delta E_V'$ perturbations to the eastward neutral wind which drives the current in the vertical direction and produces vertical polarisation field which might be responsible for the production of plasma irregularities (Tsunoda et al., 1982). We conjecture that the positive correlation seen in 210 - 250 km altitude region might be due to diffusion perpendicular to magnetic field lines. Since the ion gyroradius is much larger than for electrons, the ions tend to diffuse more rapidly down a density gradient producing electric field parallel to ∇n.

4) Sawtooth structures are evident both in E_H' and n_e. These sawtooth structures seems to be present only when E_H' exceeds certain threshold. At higher altitude this threshold is about 8 mV/m whereas at lower altitudes it is about 0.5 mV/m. In the same altitude range sawtooth structures in E_H' and n_e are of opposite character. At lower altitudes decrease in n_e is much sharper than increase which is in contrast to the higher altitudes. This appears to be a manifestation of the polarisation fields which develop to maintain the charge neutrality conditions in the presence of density gradients. Hysell et al (1994) reported sawtooth structures in electron density depletions where the right side was more steep and hence reached the conclusion that there is a preferential

direction for plasma steepening. However, the presence of sawtooth structures in our data indicates that the direction of plasma steepening might be dependent on altitude.

5) The E_V' measurements reveal the presence of high frequency components which are observed in the form of intense spikes. At the altitudes where weak irregularities occur, smaller spikes are seen. Between 210 -255 km altitude region, where strong electron density irregularities are observed, the magnitude of spike is large. Strong spikes with magnitudes exceeding 5 mV/m are observed between 220 - 230 km. However, E_H' does not show the presence of such intense spikes as seen in the vertical direction. This observation is consistent with that of Hysell et al. (1994). They attributed the spikes in vertical electric field to the ambipolar electric field which results when the ions attempt to diffuse across steep vertical gradients. Thus to maintain charge neutrality, ambipolar electric field develops so as to inhibit their transport and bind them to the electrons. This field is given by $\delta E \approx \rho^2 \Omega_i B/L$ where ρ is ion Larmor radius, Ω_i is the ion cyclotron frequency, and L is the gradient scale length. The electric field spike is more if the density gradient is steep. The relative absence of spikes in the zonal direction suggests that the most abrupt plasma gradients occur in the vertical direction.

Scope For Future Work

Optical imaging is a powerful technique for studying vary large scale structures in the plasma density such as plasma depletions by monitoring airglow intensity of appropriate emission lines. Images of plasma depletions, thus obtained, can be used for studying dynamics tilts and other properties of large scale irregularities. As the airglow emissions are altitude dependent, suitable selection of emission lines can be made for studying different altitude regions from which these lines originate. Simultaneous multi-wavelength observations of OH emission (85 km), Na 589.6 nm emission (96 km), OI 557.7 nm emission (100 km), OI 630.0 nm (250 km), 777.4 nm (F_2 peak) can be used for inferring parameters related to gravity waves, existence of shears in ambient plasma velocity in the zonal direction. These can provide useful information on the vertical propagation of waves which transport energy upwards from below. Hence, these can be used for studying the coupling between the middle and the upper atmosphere.

Comparison of measurements of zonal drift velocities of irregularities which are representative of ambient plasma drift at different locations has indicated the existence of latitudinal variation of the drift velocities. However, these measurements were not simultaneous. Co-ordinated and simultaneous observations at different latitudes should be made in order to get realistic information about the latitudinal variation of plasma drift. This knowledge would be significant for better understanding of the features like tilts of the plumes, bubbles or depletions. In chapter 3, it was seen that tilts of the plasma depletions are different in the Indian and American sector.

It is well known that spread F exhibits day to day variability. Co-ordinated measurements of optical imaging, Fabry-Perot interferometers, and other standard ionospheric instruments can help in enhancing the current understanding of the roles played by different agencies like neutral winds and presence of seeding agencies in the occurrence of spread F phenomenon. More extensive campaigns of vector wind measurements should be conducted to experimentally confirm the

predictions of numerical simulation work which highlights the importance of vertical winds.

The electron density measurements discussed in chapter 4 revealed the occurrence of irregularities in the valley region i.e. between 150 km up to the base of F-region. Radar studies have also shown the existence of such valley region irregularities which are relatively unexplored. Two earlier rocket flights launched from Natal, Brazil (Kelley, 1976; Costa and Kelley, 1978) and from Kwajalein Atoll, PLUMEX I, (Szuszczewicz et al., 1980, Kelley et al., 1982) also showed the presence of these irregularities. These were interpreted in terms of image striations of fluctuations occurring at the dip equator (Vickrey et al., 1984). However, this theory is not able to explain the occurrence of irregularities seen in our data which were not seen before in the earlier flights from SHAR. The generation mechanism of these irregularities should be looked into. Some theoretical work should be taken up for explaining (a) the break in the spectrum occurring at lower altitudes near $\lambda \approx 30$ m and (b) the change in spectral behaviour for shorter wavelengths where the spectrum becomes shallower.

Electron density and electric field structures should be simultaneously measured from rockets which go up to 700 km, preferably with long booms so as to yield dc electric fields. The attitude information of these rockets should be known very precisely so that the vector subtraction of rocket induced electric field could be made to infer dc electric fields. These measurements should be conducted simultaneously with optical imaging, MST radar, Fabry-Perot interferometer for understanding of plasma dynamics.

More observations should be made at equatorial and low latitude stations to study gravity wave parameters in the E and F-regions as seen in the present data and also suggested by recent theoretical developments (Prakash, 1996) that the electric fields produced by gravity wave winds in these regions could produce large scale electron density perturbations which act as seeds for excitation of generalised Rayleigh-Taylor instability.

REFERENCES

Aarons, J. Equatorial scintillations: A review, *IEEE Trans. Ant. Prop.*, **25**, 729, 1977.

Aarons, J. Radio Sci. **26(4)**, 1131-1149, 1991.

Aarons, J., J. P. Mullen, J. P. Koster, R. F. daSilva, J. R. Medeiros, R. T. Medeiros, A. Bushby, J. Pantoja, J. Lanat, and M. R. Paulson, Seasonal and geomagnetic control of equatorial scintillations in two longitudinal sectors, *J. Atmos. Terr. Phys.*, **42**, 861, 1980.

Abdu, M. A., I. J. Kantor, I. S. Batista, and E. R. de Paula. East-west bubble irregularity motion determined from spaced VHF polarimeters: Implications on velocity shear in the zonal F region bulk plasma motion, *Radio Sci.*, **20**, 1, 111-122, 1985.

Abdu, M. A., J. A. Bittencourt, I. S. Batista. Longitudinal differences in spread F characteristics, *Revista Brasileira de Fisica,* **13(4)**, 647-663, 1983.

Abdu, M. A. Equatorial spread F and ionosphere-Thermosphere system: A review, *Trends in Geophys. Res.*, **2**, 193-209, 1993.

Abdu M. A. Major phenomena of the equatorial ionosphere-thermosphere system under disturbed conditions, *J. Atmos. Terr. Phys.*, **59(13)**, 1505-1519, 1997.

Abreu, V J., J. H. Yee, S. C. Soloman, and A. Dalgarno. The quenching rate of $O(^1D)$ by $O(^3P)$ *Planet Space Sci.*, **34**, 1143-1145, 1986.

Aggson, T. L., W. J. Burke, N. C. Maynard, W. B. Hanson, W. R. Hogey, and J. L. Saba. Electric field observations of equatorial bubbles, *J. Geophys. Res.*, **97**, 2997, 1992.

Alpert, J.L. On electromagnetic effects in the neighbourhood of a satellite or a vehicle moving in the ionosphere or interplanetary space, *Space Sci. Rev.*, **4**, 373, 1965.

Anandarao B. G., Raghavarao R., Desai, J. N., and Haerendal, G. *J. Geophys. Res.*, **40**, 157, 1978.

Anderson, D. N. A theoretical study of the ionospheric F region equatorial anomaly-I. Theory, *Planet Space Sci.*, **21**, 409, 1973.

Anderson, D. N. Modelling ambient low latitude F region ionosphere - A review, *J. Atmos. Terr. Phys*, **43**, 753 1981.

Anderson, D. N., and M. Mendillo. Ionospheric conditions affecting the evolution of equatorial plasma depletions, *Geophys. Res. Lett.*, **10**, 541-544, 1983.

Anderson, O. N., and D. W. Rusch. Composition of the night-time ionospheric F1 region near the magnetic equator, *J. Geophys. Res.*, **85**, 569-574, 1980.

Baker, W. G., and Martyn, D. F., Conductivity of the ionosphere, *Nature*, **170**, 1090, 1952.

Balan, N., R., Balachandran Nair, G. Gopkumar and P. B. Rao. Spectra of the AC electric fields in the F region at the magnetic equator, *Adv. Space Res.*, **13(1)**, 299 - 302, 1993.

Balsley, B. B. Some characteristics of non two-stream irregularities in the equatorial electrojet, *J. Geophys. Res.*, **74**, 2333, 1969.

Balsley, B. B., G. Haerendal, and R. A. Greenwald. Equatorial spread F: Recent observations and a new interpretation, *J. Geophys. Res.*, **77**, 5625-5628, 1972.

Bamgboye, D. K., and J. P. McClure. Seasonal variation in the occurrence time of the equatorial midnight temperature bulge, *Geophys. Res. Lett.*, **9**, 457-460, 1982.

Banks, P. M. and G. Kockarts. Aeronomy, Academic Press, New York, 1973.

Barker, M.L. and Yen, V.L. Effects of the variation of angle of incidence and temperature on infrared filter characteristics, *Appl. Optics*, **6**,1343, 1967.

Basu, S., S. Basu, and B. K. Khan. Model of equatorial scintillations from in-situ measurements, *Radio sci.*, **11**, 821, 1976.

Basu, S., S. Basu, J. Aarons, J. P. McClure, and M. D. Cousins. On the co-existence of kilometer and meter scale irregularities in the night-time equatorial F region, *J. Geophys. Res.*, **83**, 4219, 1978.

Basu, S., and S. Basu. Equatorial Scintillations - a review, *J. Atmos. Terr. Phys.*, **43**, 473, 1981.

Basu S. and S Basu. Equatorial scintillations: advances since ISEA-6, *J. Atmos. Terr. Phys.*, **47**, 753-768, 1985.

Batista, I. S., J. H. Sastri, R. T. de Medeiros, and M. A. Abdu. Nighttime thermospheric meridional winds at Cachoeria Paulista (23°S, 45°W): Evidence for effects of the equatorial midnight pressure bulge, *J. Geophys. Res.*, **102(A9)**, 20,059-20,062, 1997.

Beer, T. Spatial resonance in the ionosphere, *Planet Space Sci.*, **21**, 297, 1973.

Behnke, R. A., and R. M. Harper. Vector measurements of F-region ion transport at Arecibo, *J. Geophys. Res.*, **78**, 8222, 1973.

Benson, R. F., and H. C. Brinton. Ionospheric plasma bubble encounters or F region bottomside traversals, *J. Geophys. Res.*, **88**, 6243, 1983.

Biondi M. A., and Sipler D. P. Horizontal and vertical winds and temperaturesin the equatorial ionosphere, *Planet. Space Sci.*, **33**, 817, 1985.

Bittencourt, J. A., B. A. Tinsley, G. T. Hicks, and E. I. Reed. Tropical F-region winds from OI 1356 Å and [OI] 6300 Å emissions 2. Analysis of Ogo 4 data, *J. Geophys. Res.*, **81**, 3786-3790, 1976.

Bittencourt, J. A., and Y. Sahai. F-region neutral winds from ionosonde measurements of hmF_2 at low latitude magnetic conjugate regions, *J. Atmos. Terr. Phys.*, **40**, 669-676, 1978.

Bittencourt, J. A., Y. Sahai, P. R.. Faundes, and H. Takahashi. Simultaneous observations of equatorial F-region plasma depletions and thermospheric winds, *J. Atmos. Terr. Phys*, **59(9)**, 1049-1059, 1997.

Blix, T. A., E. V. Thrane, and O. Anderson. In-situ measurements of the fine scale structure and turbulence in the mesosphere and lower thermosphere by means of electrostatic positive ion probes, *J. Geophys. Res.*, **95**, 5533, 1990.

Booker, H. G., and H. W. Wells. Scattering of radio waves by the F-region of the ionosphere, *J. Geophys. Res.*, **43**, 249, 1938.

Bourdeau, R.E., and J.L. Donley. Explorer VIII satellite measurements in the upper ionosphere, *Proceedings of Roy. Society*, **281**, 487, 1964.

Bourdeau, R.E., J.L. Donley, G.P. Serbu, and E.C. Whipple, Jr. Measurements of sheath currents and equilibrium potential on the explorer VIII satellite, *J.Astronautical Sci.*, **8**, 65, 1961.

Bowles, K. L., and R. Cohen. A study of radio wave scattering from sporadic E near the magnetic equator, Ionospheric Sporadic E , edited by E. K. Smith and S. Matsushita, Pergamon, New York, 1962.

Bowles, K. L , B. B. Balsley, and E. Cohen. Field-aligned E region irregularities identified with ion acoustic waves, *J. Geophys. Res.*, **68**, 2485, 1963.

Bowles, K. L., R. Cohen, G. R. Ochs, and B. B. Balsley. Radar echoes from field aligned ionisation above the magnetic equator and their resemblance to auroral echoes, *J. Geophys. Res.*, **65**, 1853, 1960.

Buchau, J., E. J. Weber, and J. P. McClure. Radio and optical diagnostics applied to an isolated equatorial scintillation event, Effect of the ionosphere space and terrestrial systems, edited by J. M. Goodman, p. 115, U. S. Government Printing Office, Washington, D. C., 1978.

Buneman, O. Excitation of field aligned sound waves by electron streams, *Phys. Rev. Lett.* **10**, 285, 1963.

Burke, W. J., D. E. Donatelli, R. C. Sagalyn, and M. C. Kelley. Low density regions observed at high altitudes and their connection with equatorial spread F, *J. Planet Space Sci.*, **27**, 593, 1979.

Burnside, R. G., F. A. Herrero, J. W. Meriwether and J. C. G. Walker. Optical observations of thermospheric dynamics at Arecibo, *J. Geophys. Res.*, **86**, 5532, 1981.

Chakrabarty, D. K., G. Beig, J. S. Sidhu, and S. R. Das. Fine scale structure and turbulence parameters in the equatorial middle atmosphere, *J. Atmos. Terr. Phys.*, **51**, 19, 1989.

Chamberlain, J. W. Physics of the Airglow and Aurora, Academic, New York, 1961.

Chandra, H., and R. G. Rastogi. Solar cycle and seasonal variation of spread F near the magnetic equator *J. Atmos. Terr. Phys.*, **32**, 439-443, 1970.

Chandra H., R K. Misra, M. R. Deshpande and R. G. Rastogi. Ionospheric irregularities & their drifts at Thumba during 1964-68, *Ind. J. Pure App. Phys.*, **8**, 548, 1970.

Chandra, H., and R. G. Rastogi. Spread-F at magnetic equatorial station Thumba, *Annals. Geophys.*, **28**, 37 1972.

Chandra, H., G. D. Vyas, B. M. Pathan, and D. R. K. Rao. Spectral characteristics of magnetic storm-induced F-region scintillations extending into daytime, *J. Atmos. Terr. Phys.*, Vol. 57, No. 11, 1273-1285, 1995.

Chandra. H., G. D. Vyas, H. S. S. Sinha, R. N. Misra and S. Prakash. Ionospheric scintillation observations from SHAR, *J. Atmos. Terr. Phys.*, **54**, 167-172, 1992

Chandra, H., G. D. Vyas, H. S. S. Sinha, S. Prakash, and R. N. Misra. Equatorial Spread F campaign over SHAR, *J. Atmos. Terr. Phys.*, **59**, 191-205, 1997.

Chou, S. Y. and F. S. Kuo. Simulation of neutral wind field effect on equatorial spread F, low latitude ionospheric physics., 143-149, 1993.

Clark, R. M., K. c. Yeh, and C. H. Liu. Interaction of internal gravity waves with the ionospheric F_2 layer, *J. Atmos. Terr. Phys*, **33**, 1567, 1971.

Cogger, L. L., J. S. Nurphree, C. A. Tepley and J. W. Meriwether, Jr. Measurements of E region neutral wind field, *Planet. Space Sci.*, **33**, 373, 1985.

Cohen, R., and K. L. Bowles. Secondary irregularities in the equatorial electrojet, *J. Geophys. Res.*, **72**, 822, 1967.

Costa, E., and M. C. Kelley. On the role of the steepened structures and drift waves in equatorial spread F. *J. Geophys. Res.*, **83**, 4359-4364, 1978

Cowling, T. G. The electrical conductivity of an ionised gas in a magnetic field, with applications to the solar atmosphere and the ionosphere, *Proc. Roy. Soc.*, **A183**, 453, 1945.

Cragin, B. L., C. E. Valladares, W. B. Hanson, and J. P. McClure. Bottomside sinusoidal irregularities in the equatorial F region 2. Cross correlation and spectral analysis, *J. Geophys. Res.*, **90**,1721-1734, 1985

Cunnold, D. M. Drift-Dissipative plasma instability and equatorial spread F, *J. Geophys. Res.*, **74**, 5709, 1969.

Dabas, R. S., D. R. Lakshmi, and B. M. Reddy. Effect of geomagnetic disturbances on the VHF nighttime scintillation activity at equatorial and low latitudes, *Radio Sci.*, **24**, 563-573, 1988.

Dalgarno, A., and J. C. G. Walker. The red line of atomic oxygen in the day airglow, *J. Atmos. Sci.*, **21**, 463, 1964.

Dasgupta, A., A. Mitra, and S. K. Das. Postmidnight equatorial scintillation activity in relation to geomagnetic disturbances, *J. Atmos. Terr. Phys.*, **47**, 911-916, 1985.

Davis, M. J. The integrated ionospheric response to internal gravity waves, *J. Atmos. Terr. Phys.*, **35**, 929, 1973.

Dickinson, R. E., E. C. Ridley, and R. G. Roble. Meridional circulation in the thermosphere, 1, Equinox conditions, *J. Atmos. Sci.*, **32**, 1737, 1975.

Dickinson, R. E., E. C. Ridley, and R. G. Roble. Meridional circulation in the thermosphere, 2, Solstice conditions, *J. Atmos. Sci.*, **34**, 178, 1977.

Dungey, J. W. Convective diffusion in the equatorial F region, *J. Atmos. Terr. Phys.*, **9**, 304-310, 1956.

Dyson. P. L., J. P. McClure, and W. B. Hanson. In situ measurements of the spectral characteristics of F region ionospheric irregularities, *J. Geophys. Res.*, **79**, 1497-1502, 1974

Earle, G. D., and M. C. Kelley. Spectral studies of the sources of ionospheric electric fields, *J. Geophys. Res.*, **92**, 213-224, 1987.

Eather, R.H. and Reasoner, D.L. Spectrophotometry of faint light sources with a tilting filter photometer, *Appl. Optics*, **8**, 227, 1969

Ecklund, W. L., and B. Balsley. Long term observations of Antarctic mesosphere with the MST radar at Poker Flat, Alaska, *J. Geophys. Res.*, **86**, 7775, 1981.

Farley, D. T. A plasma instability resulting in field aligned irregularities in the ionosphere, *J. Geophys. Res.*, **68**, 6083, 1963.

Farley, D. T., B. B. Balsey, R. F. Woodman, and J. P. McClure. Equatorial spread F : Implications of VHF radar observations, *J. Geophys. Res.*, **75**, 7199-7216, 1970.

Farley, D. T., E. Bonelli, B. G. Fejer, and M. F. Larsen. The prereversal enhancement of the zonal electric field in the equatorial ionosphere, *J. Geophys. Res.*, **91**, 13723-13728, 1986.

Fejer, B. G., D. T. Farley, B. B. Balsley, and R. F. Woodman. Vertical structure of the VHF backscattering region in the equatorial electrojet and the gradient drift instability, *J. Geophys. Res.*, **80**, 1313, 1975.

Fejer, B. G., D. T. Farley, B. B. Balsley, and R. F. Woodman. Radar studies of anomalous velocity reversals in the equatorial ionosphere, *J. Geophys. Res.*, **81**, 4621, 1976.

Fejer, B. G., D. T. Farley, R. F. Woodman, and C. Calderon. Dependence of equatorial F region vertical drifts on season and solar cycle, *J. Geophys. Res.*, **84**, 5792-5796, 1979.

Fejer, B. G., D. T. Farley, G. A. Gonzales, R. F. Woodman, and C. Calderon. F region east-west drifts at Jicamarca, *J. Geophys. Res.*, **86**, 215, 1981.

Fesen, C. G., G. Crowley, and R. G. Roble. Ionospheric effects at low latitudes during the March 22, 1979, geomagnetic storm, *J. Geophys. Res.*, **94**, 5405, 1989.

Fejer B. G., E. R. de Paula, S. A. Gonzales, and R. F. Woodman. Average vertical and zonal F region plasma drifts over Jicamarca, *J. Geophys. Res.*, **96**, 13901, 1991.

Fejer, B. G., and M. C. Kelley. Ionospheric Irregularities, *Rev. Geophys. Space Phys.*, **81**, 401-454, 1980.

Forbes, J. M., and Lindzen, R. S. Atmospheric solar tides and their electrodynamic effects - III. The polarisation electric field, *J. Atmos. Terr. Phys.*, **39**, 1369-1377, 1977.

Fournier, J. P., and A. F. Nagy. The contribution of photoelectron impact excitation to the total intensity of the 6300 Å dayglow, *J. Atmos. Sci.*, **22**, 732, 1965.

Francis, S. H. A theory of medium-scale travelling ionospheric disturbances, *J. Geophys. Res.*, **79**, 5245, 1974.

Fredricks, R. W., and F. W. Coroniti. Ambiguities in the deduction of rest frame fluctuation spectra computed in moving frames, *J. Geophys. Res.*, **81**, 5591-5595, 1976.

Friedman, J. F., and F. A. Herrero. Fabry-Perot interferometer measurements of thermospheric neutral wind gradients and reversals at Arecibo, *Geophys. Res. Lett.*, **9**, 785-788, 1982.

Fukao, S., T. Sato, R. M. Harper, and S. Kato. Radio wave scattering from the tropical mesosphere observed with the Jicamarca radar, *Radio Sci.*, **15**, 447, 1980.

Gdalevich, G. L., V. F. Gubsky, N. I. Izhovkina and V. D. Ozerov. Observation and theory of topside ionospheric plasma inhomogeneities, *J. Atmos. Solar Terr. Phys.*, **60**, 247-252, 1998.

Greenspan, J. A. Synoptic description of the 6300 Å nightglow near 78° west longitude, *J. Atmos. Terr. Phys.* **28**, 739, 1966.

Gonzales, C.A., M. C. Kelley, B. G. Fejer., J. F. Vickrey, and ,????? Equatorial electric fields during magnetically disturbed conditions 2. Implications of simultaneous auroral and equatorial measurements, *J. Geophys. Res.*, **84**, 5803, 1979.

Gurubaran, S. Investigations of low latitude thermosphere-ionosphere system, *Ph.D. Thesis*, Gujarat University, 1993.

Haerendal, G. Theory of equatorial spread-F, Report, Max-Planc-Institut. fur. Phys. Und. Astrophys., Garching, West Germany, 1974.

Haerendal, G., R. Lust, E. Rieger. Motion of artificial ion clouds in the upper atmosphere, *Planet. Space Sci.*, **15(1)**, 1967.

Haerendal, G. Investigation of the equatorial F-region with barium clouds: a review, paper presented at the 6th International Symposium on Equatorial Aeronomy, Sponsored by COSPAR, URSI, IUGG, and IAGA, Aguadilla, Puerto Rico, July 1980.

Hanson, W. B. Radiative recombination of atomic oxygen ions in the nighttime F region, *J. Geophys. Res.*, **74**, 3720-3722, 1969.

Hanson, W. B. A comparison of the oxygen ion-ion neutralisation and radiative recombination mechanisms for producing the ultraviolet nightglow, *J. Geophys. Res.*, **75**, 4343-4346, 1970.

Hanson, W. B., and D. K. Bamgboye. The measured motions inside equatorial plasma bubbles, *J. Geophys. Res.*, **89**, 8997, 1984.

Hanson, W. B., B. L. Cragin, and A. Dennis. The effect of vertical drift on the equatorial F region stability, *J. Atmos. Terr. Phys.*, **48**, 205-212, 1986.

Hanson, W. B., and Moffet, R. J. Ionisation transport effects in the equatorial F region, *J. Geophys. Res*, **71**, 5559, 1966.

Hanson, W. B., and S. Sanatani. Large N_i gradients below the equatorial F peak, *J. Geophys. Res.*, **78**, 1167-1173, 1973.

Hari, S. S., and B. V. Krishnamurthy. Seasonal variations of equatorial nighttime meridional winds, *J. Atmos. Terr. Phys.*, **57**, 1241-1246, 1995.

Harper, R. M., and R. F. Woodman. Preliminary multi height radar observations of waves and winds in the mesosphere over Jicamarca, *J. Atmos. Terr. Phys.*, **39**, 959, 1977.

Hays, P. B., D. W. Rusch, R. G. Roble and J. C. G. Walker. The OI (6300 Å) airglow), *Rev. of Geophys. and Space Phys.*, **16**, 225-232, 1978.

Heelis, R. A., P. C. Kendall, R. J. Moffett, D. W. Windle, and H. Rishbeth. Electrical coupling of the E and F regions and its effect on the F region drifts and winds, *Planet. Space. Sci.*, **22**, 743, 1974.

Heikkila, W.J. Aeronomy Report No. 10, An informal conference record edited by C.F. Sechrist and J.S. Shirke, University of Illionis, 1965.

Heikkila, W.J., N. Eaker, J.A. Fejer, K.R. Tipple, J. Hugill, D.E. Schneibel and W. Calvert. Comparison of several probe techniques for ionospheric electron concentration measurements, *J. Geophys. Res.* **73**, 3511, 1968.

Herrero, F A., and J. W. Meriwether. 6300 Å airglow meridional intensity gradients, *J. Geophys. Res*, **85**, 4191, 1980.

Herrero, F A., and N. W. Spencer. On the horizontal distribution of the equatorial thermospheric midnight temperature maximum and its seasonal variation, *Geophys. Res. Lett.*, **9**, 1179-1182, 1982.

Hines, C. O. Internal atmospheric gravity waves at ionospheric heights, *Can. J. Phys.*, **38**, 1441-1481, 1960.

Hines, C. O. Ionospheric movements and irregularities, *Research in Geophysics*, edited by H. Odishaw, p.299-318, MIT Press, Cambridge, Mass., 1964.

Hinteregger, H.E., K.R. Damon, and L.A. Hall. Analysis of photoelectrons from solar extreme ultraviolet, *J. Geophys. Res.*, **64**, 961, 1959.

Hudson, R. D. Critical review of ultraviolet photo-ionisation cross sections for molecules of astrophysical and aeronomic interest, *Rev. Geophys. Space Phys.*, **9**, 305, 1971.

Hudson, M. K. and C. F. Kennel. Linear theory of equatorial spread F, *J. Geophys. Res.*, **80**, 4581-4590, 1975.

Huang, C. S., and M. C. Kelley. Nonlinear evolution of equatorial spread F 1. On the role of plasma stabilities and spatial resonance associated with gravity wave seeding, *J. Geophys. Res*, **101**, 283-292, 1996a.

Huang, C. S., and M. C. Kelley. Non linear evolution of equatorial spread F 2. Gravity wave seeding of Rayleigh-Taylor instability, *J. Geophys. Res.*, **101**, 292-302, 1996b.

Hysell D. L., M. C. Kelley, W. E. Swartz, R. F. Pfaff and C. M. Swenson. Steepened structures in equatorial spread F 1. New Observations, *J. Geophys. Res.*, **99(A5)**, 8827-8840, 1994.

Hysell, D. L., M. C. Kelley, W. E. Swartz and R. F. Woodman. Seeding and layering of Equatorial spread F by gravity waves, *J. Geophys. Res.*, **95**, 17253-17260, 1990.

Iyer, K. N., and Chandra, H. Report on the third co-ordinated data analysis workshop of the satellite scintillation network during 12-17, April, 1993, Saurashtra University, Rajkot, 1993.

Jackson, J.E. and J.A. Kane. Measurement of ionospheric electron densities using an RF probe, *J. Geophys. Res.*, **64**, 1074, 1959.

Johnson, E.O., and L. Malter. A floating Double probe method for measurements in gas discharges, *Physical review*, **80**, 58, 1950.

Kashchekom, N. M., S. V. Matsiyevskiy, and M. A. Nikitin. Investigations of a non linear stage of development of Rayleigh Taylor instability in equatorial F region with allowance for longitudinal diffusion and the Pederson conductivity of the E region, *Geomagn. and Aeron.*, **29**, 442-446, 1989.

Kelley, M. C., R. C. Livingston, C. L. Rino, and R. T. Tsunoda. The vertical wave number spectrum of topside equatorial spread F: Estimates of backscatter levels and implications for a unified theory, *J. Geophys. Res.*, **87**, 5217, 1982.

Kelley, M. C. The earth's ionosphere, Plasma Physics and electrodynamics, Academic Press, San Diego, Calif, 1989.

Kelley. M. C. Equatorial spread F : Recent results and outstanding problems, *J. Atoms. Terr. Phys.*, **47**, 745-752, 1985.

Kelley, M. C., K. D. Baker, and J. C. Ulwick. Late time barium cloud striations and their possible relationship to equatorial spread F, *J. Geophys. Res.*, **84**, 1898, 1979.

Kelley. M. C., G. Haerendal, H. Kappler, A. Valenzuela, B. B. Balsley, D. A. Carter, W. L. Ecklund, C. W. Carlson, B. Hausler, and R. Torbert. Evidence for a Rayleigh-Taylor type instability and upwelling of depleted density regions during equatorial spread F, *Geophys. Res. Lett.*, **3**, 448-450, 1976.

Kelley. M. C., J. LaBelle, E. Kudeki, B. G. Fejer, S. Basu, Su. Basu, K. D. Baker, C. Hanuise, P. Argo, R .F. Woodman, W. E. Swartz, D. T. Farley, and J. Meriwether. The Condor equatorial spread F campaign : Overview and results of the large scale measurements, *J. Geophys. Res.*, **91**, 5487-5503, 1986.

Kelley, M. C., M. F. Larson, C. Lahoz, and J. P. McClure. Gravity wave initiation of Equatorial spread F : A case study, *J. Geophys. Res.*, **86**, 9087-9100,1981.

Kelley, M. C., and F. S. Mozer. A satellite survey of vector electric fields in the ionosphere at frequencies of 10 to 500 Hz, *J. Geophys. Res.*, **77**, 4183, 1972

Keskinen, M. J., and S. L. Ossakow. Preliminary report of numerical simulations of intermediate wavelength collisional Rayleigh-Taylor instability in equatorial spread F, *J. Geophys. Res.*, **85**, 1775-1778, 1980

Keskinen, M. J., and S. L. Ossakow. On the spatial power spectrum of the E X B gradient drift instability in ionospheric plasma clouds, *J. Geophys. Res.*, **86**, 6947, 1981.

Keskinen, M. J., E. P. Szuszczewicz, S. L. Ossakow, and J. C. Holmes. Nonlinear theory and experimental observations of the local collisional Rayleigh-Taylor instability in a descending Equatorial spread F ionosphere, *J. Geophys. Res.*, **86**, 5785-5792, 1981.

Kil Hyosub, and R. A. Heelis. Global distribution of density irregularities in the equatorial ionosphere, *J. Geophys. Res.*, **103(A1)**, 407-417, 1998.

King-Hele D. G., and Walker D. M. C Upper atmosphere zonal winds: variation with height and local time, *Planet Space Sci*, **25**, 313, 1977.Klostermeyer, J. Nonlinear investigation of the spatial resonance effect in the nighttime equatorial F region, *J. Geophys. Res.*, **83**, 3753-3760, 1978.

Knox, F. B. A contribution to the theory of the production of field aligned ionisation irregularities in the equatorial electrojet, *J. Atmos. Terr. Phys.*, **26**, 239, 1964.

Knudson, W. C. Tropical ultraviolet nightglow from ion-ion neutralisation, *J. Geophys. Res.*, **75**, 3862-3866, 1970.

Kochanski, A. Atmospheric motions from sodium cloud drift, *J. Geophys. Res.*, **69**, 3651-3662,1964.

Koparkar, P. V. and R. G. Rastogi. VHF radio scintillations at Bombay, *J. Atmos. Terr. Phys.*, **47**, 907, 1985.

Krishna Murthy, B. V., Hari, S. S., and Somayajulu, V. V. Nighttime equatorial thermospheric meridional winds from ionospheric h'F data, *J. Geophys. Res.*, **95(A4)**, 4307-4310, 1990.

Kudeki, E., B. G. Fejer, D. T. Farley, and H. M. Lerkic. Interferometer studies of equatorial F region irregularities and drifts, *Geophys. Res. Lett.*, **8**, 377, 1981.

Kudeki, E. Radar interferometer observations of mesospheric echoing layers at Jicamarca, *J. Geophys. Res.*, **93**, 5413, 1988.

Kudeki, E., and G. Stitt. Frequency domain interferometry studies of mesosphere layers at Jicamarca, *Radio sci.*, **25(4)**, 575, 1990.

Laakso, H., T. L. Aggson, F. A. Herrero, R. F. Pfaff, and W. B. Hanson. Vertical neutral wind in the equatorial F region deduced from J electric field and ion density measurements, *J. Atmos. Terr. Phys.*, **57**, 645-651, 1995.

Laakso, H., T. L. Aggson, and R. F. Pfaff. Downdrafting plasma flow in equatorial bubbles, *J. Geophys. Res.*, **99**, 507-11,515, 1994.

LaBelle, J., and M. C. Kelley. The generation of kilometer size irregularities in equatorial spread F, *J. Geophys. Res.*, **91**, 5504-5512, 1986.

LaBelle, J., M. C. Kelley, and C. E. Seyler. An analysis of the role of drift waves in equatorial spread F, *J. Geophys. Res.*, **91**, 5513-5525, 1986.

Linson, L. M.., and J. B. Workman. Formation of striations in ionospheric plasma clouds, *J. Geophys. Res.*, **75**, 3211, 1970.

Lyon, A. J., N. J. Skinner, and R. W. Wright. Equatorial spread-F at Ibadan, Nigeria, *J. Atmos. Terr. Phys.*, **21**, 100, 1961.

Maeda, K., T. Tsuda, and H. Maeda. Theoretical interpretation of the equatorial sporadic E layers, *Phys. Rev. Lett.*, **11**, 406, 1963.

Malcom, R., C. Miles, and B. A. Tinsley. Field aligned observations of transequatorial bubbles from Rarotonga in 1969-70, *Geophys. Res. Lett.*, **11(7)**, 665-668, 1984.

Martyn, D. F. Large-scale movements of ionisation in the ionosphere, *J. Geophys. Res.*, **64**, 2178, 1959.

Maruyama, T., and N. Matuura. Global distribution of occurrence probability of spread echoes based on ISS-b observation, *J. Radio Res. Lab. (Jpn.)*. **27**, 201, 1980.

Maruyama, T., and N. Matuura. Longitudinal variability of annual changes in activity of equatorial spread F and plasma bubbles, *J. Geophys. Res.*, **89**, 10,903-10,912, 1984.

Maruyama, T. A diagnostic model for equatorial spread F, 1, Model description and application to electric field and neutral wind effects, *J. Geophys. Res.*, **93**, 14611-14622, 1988.

Matsushita, S. Intense Es ionisation near the magnetic equator, *J. Geomagn. Geoelec.*, **3**, 44, 1951.

Mayr, H. G., I. Harris, N. W. Spencer, A. E. Hedin, L. E. Wharton, H. S. Porter, J. C. G. Walker and H. C. Carlon. Tides and the midnight temperature anomaly in the thermosphere, *Geophys. Res. Lett.*, **6**, 447-450, 1979.

McClure, J. P., and W. B. Hanson. A catalog of ionospheric F region irregularity behaviour based on Ogo 6 Retarding Potential Analyser data, *J. Geophys. Res.*, **78**, 31,7431-7440, 1973.

McClure, J. P., W. B. Hanson, and J. F. Hoffman. Plasma bubbles and irregularities in the equatorial ionosphere, *J. Geophys. Res.*, **82**, 2650-2656, 1977.

McFarland, M., D. L. Albritton, F. C. Fehsenfeld, E. E. Furguson, and A. L. Schmeltekopf. Flow-drift technique for ion mobility and ion-molecule reaction rate constant measurements. II. Positive ion reactions of N^+, O^+, and N_2^+ with O_2 and O^+ with N_2 from thermal to ~ 2 eV, *J. Chem. Phys.*, **59**, 6620-6628, 1973.

Mechtly, E.A., S.A. Bowhill, L.G. Smith, and H.W. Knoebel. Lower ionosphere electron concentration and collision frequency from rocket measurement of Faraday rotation, differential absorption and probe current, *J Geophys. Res.*, **72**, 5239, 1967.

Meek, C.E. and Manson, A.H. Measurements of structure and drift velocities of airglow (557.7 nm) irregularities: Saskatoon (52°N,107°W), Canada, *J. Atmos. Terr. Phys.*, **45**, 203, 1983

Mende, S. B., and E. H. Eather. Monochromatic all-sky observations and auroral precipitation patterns, *J. Geophys. Res.*, **81**, 3771-3780, 1976.

Mende, S. B., R. H. Eather, and E. K. Aamodt. Instrument for the monochromatic observation of all sky auroral images, *Appl. Opt.*, **16**, 1691, 1977.

Mendillo, M., and J. Baumbgarderner. Airglow characteristics of equatorial plasma depletions, *J. Geophys. Res.*, **87**, 7641, 1982.

Mendillo, M., J. Baumbgarderner, Pi, X.-Q., Sultan, P., Tsunoda, R. Onset conditions for equatorial spread F, *J. Geophys. Res.*, **97**, 13865, 1992.

Mendillo, M., and A. Tyler. Geometry of depleted plasma regions in the equatorial ionosphere, *J. Geophys. Res.*, **88(A7)**, 5778-5782, 1983.

Mendillo, M., J. Baumgardner, M. Colerico, and D. Nottingham. Imaging science contributions to equatorial aeronomy: initial results from the MISETA program, *J. Atmos. and Solar-Terr. Phys.*, **59**, 1587-1599, 1997a.

Mendillo, M., J. Baumbgarderner, D. Nottingham, J. Aarons, B. Renisch, J. Scali, and M. Kelley. Investigations of thermospheric-ionospheric dynamics with 6300 Å images from the Arecibo observatory, *J. Geophys. Res.*, **102(A4)**, 7331-7343, 1997b.

Meriwether, J. W., Jr., M. A. Biondi, and D. A. Anderson. Equatorial airglow depletions induced by thermospheric winds, *Geophys. Res. Lett.*, **12(8)**, 487-490, 1985.

Meriwether, J. W., Jr., C. A. Tepley, S. A. Price, P. B. Hays and L. L. Cogger. Remote ground-based observations of terrestrial airglow emission and thermospheric dynamics at Calgary, Alberta, Canada, *Opt. Eng.*, **22**, 128, 1983.

Metzer, P. A., and G. R. Cook. A reinvestigation of absorption cross sections of molecular oxygen in 1050-1800 Å, *J. Quant. Spectros. Radiat. Transfer*, **4**, 107, 1964.

Miller, K. L., D. G. Torr, and P. G. Richards. Meridional winds in the thermosphere derived from measurement of F_2 layer height, *J. Geophys. Res.*, **91**, 4531-4535, 1986.

Miller, C., M. Mendillo, W. Swartz, and M. Kelley. Observations of gravity - wave induced ionospheric electric fields at mid-latitudes, *EOS* 489, 1994.

Misawa, K. and Tabeuchi, I. Ground observations of the O_2(0-1) atmospheric bands at 8645 A and the [OI] 5577 A line, *J. Geophys. Res.*, **82**, 2410,1977.

Moore, J. G., and E. J. Weber. OI 6300 and 7774 Å airglow measurements of equatorial plasma depletions, *J. Atmos. Terr. Phys*, **43**, 851-858, 1981.

Moreels, G. and Herse, M. Photographic evidence of waves around 85 km level, 1977 *Planet. Spa. Sci.*, **25**, 265-273, 1977.

Morse, F. A., B. C. Edgar, H. C. Koons, C. J. Rice, W. J. Heikkila, J. H. Hoffman, B. A. Tinsley, J. D. Winningham, A. B. Christensen, R. F. Woodman, J. Pomalaza, and R. N. Teixeira. Equion, an equatorial ionospheric irregularity experiment, *J. Geophys. Res*, **82**, 578, 1977.

Mott-Smith, H., and Langmuir, I. The theory of collections in gaseous discharges, *Phys. Rev.*, **28**, 727, 1926.

Mukherjee, G. K., L. Carlo, and P. T. Patil. First all sky imaging observations from India, South Pacific STEP Workshop, University of Newcastle, Newcastle, Australia, July 5 - 9, 1993.

Muldrew, D. B. The formation of ducts and spread F and initiation of bubbles by field aligned currents, *J. Geophys. Res.*, **85**, 613, 1980a.

Muldrew, D. B. Characteristics of ionospheric bubbles determined from aspect sensitive scatter spread F observed with Alouette 1, *J. Geophys. Res*, **85**, 2115, 1980b.

Nelson and Cogger. Dynamical behaviour of the nighttime ionosphere at Arecibo, *J. Geophys. Res*, **33**, 1711, 1971. **????**

Nottingham, D., M. Mendillo, J. Baumgardner and M. Kelley. 6300 Å airglow wave structure from Aercibo in January 1993, *EOS,* 488, 1994.

Noxon, J. F. Day airglow, *Space Sci. Rev.*, **8**, 92-134, 1968.

Noxon, J. F., and A. E. Johanson. Changes in thermospheric O2 abundance inferred from twilight 6300 Å airglow, *Planet Space Sci.*, **20**, 2125, 1972.

Olsen, R. E., J. R. Peterson, and J. Moseley. Oxygen ion-ion neutralisation reaction as related to tropical ultraviolet nightglow, *J. Geophys. Res.*, **76**, 2516-2519, 1971.

Ossakow, S. L. Spread F theories - A review, *J. Atmos. Terr. Phys.*, **43**, 437-452, 1981.

Ossakow, S. L., S. T. Zalesak, B. E. McDonald, and P. K. Chaturvedi. Nonlinear Equatorial spread F: Dependence on altitude of the F peak and bottomside background electron density gradient scale length, *J. Geophys. Res.*, **84**, 17-29, 1979.

Pal S., S. Prakash, Y. B. Acharya and R. N. Misra. A payload for the study of electric field and electron density in the equatorial region, *Adv. Space Res.* **2**, 57-59, 1983.

Pal S. Studies in equatorial aeronomy, Ph.D. Thesis, Submitted to Gujarat University, 1985.

Pallam Raju, D., Sridharan, R., Gurubaran, S. and Raghavarao, R. First results from ground based daytime optical investigations of the development of Equatorial Ionisation Anomaly, *Ann. Geophys.*, **14**, 238-245, 1996.

Peterson, A. W. and Kieffaber, L. M. Infrared photography of OH airglow structures, *Nature*, **242**, 321, 1973.

Prakash. S., Generation of perturbation electric fields suitable for triggering of equatorial spread-F by gravity waves in the E-region and zonal winds in the F-region, *Indian J. Rad. & Space Phys.*, Vol. 25, 211-277, 1996.

Prakash, S., S. P. Gupta, and B. H. Subbaraya. A study of the irregularities in the night time equatorial E region using a Langmuir probe and plasma noise probe, *Planet space Sci.*, **18**, 1307, 1970.

Prakash S. and P. Muralikrishna, E and F region electric fields over dip equator, *J. Geophys. Res.*, Vol. 86, 2095-2098, 1981.

Prakash, S., S. Pal, and H. Chandra. In-situ studies of equatorial spread F over SHAR- steep gradients in the bottomside F-region and transitional wavelength results., *J. Atmos. Terr. Phys.*, **53**, 977-986, 1991.

Prakash, S., and Pandey R. On the production of large scale irregularities in the equatorial F region, *Int. Symp. Equatorial Aeronomy*, 6th 3-7, 1980.

Prakash S., and B. H. Subbaraya. Langmuir probe for the measurement of electron density and electron temperature in the ionosphere, *Rev. Sci. Inst.*, **38**, 1132-1136, 1967.

Prakash S., B. H. Subbaraya and S. P. Gupta. Rocket measurements of ionisation irregularities in the equatorial ionosphere at Thumba and identification of plasma instabilities, *Ind. J. Rad. Space Phys.*, **1**, 72-80, 1972.

Raghavarao R., J. N. Desai, B. G. Anandarao, R. Narayanan, R. Sekar, Ranjan Gupta, V. V. Babu, and V. Sudhakar. Evidence for the large scale electric field gradient at the onset of equatorial spread F, *J. Atmos. Terr. Phys.*, **46**, 355-362, 1984.

Raghava Rao R., S. P. Gupta, R. Sekar, R. Narayanan, J. N. Desai, R. Sridharan, V. V. Babu, and V. Sudhakar. In situ measurements of wind, electric fields and electron densities at the onset of equatorial spread F, *J. Atmos. Terr. Phys.*, **49**, 485-492, 1987.

Raganath Rao, H. N., and J. H. Sastri. Characteristics of the equatorial midnight temperature maximum in the Indian sector, *Ann. Geophys.*, **12**, 276-278, 1994.

Rao, T. R. and S. Prakash. Electron Plasma resonances detected by a mutual admittance probe in the equatorial ionosphere, *Space Research*, **XVIII**, 281-283, 1978.

Rastogi, R. G. Seasonal variation of equatorial spread F in the American and Indian zones, *J. Geophys. Res.*, **85**, 722, 1980.

Rastogi, R. G., H. Chandra, and R. K. Misra. Features of the ionospheric drift over the magnetic equator, *Space Res.* **XII**, 983-992, 1972.

Rastogi, R. G., and R. F. Woodman. Spread F in equatorial ionograms associated with reversal of horizontal F region electric field, *Ann Geophys.*, **34**, 31, 1978.

Richmond, A. D. Equatorial electrojet- I Development of a model including winds and instabilities, *J. Atmos. Terr. Phys.*, **35**, 1083, 1973.

Rino. C. L., R. T. Tsunoda, J. Petriceks, R. C. Livington, M. C. Kelley, and K. D. Baker. Simultaneous rocket-borne beacon and in situ measurements of equatorial spread F, *J. Geophys. Res.*, **86**, 2411, 1981.

Rees, M. H., J. C. G. Walker, and A. Dalgarno. Auroral excitation of the forbidden lines of atomic oxygen, *Planet Space Sci.*, **15**, 1097, 1967.

Reid, G. C. The formation of small scale irregularities in the ionosphere, *J. Geophys. Res.*, **73**, 1627, 1968.

Rishbeth, H. Polarisation fields produced by winds in the ionospheric F region, *Planet. Space. Sci.*, **19**, 357, 1971.

Rishbeth, H. F region storms and thermospheric circulation, *J. Atmos. Terr. Phys.*, **37**, 1055-1064, 1975.

Rishbeth, H. The F-region dynamo, *J. Atmos. Terr. Phys.*, **43**, 387-392, 1981.

Rishbeth, H., S. Ganguly, and J. C. G. Walker. Field-aligned and field perpendicular velocities in the ionospheric F_2-layer, *J. Atmos. Terr. Phys.*, **40**, 767-784, 1978.

Rishbeth, H., and O. K. Garriott. Introduction to ionospheric physics, Academic Press, New York, 1969.

Rishbeth, H., R. Gordon, D. Rees, and T. J. Fuller-Rowell. Modelling of thermospheric composition changes caused by a severe magnetic storm, *Planet. Space Sci.*, **33**, 1283, 1985.

Roach, F. E. Variations of [OI] 5557 Å emission in the upper atmosphere, *Ann Geophys.*, **17**, 172, 1961.

Roble, R. G., R. E. Dickinson, and E. C. Ridley. Global circulation and temperature structure of the thermosphere with high latitude plasma convection, *J. Geophys. Res*, **87**, 1599, 1982.

Rodrigo, R., Lopez-Monero, Lopez-Puertas, M. and Molina, A. Analysis of OI 557.7 nm NaD, OH(6-2) and $O_2(^1\Sigma)$(0-1) nightglow emissions from the ground based observations, *J. Atmos. Terr. Phys.*, **47**, 1099, 1985.

Rogister, A., and N. D'Angelo. Type 2 irregularities in the equatorial electrojet, *J. Geophys. Res.*, **75**, 3819, 1970.

Rohrbaugh, R. P., Tinsley, B. A., Rassoul, H., Sahai, T., Teixeira, N. R., Tull R. G., Doss, D. R., Cochran, W. D., and Barker, E. S. Observations of optical emissions from precipitation of energetic neutral atoms and ions from the ring current, *J. Geophys. Res.*, **88**, 6317, 1983.

Rohrbaugh, R. P., W. B. Hanson, B. A. Tinsley, B. L. Cragin and J. P. McClure. Images of transequatorial bubbles based on field-aligned airglow observations from Haleakala in 1984-1986, *J. Geophys. Res.*, **94**, 6763-6770, 1989.

Rosenbluth M. N., and N. Rostoker. Scattering of electromagnetic waves by a non equilibrium plasma, *Phys. Fluids*, **5**, 776, 1962.

Röttger, J. Wave like structures of large scale equatorial spread F irregularities, *J. Atmos. Terr. Phys.*, **35**, 1195, 1973.

Röttger, J. The macro-scale structures of equatorial spread F irregularities, *J. Atmos. Terr. Phys.*, **38**, 97, 1976.

Röttger, J. Drifting patches of equatorial spread F irregularities-experimental support for the spatial resonance mechanism in the ionosphere, *J. Atmos. Terr. Phys.*, **40**, 1103-1112, 1978.

Royrvik, O. VHF radar signals scattered from the equatorial mesosphere, *Radio Sci.*, **18**, 1325, 1983.

Sahai, Y., J. A. Bittencourt, N. R. Teixeira, and H. Takahashi. Plasma irregularities in the tropical F-region detected by OI 7774 A and 6300 A nightglow measurements, *J. Geophys. Res.*, **86**, 3496-3500, 1981.

Sahai, Y., Bittencourt, J. A., Takahashi, H., Teixeira, N. R., Sobral, J. H. A., Tinsley, B. A., and Rohrbaugh, R. P. Multispectral optical observations of ionospheric F region storm effects at low latitude, *Planet Space Sci.*, **36**, 371-381, 1988.

Sahai, Y., Aarons J., Mendillo, M., Baumgarderner J., Bittencourt J. A. and Takahashi H. OI 630 nm imaging observations of equatorial plasma depletions at 16° dip latitude, *J. Atmos. Terr. Phys.*, **56**, 1461-1475, 1994a.

Sahai, Y., Aarons J., Mendillo, M., Takahashi H., Abdu M. A. and Paula E. R. Studies of storm-time equatorial, *Low latitude Ionospheric Physics*, Kuo F. S. ed., Pergamon , 135-142, 1994b.

Sato, T., T. Tsuda, and K. Maeda. Fully developed turbulent irregularities in the ionosphere due to cross field plasma instability, *Radio Sci.*, **3**, 529, 1968.

Satyanaryana, P., P. N. Guzdar, J. D. Huba, and S. L. Ossakow. Rayleigh-Taylor instability in the presence of a stratified shear layer, *J. Geophys. Res.*, **89**, 2945-2954, 1984.

Sayers J. Aeronomy report No. 1, University of Illinois, 1963.

Scannapieco. A. J., and S. L. Ossakow. Non-linear Equatorial spread F, *Geophys. Res. Lett.*, **3**, 451-454, 1976.

Sekar, R., and R. Raghavarao. Role of vertical winds on the Rayleigh-Taylor instability mode of the nightime equatorial ionosphere, *J. Atmos. Terr. Phys.*, **49**, 981-985, 1987.

Sekar R, R. Sridharan and R. Raghavarao. Equatorial plasma bubble evolution and its role in the generation of irregularities in the lower F region, *J. Geophys. Res.*, **102**, 20,063-20,067, 1997.

Sekar, R., R. Suhasini, and R. Raghavarao. Evolution of plasma bubbles in the equatorial F region with different seeding conditions, *Geophys. Res. Lett.*, **22**, 885-888, 1995.

Sharma, R. P., and D. B. Muldrew. Seasonal and longitudinal variations in the occurrence frequency of magnetospheric ionisation ducts, *J. Geophys. Res.*, **80**, 977, 1975.

Simon, A. Instability of a partially ionised plasma in crossed electric and magnetic fields, *Phys. Fluids*, **6**, 382, 1963.

Singh, S., D. K. Bamgboye, J. P. McClure, and F. S. Johnson. Morphology of equatorial plasma bubbles, *J. Geophys. Res.*, **102(A9)**, 20,019-20,029, 1997b.

Singh, S., F. S. Johnson, and R. A. Power. Gravity wave initiation of equatorial plasma bubbles, *J. Geophys. Res.*, **102(A4)**, 7399-7410, 1997a.

Sinha, H.S.S., *PhD. Thesis*, Gujarat Univ., 1976.

Sinha, H. S. S., H. Chandra, R. N. Misra and S. Prakash. Optical imaging of plasma depletions associated with equatorial spread-F, *XX General Assembly, IUGG, Vienna*, pp 248, 1991

Sinha, H. S. S. Plasma density irregularities in the equatorial D-region produced by neutral turbulence, *J. Atmos. Terr. Phys.*, **54**, 49-61, 1992.

Sinha, H. S. S., and S. Prakash, Electron densities in the equatorial lower ionosphere over Thumba and SHAR, *Ind. J. of Rad. and Space Phys*, **24**, 184-192, 1995.

Sinha, H. S. S., R. N. Misra, H. Chandra, Shikha Raizada, N. Dutt and G. D. Vyas. Multi-Wavelength optical imaging of ionospheric plasma depletions, *Ind. J. Rad. and Space Phys.* **25**, 44-52, 1996.

Sipler, D. P., and M. A. Biondi. Equatorial F region neutral winds from nightglow OI 630.0 nm Doppler shifts, *Geophys. Res. Lett.*, **5**, 373-376, 1978.

Sobral, J. H. A., M. A. Abdu, and Y. Sahai. Equatorial plasma bubble eastward velocity characteristics from scanning airglow photometer measurements over Cachoeira Paulista, *J. Atmos. Terr. Phys.*, **47**, 895-900, 1985.

Sobral, J. H. A., H. C. Carlson, D. T. Farley, and W. E. Swartz. Nighttime dynamics of the F-region near Aericibo as mapped by airglow features, *J. Geophys. Res*, **83**, 2561, 1978.

Spencer, N. W., G. R. Carigan, H. G. Mayr, H. B. Niemann, R. F. Theis, and L. E. Wharton. The midnight temperature maximum in the earth's equatorial thermosphere, *Geophys. Res. Lett.*, **6**, 444, 1979.

Sridharan, R., S. Gurubaran, and R. Suhasini. Co-ordinated thermospheric and F region measurements from low latitudes, *J. Atmos. Terr. Phys.*, **53**, 515-519, 1991.

Sridharan, R., Haider, S. A., Gurubaran, S., Sekar, R. and Narayanan, R. OI 630.0 nm dayglow in the region of equatorial ionisation anomaly: Temporal variability and its causative mechanism, *J. Geophys. Res*, **97**, 13715-13721, 1992.

Sridharan, R., H. Chandra, S. R. Das, R. Sekar, H. S. S. Sinha, D. Pallam Raju, R. Narayanan, Shikha Raizada, R. N. Misra, R. Raghavarao, P. B. Rao, P. V. S. Ramarao, V. V Somayajulu, V. V. Babu and A. D. Danilov. Ionisation hole campaign– a co-ordinated rocket and ground based study at the onset of equatorial spread-F: First results, *J. Atmos. Terr. Phys.*, **59**,16,2051-2067,1997.

Sridharan, R., Pallam Raju, D., Raghavarao, R., and Ramarao, P. V. S. Precursor to equatorial spread-F in OI 630 nm dayglow, *Geophys. Res. Lett*, **21**, 2797-2800, 1994.

Subbarao, K. S. V., and B. V. Krishna Murthy. F-region vertical velocity and its fluctuations at the magnetic equator, *Ind. J. Rad. Space Phys.*, **12**, 94-96, 1983.

Subbaraya, B. H., S. Prakash and S. P. Gupta. Electron densities in the equatorial lower ionosphere from the Langmuir probe experiments conducted at Thumba during the years 1966-1978, *ISRO Report, ISRO-PRL-SR-15-83*, 1983.

Sudan R. N., J. Akinrimisi, and D. T. Farley, Jr. Generation of small scale irregularities in the equatorial electrojet, *J. Geophys. Res.*, **78**, 240, 1973.

Sugiura M., and Poros, D. J. An improved model equatorial electrojet with a meridional current system, *J. Geophys. Res*, **74**, 4025, 1969.

Szuszczewicz, E. P., and Takacs, P. Z. Magnetosheath effects on cylindrical Langmuir probes, *Phys. Fluids*, **22**, 2424, 1979.

Szuszczewicz, E. P., R. T. Tsunoda, R. Narcisi, and J. C. Holmes. Coincident radar and rocket observations of equatorial spread F, *Geophys. Res. Lett.*, **7**, 537, 1980.

Szuszczewicz, E. P., R. T. Tsunoda, R. Narcisi, and J. C. Holmes. Plumex II: A second set of coincident radar and rocket observations of equatorial spread **F**, *Geophys. Res. Lett.*, **8**, 803-806, 1981.

Takahashi, H., Batista, P.P., Sahai, Y. and Clemsha, B. R. Atmospheric wave propagation in the mesopause region observed by the OH (8-3) band, Na-D, O_2 A(8645 A) band and OI 5577 A nightglow emissions, *Planet. Spa. Sci.*, **33**, 381, 1985.

Takahashi, T., H. Oya, and Watanabe, S. Ionospheric Disturbances induced by substorm associated electric fields in the low latitude F region, *J. Geomag. Geoelectr.*, **39**, 187, 1987.

Tanaka, T. Low latitude ionospheric disturbances: Results for March 22, 1979, and their general characteristics, *Geophys. Res. Lett.*, **13**, 1399, 1986.

Tapely, C.A., Burnside, R. G. and Meriwether, J. W. Horizontal thermal structure of the mesosphere from observations of OH(8-3) band emissions, *Planet. Spa. Sci.*, **29**, 1241, 1981.

Taylor, M. J., J. V. Eccles, J. LaBelle, and J. H. A. Sobral. High resolution OI (630 nm) image measurements of F-region depletion drifts during the Guará campaign, *Geophys. Res. Lett.*, **24(13)**, 1699-1702, 1997.

Temerin M. Doppler shift effects on double probe measured electric field power spectra, *J. Geophys. Res*, **84**, 5929-5934, 1979.

Testud, J., and P. Francois. Importance of diffusion processes in the interaction between neutral waves and ionisation, *J. Atmos. Terr. Phys*, **33**, 765, 1971.

Tinsley, B. A., R. Rohrbaugh, H. Rassoul, Y. Sahai, N. R. Teixeira and D. Slater. Low latitude aurorae and stormtime current system, *J. Geophys. Res.*, **91**, 11257, 1986.

Tinsley, B. A., and Bittencourt J. A. Determination of F-region height and peak electron density at night using airglow emissions from atomic oxygen, *J. Geophys. Res.*, **86**, 2333-2337, 1975.

Tinsley, B. A., A. B. Christensen, J. Bittencourt, H. Gouveia, P. D. Angreji, and H. Takahashi. Excitation of oxygen permitted line emissions in the tropical nightglow, 78, No. 7, *J. Geophys. Res.*, 1973.

Tinsley, B. A., Rohrbaugh R. P., Sahai Y., and Teixeira, N. R. Low latitude aurorae and stormtime current system, *Geophys. Res. Lett.*, **9**, 543-546, 1982.

Tinsley, B. A., R. P. Rohrbaugh, and W. B. Hanson. Images of transequatorial F region bubbles in 630- and 777-nm emissions compared with satellite measurements, *J. Geophys. Res.*, **102(A2)**, 2057-2077, 1997.

Titelbaum, H. and Petitdedier, M. Nighttime variations of short period fluctuations (2-15 min) in the oxygen green line, *J. Atmos. Terr. Phys.*, **40**, 223, 1978.

Tsuda, T., T. Sato, and K. Madea. Formation of sporadic E layers at temperature latitudes due to vertical gradients of charge density, *Radio Sci.*, **I**, 212, 1966.

Tsunoda, R. T. On the spatial relationship of 1-m equatorial spread F irregularities and plasma bubbles, *J. Geophys. Res.*, **85**, 185, 1980.

Tsunoda, R. T., and B. R. White. On the generation and growth of equatorial backscatter plumes 1. Wave structure in the bottomside F layer, *J. Geophys. Res.*, **86**, 3610-3616, 1981.

Tsunoda, R. T., R. C. Livingston, and C. L. Rino. Evidence of a velocity shear in bulk plasma motion associated with the post sunset rise of the F layer, *Geophys. Res. Lett.*, **8**, 807-810, 1981.

Tsunoda, R. T. Time evolution and dynamics of equatorial backscatter plumes 1. Growth phase, *J. Geophys. Res.*, **86**, 139-149, 1981.

Tsunoda, R. T., R. C. Livingston, J. P. McClure, and W. B. Hanson. Equatorial plasma bubbles: vertically elongated wedges from the bottomside F layer, *J. Geophys. Res.*, **87**, 9171, 1982.

Tsunoda, R. T. On the generation and growth of equatorial backscatter plume 2. structuring of the west walls of upwelling, *J. Geophys. Res.*, **88**, 4869-4874, 1983.

Tsunoda, R. T. Control of the seasonal and longitudinal occurrence of equatorial scintillations by the longitudinal gradient in integrated E region Pederson conductivity, *J. Geophys. Res.*, **90**, 447-456, 1985.

Tsunoda, R. T., and D. M. Towle. On the spatial relationship of 1-m equatorial spread F irregularities and depletions in total electron content, *Geophys. Res. Lett.*, **6**, *11*, 873-876, 1979.

Untiedt, J. A model of the equatorial electrojet involving meridional currents, *J. Geophys. Res*, **72**, 5799, 1967.

Valladares, C. E., W. B. Hanson, J. P. McClure, and B. L. Cragin. Bottomside sinusoidal irregularities in the equatorial F region, *J. Geophys. Res.*, **88**, 8025-8042, 1983

Van Zandt, T. E., and V. L. Peterson. Detailed maps of tropical 6300 Å nightglow enhancements and their implications on the ionospheric F2 layer, *Ann. Geophys.*, **224**, 747, 1968.

Vats Hari Om, H. Chandra, M. R. Deshpande, R. G. Rastogi, B. S. Murthy, A. V. Janve, R. K. Rai, Malkiat Singh, H. S. Gurm, A. R. Jain, V. M. Patwari, and B. S. Subbarao. Equatorial irregularity belt and its movements during a magnetic storm, *Nature*, **272**, 345, 1978.

Vickrey, J. F., and M. C. Kelley. The effects of a conducting E layer on classical F region cross-field diffusion, *J. Geophys. Res.*, **87**, 4461, 1982.

Vickrey, J. F., M. C. Kelley, R. Pfaff, and S. R. Goldman. Low-altitude image striations associated with bottomside equatorial spread F: Observations and theory, *J. Geophys. Res.*, **89**, 2955, 1984.

Viswanathan, K. S., R. Balachandran Nair, and P. B. Rao. Simultaneous observations of E and F region electric field fluctuations at the magnetic equator, *J. Atmos. Terr. Phys.*, **55**, 185-192, 1993.

Wallace, L., and M. B. McElroy. The visual airglow, *Planet. Space Sci.*, **14**, 677, 1966.

Weber, E. J., J. Buchau, R. H. Eather, and S. B. Mende. North-south aligned equatorial airglow depletions, *J. Geophys. Res.*, **83**, 712, 1978.

Weber, E. J., J. Buchau, and J. G. Moore. Airborne studies of equatorial F layer Ionospheric irregularities, *J. Geophys. Res.*, **85**, A9, 4631-4641, 1980.

Weil, G., and J. Joseph. Premiers measures du triplet 3^5S^0-3^5P de OI, á 7772, 7774, et 7775 Å emis par le nocturne des régions tropicales, *C. R. Acd. Sci., Ser.* B, **271**, 1013-1016, 1970.

Whitehead, J. D. Instabilities in a gradient of ionisation and sporadic E, *J. Atmos. Terr. Phys.*, **29**, 1285, 1967.

Whitehead, J. D. Low frequency plasma instabilities in the ionosphere, *J. Atmos. Terr. Phys.*, **30**, 1563-1579, 1968.

Whitehead, J. D. Ionisation disturbances caused by gravity waves in presence of an electric field and background wind, *J. Geophys. Res.*, **76**, 238, 1971.

Woodman, R. F. Vertical drift velocities and east-west electric fields at the magnetic equator, *J. Geophys. Res.*, **75**, 6249-6259, 1970.

Woodman, R. F. Rastogi, R. G. and Calderon C. Solar cycle effects on the electric fields in the equatorial ionosphere, *J. Geophys. Res.*, **82**, 5257, 1977.

Woodman, R. F., and C. LaHoz. Radar observations of F region equatorial irregularities, *J. Geophys. Res.*, **81**, 5447-5466, 1976.

Woodman, R. F., D. L. Sterling, and W. B. Hanson. Synthesis of Jicamarca data during the great storm of March 8, 1970, *Radio Sci.*, **7**, 739-746, 1972.

Woodman, R. F. East-west ionospheric drifts at the magnetic equator, *Space Res.*, **12**, 969-974, 1972.

Woodman, R. F. Equatorial ionospheric irregularities as observed by the Jicamarca radar, *Low Lat. Ionos. Phy.*, 83, 1993.

Wright, J. W. Horizontal drifts accompanying large vertical motions of the nocturnal F-region, *Planet Space Sci.*, **19**, 1327, 1971.

Yee, J. H. and V. J. Abreu. Abstract IAGA paper GA2.2, IUGG XIX General Assembly, Vancouver, Canada, p.4, 9-22 August, 1987.

Yeh, K. C., and C. H. Liu. Acoustic gravity waves in the upper atmosphere, *Rev. Geophys.*, **12**, 193, 1974.

Yeh, K. C., J. P. Mullen, J. R. Medeiros, R. F. da Silva, and R. T. Medeiros. Ionospheric scintillation observations at Natal, *J. Geophys. Res.*, **86**, 7527-7532, 1981.

Zalesak, S. T., and S. L. Ossakow. Nonlinear Equatorial spread F : Spatially large bubbles resulting from large horizontal scale initial perturbations, *J. Geophys. Res.*, **85**, 2131, 1980.

Zalesak, S. T., and S. L. Ossakow. Equatorial spread F modelling, *Phys. of Space Plasma, SPI conference poceedings and reprint series, 5,* 25-51, 1982.

Zalesak, S. T., and S.L.Ossakow, and P. K. Chaturvedi. Nonlinear Equatorial spread F : The effects of neutral winds and background Pederson conductivity, *J. Geophys. Res.*, **87**, 151-166, 1982.